Grain Size Effect in Lead-Free $Bi_{0.5}Na_{0.5}TiO_3$-based Materials: Exploring the Ferroelectric Behaviour

Ruth A. McKinnon

Submitted in partial fulfilment of the requirements

of the Degree of Doctor of Philosophy

School of Engineering and Materials Science,

Queen Mary, University of London,

London, UK

December 2015

Declaration

I, Ruth Agnes McKinnon, confirm that the research included within this thesis is my own work or that where it has been carried out in collaboration with, or supported by others, that this is duly acknowledged below and my contribution indicated. Previously published material is also acknowledged below.

I attest that I have exercised reasonable care to ensure that the work is original, and does not to the best of my knowledge break any UK law, infringe any third party's copyright or other Intellectual Property Right, or contain any confidential material.

I accept that the College has the right to use plagiarism detection software to check the electronic version of the thesis.

I confirm that this thesis has not been previously submitted for the award of a degree by this or any other university.

Signature: Ruth McKinnon
Date: 21/12/15

Details of collaboration and publications:
Papers to be submitted: Grain Size Effect on $Bi_{0.5}Na_{0.5}TiO_3$, Grain Size Effect on $Bi_{0.5}Na_{0.5}TiO3$-6%$BaTiO_3$.

Collaboration with Dr. Florian Le Goupil at Imperial College London, paper on ECE effect in $Bi_{0.5}Na_{0.5}TiO_3$ -based materials, in review.

Abstract

High density ceramics of lead-free $Bi_{0.5}Na_{0.5}TiO_3$ (BNT) and 94%$Bi_{0.5}Na_{0.5}TiO_3$ - 6%$BaTiO_3$ (BNBT-6), ranging in grain size from 80 nm to 10μm, were successfully sintered from nanometre and micrometre grain size powders by spark plasma sintering and conventional sintering techniques. High temperature X-ray diffraction (XRD) was used to determine the crystal structure of the crushed ceramics while domain imaging techniques including back-scattered scanning electron microscopy and piezoresponse force microscopy were used to examine the microstructure. The influence of grain size on the intrinsic and extrinsic properties was investigated by measuring the temperature and frequency dependence of the dielectric response as well as the ferroelectric and piezoelectric properties in the unpoled and electrically poled states.

Grain size was shown to influence the room temperature defect structure in BNT, transforming the average crystal structure from rhombohedral *R3c* to monoclinic C_c with reducing grain size. The increase in dielectric permittivity with decreasing grain size observed in this material is caused by high domain wall density linked with a cross-hatched domain pattern. This finding is consistent with the literature which identifies interactions between domain walls and antiphase boundaries or tetragonal platelets as the source of the C_c nanotwin defect structure. High grain boundary density was found to restrict the electric field induced C_c-to-*R3c* transition, maintaining the multi-domain defect structure. The depoling temperature T_d associated with the *R3c*-to- C_c transition occurs at higher temperatures for larger micrograin size BNT ceramics but is independent of electric field strength. Grain boundaries are expected to have less impact on the structure of these BNT ceramics allowing the long-range *R3c* ferroelectric order to be retained to higher temperatures. Evidence of a critical grain size for ferroelectricity was not found within the investigated grain size range, however a decrease in dielectric permittivity with further reduction in grain size for ceramics with nanometer ($\leq$ 100 nm) grains suggest a grain size limit may exist for the C_c defect structure in BNT. Alternatively, the C_c defect structure may still occur and instead the reduction in dielectric permittivity results from a dilution effect caused by the high density of grain boundaries.

Grain size affects both the temperature and the permittivity value of the high temperature T_m peak, measured at 100 kHz, in BNT. T_m broadens and shifts to higher temperatures as the grain size is reduced while the increased stress exerted at the grain boundaries of the smaller grains hinders the domain wall motion suppressing the permittivity value. Although no static structural transition takes place at T_m in BNT, a gradual change in structure occurs as the *P4bm* phase increases at the expense of the *R3c*/*Cc* structure. A larger number of domain states are thought to be offered by the phase below T_m making it more stress accommodating.

Room temperature crystal structure analysis reveal a pseudo-cubic distortion of *R3c* and *P4bm* symmetries in ceramic BNBT-6 which transform to a $Pm\bar{3}m$/*P4bm* mixed phase with decreasing grain size. While the $Pm\bar{3}m$(*R3c*)/*P4bm* structure provided the best fit, the XRD data is not wholly satisfied by this refinement. Mechanical impact has a similar effect as a weak poling field on the structure of the morphotropic phase boundary (MPB) composition and may account for the uncertainty surrounding the unpoled structure. A herring-bone domain pattern consistent with a *P4mm* structure was observed in the micrograin ceramics. As the grain size is reduced the dielectric permittivity decreases. Either fewer domain walls occur in the smaller grains or their movement is restricted. Electrical poling in strong electric fields promotes the *R3c* symmetry in the micrograin ceramic while the increased density of grain boundaries in the smaller grain ceramics opposes domain reversal limiting the decrease in dielectric permittivity induced by poling. The field-strength dependence of T_d is consistent with the field-induced phase separation reported in the literature. Further evidence of a field induced *P4bm*-to-*P4mm*-to-*R3c* multiphase transition is provided by P-I-E loop tests.

The position of the high temperature permittivity peak T_m is independent of grain size, particularly the range investigated in this study. The polar nanoregions forming the domain structure of the MPB composition are thought to be too small for their dynamics to be significantly affected by grain size. The increased stress exerted at the grain boundaries of the smaller grains, however is believed to hinder the domain wall motion suppressing the permittivity value at T_m. This result is consistent with the grain size effect observed in other MPB compositions, including $Na_{0.5}K_{0.5}NbO_3$.

Acknowledgments

I would like to thank my supervisor Dr Haixue Yan for all of his support and guidance throughout my PhD.

I would especially like to thank Dr. Isaac Abrahams and Dr. Rory Wilson for their help with XRD structural analysis and refinement, Dr. Serban Lepadatu at NPL, Teddington who helped me with PFM imaging and Xin Gao and Prof. Zhijian Shen at Stockholm University, Sweden for their expertise in back-scattered SEM. I would also like to thank Dr. Qinghui Jiang who provided the sol-gel nano-powders of my compositions and Dr. Nadja Tarakina at Nanovision who helped me with TEM analysis.

I would like to thank everyone in the Ceramics group for their support and friendship.

I would like to acknowledge Knowles (UK) Ltd. and Nanoforce Technology Ltd. who provided funding for my PhD. This work was supported by EPSRC

Finally, I would like to thank my family and friends for all of their support and in particular my long suffering partner Quinlan Windle.

Glossary

AFE:	Antiferroelectric
APB:	Antiphase boundary
BNBT-6:	$94\%Bi_{0.5}Na_{0.5}TiO_3$-$6\%BaTiO_3$
BNT:	$Bi_{0.5}Na_{0.5}TiO_3$
BT:	$BaTiO_3$
C:	Cubic
CORs:	Chemically ordered regions
DC:	Direct current
d_{33}:	Piezoelectric coefficient
E_c:	Coercive field
FC:	Field cooling
FE:	Ferroelectric
FH:	Field heating
FH af. FC:	Field heating after field cooling
GPZs:	Guinier Preston zones
M:	Monoclinic
NT:	Nanotwin
O:	Orthorhombic
pC:	Pseudo-cubic
PDF:	Pair distribution function
PE:	Paraelectric
PFM:	Piezoresponse force microscopy
P-I-E loops:	Polarisation-current-electric field loops
PLM:	Polarised light microscopy
PNR:	Polar nanoregion
P_r:	Remnant polarisation
P_{sa}:	Saturated polarisation
R:	Rhombohedral
RFs:	Randomly ordered, local electric fields
RMC:	Reverse Monte Carlo
ρ:	Relative density (actual/theoretical)
SEM:	Scanning electron microscopy
SHG:	Second harmonic generation

SPS:	Spark Plasma Sintering
STA:	Simultaneous thermal analysis
T:	Tetragonal
TEM:	Transmission electron microscopy
TP:	Tetragonal Platelets
T_B:	Burns temperature
T_C:	Curie point
T_d:	Depolarisation temperature
T_{db}:	Depoling temperature in an applied DC bias-field
T_{do}:	Depoling temperature after cooling in an applied DC bias-field
T_f:	Freezing temperature
T_m:	Relaxor dielectric permittivity peak
T_{me}:	Elastic compliance peak
T_{mp}:	Melting point
T_{RE}:	Relaxor transition temperature
T_s:	Shoulder in dielectric permittivity
T_{VF}:	Vogel-Fulcher freezing temperature
XAFS:	X-ray absorption fine structure
XRD:	X-ray diffraction
ZFC:	Zero field cooling
ZFC af. FH:	Zero field cooling after field heating
ZFH:	Zero field heating
ZFH af. FC:	Zero field heating after field cooling

Table of Contents

Abstract i

Acknowledgements iii

Glossary iv

Table of Contents vi

Chapter 1 Introduction 1

Chapter 2 Literature Review 4

2.1 Energy Storage in Dielectric Materials 4

2.2 Antiferroelectrics 8

2.3 Relaxor Ferroelectrics 10

2.4 Morphotropic Phase Boundary in Ferroelectric Materials 14

2.5 $Bi_{0.5}Na_{0.5}TiO_3$ 20

2.6 $(1\text{-}x)Bi_{0.5}Na_{0.5}TiO_3\text{-}xBaTiO_3$ 57

2.7 Grain Size Effect in Ferroelectric Materials 80

Chapter 3 Experimental Methods 89

3.1 Powder Preparation and Ceramic Processing 89

3.2 Determining the Crystal Structure 91

3.3 Microstructure Imaging Techniques 93

3.4 Electrical Response 95

Chapter 4 Grain Size Effect in $Bi_{0.5}Na_{0.5}TiO_3$ 98

4.1 Ceramic Processing 99

4.1.1 Stoichiometry 99

4.1.2 Determining the Calcination Temperature 102

4.1.3 Ball-Milling 104

4.1.4 Chemically Prepared Powder 106

4.1.5 Sintering Techniques 107

4.1.6 Determining the Sintering Temperature 111

4.1.7 Determining the Grain Size 114

4.1.8 Ceramics Prepared from High-Speed Ball-Milled Powder 118

4.2 Results 121

4.2.1 High Temperature X-ray Diffraction 121

4.2.2 Transmission Electron Microscopy 130

4.2.3 Back-Scattered SEM 131

4.2.4 Piezoforce Microscopy 137

4.2.5 Dielectric Response vs. Frequency 139

4.2.6 Dielectric Response vs. Temperature 141
4.2.7 Polarisation and Current vs. Electric Field 151
4.2.8 Piezoelectric Response vs. Temperature 156
4.3 Discussion 158
4.4 Summary 166
Chapter 5 Grain Size Effect in 94%$Bi_{0.5}Na_{0.5}TiO_3$-6%$BaTiO_3$ 168
5.1 Ceramic Processing 169
5.1.1 Determining the Calcination Temperature 169
5.1.2 Ball-Milling 171
5.1.3 Chemically Prepared Powder 174
5.1.4 Sintering Techniques 174
5.1.5 Determining the Sintering Temperature 176
5.1.6 Determining the Grain Size 178
5.1.7 Ceramics Prepared from High-Speed Ball-Milled Powder 181
5.2 Results 185
5.2.1 High Temperature X-ray Diffraction 185
5.2.2 Back-Scattered SEM 193
5.2.3 Piezoforce Microscopy 197
5.2.4 Dielectric Response vs. Frequency 200
5.2.5 Dielectric Response vs. Temperature 202
5.2.6 Polarisation and Current vs. Electric Field 217
5.2.7 Piezoelectric Response vs. Temperature 224
5.3 Discussion 226
5.4 Summary 232
Chapter 6 Conclusions and Future Work 234
6.1 Powder Preparation and Ceramic Processing 234
6.2 Grain Size Effect in $Bi_{0.5}Na_{0.5}TiO_3$ 235
6.3 Grain Size Effect in MPB Composition 94%$Bi_{0.5}Na_{0.5}TiO_3$-6%$BaTiO_3$ 236
6.4 Comparing the Grain Size Models 238
6.5 Future Work 239
Chapter 7 Appendix 243
7.1 Grain Size Effect in $Bi_{0.5}Na_{0.5}TiO_3$: Crystal Structure 243
7.2 Grain Size Effect in 94%$Bi_{0.5}Na_{0.5}TiO_3$-6%$BaTiO_3$: Crystal Structure 251
List of Publications 260
References 261

Chapter 1 Introduction

With their high power density dielectric capacitors form key components in many electronic devices which require a pulsed voltage or current.[1] The energy storage capability of these materials however cannot currently compete with those achieved by batteries. Improving the energy density of the dielectric would lead to the commercialisation of innovative super-high power systems as well as the miniaturisation of many electronic devices.[1] As a result of its high dielectric strength and reliability the most commonly used dielectric material in commercial capacitors is the ferroelectric perovskite $BaTiO_3$. Higher energy density values however are achieved in materials which undergo a reversible field-induced phase transition from a paraelectric (PE) to a ferroelectric (FE) state. A key characteristic of antiferroelectric (AFE) materials, the electric field induced phase transition also enables higher charge releasing speeds making them ideal candidates for use in super-high power electronic systems.[1]Depending on the response of their characteristic nanometer size polar regions (PNRs) to external electrical stimuli a similar phase transition can also be induced within FE relaxors. [1]

One of the best known AFE compounds is $PbZrO_3$.[2],[3] Discovered in 1951 following the theorisation of the AFE state by Kittel[4], energy densities of up to 12.4 J/cm^3[5] have since been achieved in composites of this material. $PbZrO_3$ forms one constituent of the technologically important piezoelectric compound $Pb(Ti_xZr_{1-x})O_3$ (PZT). The substitution of Zr with Ti, promotes a long-range FE ordering within this system. A morphtropic phase boundary (MPB) develops within this system at x=0.46[6] separating adjacent tetragonal and rhombohedral FE structures. Materials which exhibit a MPB are of great practical interest because of the large dielectric and electromechanical properties which accompany this transition. [7]

Alternatives to the lead-based perovskites are of particular interest following the introduction of new environmental legislation, implemented in many countries, restricting the use of lead in electronic devices. One of the most promising candidates to replace this group of materials is $Bi_{0.5}Na_{0.5}TiO_3$ (BNT). Initially, an intermediate AFE phase was thought to separate the high temperature PE phase from the FE phase between 200-320˚C following the discovery of characteristic double hysteresis loops within this temperature range in $(Bi_{0.5}Na_{0.5})_{(1-x)}Sr_xTiO_3$.[8] Interest in this lead-free AFE then grew, with hundreds of papers reporting the properties of BNT being published.

However, no structural evidence of an AFE phase was found to exist in this material.[9],[10] The AFE-like loops have since been associated with a relaxor-type behaviour associated with the *P4bm* PNRs.[11] The solid solution with Ba, (1-*x*)$Bi_{0.5}Na_{0.5}TiO_3$-*x*$BaTiO_3$ (BNBT-100*x*), forms a MPB between $0.06 \leq x \leq 0.0675$.[12] As well as enhancing the electrical properties of the system, the MPB lowers the temperature of the FE-to-relaxor phase transition, T_d, towards room temperature.[13]

Many different compositional modifications to the basic end member BNT have been tested. Significant progress has been made in understanding how to tailoring the composition to achieve the desired properties. MPBs have been discovered in several other BNT-based solid solutions including $Bi_{0.5}Na_{0.5}TiO_3$-$Bi_{0.5}K_{0.5}TiO_3$ (BNT-BKT)[14] and $Bi_{0.5}Na_{0.5}TiO_3$-$K_{0.5}Na_{0.5}NbO_3$(BNT-KNN)[15]. More complex solid solutions with three end members have also been developed, for example BNBT-KNN[16], KNN, BNBT-BKT[17] and $Bi_{0.5}Na_{0.5}TiO_3$-$BaTiO_3$-$CaTiO_3$[18]. The degrees of freedom offered by these systems allow for greater tuning of their properties.[18]

The true crystal structure and associated phase transitions exhibited by BNT and its solid solutions remain uncertain as no clear correspondence exists between structural and physical property investigations.[19] Distortion from the basic perovskite structure is very small in BNT, consequently, the lattice parameter are numerically very close to cubic making refinement of the structural data difficult. Limitations in the investigative techniques and the complex nature of the compound have resulted in much controversy over the true structural model of BNT.[20]

In an attempt to gain a better understanding of this material and develop the energy storage potential of the system for practical uses, the effect of grain size on the crystal structure, domain morphology and electrical properties of the basic end member BNT was investigated followed by the MPB composite 94%$Bi_{0.5}Na_{0.5}TiO_3$-6%$BaTiO_3$ (BNBT-6). Different powder processing techniques and sintering condition were employed to control the grain size of the ceramics allowing high density BNT and BNBT-6 samples with average grain sizes ranging from the nanometre to the micrometre scale to be prepared. The effect of grain size on the crystal structure of the ceramics at different temperatures was measured by powder X-ray diffraction. While the change in domain morphology between the different size grains was investigated by scanning probe microscopy and electron microscopy imaging techniques. The temperature dependence of the dielectric response, piezoelectric response and

polarisation-current-electric field loops of the ceramics was also measured. By combining the electrical property results with the domain images and structural refinement data of ceramics of different grain size, an improved understanding of the FE behaviour of BNT and the MPB of BT doped BNT was gained.

An extensive review of the published work on BNT and the MPB composition with $BaTiO_3$ are given in Chapter 2. Also included within this chapter are short summaries on the energy storage potential of dielectric materials, in particular AFE and relaxor FE, phases both used to describe BNT-based systems. Examples of well studied lead-based perovskites are used to help define the characteristics of these different phases as well as the MPB. A review on how grain size is thought to influence the properties of ferroelectric materials, notably $BaTiO_3$, is also given. The experimental design and methodologies used as part of this PhD research are described in Chapter 3. The experimental results and discussion of the effect of grain size on the crystal and domain structures and the electrical properties of BNT and BNBT-6 are explained in Chapters 4 and 5, respectively. In Chapter 6 the main conclusions of this research are given, including a comparison between the different grain size effects observed in the two compositions. Future work that should be completed to further test the conclusions of this research and expand the understanding of the subject is outlined in Chapter 6.

Chapter 2 Literature Review

2.1 Energy Storage in Dielectric Materials

Batteries and capacitors are common components in many commercial devices which require a source of stored electrical energy. A stable, long-term energy supply can be provided by batteries which typically posses a high energy density (10-300 W.h/kg) but low power density (> 500 W/kg) due to the slow movement of their charge carriers. Capacitors with their high power density (up to 10^8 W/kg) are generally used to provide a pulsed voltage or current.[1] The energy density of commercial dielectric capacitors (10^{-2}-10^{-1} W.h/kg), however, is much smaller than batteries.[21] Improving the energy density capabilities of the dielectric would lead to the commercialisation of some innovative super-high power systems as well as the miniaturisation of many electronic devices.[1]

The most commonly used dielectric material in commercial multi-layer capacitors is the ferroelectric (FE) perovskite $BaTiO_3$. Extremely high dielectric permittivity values are achieved within this material at the FE-paraelectric (PE) phase transition (T_c). Chemical substitution is used to both lower and broaden the temperature of this phase transition enhancing the capacitance of the dielectric within the desired operating range (-60-180 °C).[22],[23] Disappointingly, the effective capacitance of $BaTiO_3$ decreases sharply with applied voltage limiting the energy storage capabilities of these materials (Fig.2.1.1(a)).[24] A feature of FEs, this decrease is caused by saturation of the polarisation with increasing electric field.[4]

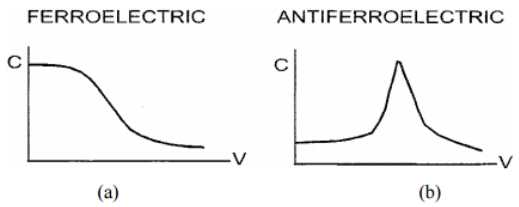

Fig.2.1.1: Schematic showing how the capacitance changes with applied DC voltage for (a) a FE (e.g. $BaTiO_3$) and (b) an AFE. [24]

The energy storage capabilities of a dielectric capacitor (J) can be calculated from the measured electrical displacement (D) of the dielectric in an applied electric field (E).[1]

For high permittivity dielectrics, the electrical displacement and electrical polarisation (P) values are interchangeable, so

$$J = \int_0^{Emax} PdE.$$

In the case of a linear dielectric, the permittivity is independent of the applied electric field so the energy stored can simply be calculated from the expression

$$J = \int_0^{Emax} PdE = ½\varepsilon_0\varepsilon_r E^2.$$

The total electrical energy stored by the system (J_{store}) during charging is represented by the red and green areas in the polarisation-electric field (P-E) curve shown in Fig.2.1.2.

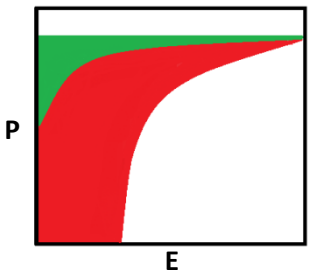

Fig.2.1.2: P-E hysteresis curve illustrating the recoverable (green) and unrecoverable (red) energy in the dielectric.[adapted from [1]]

The green area illustrates the recoverable energy per unit volume (J_{reco}) of the dielectric on discharge.[24],[25] The unrecoverable energy which is absorbed by domain switching and remains within the system as remanence is represented by the red shaded area.[25] The ideal candidate for energy storage is one which has zero remnant polarisation (P_r) and can reach a very high saturation polarisation (P_{sa}) before electrical breakdown. The P-E loops expected for typical linear, FE, relaxor and antiferroelectric (AFE) materials are shown in Fig.2.1.3.

Linear dielectric capacitors have zero remanence; however because of their low dielectric permittivity value a very high applied field is needed to store any significant level of electrical charge. Consequently, an extreme dielectric strength is required of these materials making them unsuitable for high energy storage applications.[25] FEs, on the other hand, typically achieve a much higher P_{sa} values than linear dielectrics however a lot of that stored energy remains as remanence during discharge leading to low efficiency.[1] The hysteresis loop in the P-E curve (Fig.2.1.3(b)) is a direct consequence of polarisation reversal by an electric field, a defining feature of FSs. The

switching of domains with unfavourable dipole direction results in a rapid, non-linear increase in polarisation not observed in linear dielectrics. This switching takes place by the growth of existing domains parallel with the applied field, by domain wall motion and, by nucleation and growth of new domains. The low energy storage efficiency is a consequence of the domains inability to fully switch back when the applied field is decreased to zero. A zero polarisation state is only re-established when the field is reversed.[26]

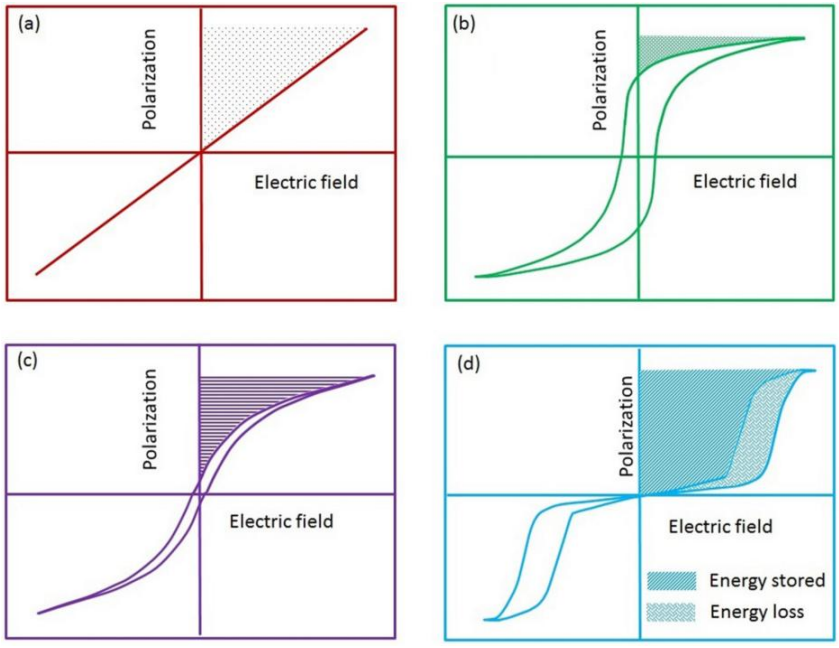

Fig.2.1.3: P-E loops for (a) linear dielectric, (b) FE, (c) relaxor FE and (d) AFE. The filled area shows the energy recovered J_{reco} during discharge.[5]

Maximum energy storage is not obtained in dielectrics with the highest permittivity values[21] but in materials which undergo a reversible field-induced phase transition from a PE state with zero remanence to a FE phase with a large P_{sa} value.[24],[25] Double hysteresis P-E loops, demonstrated in Fig.2.1.3(d), have been achieved in AFEs. Unlike a FE, the polarisability of an AFE typically increases with increasing electric field, over some voltage range, allowing for a large electrical charge to be stored at nonzero bias (Fig.2.1.1(b)).[21] AFEs also undergo a higher charge releasing speed due to the electric field induced phase transition making them ideal candidates for use in super-high power electronic systems.[1] Another potential candidate for energy storage are relaxor FEs. Relaxors typically display a slim P-E curve with large differences between P_r and P_{sa} value (Fig.2.1.3(c)).[1] Depending on the response of the characteristic nanometer size polar regions to external electrical stimuli a ‘normal’ FE state can be induced within this

system.[1] Ultimately, materials which display the highest dielectric strength and reliability are of most interest for commercial application.[21]

2.2 Antiferroelectrics

The theory of antiferroelectricity was first proposed by Kittel[4] in 1951 who defined an antiferroelectric (AFE) as a non-polar state where chains of ions in the crystal are spontaneously polarised but in an antiparallel direction to their neighbouring chains. An intrinsic feature of the antipolar structure is its proximity to an alternative low free-energy polar structure. The electric-field induced phase transition from the AFE state to a related ferroelectric (FE) state is a characteristic property of these materials and results from the low free-energy difference between the two structures (Fig.2.2.1).[27],[28] The abrupt change in polarisation associated with this transition appears as a signature double hysteresis P-E loop. Significant changes to optical properties as well as large electrostriction coefficients and giant electrocaloric effects also accompany this transition. A distinction between the FE and AFE states can be made from the piezoelectric response. Unlike the FE state which generally exhibits a large piezoelectric effect, the AFE state has a centre of symmetry so is not considered to be a piezoelectric.[4]

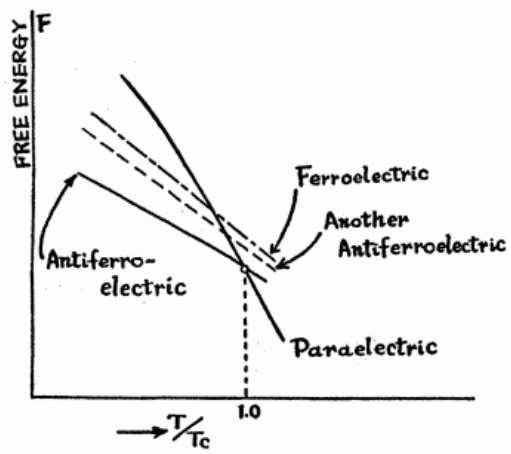

Fig.2.2.1: A schematic of the free-energy curves in AFE $PbZrO_3$ showing the close proximity of the AFE phase to an alternative FE phase.[28],[29]

According to Kittel's model an applied electric field is expected simply to reverse the polarisation of one of the two antiparallel sublattices forming the polar crystal structure.[29] However, no known AFE has been found to conform to this classic model. For example, antiferroelectricity in $PbZrO_3$ primarily originates from the commensurate modulation of Pb^{2+} displacements which average as an incommensurate modulation with a periodicity of between 7 and 8 psuedocubic <110> planes, illustrated in

Fig.2.2.2.[30] Rather than simply reorientating the antiparallel dipoles, the non-polar orthorhombic *Pbam* structure transforms to the FE *R3c* structure with polar <111> direction in an applied electric field.[26] The relation between the nonpolar and FE structures is recognised as varying as a continuum where the classic Kittel two-sublattice model is at one extreme. At the other extreme, the two structures are only distortions of the same high-symmetry reference structure. Despite the difference in structural mechanisms, all of these materials exhibit a first order electric-field induced transition considered a characteristic of AFEs.[29]

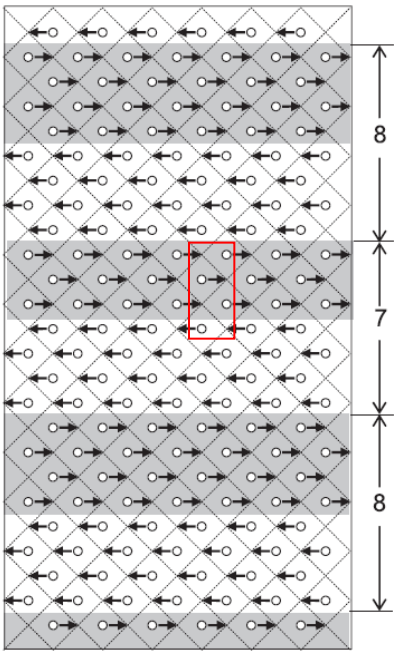

Fig.2.2.2: Atomic arrangement of $PbZrO_3$. The arrows represent the antiparallel displacement of the Pb^{2+} ions along the pseudocubic <110> plane. The red box shows the orthorhombic unit cell.[30]

2.3 Relaxor Ferroelectrics

Relaxor ferroelectrics have a unique structure of locally correlated polar nanometer-size regions (PNRs). A common feature of these materials is a broad maximum in the temperature dependent dielectric permittivity that has a peak position T_m which shifts to higher temperatures with increasing frequency (Fig.2.3.1).[31],[32] This peak is unrelated to the ferroelectric (FE) transition from the paraelectric cubic structure observed in conventional FEs at the Curie temperature T_C.[33],[34] The PNRs first appear at temperatures above T_m, at the Burns temperature T_B.[35] Instead of forming a long-range ordered FE state, the polarisation is correlated on the nanometer-scale (Fig.2.3.2) and the system remains macroscopically nonpolar.[31] The PNRs are very small and can be considered as individual thermally activated dipoles.[33]

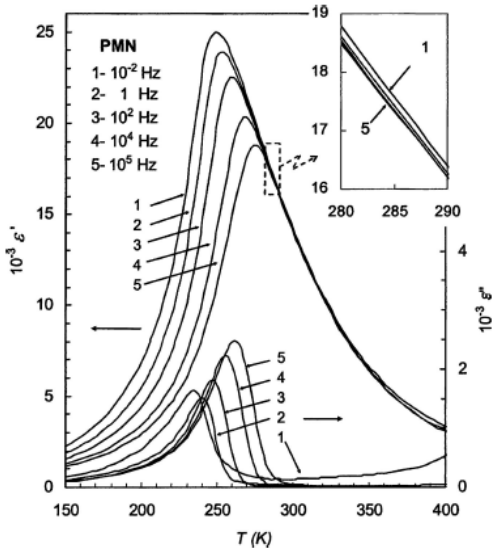

Fig.2.3.1: Dielectric response vs. temperature of prototypical relaxor $Pb(Mg_{⅓}Nb_{⅔})O_3$, measured at different frequencies, shows the peak position T_m shift to higher temperatures with increasing frequency.[33]

The structural and charge inhomogeneties characteristic of relaxors are closely related to the origin of these PNRs. Randomly ordered, local electric fields (RFs) generated within the individual grains of relaxors promote the nucleation of the PNRs while preventing the phase transition to a long-range ordered state.[31] Nanosized chemically ordered regions (CORs) of inhomogenously distributed A or B-site cations are thought to form within the disordered system (Fig.2.3.3).[33] For example, within $Pb(Mg_{⅓}Nb_{⅔})O_3$ (PMN) two different B-sublattices have been identified for the CORs,

one exclusively occupied by B^{5+} ions and the other containing a random distribution of B^{2+} and B^{5+} ions in a 2:1 ratio.[36] The local charge mismatch between these regions as well as the random distribution of the B^{I} and B^{II} cations are expected to produce these quenched local fields.[37],[38],[39] Relaxor behaviour is also known to occur in systems without an inherent charge mismatch, for example isovalent-subsituted $BaTiO_3$.[31] In this case, the B-site substitution breaks the cooperative Ti^{4+} off-centring and associated long-range polar order of the host lattice creating perturbed polarised clusters.[40] RFs are generated when nanoscale regions with an enriched concentration of substituting cations form and their associated distortions result in a redistribution of charges and the formation of local charge centres.[31],[41],[42]

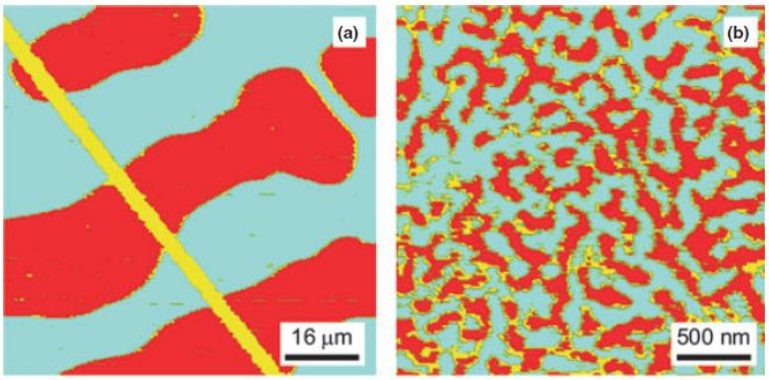

Fig.2.3.2: PFM images demonstrating the transition from (a) a long-range ordered FE state with 90˚ and 180˚ domains to (b) a polar nanometer domain structure (PNRs) following chemical substitution. (a) $PbTiO_3$ and (b) $Pb_{0.9125}La_{0.0975}(Zr_{0.65}Ti_{0.35})_{0.976}O_3$.[31]

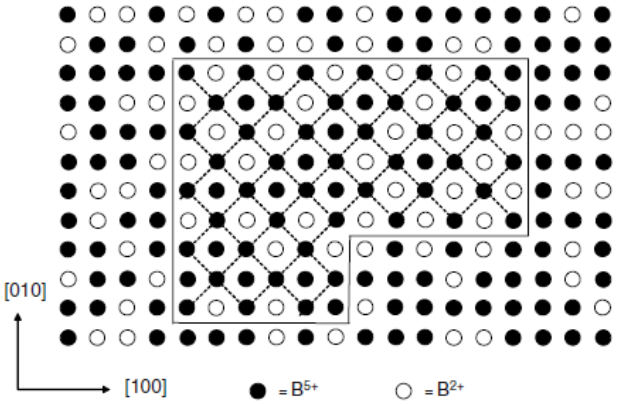

Fig.2.3.3: Schematic showing a nanosized COR (solid line) within the disordered matrix $Pb(B^{2+}_{1/3}B^{5+}_{2/3})O_3$. One of the sublattices within this region, highlighted by the dashed lines, is exclusively occupied by B^{5+} ions.[33]

The polarity of the PNRs is controlled by the fluctuations of the RFs.[43] Near T_B, the PNRs are weakly correlated and the dipole moments thermally fluctuate between equivalent polarisation directions[44] forming an ergodic relaxor state[33]. On cooling below T_m, the dynamics of the PNRs slow as the interaction between the regions becomes stronger and the PNRs grow. The relaxation time related to the reorientation of the PNRs by an external field is broad due to the large distribution of PNR size and the irregularity of their interactions resulting in the strong dielectric dispersion at T_m.[31] In typical relaxors, such as PMN, freezing of the PNR dynamics occurs when the smaller regions merge into larger ones forming a nonergodic glass-like state at T_f.[45],[46] In this state, the polar order remains short-range.

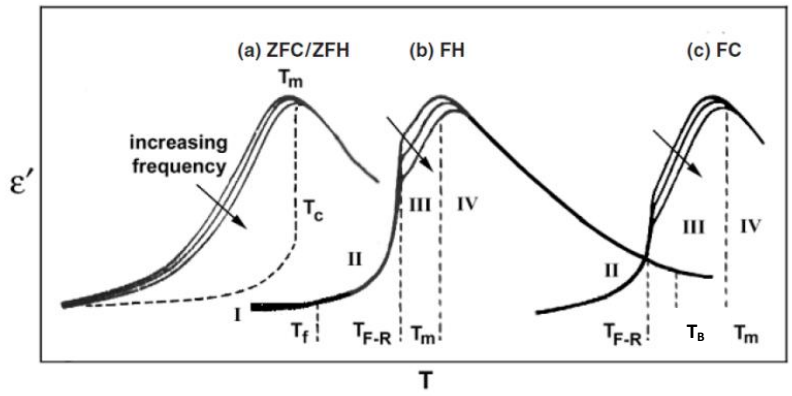

Fig.2.3.4: Dielectric response of a typical relaxor (a) without and (b),(c) with an electric field bias. The dashed curve in (a) depicts the frequency independent FE response when the relaxor is subject to a large (poling) bias field.[52]

A long-range ordered FE-like state may be induced within relaxors by electrical poling, mechanical strain and chemical substitution.[47],[48],[49] However, this state is not a true 'normal' FE state as PNRs still persist, even at low temperatures.[50],[51] An insight into the nature of the FE 'transition' can be gained from dc bias field measurements, shown in Fig.2.3.4.[52],[53] When the relaxor is subject to a weak bias field on heating (FH), Fig.2.3.4(b), below T_f (region I) the thermal energy is not large enough to unfreeze the PNRs and align them with the field. As the temperature is increased (region II), the frequency dispersion vanishes as the nanodomain align and grow forming FE macrodomains. At temperatures above T_{F-R} (region III), the thermal fluctuations become too strong breaking the macrodomains into randomly oriented, slowed down PNRs forming a dispersive relaxor state. The nanodomains undergo rapid thermal fluctuation above T_m (region IV) and enter a paraelectric state. A nonergodic glass-like state

(region I) does not occur when the relaxor is cooled in a bias field (FC), show in Fig.2.3.4(c). The macrodomains formed below T_{F-R} (region II) remain stable to low temperature while in the presence of the field.[52]

2.4 Morphotropic Phase Boundary in Ferroelectric Materials

The morphotropic phase boundary (MPB), according to Cook and Jaffe (1971)[56], is defined as a compositionally induced structural transition. Originally discovered in $Pb(Ti_xZr_{1-x})O_3$ (PZT) (Fig.2.4.1) over 60 years ago, the boundary typically separates adjacent tetragonal and rhombohedral structures in the phase diagram of many ferroelectric (FE) solid-solutions. Materials which exhibit a MPB are of great practical interest because of the large dielectric and electromechanical properties which accompany the transition, highlighted in Fig.2.4.2.[7] Particularly high piezoelectric values (d_{33}) have been reported at the MPB of $PbTiO_3$-based solid solutions with $PbZrO_3$, $Pb(Mg_{1/3}Nb_{2/3})O_3$ and $Pb(Zn_{1/3}Nb_{2/3})O_3$.

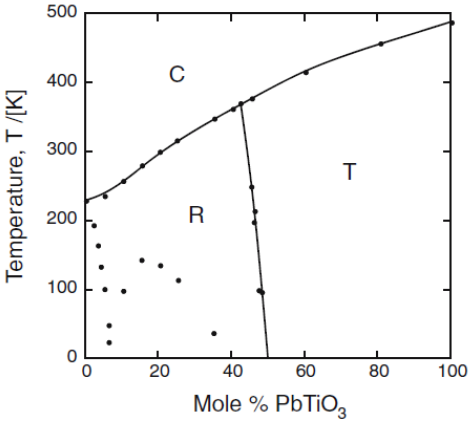

Fig.2.4.1: Original phase diagram for PZT showing MPB separating rhombohedral R and tetragonal T phases.[55],[56]

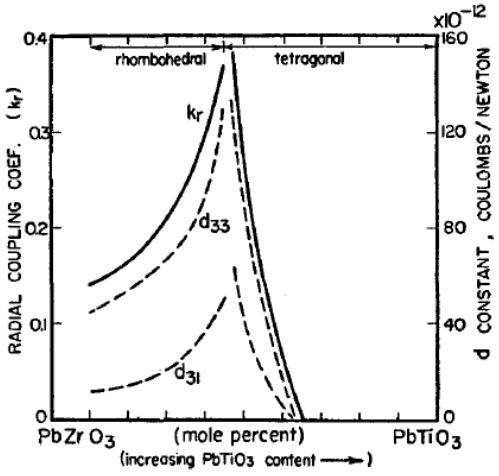

Fig.2.4.2: Enhanced electromechanical properties observed in PZT at the MPB.[7]

Extensive research into the origin of the strong piezoelectric response in PZT has uncovered a number of different and sometimes opposing views of what an MPB is in FEs.[55],[57] The generally accepted phase diagram for PZT, originally proposed by Cook and Jaffe (1971)[56], comprises a near vertical MPB separating the rhombohedral *R3m* phase at the zirconium-rich side from the titanium-rich tetragonal *P4mm* phase. For a very long time, the large piezoelectric response found at the boundary was believed to result from the coexistence of the two phases. The large number of domain variants provided by the combined phases was thought to allow for a greater volume of material to align their polar axis along the direction of the poling field enhancing the polarisability of the system.[56] This view was later found to be flawed following single crystal studies reporting the highest piezoelectric and dielectric values along directions away from the polar axis (Fig.2.4.3).[58],[59] The unexpected discovery of a monoclinic phase adjacent to the MPB of PZT by high resolution X-ray diffraction (XRD)[60],[61] dramatically changed the understanding of the mechanisms involved within this region. Four different views of the source of the MPB have since emerged.[62]

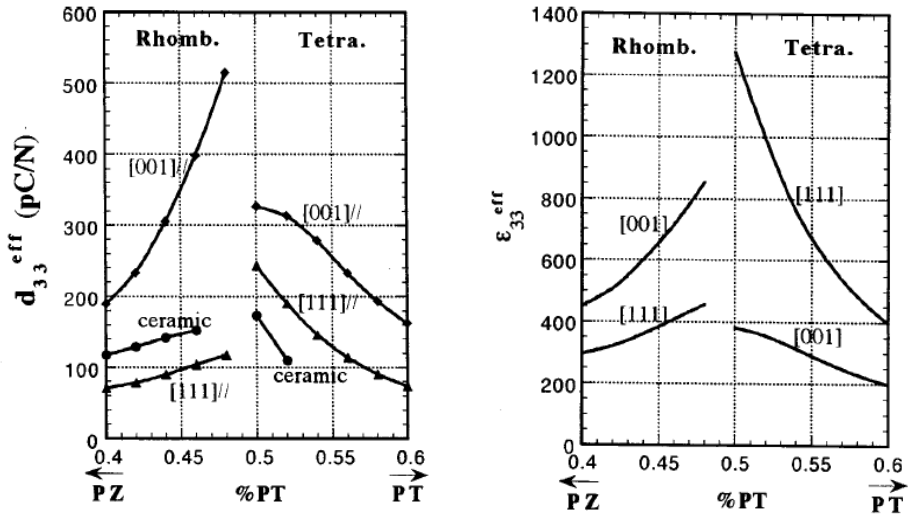

Fig.2.4.3: In PZT the highest (a) piezoelectric d_{33} and (b) dielectric permittivity values are observed along directions away from the corresponding polar axis.[59]

The first considers the MPB as a monoclinic phase, which acts as a structural bridge between the rhombohedral and tetragonal phases providing a pathway for continuous rotation of the polar vector on changing composition across the boundary (Fig.2.4.4).[60],[63] Monoclinic phases have similarly been observed in other solid solutions and were thought to be a universal feature of MPB diagrams.[64] However, this conclusion was later criticised by Kisi et al.[65] who suggested that a monoclinic phase was not

necessary to produce the large piezoelectric response and that the monoclinic symmetry should be considered as a distortion instead of a true phase.

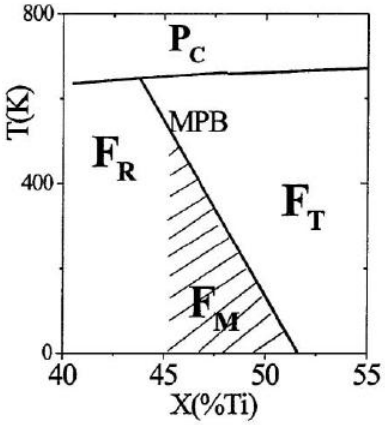

Fig.4: Phase diagram for PZT showing the structurally bridging monoclinic phase.[63]

In the second view, no sharp boundary is considered to occur across the MPB. Rather the Pb cationic shifts in the rhombohedral and tetragonal phases are monoclinically distorted and only the length of the structural order changes across the phase diagram.[66],[67] Local monoclinic symmetry results within the rhombohedral phase when locally-correlated $[1\bar{1}0]_C$, $[10\bar{1}]_C$ or $[01\bar{1}]_C$ shifts are superimposed upon the long-range rhombohedral $[111]_C$ displacements, as shown in Fig.2.4.5(a).[68] Local $[110]_C$ shifts of the long-range ordered tetragonal $[001]_C$ displacements produce the same monoclinic structure (Fig.2.4.5(c)).[61] At the MPB an order-disorder transition occurs where the disordered Pb cationic shifts condense along one direction forming a long-range order, lowering the average symmetry to monoclinic.[6],[67] In both cases, the monoclinic phase is believed to facilitate the polarisation rotation mechanism by allowing for free rotation within the mirror plane of the C_m unit cell. Instead of being confined along a particular symmetry axis such as *R3m* or *P4mm* the polar vector can rotate towards the direction of an off-axis poling field leading to the enhanced piezoelectric properties observed within this region.[66]

The third view regards the monoclinic distortion as an effect of the coexistence between the tetragonal microdomains and the rhombohedral nanodomains, demonstrated in Fig.2.4.6.[6] Near the MPB, a sharp reduction in the domain wall energy reduces the dimensions of the domain structure of the two phases to the nanometer scale. A domain-averaging effect occurs that can mimic the coherent diffraction of a monoclinic structure

when viewed using XRD.[70],[71] According to the adaptive phase model, the high domain wall mobility and progressive switching of the rhombohedral and tetragonal nanotwins eases polarisation rotation, enhancing the response of PZT at the MPB.[70],[72] This domain structure approach, however, cannot explain the enhanced properties expected from the lattice (i.e. a monodomain single crystal). Rather, the domain structure and domain wall effects observed in PZT ceramics only add to the already large response of the individual crystallites and domains.[73]

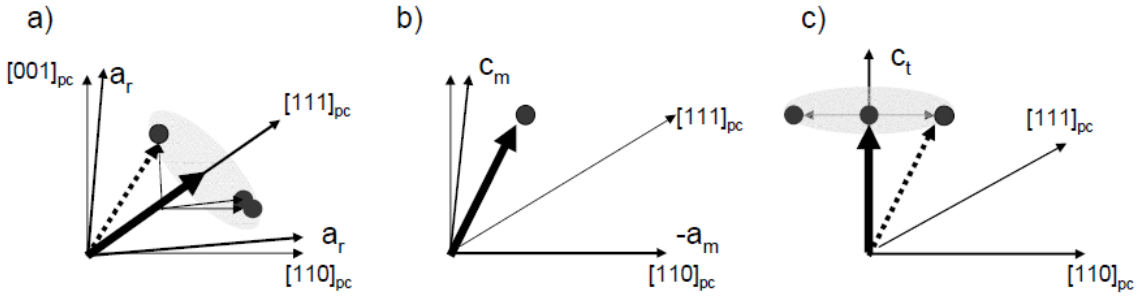

Fig.2.4.5: Schematics of the (a) rhombohedral, (b) monoclinic and (c) tetragonal unit cells along (110) showing the Pb cation displacements.[67]

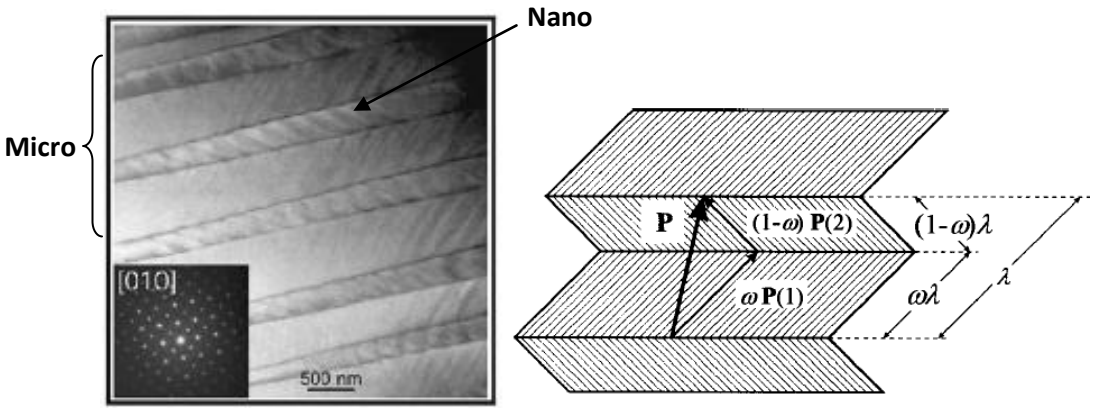

Fig.2.4.6: (a) TEM image of PZT (Zr/Ti:54/46) showing rhombohedral nanodomain structure embedded within the tetragonal microdomain.[6] (b) Illustration demonstrating the adaptive phase theory. **P**(1) and **P**(2) are the polarisations within the microdomains and **P** is the resultant polarization of the adaptive phase.[70]

For the fourth view, the true origin of the MPB is considered to be a consequence of chemical pressure.[74],[75] At 0K, $PbTiO_3$ was shown to exhibit an external pressure-induced tetragonal to monoclinic to rhombohedral phase transition sequence indicative of a MPB (Fig.2.4.7).[76] The internal chemical pressure exerted by the end member

$PbZrO_3$ in PZT is believed to only tune this phase transition to ambient pressure and temperature.[74]

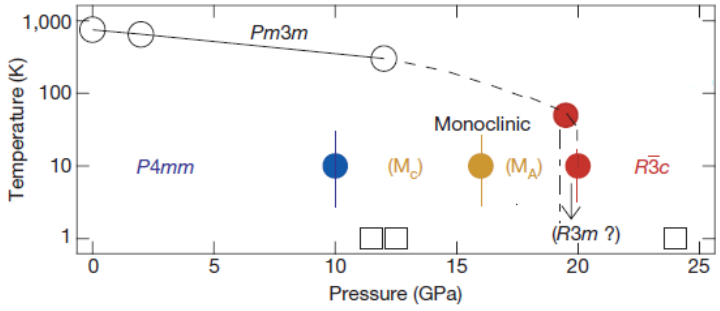

Fig.2.4.7: Pressure-induced phase diagram of $PbTiO_3$.[74]

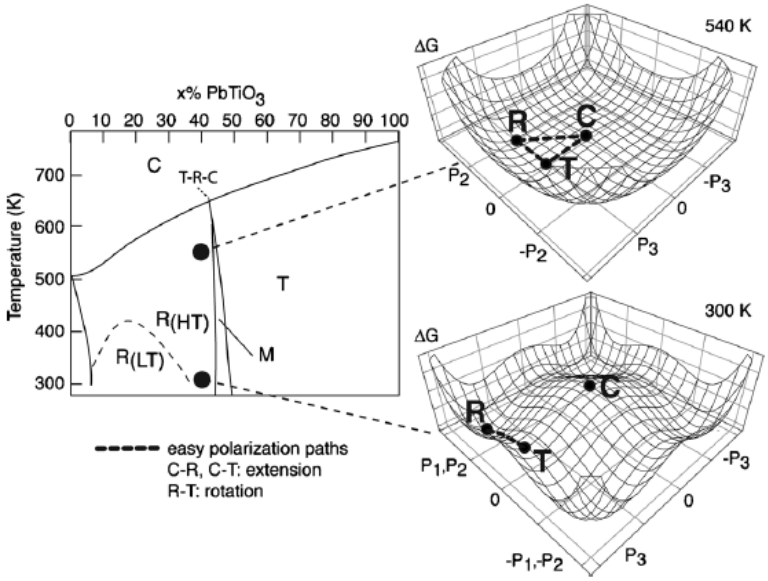

Fig.2.4.8: Phase diagram and Gibbs free-energy profiles for PZT (Zr/Ti:60/40). Polarisation extension is favoured along the T–C and R–C pathways while polarisation ration occurs along the R–T path.[81]

The importance of the monoclinic phase in enhancing the properties of PZT was further questioned following substantial theoretical and experimental evidence showing the highest piezoelectric response at the nonpolar side of the phase transition boundary.[74],[76],[77] A free energy structural instability rather than a particular crystal symmetry is thought to be the true origin of the enhanced properties at the MPB.[73] The flattening of the free energy profile in the phase transition region, demonstrated in Fig.8, facilitates easy pathways for polarisation change.[78] This mechanism is common to many stress-[76], electric field-[79],[80] and temperature-[81],[82] driven phase transitions. Free-energy flattening can be linked to many of the phenomena observed at the MPB,

including instability of the polarisation vector against rotation, the reduction in domain size as well as the chemical and structural disorders stabilising localised low symmetry phases.[55],[83] Domain wall motion is also expected to have an equally strong influence on the properties of the MPB composition as the intrinsic structural stabilities.[81]

Polarisation rotation has been firmly established as the main intrinsic pathway for the enhancement of the electromechanical properties in PZT.[81] Consequently, the search for new lead-free materials with properties similar to those of the MPB composition of PZT has focused on the polarisation rotation mechanism.[81] Enhanced piezoelectric properties can also be achieved by polarisation extension[73], where an electric field applied along the polar axis elongates the polar vector.[155] For example, the largest piezoelectric coefficient ever reported was for polarisation extension in KH_2PO_4 (d_{33}≈20 000 pm/V)[85]. However, easy polarisation extension paths in a free energy profile are typically temperature-driven. The random orientation of the grains in polycrystalline materials will also hinder the full effect of polarisation extension. The search for new materials should instead focus on solid-solutions with an MPB with easy pathways for both polarisation rotation and extension.[81] A hypothetical phase diagram with a MPB region where both mechanisms can occur has been proposed by Damjanovic is shown in Fig.2.4.9[81].

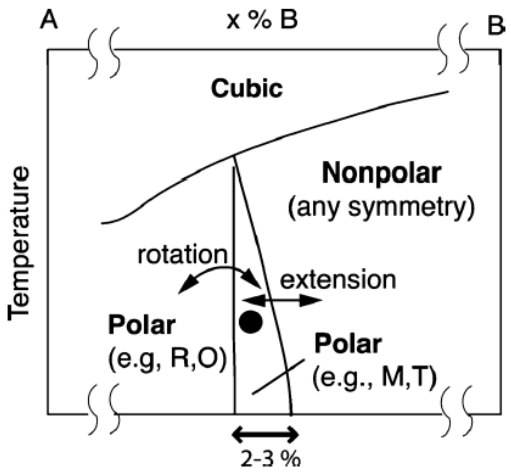

Fig.2.4.9: Hypothetical phase diagram for $A_{1-x}B_x$ showing where the polarisation rotation and polarisation extension mechanisms are strongest about the MPB region. The black dot represents the composition that benefits from both polarisation mechanisms. Possible structures in phase diagram R: rhombohedral, O: orthorhombic, M: monoclinic, T: tetragonal.[81]

2.5 $Bi_{0.5}Na_{0.5}TiO_3$

The room temperature ferroelectric (FE) properties of the A-site substituted perovskite $Bi_{0.5}Na_{0.5}TiO_3$ (BNT) were initially reported in 1961 by Smolensky et al.[86]. The nature of the FE phase was not comparable to any other tetragonal titanate being researched at that time.[87],[88] In addition to a maximum in the temperature dependant dielectric permittivity at 320 ˚C (T_m) a second anomaly was observed at 200 ˚C (T_s), shown in Fig.2.5.1. Initially, an intermediate antiferroelectric (AFE) phase was thought to separate the high temperature paraelectric (PE) phase from the FE phase following the discovery of characteristic double hysteresis loops between 150 ˚C and 240 ˚C for $(Bi_{0.5}Na_{0.5})_{0.85}Sr_{0.15}TiO_3$ (Fig.2.5.2(a))[8]. The phase diagram for Sr-doped BNT is shown in Fig.2.5.2(b). No pyroelectric current was detected in BNT for temperatures above 210 ˚C[8],[89] confirming the non-polar character of this intermediate phase. Interest in this lead-free AFE then grew, with hundreds of papers investigating BNT's properties being published.

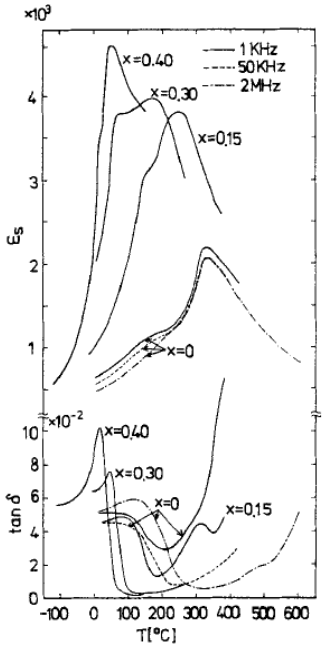

Fig.2.5.1: Temperature dependence of the dielectric response of solid-solution $(Bi_{0.5}Na_{0.5})_{1-x}Sr_xTiO_3$.[8]

Despite thorough investigation of the structural properties of the lead-free perovskite, much uncertainty still remains over the average and local structure and even the crystallographic symmetry of BNT. Structural studies, in particular neutron and X-ray powder diffraction, typically use techniques such as Rietveld refinement to fit data to pre-existing structural models. When the structural models are closely related,

refinement can be made challenging by additional parameters describing peak shape and background. Distortion from the basic perovskite structure is very small in BNT, consequently, the lattice parameter are numerically very close to cubic making refinement of the structural data difficult. Significant disorder arising at the substituted A-site and the accompanying strongly diffuse diffraction scattering has made structural investigations even more difficult. Limitations in the investigative techniques and the complex nature of the compound have resulted in much controversy over the true structure model of BNT.[90] Many of the structural models proposed do not account for the phase transitions expected from the physical property measurements. [91]

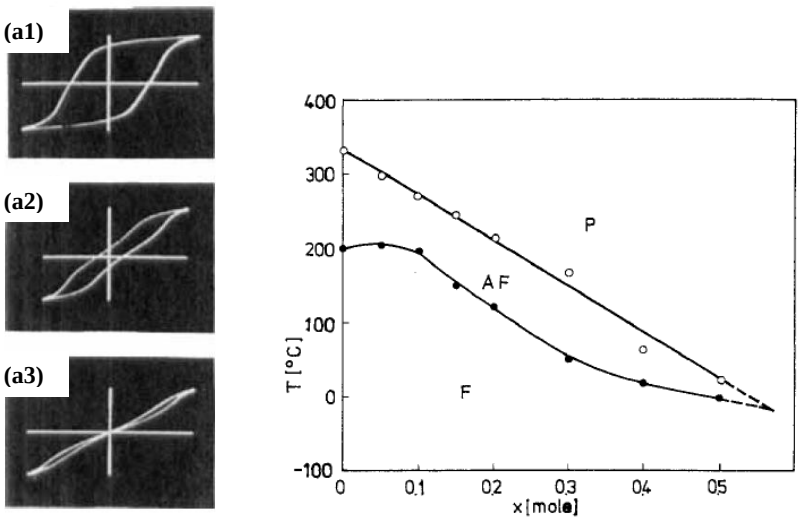

(a) (b)

Fig.2.5.2: (a) D-E hysteresis loops measured for $(Bi_{0.5}Na_{0.5})_{0.85}Sr_{0.15}TiO_3$ at (a1) 25 ˚C, (a2) 100 ˚C and (a3) 170 ˚C. (b) Phase diagram for $(Bi_{0.5}Na_{0.5})_{1-x}Sr_xTiO_3$.[8]

In this review a chronological outline of the different structural models will be described. This will demonstrate how newer models have commonly refined and built on previous theories. Many of the models are based primarily on studies investigating the structure and properties of the room temperature and intermediate 'AFE' phase. To help the reader a summary will be given before the individual models are discussed in more detail.

2.5.1 Summary

The AFE cluster model was one of the first models proposed for BNT: AFE regions were thought to grow within the tetragonal PE phase on cooling, merging to form an 'infinite' AFE cluster.[92] However, this model came into question after no structural evidence of an AFE phase was found to exist.[9],[10] Instead of an AFE phase, the properties were then linked to relaxor-type behaviour. A new model based on a thermally evolving FE rhombohedral *R3c*/PE tetragonal *P4mm* matrix was then proposed for this system.[10] Doubts were cast on the centrosymmetric nature of the tetragonal structure following a study combining neutron diffraction with second harmonic generation (SHG).[110],[111] A small SHG signal indicative of a weakly polar structure was detected for the tetragonal phase. A detailed structural model ranging from -268 ˚C to above 540 ˚C was proposed for BNT. Coexisting rhombohedral and tetragonal phases were similarly found for the intermediate phase, however the tetragonal structure is polar *P4bm* rather than PE. This model cannot explain the physical properties of BNT as the structural transitions occur at different temperatures to the expected phase transitions.

In an attempt to interpret the physical properties of BNT, many of the investigations began to focus on its local structure. A short-range ordering of the A-site cations was found to distort the room temperature rhombohedral structure. Two different ordering structures based on $Bi^{3+}TiO_3/Na^{+}TiO_3$ clusters[114] and Guinier Preston zones (GPZs) of tetragonal cation displacements[115] emerged. A structural model of tetragonal $a^0a^0c^+$ platelets in a rhombohedral matrix developed from this research and was indirectly linked with the relaxor behaviour of BNT[116]. A 'two phase orthorhombic model' was later proposed for BNT following the observation of superstructure spots above 200˚C linked to an orthorhombic *Pnma* ($a^-a^-c^+$) symmetry.[139],[140] A modulated AFE phase, composed of orthorhombic sheets layered between rhombohedral *R3c* blocks assists the transition from the room temperature rhombohedral phase to a purely orthorhombic phase below T_m. Although this model can account for the physical properties reported for BNT, evidence for $a^-a^-c^+$ tilting at {001} twin boundaries or sheets of local Na/Bi ordering underpinning this model could not be found by other authors.[143],[144]

The room temperature structure of BNT was further investigated. A transitional region separating the tetragonal platelets from rhombohedral structure is thought to lower the average symmetry of the room temperature phase.[144] A monoclinic *Cc* symmetry was

suggested for the modulated room temperature state, however this structure could not fully account for the XRD pattern.[148] Both mechanical and electrical stimuli irreversibly transform the structure to rhombohedral *R3c*.[149] The monoclinic structure was initially thought to describe the room temperature equilibrium state[147], however this structure was found to coexist with the rhombohedral phase after thermal annealing[150]. The Bi cation was found to play a prominent role in the departure of the local atomic structure from the average structure of BNT.[153]

In defence of the two phase orthorhombic model, a single phase 'continuous tilting' model has recently been suggested for BNT.[133] No distortions associated with any tetragonal platelets could be observed by the authors of this model. Instead, the average monoclinic/rhombohedral structure is thought to arise from sampling of unequal fractions of nanoscale orthorhombic domains that form from in-phase tilting along each of the three orthogonal axes: $a^-a^-c^+$, $a^-c^+a^-$ and $c^+a^-a^-$. The intermediate orthorhombic *Pnma* structure is thought to evolve from the room temperature state by increasing the coherence length of the in-phase tilts, which becomes favoured at high temperatures, stabilising the anti-parallel A-cation displacements.

Further investigation into the true nature of the room temperature state of BNT has revealed the structure to be globally rhombohedral.[157] A defect structure of tetragonal platelets and planer boundaries are thought to be responsible for the different room temperature structures observed in BNT. In order to maintain the structural continuity of the oxygen octahedra, the local tilt system surrounding the planer defects is expected to differ from that of the bulk in the form of a transitional region with local symmetry $a^-a^-c^-$. An average monoclinic *Cc* structure will be assigned to BNT by large-scale diffraction techniques when it has a high density of defects. The authors do not dismiss the possibility of a system of orthorhombic tilts forming the local structure of BNT[133] which maintain an average anti-phase $a^-a^-a^-$ tilt system over longer distances.

2.5.2 *Structural Models of BNT*

2.5.2.1 AFE Cluster Model

An AFE cluster model based on the growth of AFE regions within PE layers to form 'infinite' AFE clusters was used by Pronin et al.[92] to explain the temperature hysteresis effects observed in BNT. A temperature hysteresis of 50-55˚C was reported between the heating (255-305 ˚C) and cooling (250-200 ˚C) dielectric runs, shown in Fig.2.5.3. Similar temperature hysteresis effects were observed in DSC and birefringence measurements, neither of which exhibited any features relating to the phase transition at T_m. These techniques also revealed a new anomaly at 540 ˚C assumed to be a crystallographic transition due to its absence from the dielectric data. Isolated microregions of AFE phase are expected to appear at this temperature which increase in number and grow on cooling. At T_m, the crystal volume of AFE phase is thought to equal that of the PE phase, maximising the dielectric response. An ordering and joining of the AFE regions takes place with further cooling forming 'infinite' AFE clusters. The low elastic energy associated with these clusters is expected to hinder the back switching of the AFE regions on heating creating the hysteresis effect.

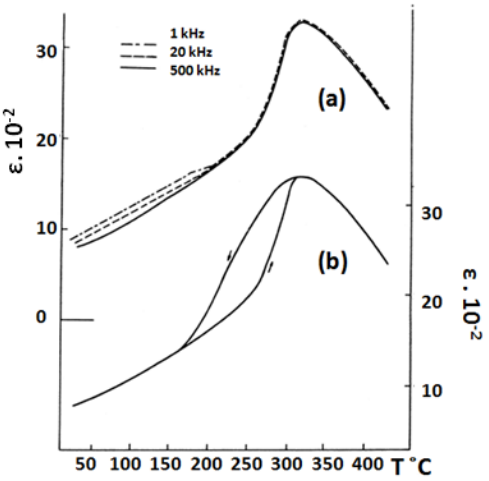

Fig.2.5.3: Temperature dependence of the dielectric permittivity of single crystal BNT (a) measured on heating at 1, 20 and 500 kHz and (b) its temperature hysteresis at 500 kHz.[91]

A full X-ray diffraction (XRD) analysis of the phase transitions in BNT revealed two 1st order structural transitions[9], in arrangement with the DSC peaks observed by Pronin et al.[92]. BNT was shown to be cubic with space group $Pm\bar{3}m$ which transformed at 520 ˚C on cooling to tetragonal *P4mm*. No temperature hysteresis was observed at this transition. BNT then transforms to a rhombohedral structure with space group *R3c* at

260 ˚C. The *P4mm*-to-*R3c* structural transition occurs in close proximity to a small peak in the high frequency permittivity data. Zvirgzds et al.[9] used this as evidence for a collapse in the polarisation state leading to the suggestion that the tetragonal phase is AFE. Despite evidence of a decrease in lattice distortion and cell volume in this intermediate phase, the existence of an AFE phase could not be confirmed due to the absence of X-ray reflections associated with a multiple cell.

In order to make sense of the often unusual and contradictory properties reported for BNT at that time, Isupov et al.[93] adapted the AFE cluster model to consolidate the optical and dielectric properties with Zvirgzds et al.'s structural study[9]. In this new model, the AFE nuclei are thought to first appear within the tetragonal phase at a temperature above T_m. The optical analysis revealed no change in the behaviour of the domain structure in BNT at T_s as well as an unexpected change in birefringence sign and isotropisation at 230 ˚C and 280 ˚C on cooling and heating, respectively. In order to satisfy these constraints, a pseudo-rhombohedral distortion such as triclinic was suggested for the FE and AFE phases rather than a rhombohedral structure. The distortion in these phases is suggested to be similar, explaining the absence of this transition from the XRD analysis.

The AFE cluster model assumes that a PE-AFE transition occurs on cooling at T_m. However, no structural evidence exists to support this claim. In the adapted model, the AFE nuclei are assumed to be very small and are invisible when probed on the length scale of x-rays. Yet further doubts were raised after a neutron diffraction investigation[10] failed to detect any AFE displacements of the ions as well as any far range ordering. A new model, not based on the existence of an AFE phase, was needed to explain the properties of BNT.

2.5.2.2 Rhombohedral/Tetragonal Matrix where T phase is non-polar

A short-range ion ordering was revealed by neutron diffraction[10] to exist in the temperature range of the proposed AFE phase. In light of these new results a new 'low-temperature non-polar' (LTNP) phase was ascribed to the intermediate state rather than an AFE phase. The rhombohedral phase is thought to accumulate within a PE tetragonal matrix on cooling resulting in a change in the matrix symmetry at the phase transition temperature T_m recorded by Zvirgzds et al.[9] Polar regions are thought to exist dynamically in BNT up to 500 ˚C, forming stable microregions of pure rhombohedral

FE phase on cooling at the crystal isotropisation point. The interwoven nature of LTNP phase with the FE regions is used to explain the diffuse nature of the phase transition. The coexistence of tetragonal and rhombohedral phases within this intermediate state was later confirmed by another neutron scattering study.[94]

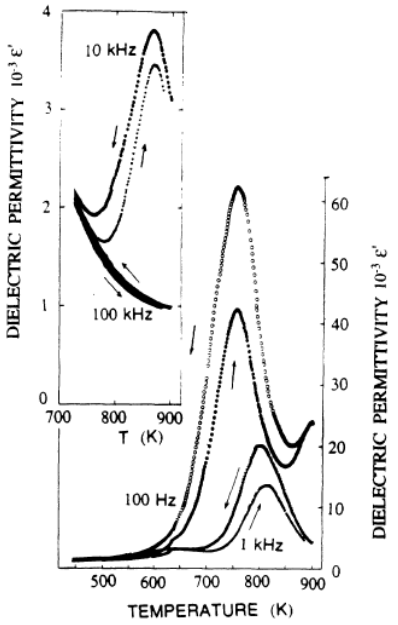

Fig.2.5.4: Dielectric response of single crystal BNT showing a high temperature peak in the 100 Hz near the ferroelastic phase transition at T_{c1}~820K.[98]

Investigations into the electrostrictive strain[95] and time dependence of the pyroelectric current[96] and permittivity[97] of BNT also show polar regions to exist below the tetragonal-cubic structural transition (~520 ˚C).[10] The maximum in the dielectric permittivity T_m is thought to results from a change in size and dynamics of these polar regions rather than a phase transition.[95] In light of this discovery, Tu et al.[98] went on to investigate the dynamic behaviour of these polar regions in an electric field. Tu et al. reasoned that the time dependence of the dielectric response in the intermediate state is the result of a trigonal phase exhibiting AFE and/or incommensurate characteristics. A new high temperature peak, shown in Fig.2.5.4, was observed by Tu et al. in the low-frequency permittivity data near the tetragonal-cubic transition. The dynamic behaviour of this region was believed to be controlled by ionic diffusion related to the charge carrier redistribution rather than the fluctuation of polar regions. The FE ordering in the tetragonal phase is inhibited by the formation of superparaelectric clusters[34]. The high temperature peak is thought to mark the cross over region where the independent dipole

moments in the PE cubic phase divide into clusters because of the random placement of Bi^{3+} and Na^{+} charge carriers.

The random distribution of these charge carriers conflicts with the Raman results which predict a limited long range order of microdomains with *Fm3m* symmetry in the cubic phase.[99] Small volumes of these ordered regions arise as precursor clusters in the cubic phase and remain limited in size on cooling. These clusters are prevented from growing by the chemical inhomogeneity created by the disordered A-site, retaining the pseudo-cubic structure in BNT.[100] The observation of weak superlattice reflections (*h*+½, *k*+½, *l*+½) in single-crystal rotation camera experiments further supports a low degree of ordering at the A-site in the high temperature phase.[101] Nonstoichometry has been noted as a common driving force toward disorder.[101]

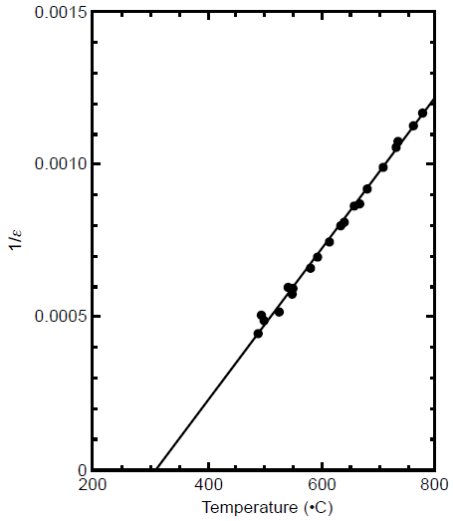

Fig.2.5.5: Curie-Weiss plot of polycrystalline BNT above T_m.[103]

The PE nature of the tetragonal phase was further tested by Park et al. [102]. The authors found this high temperature peak to originate from a combined effect of space-charge polarisation, responsible for the large polarisation relaxation between 300-550 ˚C, and an electrode reaction with the BNT ions, resulting in a variation in the conductivity. Electric modulus calculations also revealed a surface layer/electrode polarisation effect rather than an intrinsic change in the bulk permittivity of BNT at the peak temperature.[103]

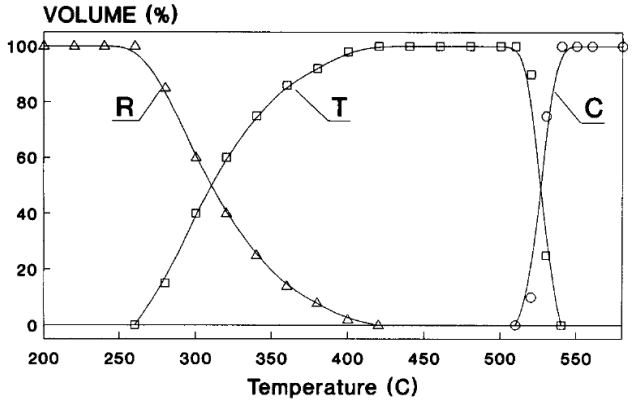

Fig.2.5.6: Phase volumes refined for BNT at different temperatures from XRD analysis.[106]

Despite evidence showing BNT to obey the Curie-Weiss law above T_m (Fig.2.5.5)[103],[104] and therefore to exist in a PE state above this temperature, both space-charge polarisation and dipolar fluctuations are thought to contribute to the relaxation process up to 560 ˚C for frequencies below 1 MHz.[105] A XRD study into the temperature dependence of the phase concentrations in BNT (Fig.2.5.6) revealed the coexistence of the rhombohedral and tetragonal phases to span a temperature range, 260-420 ˚C[106], much wider than the 55 ˚C reported by Zvirgzds et al. [9].

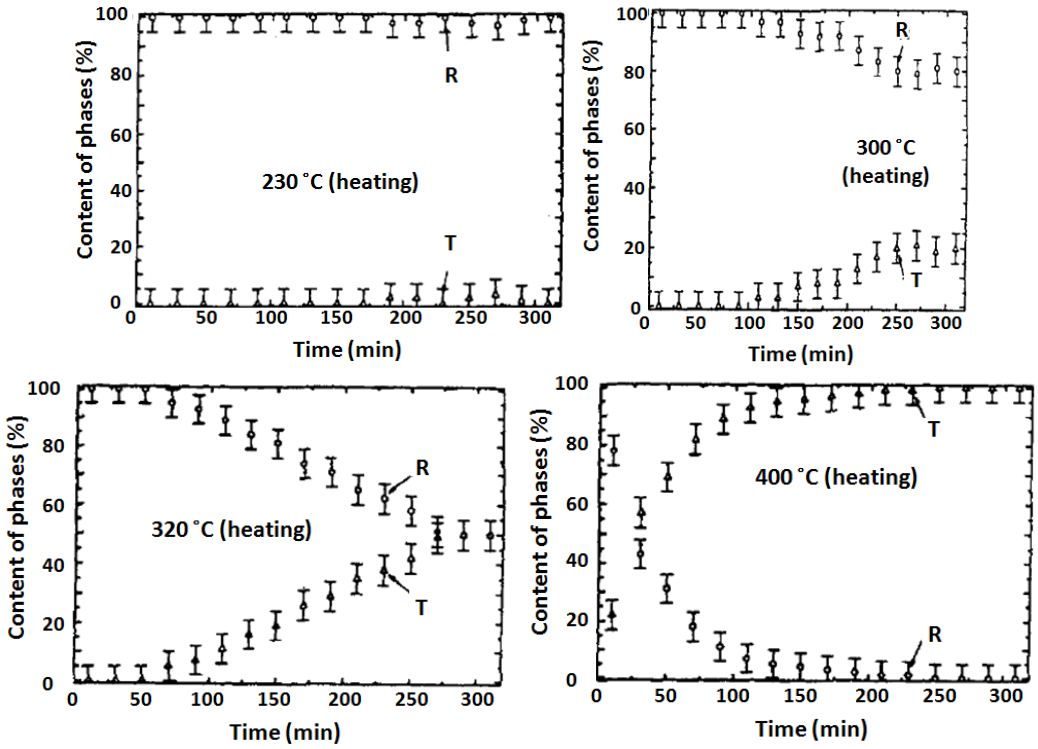

Fig.2.5.7: Time evolution of the phase boundary interactions between rhombohedral and tetragonal structures in single crystal BNT.[109]

The relaxor behaviour of BNT was explained by the time evolution of the phase boundary interactions between the polar rhombohedral regions and the non-polar tetragonal matrix shown in Fig.2.5.7. [105],[107] As the polar regions grow in size with decreasing temperature, the relaxation moves towards lower frequencies, this process is most prominent in the temperature range 320-280 ˚C. The relaxation becomes very weak and appears to be nearly independent of temperature below 200 ˚C.[108] A time evolution of 300 minutes is required for the isothermal structural transformation of these regions[107],[109] even in the 'stable' microregion below 280 ˚C. This delay is believed to be responsible for the long-term aging of BNT's properties at low temperature.[97] The transformation to the rhombohedral symmetry at the proposed transition temperature is never complete. The weak relaxation found below 200 ˚C may originate from the movement of the phase boundaries between the polar and non-polar region in an electric field. The continued interaction between these regions excludes the existence of 'pure' structural phase transitions in BNT.[107] The global cubic symmetry implied by the isotropisation of BNT further supports the existence of a mixture of both rhombohedral and tetragonal regions.[101] The double hysteresis loop, originally thought to be related to antiferroelectricity[8], could simply result from local phase transitions between the coexisting phases induced by a strong electric field (Fig.2.5.8).[108]

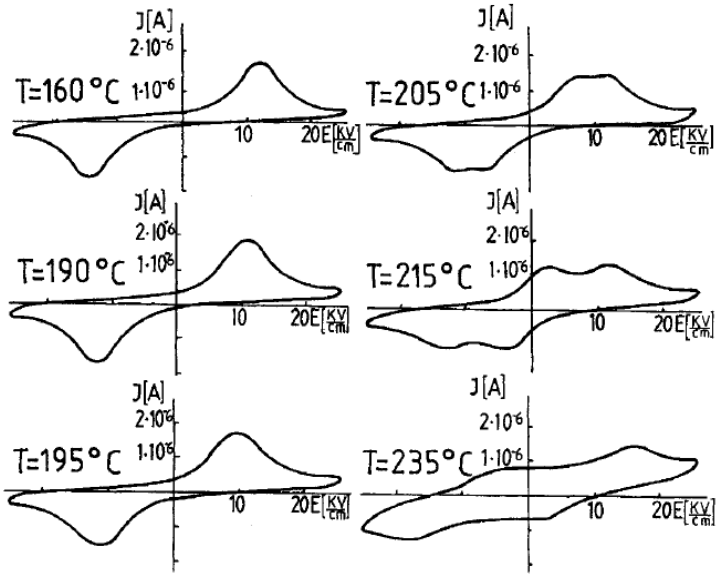

Fig.2.5.8: I-E hysteresis loop of ceramic BNT showing multiple current peaks at temperatures above 215 ˚C.[108]

The model of polar regions in a non-polar tetragonal matrix conveniently uses the change in dynamics and size of the polar regions to explain the properties of BNT rather

than ‘pure’ structural transitions. The centrosymmetric nature of the tetragonal structure used in this model, however, was questioned following a study combining neutron diffraction with SHG.

2.5.2.3 Rhombohedral/Tetragonal Matrix where T phase is polar

A comprehensive neutron powder diffraction study by Jones and Thomas[110],[111] uncovered a new structural model for BNT. Superstructure reflections and a doubling of the unit-cell axes consistent with the rhombohedral space group *R3c* were observed over the temperature range -268-255 ˚C. In this structure, illustrated in Fig.2.5.9, the oxygen octahedral is tilted about the [111] pseudo-cubic axes along the anti-phase direction $a^-a^-a^-$ (Glazer notation). To minimise the electrostatic energy associated with this tilt system, the Bi/Na and Ti cations are displaced parallel to one another along the [111] axes giving rise to a FE phase.

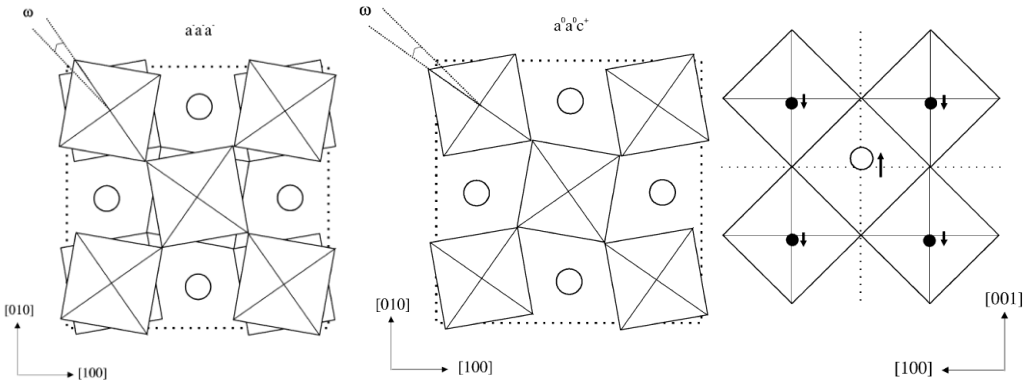

(a) (b) (c)

Fig.2.5.9: Projections of the (a) *R3c* and (b) *P4bm* structures along [001]. (c) The cation displacements in the *P4bm* structure along [010]. The open circles represent the Bi/Na sites while the filled circles represent the Ti sites.[111]

At 400 ˚C, BNT enters a *P4bm* tetragonal phase with an $a^0a^0c^+$ in-phase octrahedral tilt as indicated by *h* odd, *k* odd, *l* even superstructure reflections and a cell doubling in the [100] and [010] directions. A schematic of the *P4bm* is shown in Fig.2.5.9. The assignment of this tilt system agrees with the earlier observation of parallel rotations of the oxygen octahedral about the cubic axis by Vakhruskev et al.[10]. Jones and Thomas[111] observe no superstructure reflections associated with the non-centrosymmetric *P4mm* symmetry previously reported as the space group for the tetragonal phase[9]. In the *P4bm* phase, the Na/Bi cations are displaced anti-parallel to the Ti cations along the polar [001] axes establishing a weakly polar (ferrielectric)

arrangement in the unit cell (Fig.2.5.9). Unlike the rhombohedral phase, the A-site environment created by the octahedral tilts in the tetragonal phase is indistinguishable along the polar axis discouraging any displacement. The cation displacements in this phase are thought to result from the need to accommodate the stereochemically active lone pair on Bi^{3+} generating this unusual structure. The valence deficiency in Bi^{3+} is generally expected to drive displacements of the A-site of the perovskite structures in rhombohedral, tetragonal and orthorhombic polar phases, however it is unable to achieve a perfect match to its valency. The non-centrosymmetry of the tetragonal phase was further confirmed by SHG, which displayed a small signal indicative of a weakly polar structure. SHG is an optical effect that only occurs in materials without an inversion centre (non-centrosymmetric).

No octahedral tilts or cation displacements were observed above 540 ˚C resulting in an ideal cubic perovskite structure with space group $Pm\bar{3}m$. Only a weak SHG signal was detected within this phase up to 620 ˚C.

Between 255 ˚C and 400 ˚C, the rhombohedral and tetragonal phases coexist, indicated by the presence of both types of superstructure reflections. No structural evidence of any long-range AFE order was found for this intermediate state. The tetragonal and cubic phases were also found to coexist over the temperature range 500-540 ˚C, as previously reported by Suchanicz et al.[106]. The temperature range of this coexisting region is much wider than the 20 ˚C overlap suggested by birefringence measurements[112]. Jones and Thomas note very little difference between the profiles of the tetragonal/cubic and the pure cubic phases due to the very weak tetragonal superstructure reflections. There is also much contention regarding the temperature range over which the rhombohedral/tetragonal coexistence. XRD analysis[106] show a coexisting region of 160 ˚C, not dissimilar to the neutron diffraction results, whereas optical studies[112] report a much short temperature interval of 50 ˚C. The large temperature hysteresis between heating and cooling may account for these differences.[111] A strong drop in the piezoelectric activity of BNT at 200 ˚C followed by the persistence of a small piezoelectric response connect with d_{33} up to 280˚C is consistent with Jones and Thomas's[111] observation of a weak SHG signal in this temperature region. [113] Variation of the SHG signal intensity at 227 ˚C and 337 ˚C are thought to be associated with the coexisting rhombohedral/tetragonal and tetragonal phase transitions.[111]

Finally, no clear evidence of long-range ordering of the A-site cations was observed. The absence of any superstructure peaks associated with this type of ordering is not unexpected given the similarity in size of the ionic radii. The primitive space group proposed for the cubic phase takes into account this random distribution of the A-site cations. However, Jones and Thomas[110],[111] do not dismiss the possibility of a short-range ion ordering within BNT.

The structural model proposed by Jones and Thomas[110],[111] does not account for the phase transitions expected from the physical property measurements. Neither of the features T_s or T_m in the dielectric permittivity coincide with the structural transition temperatures. The structural model is summaries below

$$R3c \xrightarrow{255\,^{\circ}C} R3c/P4bm \xrightarrow{400\,^{\circ}C} P4bm \xrightarrow{500\,^{\circ}C} P4bm/Pm\bar{3}m \xrightarrow{540\,^{\circ}C} Pm\bar{3}m$$

2.5.2.4 Local Structure: Ordering of the A-site cations

The structural model proposed by Jones and Thomas[110],[111] for BNT was largely accepted by the research community at that time. In an attempt to interpret the physical properties of BNT, many of the investigations began to focus on its local structure, particularly the ordering of the A-site cations. While BNT shows no clear evidence of any long-range ordering, the possibility of a short-range order was not dismissed by Jones and Thomas[110],[111]. A local departure from the average rhombohedral room temperature structure was later discovered following evidence of a short-range order in BNT[23]. Two models for the ordering emerged based on (i) $Bi^{3+}TiO_3/Na^{+}TiO_3$ clusters[114] and (ii) Guinier Preston zones (GPZs) of tetragonal cation displacements[115]. A structural model of tetragonal platelets in a rhombohedral matrix developed from this research and was indirectly linked with the relaxor behaviour of BNT[116]. Studies on the ferroelastic structure of BNT further support a deviation from the average room temperature structure, showing the rhombohedral FE structure to inherit a tetragonal ferroelastic structure on cooling[117],[118]. Different models for the chemical ordering in BNT have also been proposed.

2.5.2.4 (i) $Bi^{3+}TiO_3/Na^{+}TiO_3$ Cluster Model

A short range order of local cation clusters has been observed in BNT by Raman spectroscopy. The broad nature of the Raman bands detected for BNT results from disorder at the A-site[100] as well as overlapping of different Raman modes. A limited long-range order of microdomains with *Fm3m* symmetry were initially predicted for the high temperature phase by Siny et al.[99] after deconvolving the Raman spectra into three peaks. Greater deconvolution of the spectra by Kreisel et al.[114] later revealed a new vibrational mode, undetected by Siny et al.[99], associated with nanometre sized domains. These domains are seen as one-dimensional $Bi^{3+}TiO_3$ and $Na^{+}TiO_3$ chains spanning several unit cells. Weak diffuse x-ray scattering also supports the existence of a short range order, indicating a local departure from the average structure.

A change in the polar character of the nanosized $Bi^{3+}TiO_3$ and $Na^{+}TiO_3$ clusters may help to explain the AFE-like behaviour observed for the intermediate phase. High pressure studies reveal BNT to undergo a phase transition from the ambient pressure rhombohedral structure to an orthorhombic distortion with *Pnma* symmetry.[119] The polar volume of the $Bi^{3+}TiO_3$ and $Na^{+}TiO_3$ clusters was noted to decrease with applied pressure forming the long-range AFE order expected for the orthorhombic structure. For antiferroelectricity to develop within BNT, a small fraction of ordered AFE domains are expected to already exist at ambient pressure.[120] Birefringence images of the rhombohedral phase reveal a complex domain pattern coupled with an induced strain, shown in Fig.2.5.10.[112] Inequivalent parallel or antiparallel dipole ordering between the short range ordered clusters and the matrix could account for the observed strain in BNT. [120]

Broad phonon spectra in a Raman study, performed by Petzelt et al.[121], indicate strong lattice disorder in agreement with neutron diffraction and XRD studies[111]. However high frequency dielectric spectroscopic data support local Na-Bi order even in the high temperature phase. [121] Locally ordered regions may in this case support a $P4_2nm$ space group for the tetragonal phase. Assuming local Na-Bi cation ordering in BNT, the dynamic nature of the polar clusters, observed by Raman, is thought to originate from both highly anharmonic vibrations of the Na(Bi) ions as well as fast hopping of the ions among the off rhombohedral sites, preserving the time averaged rhombohedral structure. Below room temperature, the Raman mode corresponding to the hopping of the Bi(Na) ions disappears. Only volume fluctuations (breathing) of frozen polar clusters, corresponding to different off-rhombohedral (001) displacements, occur below this

temperature.[121] The dynamics of the phase transitions therefore belong to the crossover between a displacive and an order-disorder behaviour.[100],[121]

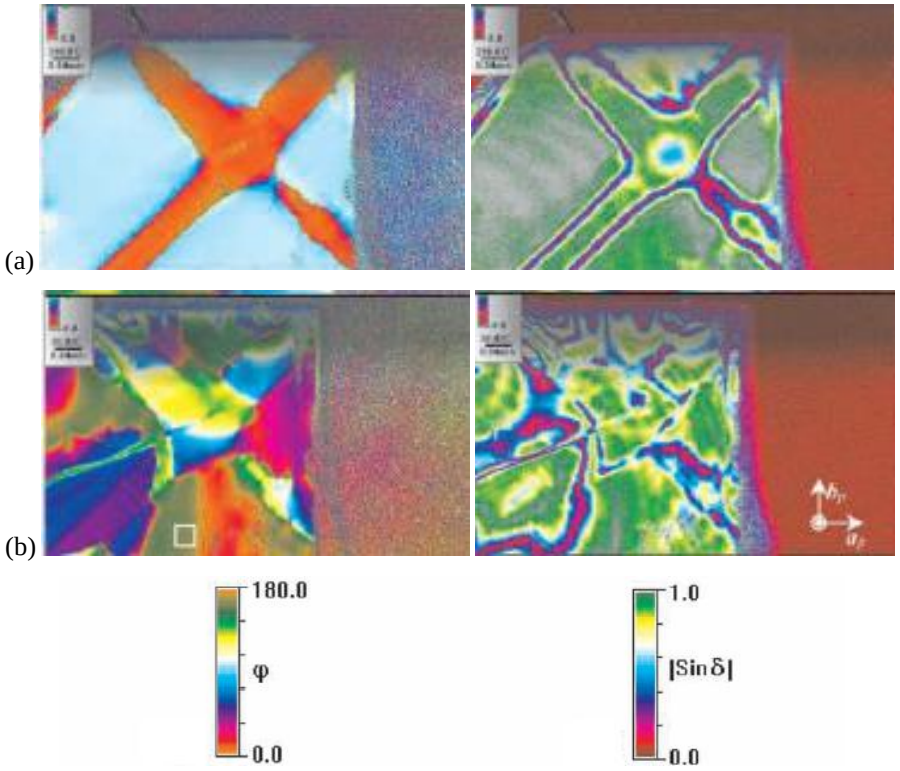

Fig.2.5.10: Birefringence images of single crystal BNT showing residual signs of the high temperature tetragonal twin structure, observed at 553K in (a), remaining in the pure rhombohedral phase at 304K in (b).[112]

Shuvaeva et al.[122] has used X-ray absorption fine structure (XAFS) spectroscopy to investigate the local structure of BNT. The changes of the macroscopic symmetry observed at the phase transitions using this technique do not lead to changes of the radial atomic distribution around Ti, which remains off-centre over the whole temperature range including the PE cubic phase. The symmetry of the high-temperature phase was found to be cubic only on a macroscopic scale and emerges as a result of the averaging of the spatial orientation of the low-symmetry units.[122] The detection of a weak SGH signal at temperatures above the tetragonal to cubic phase transition[111] supports the persistence of local distortions within the cubic structure. Shuvaeva et al. [122] conclude that only an order-disorder type mechanism is responsible for the phase transitions in BNT. No evidence of any change in the relative atomic displacements of the B-site ion support the displacive type mechanism proposed by Petzelt et al.[30]. An impedance spectroscopy investigation into the electrical conduction mechanism in BNT

further supports short range hopping of the charge carriers in a temperature dependent correlated barrier hopping mechanism.[123]

The $Bi^{3+}TiO_3$ and $Na^{+}TiO_3$ cluster model, however, do not satisfy the local requirements for electro-neutrality within BNT.[121]

2.5.2.4 (ii) Guinier Preston Zones (GPZs) Model

An alternative form of nano-ordering which takes into account the radical rearrangement of the octahedral tilts from $a^0a^0c^+$ to $a^-a^-a^-$ and the redirection of the average cation displacements from [001] to [111] at the tetragonal/rhombohedral phase transition[111] has been suggested by Kreisel et al.[115]. Assuming Na-Bi disorder, Monte Carlo simulations were combined with X-ray diffuse scattering (XRDS) data to investigate the nanoscaled characteristics of BNT. Asymmetric sharp streaks emanating from the low angle side of the Bragg peaks and extending along the <100> direction, shown in Fig.2.5.11, were attributed to the existence of planer defects reminiscent of GPZs. Typically, these GPZs give rise to rods of diffuse scattering in reciprocal space, in directions normal to the planes of the defects. The nature of the low temperature structural phase transition is recalled by the local structure of the rhombohedral phase which retains elements of the tetragonal cation displacements in the GPZs. These zones are orientated perpendicular to all $<100>_c$ pseudo-cubic directions of the rhombohedral cell. The displacement of the Na/Bi ions in the <001> direction from the [111] axis decreases the local symmetry of the rhombohedral structure to the monoclinic space group C_m. The authors believe that the existence of these local monoclinic unit cells within the random matrix provide a mechanism for the transformation between the cation displacements. Strain fields induced by the different octahedral tilts of the matrix and GPZs contract the GPZs along a direction perpendicular to the cation displacements, illustrated in Fig.2.5.12, giving rise to the observed 'L-shaped' scattering pattern.[115],[124] The relaxor properties in dielectrics are generally accepted to originate in local polar zones which differ from the average structure. Kreisel et al.[115] claim that the polar zones (GPZs) responsible for the relaxor properties in BNT are unusually decorrelated from the chemical order of the A-site, which appears as separate broad diffuse scattering regions. Rather than forming a purely random distribution, a local short-range ordering of alternate Bi- and Na-containing unit cells is expected to occur in directions normal to each <100> direction. The formation of this short range chemical order however is of minor importance compared to the structurally ordered GPZs.[115]

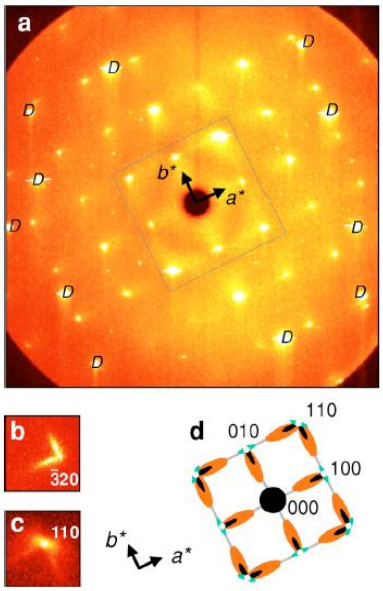

Fig.2.5.11: Room temperature XRD images showing scattering regions around the Bragg peaks for BNT at a hydrostatic pressure of 0.6 GPa. The asymmetric diffuse scattering around the $(3\bar{2}0)$ and (110) reflections are enlarged in (b) and (c), respectively. A schematic representation of the highlighted area in (a) is given in (d).[115]

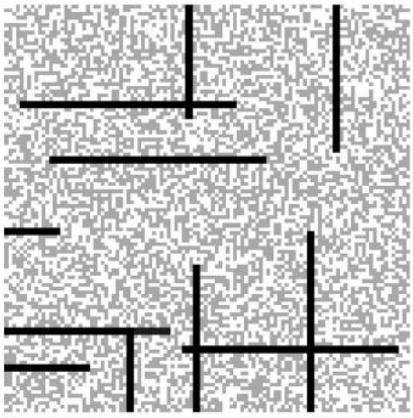

Fig.2.5.12: GPZ model structure. The gray and white pixels represent the unit cells containing Bi and Na, respectively, while the black pixels are the GPZs.[115]

A NMR study into the local order of ^{23}Na further supports the existence of local monoclinic regions within BNT where Bi/Na ions experience additional displacements away from the $[111]_{pc}$ direction along one of the six $[100]_{pc}$-type directions.[125] Aleksandrova et al. [125] also note the coexistence of the monoclinic clusters with tetragonal nuclei which exhibit a very small displacement along the $[111]_p$ direction over the temperature range 307-337 ˚C.

Further support for the GPZ model[115] has been provided by an XAFS study investigating the position of the Bi^{3+} ion within the A-site of BNT.[122] The structural model proposed from neutron diffraction studies locates the Bi cations on the three-fold axis of the rhombohedral symmetry.[111] The Bi-O coordination expected from this structure does not satisfy the bond valence of Bi, which is grossly underbonded while the Na is overbonded. XAFS revealed the Bi ion to be strongly displaced off-centre in the oxygen polyhedron, creating a local dipole moment much larger than previously thought. The Bi-O bond length measured using this technique is much shorter than that expected of the structure refined from neutron diffraction data. The local structure of Bi was then suggested to be different from the apparent structure. A new model has been recommended for the rhombohedral phase of BNT where the Bi atoms are statistically disordered around the threefold axis, demonstrated in Fig.2.5.13. The position of the Bi in the original averaged structure is replaced by three Bi atoms each with one-third occupancy and displaced off the polar axis along the pseudocubic $[\overline{1}01]$ direction, providing an additional component of Bi displacement along the polar [111] axis.[122] The coupled displacement of the Bi cations is supportive of the GPZ model[115].

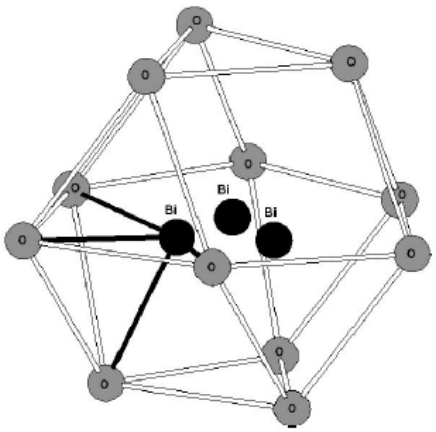

Fig.2.5.13: Schematic showing the Bi position statistically disordered around the three-fold axis of the oxygen polyhedron. The black lines show the geometry of the shortest Bi-O bonds.[122]

2.5.2.4 (iii) Tetragonal Platelets in a Rhombohedral Matrix

The structure of the room temperature phase of BNT is no longer regarded to be truly rhombohedral, but instead contains tetragonal platelets reminiscent of the precursor tetragonal phase.

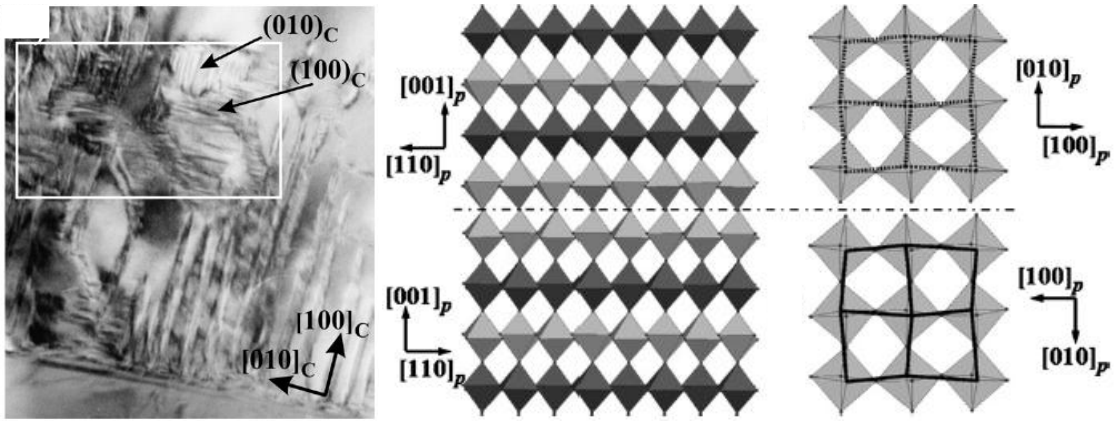

(a) (b)

Fig.2.5.14: (a) TEM image showing $(100)_c$ and $(010)_c$ FE domain walls in BNT. (b) Crystallographic model of the pseudo-merohedral $\{100\}_c$ twin boundary. The dashed line shows the position of the strained $(001)_c$ twinning plane separating the two *R3c* domains.[127]

Neutron studies show atomic ordering of the A-site along the tetragonal [001] direction to incommensurately modulate the rhombohedral phase along the four-fold axis of the precursor tetragonal phase.[126] In a related observation, $(001)_T$ platelets of high-temperature symmetry have been observed in the ambient rhombohedral phase using transmission electron microscopy (TEM).[127] The platelets are thought to form within the stability range of the cubic phase as they have developed along the three equivalent basal planes of the cubic cell. These platelets are reasoned to be nanostructural analogues of the GPZs proposed by Kreisel et al.[115]. Dorcet and Trolliard[127] attribute the local departure from the average room temperature structure to the strained $\{100\}_c$ interfaces caused by a change in tilting conditions of the octahedra in the alternating rhombohedral $a^-a^-a^-$ and tetragonal $a^0a^0c^+$ structures (Fig.2.5.14). Calling on evidence of local A-site ordering in IR and Raman spectroscopy[121], Dorcet and Trolliard[127] describe the $(001)_T$ platelets as relics of high temperature ordered regions trapped within the rhombohedral matrix. The platelets are not thought to be directly involved in the relaxation process of BNT due to the limited number of crystallographically equivalent positions allowed by the $a^0a^0c^+$ tilting system, thereby fixing the orientation of the polar vector. More random cationic displacements are expected to occur at the interfacial regions between the platelets and the rhombohedral matrix, indirectly connecting the platelets with the relaxor behaviour.

2.5.2.4 (iv) Chemical Ordering

Based on a purely ionic model, the chemical ordering of BNT is expected to have a rocksalt-type structure with alternating layers of Bi^{3+} and Na^{+} along the <111> direction, illustrated in Fig.2.5.15(a).[128] This type of configuration best describes the average properties of BNT.[129] However, first-principle calculations with a cluster expansion fitting, support a ground state (0K) with a 40-atom supercell with space group symmetry *P11m* rather than the rocksalt ordered $Fm\bar{3}m$ symmetry. This chemically ordered monoclinic structure consists of criss-cross rows of Na and Bi cations perpendicular to [001] (Fig.2.5.15(b)).[130] No such chemical ordering was observed by Kling et al.[131] who combined first-principle calculations with high resolution TEM to investigate the Na/Bi distribution in the solid solution with $BaTiO_3$. The A-site occupation was found to be homogeneous and could not be derived from the ground state predicted by Burton et al.[130]. Any non-uniformity in the TEM images was related to a slight tilting of the structure rather than any chemical ordering. By means of total energy calculations within density functional theory, the effect of pressure on the phase stability of BNT with different chemical ordering configurations has been investigated by Groting et al.[131]. Under compressive and tensile pressures, above 3 GPa and below -5 GPa, BNT adopts stable *Pbnm*- and *P4mm*-like structures, respectively, independent of the cation configuration. At ambient pressure, BNT is described as a structurally frustrated system where the structure depends on both the type and degree of chemical order. Hybridisation between the Bi $6s^2$ and O $2p^4$ electrons was previously noted to lead to stereochemically active Bi^{3+} lone pairs which increase the stability of structures with layers of high Bi concentrations in the {001}-planes as well as drive a strong displacive disorder in the oxygen sublattice.[132] GPZs of Bi-rich planes have similarly been used by Kreisel et al.[115] to explain the diffuse scattering patterns observed for BNT. Nanoregions with a local *Pbnm*-like structure are believed to form as a result of the (001)-layered short-range chemical ordering and act as a precursor for the high pressure phase.[131],[132] The local structure is constrained by crystal continuity to form an average chemically disordered *R3c*-like matrix.[131] The areas of short range chemical order are expected to favour different cation displacements and octahedral tilting thereby acting as nucleation sites for polar nanoregions (PNRs). [132] Experimental evidence however does not support the 'criss-cross'[128],[130] or '{001} layered'[131],[132] models predicted from first-principle calculations due to the lack of ½{*eeo*} diffraction spots expected from these models.[133]

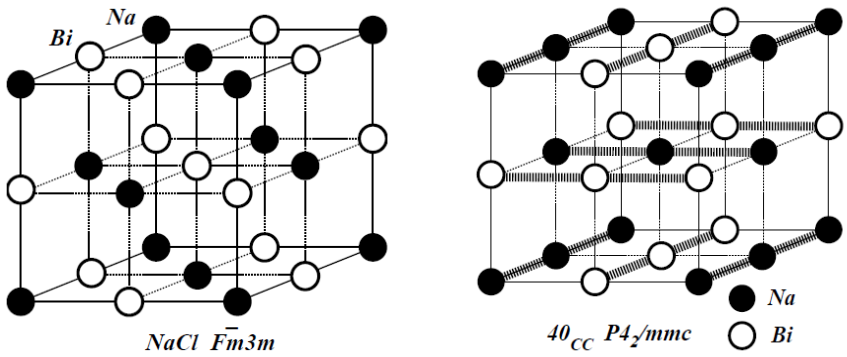

(a) (b)

Fig.2.5.15: A-site chemical ordering models: (a) Rocksalt[130] and (b) 40_{CC}[128].

2.5.2.5 Ferroelastic Structure

Neutron diffraction measurements show BNT to enter a ferroelastic state at the cubic to tetragonal structural transition.[94] Frozen tetragonal twin configurations oriented along the <110> direction have been observed in BNT at room temperature using polarised light microscopy (PLM) (Fig.2.5.16) [101], indicating that ferroelasticity persists into the rhombohedral phase. [102],[117] Superlattice reflections consistent with a ferroelastic distortion of an $a^0a^0c^+$ in-phase octahedral tilt have also been observed in single crystal BNT up to 700 ˚C.[134]

Irrespective of the polar phase transformations undergone in BNT, PLM images show the high temperature tetragonal ferroelastic domains to remain unchanged on cooling from 520 ˚C to 25 ˚C. The ferroelastic tetragonal structure has been observed to geometrically and elastically restrict the polar rhombohedral phase as they form within the ferroelastic domains.[135]

A cross-hatched FE domain pattern of lamellar and needle-shaped morphology has been imaged using bright field TEM in the (001) oriented plane (Fig.2.5.17).[117],[134] These domains tend to organise along the <110> directions and show a typical size of 50-100 nm.[117],[134] The tetragonal ferroelastic domains, imaged by PLM and shown in Fig.2.5.18, have a much larger domain size with a width of 5-20 μm and a length on the order of hundreds of microns.[117] The FE nanodomains nucleate within large ferroelastic domains forming a hierarchical domain structure pinned by planar defects with the same <110> orientation as the ferroelastic domains. The planer defects interrupt the lattice coherency and partially relax the elastic energy of the system.[135]

The tetragonal domains are described as proper[136] ferroelastic domains and are not influenced by the stress accommodation of the FE ones.[137]

Residual stress induced by rapid cooling has been shown to suppresses the ferroelastic twin configuration in BNT[102]. The influence of the ferroelastic structure on the polar structure may influence the time for the isothermal structural transformations to occur in BNT. The technique of cooling by quenching applied by Kusz et al. [138] may account for the much shorter time interval recorded for the formation of the rhombohedral phase at the isotropisation point (10 min compared to 300 min[107]).

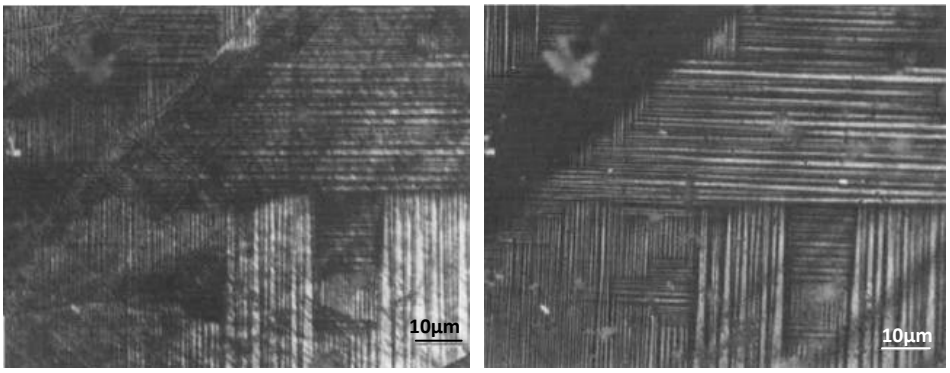

(a) (b)

Fig.2.5.16: PLM images of single crystal BNT at (a) room temperature and (b) 350 ˚C, showing the frozen tetragonal twin configuration.[101]

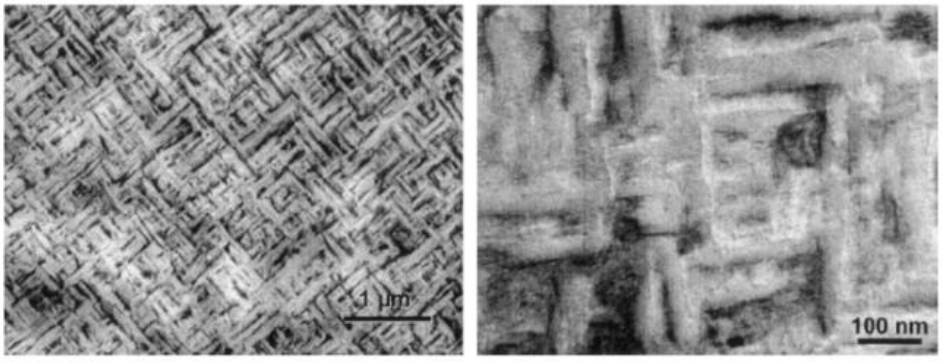

Fig.2.5.17: Bright field TEM images showing a cross-hatched FE domain pattern in the (001) oriented plane of single crystal BNT.[134]

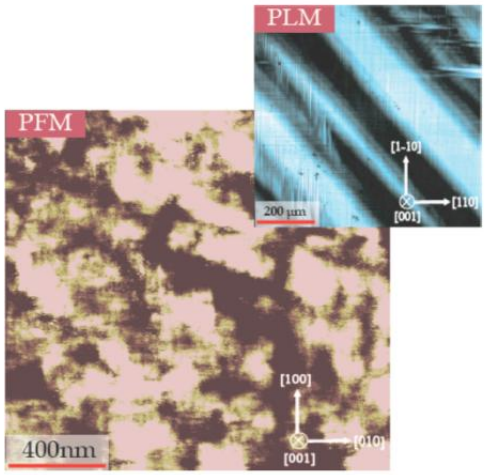

Fig.2.5.18: FE domain structure of single crystal BNT imaged by piezoresponse force microscopy (PFM) and its corresponding ferroelastic domain structure imaged by PLM.[117]

2.5.2.6 Two Phase Orthorhombic Model

An alternative model for the structural phase of BNT which takes into account the reported physical properties has been devised by Dorcet et al.[139] and Trolliard and Dorcet[140].

Extensive TEM investigations of ceramic BNT reveal tetragonal *P4bm* platelets of BNT to reside within the FE rhombohedral *R3c* matrix below 200 ˚C. The destabilisation of the rhombohedral phase is indicated by the disappearance of the FE domains near 200 ˚C. Above 200 ˚C, superstructure spots originating from (010) thin sheets appear at *½*(*oee*) and are elongated along [010]. Neither the *R3c* nor *P4bm* phases can generate these types of spots. Only an orthorhombic *Pnma* ($a^-a^+a^-$) space group can account for both the in-phase and anti-phase rotations of the oxygen octahedral and the assumed disordered average structure of BNT. The observation of these *½(oee)*spots lead Dorcet and Trolliard[139],[140],[141] to suggest the existence of a modulated phase shown in Fig.2.5.19, composed of orthorhombic *Pnma* sheets layered between rhombohedral *R3c* blocks, that assists the transition from the room temperature phase to a purely orthorhombic *Pnma* phase observed above 290 ˚C. Thermal hysteresis is generally observed in modulated incommensurate phases. The periodicity of the modulation is in agreement with the incommensurately modulated rhombohedral phase proposed by Balagurov et al.[126]. An orthorhombic intermediate phase has not been detected by either X-ray or neutron diffraction studies of BNT. Dorcet et al.[139] reason that the strong structural affinity of the rhombohedral and orthorhombic structures masks this

intermediate phase. Further, the small size of the regions, from which the superstructure originates, hinders their detection.

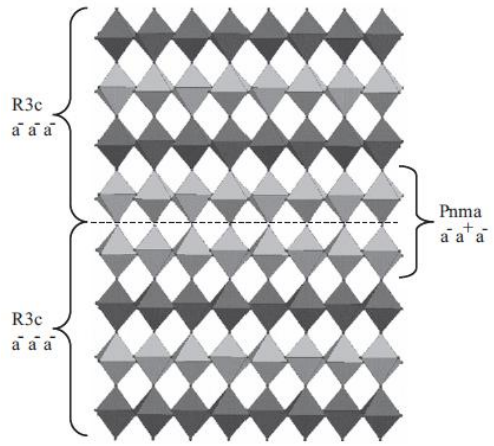

Fig.2.5.19: Two Phase Orthorhombic Model. Octahedral representation along (010) showing the *Pnma* sheet forming a twin boundary between two *R3c* FE domains.[141]

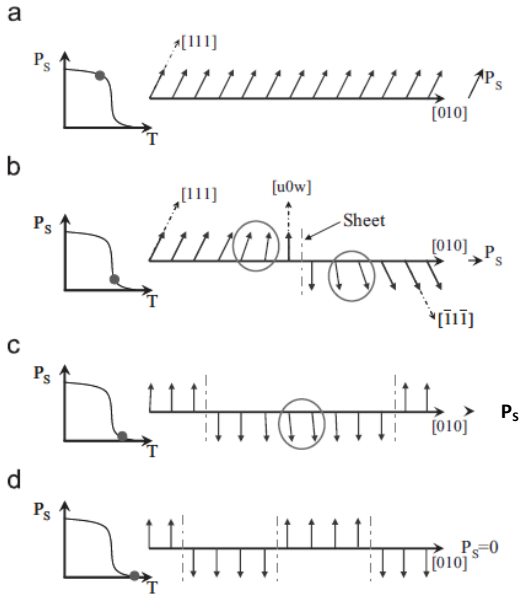

Fig.2.5.20: A schematic of the microtwinning process showing the cationic displacements: (a) polar *R3c* phase, (b) and (c) are the intermediate states highlighting the intermediate directions of the displacements and (d) is the AFE modulated phase.[141]

In an attempt to explain the AFE properties of BNT within this temperature range, Dorcet and Trolliard[139],[140],[141] model the *Pnma* sheets as twin boundaries between two *R3c* FE domains which increase in density through a microtwinning process with increasing temperature (Fig.2.5.20). Within the *Pnma* sheets the cations are displaced along $[u0w]_{pc}$, leading to a reorientation of the polar vector within the depleted *R3c* matrix. The pseudo-merohedral twinning law allows two successive ferroelastic and FE

R3c domains to present polar vectors oriented in opposite directions in a plane perpendicular to the modulation direction. The modulated phase also enables Dorcet and Trolliard to ascribe the relaxor behaviour, typically observed in physical property experiments, to cationic rearrangements between two atomic positions associated with displacements in the [111] and $[u0w]_{pc}$ directions defined by the local structure of the *R3c* blocks and *Pnma* sheets, respectively.

The orthorhombic phase then transforms to a tetragonal phase near 300 ˚C; the anti-phase tilting of the oxygen octahedra along the orthorhombic *x* and *z* directions progressively decreases to zero while the in-phase tilting along the orthorhombic *y* axis is roughly maintained resulting in a tetragonal $a^0a^0c^+$ tilt system. A doubling of the unit cell along the pceudocubic directions, as indicated by the presence of ½(000) superstructure reflections above 400 ˚C, are characteristic of a Na-Bi order along the $[111]_{pc}$ direction. In order to preserve the AFE nature of BNT, Dorcet and Trolliard assign a centrosymmetric *P4/mbm* space group to this phase, rather than the polar *P4bm* space group, with an equivalent tilt system, suggested by Thomas et al.[110]. Given that a structural Na-Bi ordering was never observed by X-ray or neutron diffraction, Dorcet et al. conclude that the PE tetragonal phase is a globally disordered structure that is locally ordered on the nanoscale at the A-site. Above 400 ˚C, the ordered nanodomains are described as having a $P4_2/mnm$ structure in agreement with the centrosymmetric and nonpolar properties observed at these elevated temperatures. The polar *4mm* point group structures previously proposed by Jones et al.[110],[111] and Zwirgzds et al.[9] are attributed to the presence of impurities and/or defects within the samples, preventing the refinement of a non polar space group for the tetragonal phase. BNT then enters a cubic $Pm\bar{3}m$ phase at 520 ˚C. In agreement with Petzelt et al. cation order within the stability domain of the cubic phase persist, with evidence of very weak *½(000)* reflections at 620 ˚C. Signs of Na/Bi ordering then progressively vanish with increasing temperature. The structural model is summarised in Fig.2.5.21.

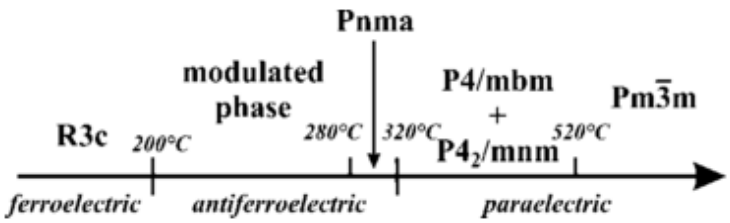

Fig.2.5.21: Schematic of the 'Two Phase Orthorhombic Model'.[140]

Diffuse lines observed in the TEM results by Dorcet et al.[127] and initially related to an aperiodic distribution of tetragonal platelets in the rhombohedral matrix are shown to be present up to 620 ˚C, well above the stability range of the tetragonal phase. The coexistence of the diffusion with the ½(000) reflections have led Dorcet et al.[140] to suggest that the diffusion is linked to the establishment of cation order rather than the presence of the tetragonal platelets in the high temperature cubic phase.

2.5.2.7 Modulated Room Temperature Structure with lower than R3c Symmetry

Following the publication of research into the A-site ordering in BNT and the controversial two phase orthorhombic model, a response to the new results was published by the authors Jones and Thomas[110],[111] in Thomas et al.[143] and Beanland and Thomas[144]. While they disagree with the results of Dorcet and Trolliard[139],[140] which underpin the orthorhombic model, similarities were acknowledged in the X-ray scattering data previously used by Kreisel et al.[115] to form the GPZ model. Thomas et al.[143] do not observe direct evidence of a c^+ tilt consistent with inclusions of a tetragonal phase[127] however they do recognise that a transitional region separating the rhombohedral and tetragonal structures may form a significant fraction of the crystal volume leading to the observation of an average structure with a lower than rhombohedral symmetry[144].

Distinct satellite peaks have been identified by Thomas et al. [143] in the asymmetric streaks of extended scattering previously observed by Kreisel et al.[115] using XRDS spectroscopy. However, Thomas et al.[143] note that the model of tetragonal plate-like inclusions proposed by Kreisel et al.[115] would be under greater strain than suggested by the lattice parameters, refined from the diffraction peaks, as the surrounding average rhombohedral matrix cools around these regions. Thomas et al.[143] also do not observe the additional $(310)_{dpc}$ reflection used by Dorcet and Trolliard[127] as evidence of a c^+ tilt consistent with inclusions of a tetragonal phase. To determine the origin of these satellite peaks, Thomas et al.[143] use the results from an optical birefringence experiment which use crystals grown from the same batch of BNT. Tweed-like 90˚ domains corresponding to the three optically distinct directions of the [001] axis of the tetragonal phase, persist on cooling into the rhombohedral phase, where they break up into smaller regions while maintaining the stripe pattern. Each domain preserves the memory of a particular *c*-axis orientation in the tetragonal phase. Building on the theory of a tetragonality modulated rhombohedral phase proposed by Balagurov et al.[126], the

domains of the rhombohedral phase are concluded to differ in the direction of the tetragonal modulation axis in sympathy with their original orientation in the tetragonal phase. These satellite peaks, imaged using synchrotron XRD, are thought to arise from a network of modulated domains, where each modulation has a real space period of ~40 Å.[143]

Gorfman et al.[145] failed to images any domain boundaries corresponding to a rhombohedral symmetry below 300 ˚C using optical birefringence microscopy despite the optical indicatrix indicating the transformation to this structure from the tetragonal phase. At low temperatures, the optical orientation of BNT has a broad angular distribution where the domain walls appear to be unrestricted by crystallographic direction, leading Gorfman et al.[145] to suggest a monoclinic symmetry for this phase. A lower than rhombohedral symmetry in single crystal BNT has similarly been observed by Gorfman and Thomas[90]. Refinement of the X-ray diffraction 2θ splitting data by a least-squares fit gives a *C*-centred monoclinic *M(C)* solution best described by the pair of angles $\alpha=\beta=89.944^{\circ}$ and $\gamma=89.646^{\circ}$. A possible space group suggested by Gorfman and Thomas for the room temperature phase is C_c, which is a monoclinic subgroup of *R3c* that allows the $\{h+½, k-½, l+½\}$ tilt system observed in the single crystal and the *M(C)* lattice described by the splitting of the Bragg peaks. The C_c signature reflection at $\{½\ ½\ ½\}_{pc}$ has not been observed by either neutron or X-ray diffraction and only appears as a double diffraction effect in synchrotron XRD and therefore cannot be used to describe the room temperature phase. Refinement of BNT with the C_c symmetry still leaves the Bi under-bonded and the shorter Bi-O bond length, observed by XAFS spectroscopy[122], unaccounted for. The inability of the authors to detect any tetragonal platelets may originate from a transitional region separating the two structures previously recognised by Dorcet and Trolliard[127]. Beanland and Thomas[144] suggest, from TEM observations of single crystal BNT (Fig.2.5.22), that if continuity of the oxygen octahedra is maintained about [100] and [010] for a {001} plane, for example, a thin transitional region between the two structures of the form $a^0a^0c^+ \rightarrow a^-a^-c^+ \rightarrow a^-a^-a^-$ or $a^0a^0c^+ \rightarrow a^-a^-c^- \rightarrow a^-a^-a^-$ is necessary. The tetragonal platelets were noted to be inhomogeneously distributed within the single crystal. Consequently, in regions with a very high density of platelets the transitional region may form a significant fraction of the crystal volume leading to the observation of an average structure with a lower than rhombohedral symmetry. Beanland and Thomas[144] note that the nanoscale $a^0a^0c^+$ platelets should be visible in a variety of imaging conditions and that the observed

contrast in the TEM images is not consistent with $a^-a^-a^+$ tilting at {001} twin boundaries or with sheets of local Na/Bi ordering, proposed by Dorcet et al.[139],[140].

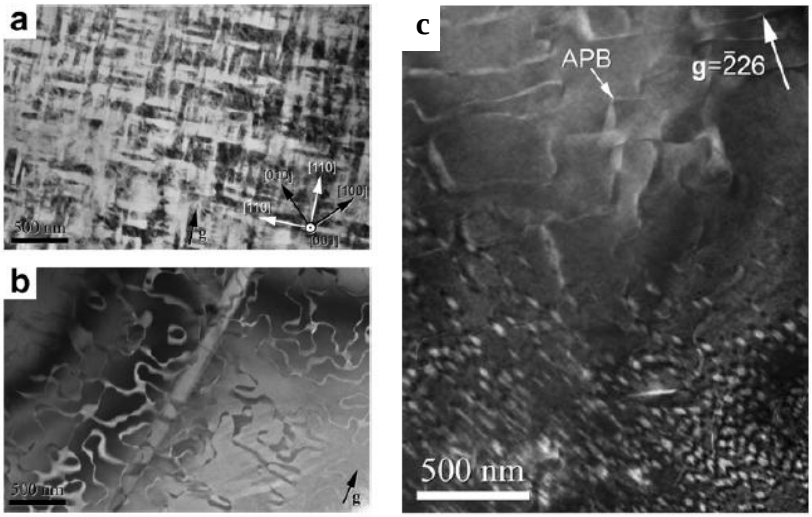

Fig.2.5.22: TEM images of single crystal BNT showing (a) high density and (b) low density defect regions. Individual APBs (curved) and domain walls (straight) are visible in (b). In the lower half of (c), thin platelet-like defect are visible.[144]

2.5.2.8 Monoclinic Room Temperature Structure

Following the observation of a monoclinic C_c symmetry in the room temperature phase, a new structural model for BNT was developed. The effect of processing conditions and electrical poling on the room temperature structure were also investigated.

Room temperature high resolution XRD analysis of calcinated and sintered BNT powders, completed by Aksel et al.[147], reveal a splitting of the (110) diffraction peak associated with a monoclinic C_c structure for the sintered powder. The broad and symmetric nature of the (110) peak demonstrated by the calcinated powder may have contributed to some misinterpretation of the structure in the past. Microstructural contributions to the peak broadening are thought to obscure this peak splitting, resulting in the adoption of the *R3c* model for this room temperature phase. Local distortions in the structure of BNT may lead to small variations in the diffraction patterns which cannot be entirely modelled with a single C_c structure. Aksel et al.[148] have used a second phase with space group $Pm\bar{3}m$ to account for this local disorder which may arise from either anti-phase boundaries, domain walls, local A-site order, microstrains or platelets of *P4bm* or *Pnma* structure. The growth in volume fraction of the short range regions, modelled as the cubic phase, with increasing temperature correlates well with

the thermal depoling behaviour seen for BNT. Aksel et al.[148] associate the loss of long-range FE order within BNT with either a decrease in volume fraction of the major C_c phase or the associated percolation of disordered nano-scale platelets. Neither superlattice reflections associated with long-range *P4bm* nor *Pnma* symmetries were observed below 280 ˚C.

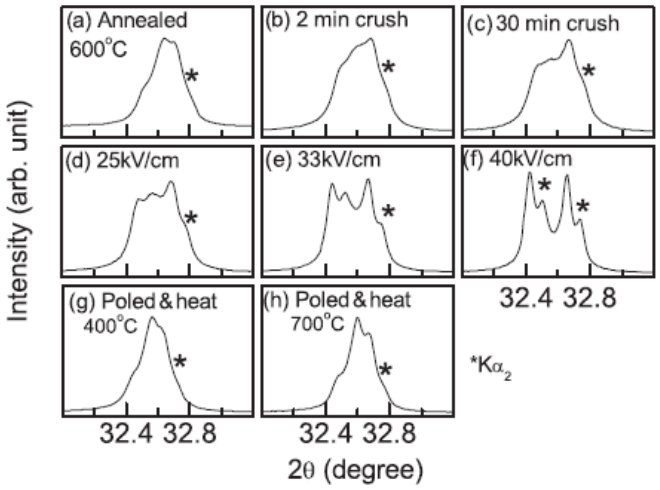

Fig.2.5.23: Powder XRD patterns of the $\{110\}_{pc}$ peak of BNT subject to different thermal, mechanical and electrical treatments. In (g) and (h) a poling field of 70 kV/cm was applied to the ceramic.[150]

An irreversible electric-field-driven monoclinic to rhombohedral phase transformation has been observed in the room temperature structure of BNT. Rao et al.[149], using powder XRD, have attempted to analyse this transformation in the framework of two alternative theories: (i) an intrinsic polarisation rotation and (ii) the adaptive phase theory. (i) In the case of the rotation theory, the unpoled system has a bulk C_c phase and the structural transition is thought to result from the rotation of the polarisation vector, which remains on the $(1\bar{1}0)_{pc}$ plane, towards the $[111]_{pc}$ direction. (ii) Alternatively, the monoclinic distortion is an interference effect which emanates from twinned rhombohedral nanotwins (NTs), whose dimensions are less than the coherence length of the X-rays.[71] Two variants of the twinned rhombohedral nanodomains are thought to combine in such a way that their resultant polarisation vector lies in the $(1\bar{1}0)_{pc}$ plane, yielding the monoclinic symmetry. NTs of the type {100} have been revealed by TEM to exist as a majority within BNT.[133] In the case of the adaptive phase theory, the field-induced transformation, as seen by XRD, originates from the merger and growth of the rhombohedral NTs to an extent that the adaptive diffraction effect becomes irrelevant as

the coherence length of the rhombohedral structure becomes larger than that of the X-rays, revealing the intrinsic structure.

After unravelling the effect of electrical poling on the room temperature structure of BNT, Rao et al.[150] preformed a comparative structural analysis of poled and thermally annealed samples using synchrotron XRD. This study revealed BNT to be highly sensitive to thermal, mechanical and electrical stimuli (Fig.2.5.23). The inability of the monoclinic C_c structure to fully account for the room temperature diffraction pattern had previously been noted by Aksel et al. [148]. In the equilibrium room temperature state, achieved after annealing, both monoclinic C_c and rhombohedral *R3c* phases were found to coexist. Mechanical and electrical stresses were found to drive the system away from equilibrium by increasing the volume fraction of rhombohedral phase. Rao et al.[150] suggest that this MPB like-feature in BNT is an accidental consequence of the independent transformation of the tetragonal and orthorhombic phases to the *R3c* and C_c structure on cooling. The local and global structures of BNT were further investigated by combining first-principle calculations with electric field dependent electron, neutron and XRD experiments. The monoclinic distortion observed in bulk diffraction techniques was found to result from the strain generated by localised in-phase $a^-a^-c^+$ tilted regions in the rhombohedral matrix. The coherence length of these tilted regions decrease with applied field (Fig.2.5.24(a)), thereby revealing the ground state rhombohedral phase on poling.[151] Near the depolarisation temperature, the long range coherence of the field-stabilised rhombohedral phase suddenly decreases with the onset growth of the incompatible in-phase tilted regions (Fig.2.5.24(b)). The rhombohedral phase persists up to 300 ˚C, despite the seeming completion of depolarisation at 200 ˚C. The system then retains some memory of the field-stabilised distortion after cooling from 300 ˚C. The Raman study also reveal the localised in-phase octahedral tilted regions to stem from a positional disorder on the oxygen sublattice resulting from the contrasting character of the Bi-O and Na-O bonds.[151]

Neutron elastic scattering experiments reveal only a very weak peak near (½½½), the superlattice reflection allowed by the C_c structure and forbidden by the *R3c*. Ge et al.[104] conclude that the scattering from the crystal bulk is representative of a rhombohedral structure, in agree with Balagurov et al.[126], and cannot be monoclinic. Given the large penetration depth of the neutron, the observed scattering is dominated by the bulk of the crystal however a small contribution from the near-surface will be

present, in this case as a very weak monoclinic reflection. The presence of two different room temperature structures in BNT was reconciled by considering the monoclinic phase as a skin effect.[104]

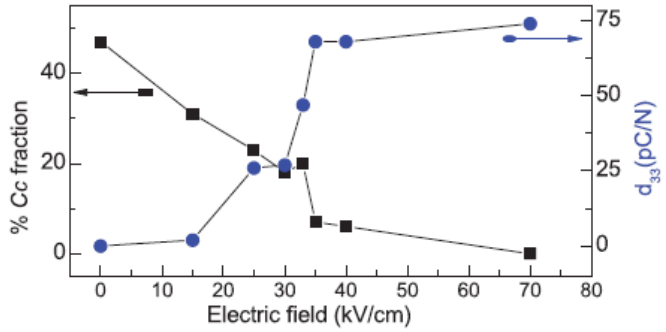

(a)

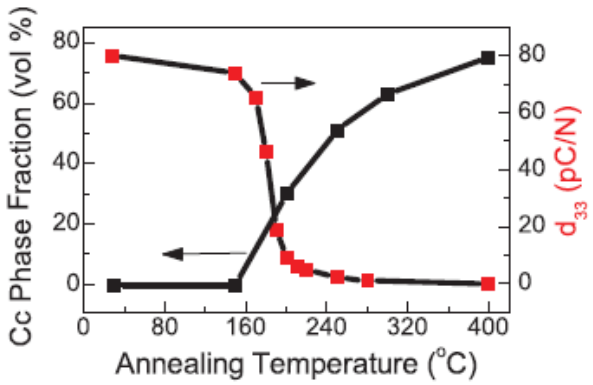

(b)

Fig.2.5.24: Variation of monoclinic phase fraction and piezoelectric coefficient d_{33} with (a) electric field[151] and (b) annealing temperature[150].

2.5.2.9 Local Structure: Role of Bi in FE Properties of BNT

The Bi cation was found to play a prominent role in the departure of the local atomic structure from the average structure of BNT.

The short-range structure of BNT was investigated by Jeong et al.[152] using total neutron scattering with Reverse Monte Carlo (RMC) modelling. Inter-comparison of the bonding environments of the A and B site ions in BNT and the Na substituted $Bi_{0.5}(Na_{0.75}K_{0.25})_{0.5}TiO_3$ system revealed little change in the Ti-O bond length distribution despite the long-range symmetry difference of these two materials. The K^+ substitution does not appear to influence the off-centring of the Ti ion, indicating a decoupling of the A- and B-site displacements. The bonding environments of Bi and Na with O were found to differ when examined on a length scale of < 4 Å. The large degree

of directional off-centring of the Bi^{3+} ion relative to the rhombohedral *R3c* cell is believed to be responsible for the FE nature of BNT.

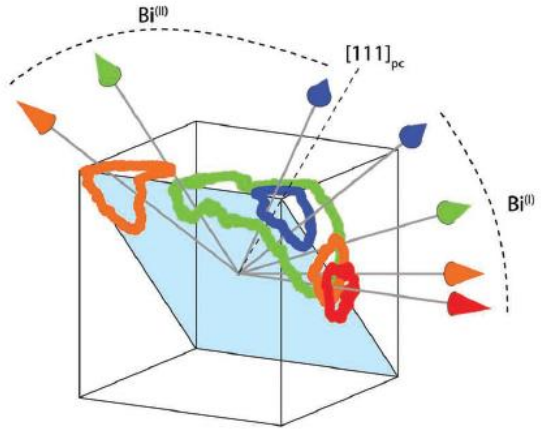

Fig.2.5.25: A schematic of the bifurcated polarisation rotation model showing the position of two distinct Bi cation displacements: $Bi^{(I)}$ and $Bi^{(II)}$, as a function of temperature from -263 ˚C (blue) to 493 ˚C (red).[153]

BNT shows significant nanoscale distortion on the local scale. In an attempt to understand how the local competing interactions determine the average structure and influence the phase transitions of BNT, Keeble et al.[153] use stereographic projections of the A-site environment, determined from RMC profiles of neutron pair distribution function (PDF) data, to distinguish the size and polar displacements of the cations on a local level. The local structure was found to be characterised by competing structural distortions between both the varying symmetries on the A-site and the rhombohedral symmetry of the Ti cations; and also between distinct displacements in the A-site.[153] The rhombohedral displacement of the Ti cation along the $<111>_{pc}$ direction is consistent with XAFS studies[122] which find the B-site ion to remain off-centre even in the high temperature phase. Two distinct Bi cation displacements coexist within the high temperature rhombohedral phase: $Bi^{(I)}$ directed in the monoclinic plane and $Bi^{(II)}$ approaching the orthorhombic $[011]_{pc}$ direction. The local environment of the Bi cation is expected to be far more distorted than the average structure suggests.[122] The displacements are confined to the monoclinic plane and counter rotate through this plane forming a bifurcated polarisation rotation model as the temperature increases (Fig.2.5.25). The two rotation pathways involve different transition sequences on transforming from the rhombohedral to the tetragonal phase. $Bi^{(I)}$ undergoes a second order-type rotation $R \rightarrow M_A \rightarrow T$ while $Bi^{(II)}$ yields the sequence $R \rightarrow M_B \rightarrow O \rightarrow M_B \rightarrow T$,

where M_A and M_B denote different monoclinic segments relating to the direction of the cation displacement. The Na cation is also displaced within the monoclinic plane however, unlike the Bi cation, it shows no visible preference in displacement direction and remains significantly less displaced along the polar direction. The biphasic nature of the Bi underlies the complex nanostructure observed in BNT.

The prominent role played by the Bi cation in the departure of the local atomic structure from the long-range average structure of BNT was confirmed by Aksel et al. [154]. The long-range structure was found to better describe BNT after sintering. A-site ordering is not considered to be the source of the local structure deviation. Information about the length scale of the local atomic order and the local cation bonding environments was obtained by fitting neutron PDF data to a 'box-car model'. The bond environments were found to change when averaged over different length scales, consequently, the bond valence of Bi^{3+}, calculated from these values, is different locally from its average value. The ideal value of the bond valence is significantly larger than that calculated from the average structure and may facilitate the local structural deviation. The difference in spread of the bond lengths of the A and B site ions with oxygen indicate significant Bi disorder. However, the constraint imposed by the small box model on the position of the A site ions masks the effect of a change in positions of O^{2-} around the Bi^{3+} site on the local scale. The Bi^{3+} and Na^{+} positions are not expected to be identical, the lone pair on the Bi^{3+} typically distorts the Bi-O coordination, while no such disorder is expected for Na^{+}. The RMC model, which permits unique positions for the different A cations, reveal the Na and Bi cations to shift only slightly from their average crystallographic positions forming symmetric Na-O bonds and asymmetric Bi-O bonds, thus enabling the ions to satisfy the sum charge of their bonds with oxygen. The long-range monoclinic structure appears to be an average of the unique bonding environments created by the cations with oxygen. Aksel et al.[154] note the different starting model used by Jeong et al.[152] to describe the average structure for a similar neutron scattering experiment. The monoclinic model used by Aksel et al.[154] contains the large Bi^{3+} displacement seen by Jeong et al.[152] who use a higher-symmetry rhombohedral structure when fitting their data. Aksel et al.[154] argue that this difference provides further support for the classification of BNT in the C_c space group.

2.5.2.10 Single Phase 'Continuous Tilting' Model

A single phase 'continuous tilting' model has been proposed by Levin and Reaney[133] following an extensive TEM study of the room temperature phase. The structure of BNT is described as exhibiting a coherent assemblage of three nanoscale domain variants featuring local orthorhombic tilting: $a^-a^-c^+$, $a^-c^+a^-$ and $c^+a^-a^-$, shown in Fig.2.5.26.

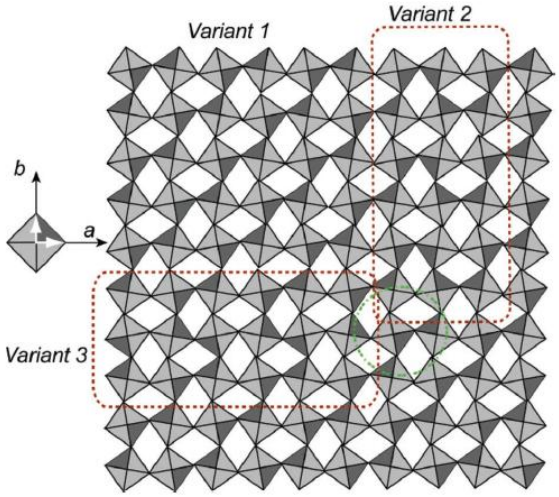

Fig.2.5.26: A schematic of the three nanoscale domain variants featuring local orthorhombic tilting: $a^-a^-c^+$, $a^-c^+a^-$ and $c^+a^-a^-$. The coherence length of the in-phase tilting is significantly shorter than the anti-phase tilting.[133]

Each orthogonal axis exhibits a short-range (1-2 nm) ordered in-phase tilting superimposed on a long-range (>5 nm to 10 nm) ordered anti-phase $a^-a^-a^-/a^-a^-c^-$ tilting which when probed on the length scale of X-rays yields an average pseudo-rhombohedral or monoclinic structure.[133] In order to accommodate for any strain associated with the boundaries between differently orientated $a^-a^-c^+$ tilting regions, Levin and Reaney[133] assume a disorder in the relative magnitude and directions of the octahedral rotations about the three cubic axes. No distortions associated with any tetragonal ($a^0a^0c^+$) platelets could be seen. The absence of ½{*eeo*} reflections in the electron diffraction patterns of BNT is typically used as an argument against domains with $a^-a^-c^+$ tilting. These reflections arise from anti-parallel displacements of the A-cations along the <110> direction aligned with the orthorhombic *a*-axis. Levin and Reaney[133] reason that disorder of the cation displacements along the <111> direction, indicated by diffuse electron scattering, create disorder in the <110> displacements which in turn mask the ½{*eeo*} reflections. The cation displacements are noted to be decoupled from the tilting structure. Using this model, the intermediate orthorhombic

Pnma structure, proposed by Dorcet et al.[139], is thought to evolve from the room temperature state by increasing the coherence length of the in-phase titling, which becomes favoured at high temperatures, and stabilises the anti-parallel A-cation displacements.[133] The departure from the average monoclinic structure, previously identified by Aksel et al.[148], could result from the sampling of unequal fractions of the pseudo-orthorhombic variants by the X-ray diffracting volumes.

2.5.2.11 Defect Structure

Two different approaches have been taken to resolve the true nature of the room temperature structure of BNT.

Ma et al.[156] have applied the technique of selected area electron diffraction (SAED) to analyse the octahedral tilting of BNT under TEM. This technique is unaffected by adaptive diffraction effects[71], previously considered by Rao et al.[149], thereby allowing for a clear distinction to be made between the *R3c* and C_c symmetries even in the unpoled multi-domain state. A statistical approach based on the presence or absence of particular superstructure reflections in the diffraction patterns taken along a direction perpendicular to the oxygen octahedral tilt axis was used to determine the structure. The presence of superstructure spots in the plane of the $\{100\}_{pc}$ domain wall along two different $<110>_{pc}$ directions, 90˚ apart, only occurs in C_c symmetries leading Ma et al.[156] to assignment the monoclinic structure to this phase. Information regarding the dynamical diffraction effects, however, is not provided by the SEAD patterns collected by Ma et al.[156].

Beanland and Thomas[157] have employed the technique of convergent beam electron diffraction to take into account this effect. Patterns with and without mirror planes as well as superstructure spots can be generated using this technique providing several ways to distinguish between *R3c* and C_c symmetries. By examining a defect free area of BNT Beanland and Thomas[157] ascribe a rhombohedral symmetry to the averages structure. The authors also note the agreement of their data with a simulated pattern of the *R3c* structure where the Bi occupies multiple positions, previously proposed by Keeble et al.[153]. The local orthorhombic tilt system proposed by Levin and Reaney[133], is not dismissed by the authors as it is expected to form a global $a^-a^-a^-$ tilt. A defect structure of tetragonal $a^0a^0c^+$ platelets and planer boundaries, including antiphase boundaries (APB) and domain walls with locally different symmetries is thought to be

responsible for the different room temperature structures observed in BNT. The dimensions of the tetragonal platelets were noted to match well with the incommensurate modulations[126] and the thickness of the planer zones (GPZs)[115] derived from other diffraction techniques. NTs are expected to form at the point where a domain wall passes through either an APB or tetragonal platelet, as demonstrated in Fig.2.5.27.

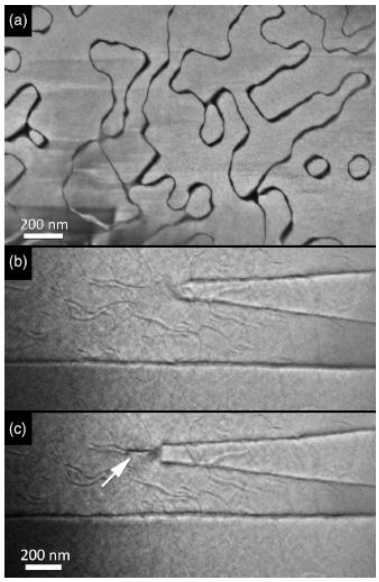

Fig.2.5.27: TEM images of single crystal BNT: (a) only APBs are visible in the thin sample (t<40 nm), in (b) and (c) a wedge-shaped domain moving under the influence of an electric field interacts with an APB forming a NT (arrow). The domain is bound by $\{110\}_{pc}$ domain walls.[157]

In order to maintain the structural continuity of the oxygen octahedra, the local tilt system around the planer defect is expected to differ from that of the bulk in the form of a transitional region with local symmetry $a^-a^-c^-$(Fig.2.5.28). An average monoclinic *Cc* structure will be assigned to BNT by large-scale diffraction techniques when it has a high density of defects. Beanland and Thomas[157] suspect the material adjacent to the $\{100\}_{pc}$ domain wall, examined by Ma et al.[156], to also adopt the symmetry of the transitional region, resulting in the assignment of an average monoclinic structure by Ma et al.[156]. High poling fields are expected to remove the high density of NTs forming the defect structure in BNT causing the irreversible change in symmetry from *Cc* to *R3c* observed by Rao et al.[149] using a large-scale diffraction measurement.

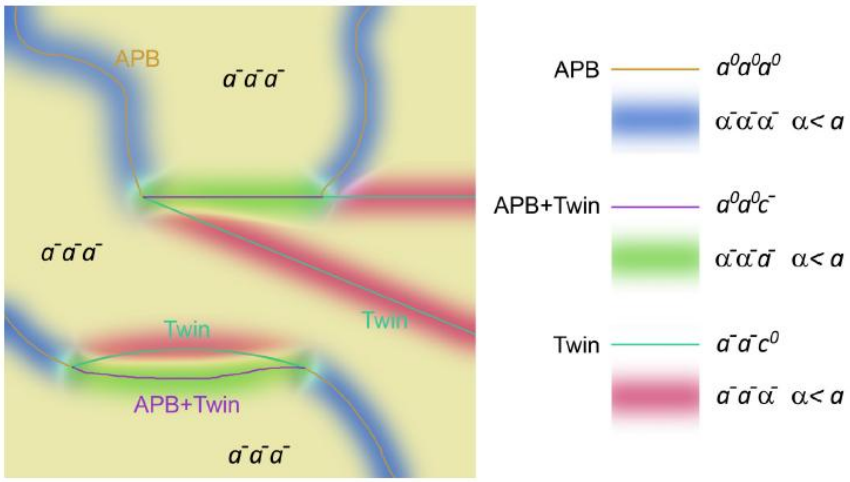

Fig.2.5.28: A schematic of the local octahedral tilt system surrounding the $\{110\}_{pc}$ domain walls which interact with APBs.[157]

2.6 (1-x)$Bi_{0.5}Na_{0.5}TiO_3$-x$BaTiO_3$

The BNT-based solid solution with Ba, (1-*x*)$Bi_{0.5}Na_{0.5}TiO_3$-*x*$BaTiO_3$ (BNBT-100*x*), was initially investigated in 1991 by Takenaka et al.[13] as part of the search for a new group of lead-free piezoelectric ceramics. The dielectric and piezoelectric properties measured for this solid solution using poled samples revealed a morphotrophic phase boundary (MPB) in the region *x*=0.06~0.07, illustrated in Fig.2.6.1. The boundary was believed to separate the rhombohedral *R3c* and tetragonal *P4mm* ferroelectric (FE) phases, isostructural with the pure BNT and $BaTiO_3$ (BT), respectively.[13]

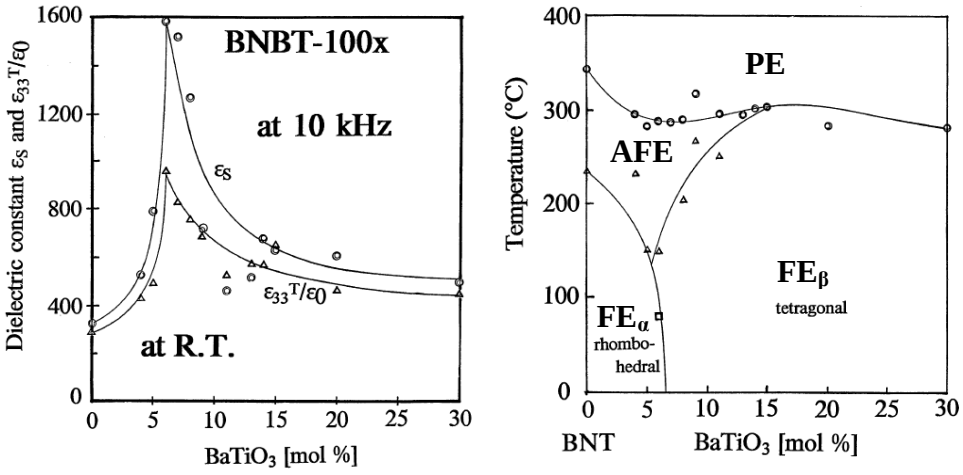

(a) (b)

Fig.2.6.1: (a) The room temperature dielectric constant of unpoled ε_s and poled $\varepsilon_{33}^T/\varepsilon_0$ BNBT shows a maximum in the region *x*=0.06~0.07 and (b) the phase diagram of BNBT determined from structural X-ray diffraction (XRD) data and dielectric and FE properties.[13]

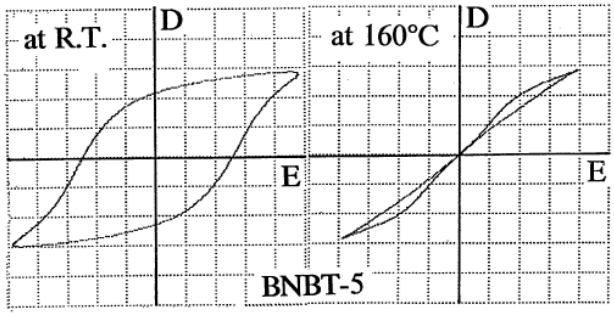

Fig.2.6.2: Double P-E hysteresis loop observed in BNBT-5 above T_d.[13]

Splitting of the XRD peaks consistent with both rhombohedral and tetragonal symmetries were observed at this boundary.[158] The solid solution with compositions ranging 0-15 mol% BT, were initially believed to undergo a phase transition from a FE

to an antiferroelectric (AFE) phase at the depolarisation temperature T_d, following the observation of double P-E hysteresis loops (Fig.2.6.2).[13] A giant strain measured in the butterfly bipolar strain-electric S(E) curve, above this temperature, also provided evidence of an AFE to FE field-induced phase transition. [159, 160] The system was then thought to transform to a paraelectric (PE) state at T_m.

However, as was also the case for BNT, the onset of the AFE order determined from the pinched P-E loop (~100 ˚C) was found to occur at a much lower temperature than T_d (~125 ˚C).[159] The low temperature feature in the dielectric permittivity associated with the depolarisation temperature T_d does not exist for all compositions, particularly in as-sintered unpoled samples, shown in Fig.2.6.3(b).[159, 162] In these cases, T_d can only be determined from the peak in the dielectric loss after poling(Fig.2.6.3(a)).

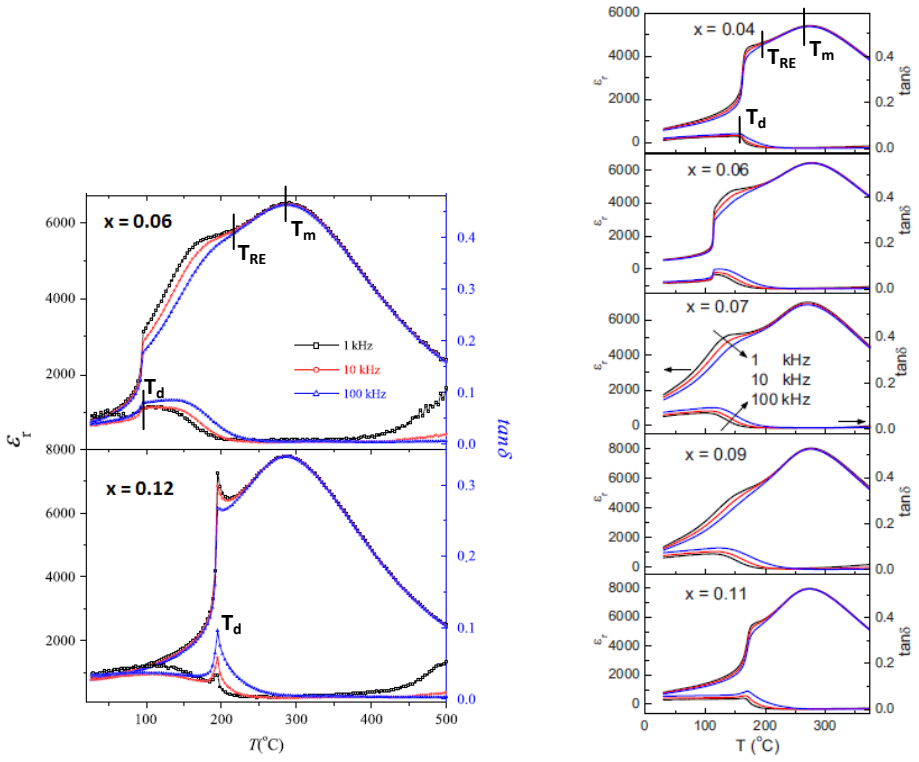

(a) (b)

Fig.2.6.3: The temperature dependence of the dielectric response of (a) poled[161] and (b) unpoled[162] BNBT for compositions at and near the MPB region, showing features T_d, T_{RE} and T_m. T_d cannot be defined for *x*= 0.04, 0.07 and 0.09 in the unpoled state.

The true origin of the depolarisation temperature T_d was investigated by Jo et al. [11]. TEM images of ceramic BNBT-6 were examined in conjunction with dielectric data. The proposed T_d was found not to involve any phase transition, but develops as a result of the thermal evolution of the coexisting rhombohedral and tetragonal polar

nanoregions (PNRs) which are also believed to be responsible for the peak in the permittivity T_m. The tetragonal phase is best described by the weakly-polar *P4bm* space group rather than the polar *P4mm* symmetry isostructural with BT. The small difference in free energy between the *R3c* and *P4bm* PNRs at room temperature enable the easy interconversion of the two symmetries. The *R3c* PNRs are expected to transform into *P4bm* PNRs with increasing temperature. The feature at T_d is thought to be merely a consequence of a relaxor forming a long-range FE order on electrical poling.

Another phase transition temperature T_{RE} was identified from the permittivity data (Fig.2.6.3(b)). This transition marks the temperature where the frequency dispersion vanishes on heating.[163] Below T_{RE}, BNBT exhibits relaxor characteristics which also coincide with the proposed AFE phase. The relaxor transition T_{RE} was found to match the Vogel-Fulcher freezing temperature (T_{VF}) of the unpoled state of the MPB composition BNBT6. The continued dispersion of the dielectric behaviour below T_{VF} is not indicative of a normal FE state. Rather the system is believed to form a dipolar glass state were the PNRs can no longer grow and merge to form a long range FE order. This frozen dipolar configuration is thought to aid the formation of long range polar domains on poling, resulting in the irreversible transformation to the normal FE state.[12] The AFE to FE field-induced phase transition previously suggested is simply the consequence of the relaxor forming a long-range FE order[11, 164].

A Burns temperature (T_B) of 460 ˚C, determined from the temperature where the system no longer obeys the Curie-Weiss law, was reported by Chen et al. [165] for single crystal BNBT-7. It is below this temperature that the PNRs begin to develop.

Structural evidence from unpoled BNBT is unsupportive of the MPB proposed from the enhancement of the dielectric and electromechanical properties measured in the poled state. Electrical poling can irreversibly alter the phase structure of a material. Different phase diagrams are therefore required for the unpoled and poled states of BNBT. The structures of both the unpoled and poled states of the solid solution are reviewed.

2.6.1 Structure of Unpoled BNBT

XRD reveals BNBT to undergo a rhombohedral to nearly cubic phase transition at x=0.06, where it shows little distinction from cubic symmetry up to x=0.10. Evidence of a transition to the anticipated tetragonal *P4mm* structure finally occurs at x=0.10. [161, 166,

[167] Yet a Raman spectroscopy study in combination with XRD revealed the MPB to lie at the specific composition x=0.055. [168] The MPB detected by Raman spectroscopy appears only as a structural discontinuity rather than a structural displacement expected from the coexistence of two phases.[169] The existence of an AFE phase was further questioned as no structural discontinuity consistent with a FE-AFE phase boundary could be detected. Only a loss of long-range FE order and a rapid reduction in the correlation length of the FE order parameter was observed in the Raman spectra of x=0.055 at the proposed AFE transition temperature (~100 ˚C).[169] This observation contradicts other Raman studies[159, 170] which report similar evidence for a FE rhombohedral *R3c* -AFE orthorhombic *Pnma* phase transition that occurs in BNT when it is subject to high pressure[114]. The general features of the Raman spectra were noted to be similar in all the phase regions of the solid solution, with only subtle difference revealed after deconvolution using different fitting techniques. This may account for different results obtained by the authors.[170]

Early structural evidence gained from XRD and Raman could not account for the enhanced properties observed at the MPB composition. Research then focused on the FE and ferroelastic domain structures of unpoled BNBT. The influence of A-site ordering on the domain structure was also discussed. Following the discovery of a monoclinic phase in the room temperature structure of BNT, a bridging phase with *Cc* symmetry has since been suggested for the MPB.

2.6.1 (i) FE Domain Structure in BNBT

The room temperature structure of unpoled ceramic BNBT for a series of compositions in the MPB region ($0.04 \leq x \leq 0.11$) has been investigated by Ma et al. [162, 163] using TEM (Fig.2.6.4). Prior to this investigation, no evidence of FE domains using TEM could be found in either BNBT-3 or BNBT-8 despite the presence of superstructure reflections consistent with a $a^0a^0c^+$ tilt system.[134] However, this is now thought to be a consequence of an electron beam effect.[137] A complex domain morphology formed of colonies of differently oriented domains with *R3c* crystal symmetry and $a^-a^-a^-$ octahedral tilt, isostructural to BNT, was imaged for x=0.04.[162] For x=0.06, ~40% of the grains have a core-shell structure with the *R3c* complex domain forming the core and a *P4bm* nanodomain structure with $a^0a^0c^+$ tilt system forming the shell. The nanodomains occupy the remainder of the grains. The crystal structure of the nanodomains is identical to BNT in the high temperature 'AFE' phase. Only

nanodomains with *P4bm* symmetry were observed for *x*=0.07 and 0.09. The pseudo-cubic distortion detected by XRD for compositions x=0.06-0.10 is a direct consequence of the short coherence length of the *R3c* and *P4bm* symmetries.[11] The absence of large domains in the grains has been noted to correlate with the absence of T_d in the permittivity data of these composites. Large lamellar FE domains consistent with *P4mm* $BaTiO_3$ structure occupy the majority of the grains in *x*=0.11. With only 20% of the grains containing a small core of *P4bm* nanodomains, a compositional phase boundary marking the transition from *P4bm* BNT to *P4mm* BT has been suggested to occur near *x*=0.11.

Ma et al. [171] have also used hot-stage TEM to investigate the structural transitions for *x*=0.06 and 0.11, shown in Fig.2.6.5. The core structure observed in the ceramic grains of x=0.06 shrinks with increasing temperature such that the whole volume of the grain is occupied by *P4bm* nanodomains above T_d. Similarly, a *P4mm* to *P4bm* structural transition was observed at T_d for *x*=0.11. The *P4bm* nanodomain structure remains unchanged until temperatures well beyond T_m for both *x*=0.06 and 0.11. This observation led Ma et al.[171] to suggest that neither T_{RE} nor T_m correspond to any structural phase transitions. The tetragonal to cubic structural transition is observed as a gradual weakening and diffusion of the *P4bm* superstructure spots from 335-500 ˚C for *x*=0.06 and at the slightly lower temperature range of 310-425 ˚C for *x*=0.11.

In light of this structural evidence a new phase diagram, shown in Fig.2.6.6, was proposed for BNBT. A broad anomaly in the elastic compliance for *x*>0.05 further demonstrates the diffuse nature of this phase transition which develops progressively with the decrease in size and population of the *P4bm* nanodomains with increasing temperature.[164] Residues of ½(*ooe*) spots above the structural transition in both compositions reveal the presence of local *P4bm* distortions within the cubic phase previously observed up to 620 ˚C in BNT[110, 111]. Evidence of a high temperature local polarisation due to asymmetric Ti-O vibrations has similarly been reported for BNBT compositions x=0.056, 0.06 and 0.08 in different Raman studies.[170, 172] Further, the persistence to elevated temperatures of a Raman peak associated with Bi vibrations, not allowed by $Pm\bar{3}m$ symmetry, indicates the presence of off-centred Bi^{3+} cations in the PE state of these solid solutions.[172]

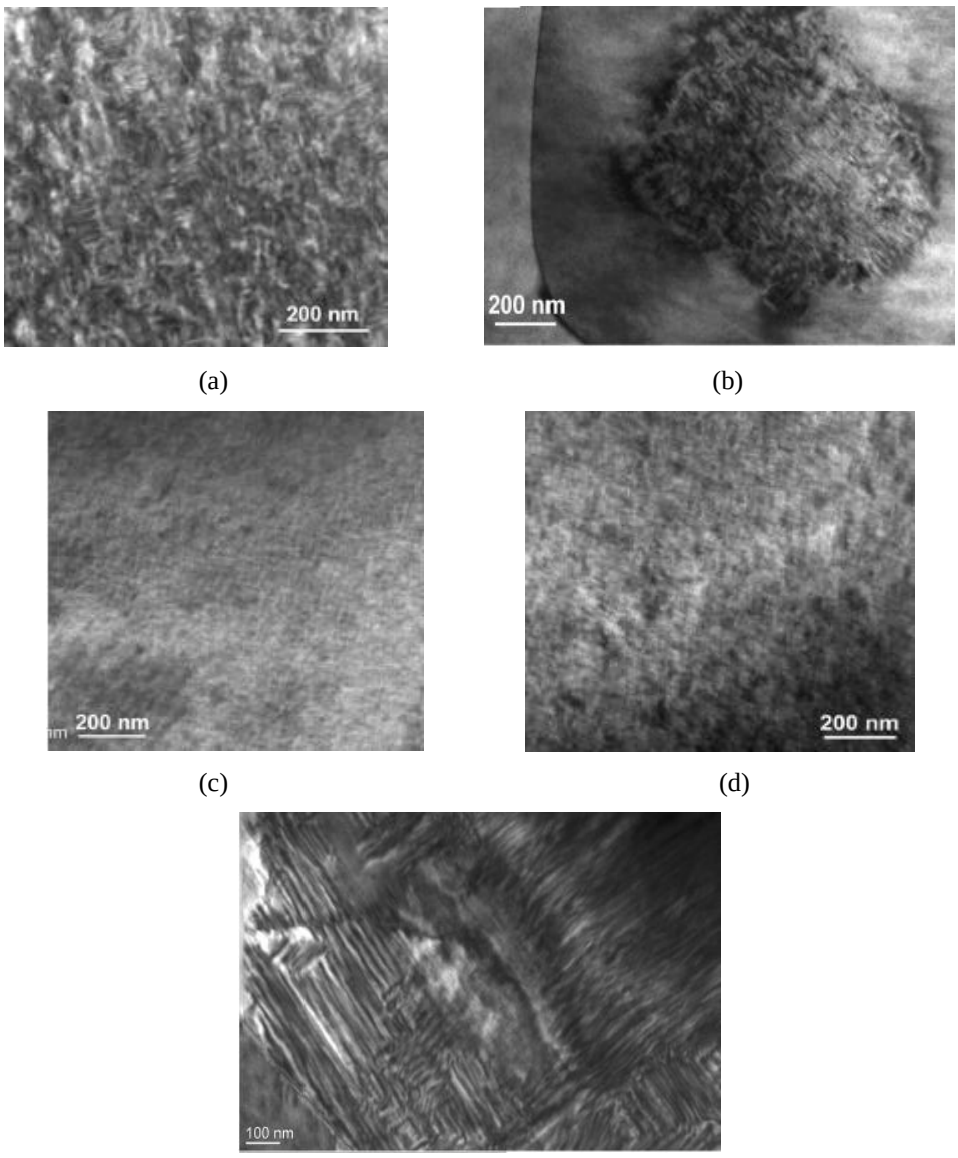

(a) (b) (c) (d) (e)

Fig.2.6.4: Room temperature TEM bright field images of BNBT x=0.04, 0.06, 0.07, 0.09 and 0.11 [(a)-(e), respectively] tilted along the [011] zone axis.[162]

Ma et al.[163] have associated the unique relaxor AFE behaviour observed in BNBT ($0 \leq x \leq 0.11$) with the *P4bm* nanodomains. Randomly oriented antiparallel dipoles are speculated to form within the nanodomains, illustrated in Fig.2.6.7, which dynamically fluctuate giving rise to the frequency dispersion observed in the dielectric data. This theory is supported by presence of antiparallel cation displacements in the *P4bm* structure observation in BNT[111]. Minimal frequency dispersion is observed for x=0.11 due to the dominating presence of large lamellar domains forming a long range FE order.[163]

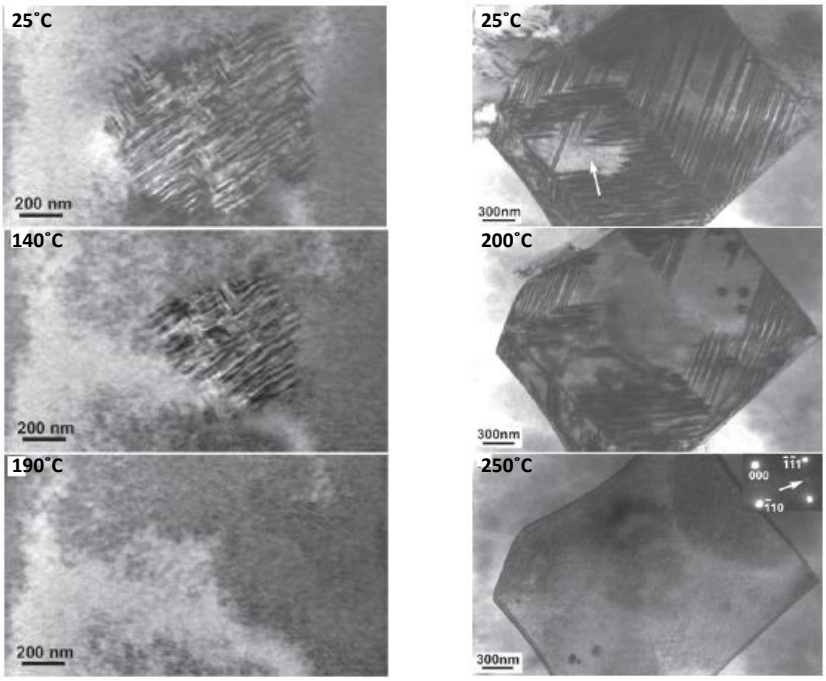

(a) (b)

Fig.2.6.5: TEM bright field images of BNBT (a) x=0.06 and (b) x=0.11 at different temperatures.[171]

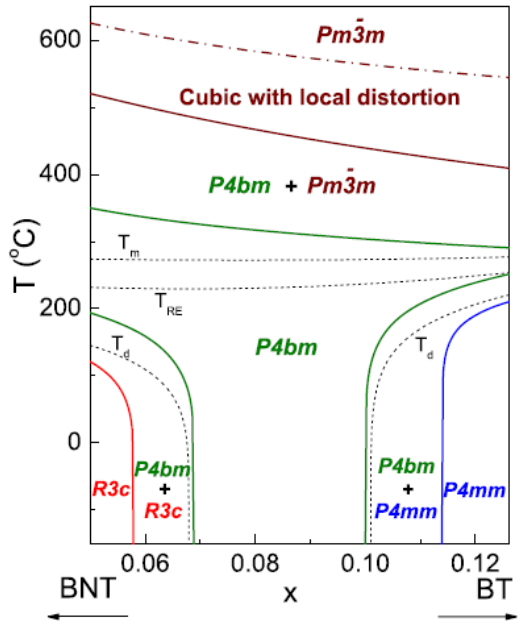

Fig.2.6.6: Phase diagram for unpoled BNBT proposed by Ma et al.[171].

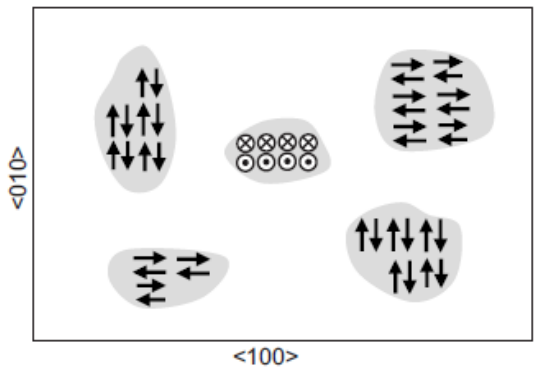

Fig.2.6.7: A schematic of the antiparallel cation displacements in the *P4bm* nanodomains (gray area) responsible for the AFE relaxor behaviour. The antiparallel arrow pairs fluctuate among the six equivalent $<001>_c$ directions. The white background represents the undistorted cubic matrix.[162]

2.6.1 (ii) Ferroelastic Domain Structure in BNBT

Piezoresponse force microscopy (PFM) and polarised light microscopy (PLM) have similarly been used to investigate the domain structure of BNBT single crystals for x=0.045 and 0.055[137]. Polar nanoregions, imaged at room temperature, become refined and increasingly self-organised along <110> direction with increasing BT content (Fig.2.6.8). No high temperature proper tetragonal ferroelastic phase exists in either x=0.045 or 0.055. Instead, a FE domain structure forms which stress-accommodates by geometrically arranging the rhombohedral domains into large domain platelets oriented along the <100> direction shown in Fig.2.6.9. The domain platelets are improper ferroelastic and form because of the electrostrictive coupling of the spontaneous polarisation to the lattice. The platelets disappear on heating above T_d for both compositions. A notable increase in platelet size is also observed with increasing BT content. Yao et al.[137] note that refinement of stress-accommodating FE domains near the MPB leads to an increased domain-wall density which may act as natural nucleation sites for inducing phase transitions thereby improving the piezoelectricity at the MPB. For crystals with a lower BT content ($x \leq 0.02$), the piezoelectric properties are considered to be suppressed by proper ferroelastic domains that form independently from the polar rhombohedral nanodomain but suppress the ability of the FE domains to stress-accommodate. Unlike improper ferroelastic domains, proper ferroelastic domains have strain as a spontaneous order parameter.[137] PLM images combined with high-resolution XRD also reveal the structural boundary between the tetragonal and cubic phases to decrease dramatically with increasing BT content within this composition range.[173]

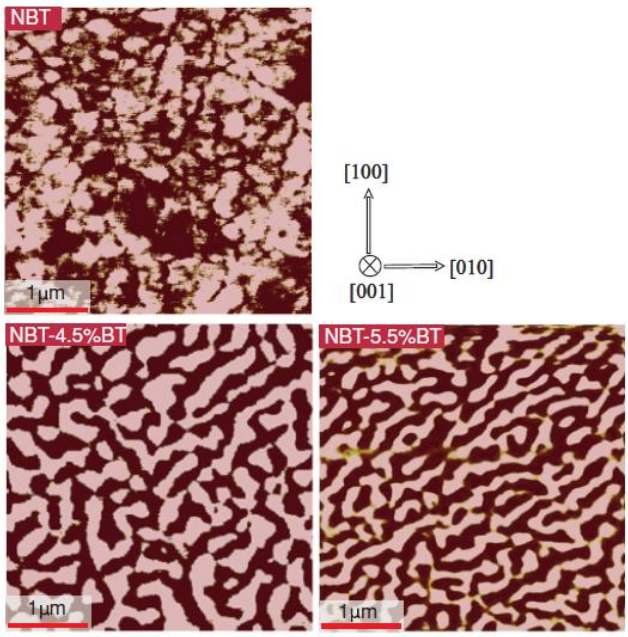

Fig.2.6.8: PFM images of (001)-oriented BNT, BNBT-4.5 and BNBT-5.5 crystals.[137]

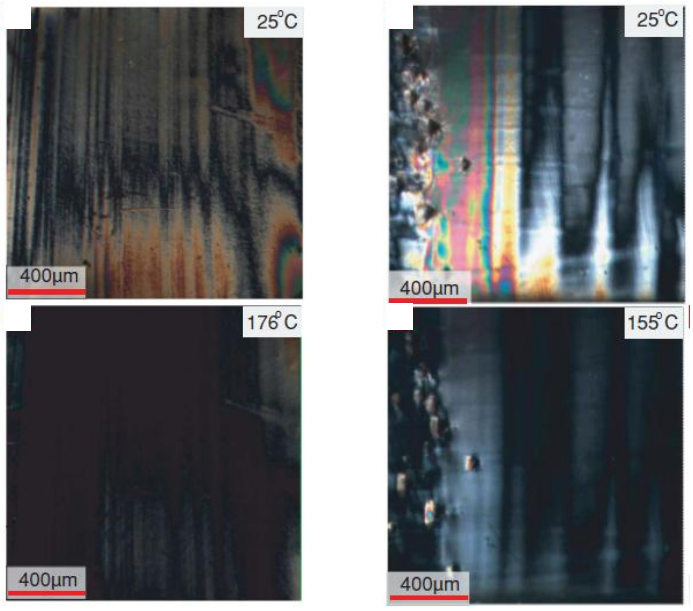

(a) (b)

Fig.2.6.9: PLM images of (001)-oriented (a) BNBT-4.5 and (b) BNBT-5.5 crystal at different temperatures.[137]

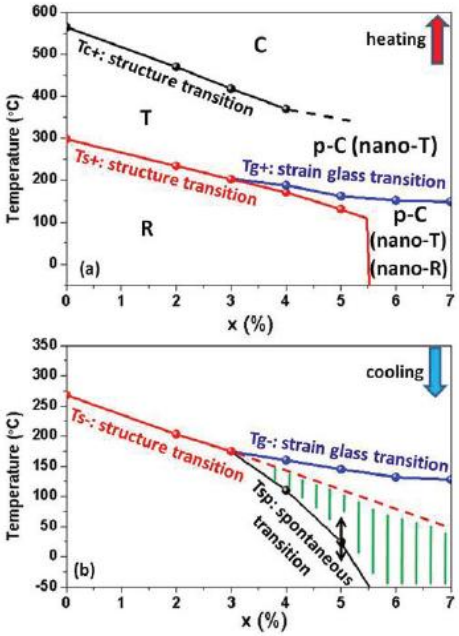

Fig.2.6.10: Transition diagram for BNBT on (a) heating and (b) cooling, highlighting the metastable glass phase (green lines). p-C: pseudo-cubic matrix formed of T nanodomains or T and R nanodomains.[176]

The solid solution BNBT enters a room temperature strain glass state within the MPB region $0.05<x<0.08$, where a frozen disorder ferroelastic state with a short-range strain order forms. A typical ferroelastic transition is observed for BNBT compositions with $x<0.05$.[174] The temperature of the strain glass transition from the high temperature paraelastic state matches well with the maximum in the elastic compliance measured by Cordero et al.[175]. Yao et al.[176], using dynamic mechanical analysis (DMA) combined with differential scanning calorimetry (DSC) identified a crossover region for the MPB compositions where the structural transition from the tetragonal to the rhombohedral phase interacts with the strain glass transition, on cooling, forming a metastable glass phase for $0.03<x<0.08$. A phase diagram illustrating these transitions is shown in Fig.2.6.10. The BNBT compositions x=0.04 and 0.05 escape from the frozen state by undergoing a spontaneous transition to a thermodynamically favourable long-range ordered state above room temperature; no such transition is observed for x =0.06 or 0.07 above -140 ˚C. However, the isothermal transformation of this phase over time to the long-range ordered state is believed to account for the different structural behaviour reported for the MPB region. If the system is left for a long enough period of time, a rhombohedral structure rather than a pseudo-cubic (*pC*) symmetry will be observed for the room temperature phase.[176]

2.6.1 (iii) Local Structure: A-site Ordering

The X-ray diffuse scattering features of single crystal BNT are significantly altered with the addition of Ba (Fig.2.6.11).[124] A narrowing of the broad scattering regions observed around all the Bragg peaks indicate a suppression of the chemical short range ordering of the Na/Bi on the A-site in single crystal BNBT-5.6.

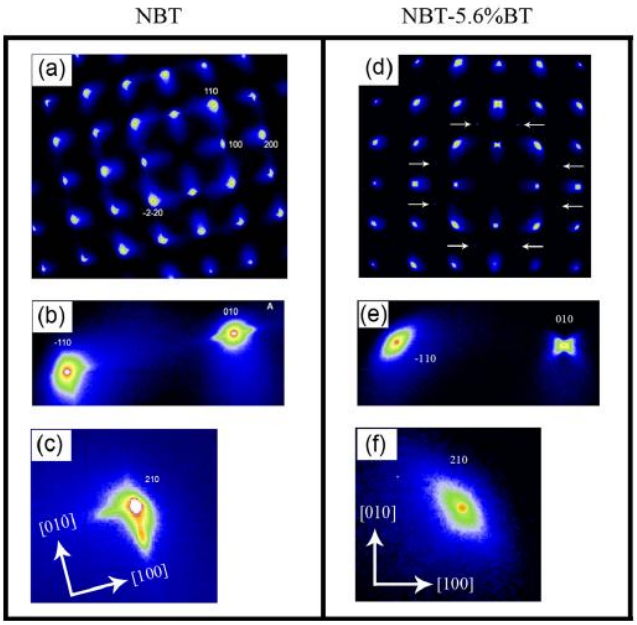

Fig.2.6.11: Room temperature XRD images showing a narrowing of the scattering regions around the Bragg peaks with the addition of Ba. The diffuse scattering around the (-110), (010) and (210) peaks are enlarged in (b), (c), (e) and (f). The arrows mark the (3/2, 1/2, 0/2) superstructure reflections indicative of $a^0a^0c^+$ octahedral tilting.[124]

A significant increase in the volume fraction of $a^0a^0c^+$ tilt regions was also observed in the Ba modified single crystal. The system releases the strain associated with the mismatch between the tilts of the $a^-a^-a^-$ matrix and $a^0a^0c^+$ Guinier-Preston zones (GPZs), by increasing the domain wall density through refinement of the domain size.[124] A reduction in the average size of the PNRs as well as an enhancement of the self-organisation of these regions along the <110> direction with increasing BT concentration has previously been imaged by PFM[137] and bright field TEM[117, 177]. The PNRs decrease in size from 50-100 nm for BNT to 20-50 nm for BNBT-5.5.[117, 177] The asymmetric L-shaped diffuse scattering observed in BNT is transformed with Ba modification to a symmetric butterfly-shaped diffuse scattering around (010) and ellipsoidal-shaped contours around ($\bar{1}$10) and (210). The GPZs are reoriented along the <110> direction allowing for a higher degree of mobility of the PNRs without strain

confining BNBT-5.6.[124] The effect of BT doping on the neutron diffuse scattering of single crystals BNT has been investigated by Zhang et al.[178] (Fig.2.6.12). PNRs induced by Bi^{3+} displacements appears as peculiar L-shaped diffuse streaks along the $<001>_{pc}$ direction. The streaks evolve into an ellipsoid along $<011>_{pc}$ on doping, where the Bi^{3+} displacements is thought to rotate towards the $<111>_{pc}$ direction.

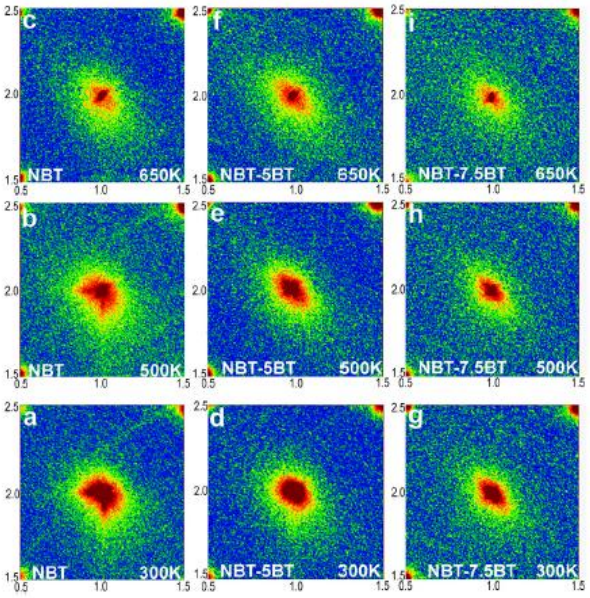

Fig.2.6.12: Neutron diffuse scattering in BNT, BNBT-5 and BNBT-7.5 near $(012)_{pc}$ at 300, 500 and 650K.[178]

A broadening of the Raman spectra with the addition of Ba indicates an increase in structural disorder within the BNBT solid solution.[179] The change in average structure from rhombohedral to tetragonal is accompanied by a step-wise change in the Raman peak associated with A-BO_3 vibrations rather than a progressive change with increasing BT concentration. The sensitivity of this peak to coupling processes between off-centred Bi^{3+} and Ti^{4+} cations suggests that the structural alteration occurs as an indirect chemically driven effect rather than a direct one. The addition of Ba into the A-site stabilises the coupling between the off-centred Ti^{4+} cations while destabilising the coupling of the off-centred Bi^{3+} cations[172, 180]. Classical soft-mode behaviour is only demonstrated by this mode for the MPB composition where a strong coupling between the Bi and Ti subsystems drives the material into the FE state. A delicate balance between coupled and uncoupled A-site cations is required to achieve this state.[172] The depolarisation temperature T_d has been shown by Schütz et al.[180] using Raman spectroscopy to result from the breaking of the Bi-O hybridisation and the reinstatement of a crystal symmetry dictated by the ionic radius. The introduction of Ba into BNT is

expected to have a similar effect, leading to the introduction of a mixture of nanodomains in a psuedocubic matrix.[180] The abnormal growth of these PNRs in the MPB composition explains the large correlation length of Bi^{3+} ion displacements detected using single crystal neutron diffuse scattering[178].

2.6.1 (iv) Alternative Structure for MPB Region

A possible monoclinic symmetry been suggested for the MPB composition following the observation of a new transition T_{ME}, related to a maximum in the elastic compliance, which lies between the dielectric anomalies T_d and T_m, shown in Fig.2.6.13. The diffuse behaviour of the transitions at T_{ME} and T_m is related to the existence of polar modes with a short coherence length. These local monoclinic distortions are thought to form an intermediate phase that allows for continuous rotation of the polarisation between the pseudocubic [100] and [111] directions.[175] A local monoclinic symmetry has similarly been proposed for BNT following diffused X-ray scattering measurements revealing the displacement of the A-site cations along the tetragonal [100] axis, away from the rhombodedral [111] direction.[115]

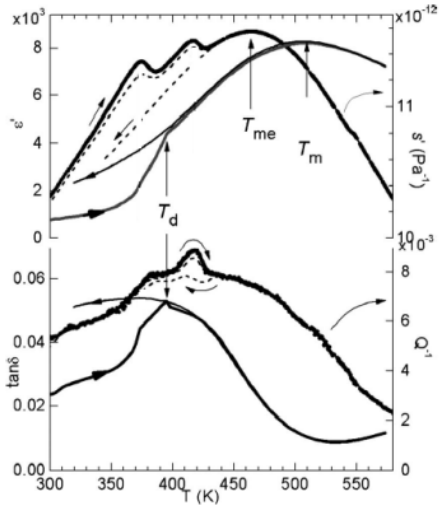

Fig.2.6.13: A maximum T_{me} occurs in the elastic compliance *s'* between anomalies T_d and T_m in the dielectric response of BNBT-6.[175]

High resolution TEM and nano-beam diffraction analysis preformed on BNBT-7 polycrystalline nano-whiskers further support the theory of a monoclinic bridging phase following the direct observation of monoclinic C_c nanotwins (nanodomains) shown in Fig.2.6.14. Despite the observation of a monoclinic symmetry at the local scale, the whiskers retain an average rhombohedral *R3c* structure. The lowering of the crystal

symmetry within the nanotwins is thought to result from a loss of point group symmetry during the phase transition from the high temperature PE cubic phase to an intermediate ferroelastic tetragonal phase.[181] The giant strain and enhanced piezoelectric response of the MPB composition is related to the high mobility of the nanotwins as well as the high density of twin boundaries, which can accommodate a higher degree of deformation.[181]

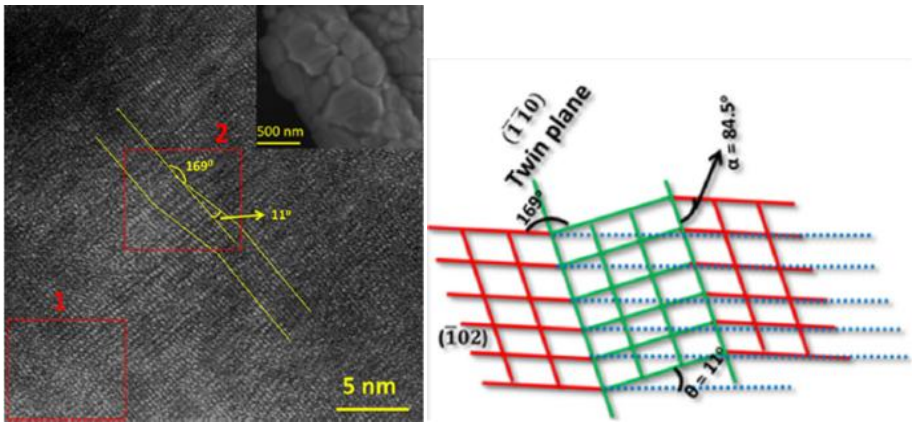

Fig.2.6.14: (a) High-resolution TEM and SEM (inset) images of a BNBT-7 polycrystalline nano-whisker. (b) A schematic representation of the twin arrangement highlighted by label 2 in (a). [181]

2.6.2 Structure of Poled BNBT

The pseudo-cubic structure detected by XRD for the MPB composition in the unpoled state is irreversibly altered by the application of an electrical poling field. The rhombohedral and tetragonal distortions that form the room temperature structure only become visible with the application of an electric field.[11] Electric-field induced volume changes detected by measuring the induced strain in the solid solution confirm a transition to the FE state for $x \leq 0.06$ (Fig.2.6.15).[182] A high resolution neutron diffraction study further supports the coexistence of near cubic phases with $a^-a^-a^-$ and $a^0a^0c^+$ octahedral tilts which transform to a predominantly rhombohedral $a^-a^-a^-$ tilting system with the application of an electric field.[183] Daniels et al.[184] has directly linked the rhombohedral PNRs in single crystal BNBT-4 to local correlated atomic displacements or GPZs, similarly observed in BNT[115]. Significant streaking of the superlattice reflections along <100> direction, detected by synchrotron XRD, is indicative of a planar stacking fault with tetragonal *P4bm* symmetry separating two successive tilt systems. Poling removes these staking faults resulting in the growth of the rhombohedral domains. The correlated reduction in intensity of the diffuse

scattering after poling directly links the behaviour of the GPZs with the *P4bm* fault layers.[184]

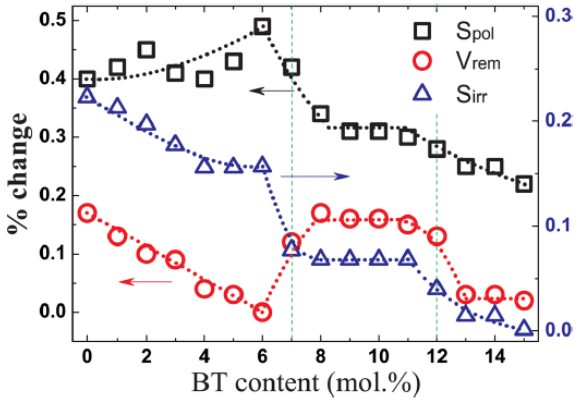

Fig.2.6.15: Electric-field induced poling strain S_{pol}, the remnant volume V_{rem} and irrecoverable strain S_{irr} parameters measured for BNBT.[182]

The pseudo-cubic MPB compositions ($0.06 \leq x \leq 0.08$) experience a strong enhancement of the tetragonal volume fraction with electrical poling (Fig.2.6.16).[185] An electric-field induced phase transformation from the pseudo-cubic structure to a tetragonal structure has been detected in BNBT-7 using high-energy XRD[185]. Significant rhombohedral and tetragonal distortions only become visible to large-scale diffraction techniques after electrical poling.[11] The high strain of the induced phase arises from the alignment of the spontaneous polarisation P_s with the applied field creating a strong domain texture.[186] Wylie-Van Eerd et al.[169] note the vertical MPB boundary to shift to 6-7mol%BT after poling, however they observe no difference between unpoled or poled Raman spectra for the BNBT-7 composition observed by Daniels et al.[186], highlighting the contrasting scales probed by Raman and XRD.[169]

A subsequent synchrotron XRD study[187] investigating the correlation between structure and electrical properties over the composition range $0 \leq x \leq 0.15$ in polycrystalline form assign a broad MPB region for the unpoled system where the bulk structure transforms from *R3c* to *R3m* at BNBT-5 then to *P4mm* at BNBT-11 (Fig.2.6.17). The P4bm symmetry is only detected after poling where it coexists with the *R3c* phase between $0.04 \leq x < 0.07$ before transforming to the *R3c*/*P4mm* mixed phase at BNBT-7,[187] where a maximisation of the dielectric and electromechanical properties occurs[164, 182, 187]. The structural MPB at BNBT-11 remains unaffected by poling.

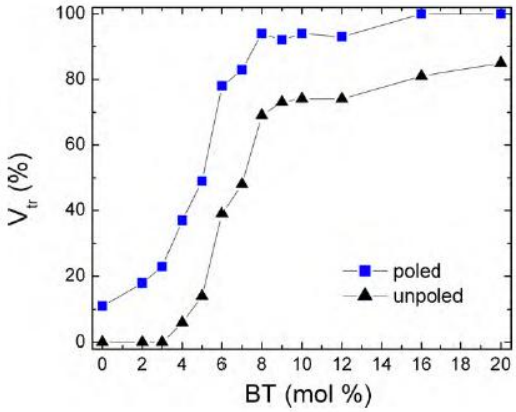

Fig.2.6.16: The tetragonal volume fraction determined from XRD for unpoled and poled BNBT at room temperature.[185]

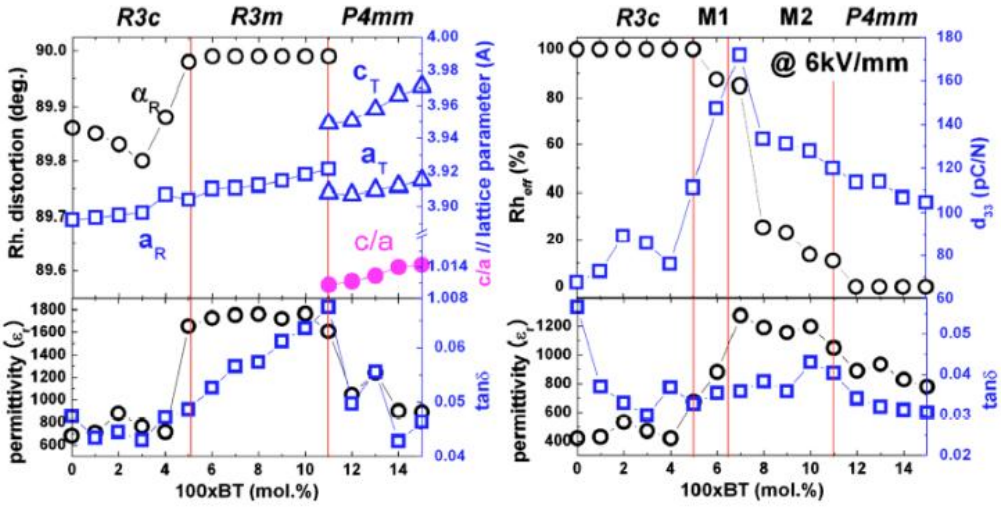

(a) (b)

Fig.2.6.17: Phase diagram for (a) unpoled and (b) 60 kV/cm poled BNBT including dielectric and piezoelectric properties and structural parameters. *M1* and *M2* represent two-phase mixtures *R3c*/*P4m(b)m* and *R3m*/*P4mm*, respectively.[187]

Depending on the orientation and strength of the field, electrical poling can alter the domain texture as well as the average and local structures of BNBT.

2.6.2 (i) Domain Texture

To understand why the specific composition BNBT-7 experiences enhanced electrical properties after poling whereas other compositions with the mixed phase do not, Jo et al.[187] compared the pole density values of compositions x=0.07 and 0.09. A maximum degree of domain texture was uncovered in both the *R3c* and *P4mm* phases in BNBT-7 whereas no domain switching was found in the electric field induced *P4mm* phase for BNBT-9. The ability of the domains to re-orientate within the coexisting phase region is

vital in achieving the high electrical properties.[187] The FE domain texture along with volumetric and lattice strains associated with the electric field induced phase transition all contribute to the large macroscopic strain induced in ceramic BNBT-7.[186, 188] Likewise, the reversal of this transition to a phase with a saturated domain texture accounts for the significant strain recovery observed within this system at elevated temperatures. [189]

The degree of texture remains effectively unchanged with further increase of poling field in the MPB composition BNBT-7. [187] This observation supports a two-step transition from the nonergodic relaxor to the FE state on poling, where the randomly oriented PNRs first align along the direction of the applied field before forming long-range FE domains. [190, 191, 192] Chen et al.[165] using high resolution TEM, have similarly observed a field-induced transition from PNRs with *P4bm* symmetry to the long-range ordered *P4mm* phase in single crystal BNBT-7. The electric-field induced ordering of the nanodomains and their associated low domain wall energy is believed to be responsible for the high piezoelectric response of this material.[193] An enhancement of the properties due to a reversible polarisation rotation that occurs in lead-based solid solutions could not be found in BNBT. Instead the induced long-range order remains stable below T_{RE}, in the absence of an applied field. Schneider et al.[194] record an anomaly in the poling behaviour of the strain in the <001> oriented single crystal BNBT-6.5 thought to be caused by an irreversible polarisation rotation from *R3c* to *P4mm* symmetry.

On heating from the poled state, the induced FE domains lose their FE/ferroelastic texture at T_d before dissociating into discrete nanoscale entities at the relaxor transition T_{RE}.[190] A short range structural rearrangement of the bonds parallel to $[001]_c$ has similarity been suggested by Foronda et al.[179] following evidence of a second order transition at T_d in the temperature dependent Raman spectra of ceramic BNBT-6.

Ge et al.[195] have combined a dielectric analysis with XRD and PLM to investigate the effect of electric field history in single crystal BNBT-5.2. In the unpoled state, the rhombohedral phase coexists with a small volume fraction of tetragonal phase which irreversibly transforms into a single *c*-domain tetragonal state on <001> directional poling. A 'bridging' orthorhombic structure was detected on heating from the poled state, corresponding in temperature with the normal to relaxor transition detected in the

dielectric data. This lower symmetry intermediate structure is thought to aid the transition from the tetragonal phase at 130 ˚C to the rhombohedral/pseudo-cubic structure above 140 ˚C.[195]

2.6.2 (ii) Orientation of Poling Field

The phase stability of BNBT near the MPB is dependent on the direction of the poling field. [196] The pseudocubic structure of single crystal BNBT-5.6 transforms to average rhombohedral and tetragonal symmetries for fields applied along the <111> and <001> directions, respectively. [196] The same directional dependence was noted by Ge et al.[195] for single crystal BNBT-5.2. A phase of coexisting structures is identified within BNBT-5.6 when the field is applied along <101>.[197] The crystallographic dependence of the induced phase transitions is attributed to the response of the *P4bm* and *R3c* PNRs forming the pseudocubic structure[11, 177] to the field when it is applied along their respective polar directions.[196]

2.6.2 (iii) Poling Field Strength

The effect of poling on the MPB of the solid solution was further investigated by Ma et al.[198] using *in situ* TEM experiments. The MPB has a strong dependence on the strength of the electrical poling field, with two field-induced phase transitions occurring on poling. An intermediate *P4mm* phase forms from the *P4bm* phase between 32-36 kV/cm, which initially coexists with the *R3c* phase in the unpoled state of ceramic BNBT-6 (Fig.2.6.18). The mixed *R3c*/*P4bm* phase then transforms into the single *R3c* phase on application of a higher electric field (>50kV/cm), destroying the MPB. The original *R3c* phase in the unpoled state does not experience any phase transitions. For BNBT-7, the pure *P4bm* phase irreversibly transforms into lamellar *P4mm* domains at 25 kV/cm. The *P4mm* phase then transforms into *R3c* domains however, the transition is not complete, unlike in BNBT-6, and the induced *R3c*/*P4mm* MPB survives the high poling fields.[198] This electric-field dependent is summarised in the phase diagram shown in Fig.2.6.19. Conversely, a high resolution neutron powder diffraction and high-energy synchrotron XRD study reveal only the *P4bm* phase to exist in single crystal BNBT-7 which remains stable after electrical poling.[199] Kitanake et al.[199] attribute the difference in the poled states of the ceramic and single crystal to an inhomogeneous stress created by the deformation of the randomly oriented grains along their respective polar axis. The similarity in the free energy of the *R3c*, *P4mm* and *P4bm* phases[198] are also thought to contribute to the formation of a metastable state in the poled ceramic.[199]

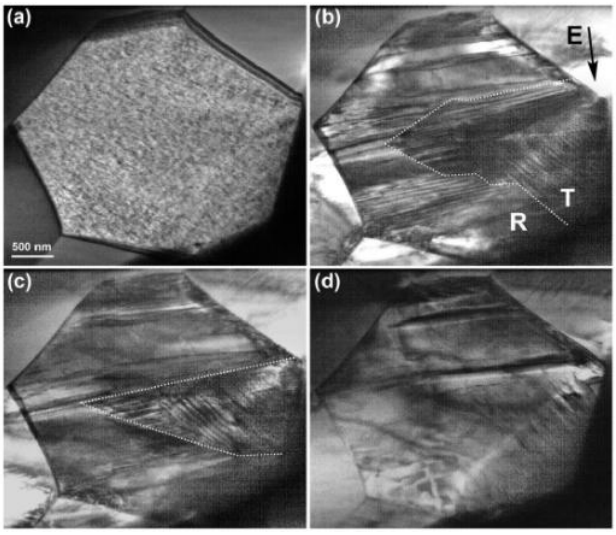

Fig.2.6.18: TEM images of BNBT-6 in a (a) 0 kV/mm, (b) 3.2 kV/mm, (c) 3.6 kV/mm and (d) 4 kV/mm electric field. The *P4bm* nanodomain structure in (a) transforms into *R3c* wedge-shaped domains (region R) and *P4mm* lamellar domains (region T) (b)-(c) on poling before fully transforming to the rhombohedral structure at higher fields (d). [198]

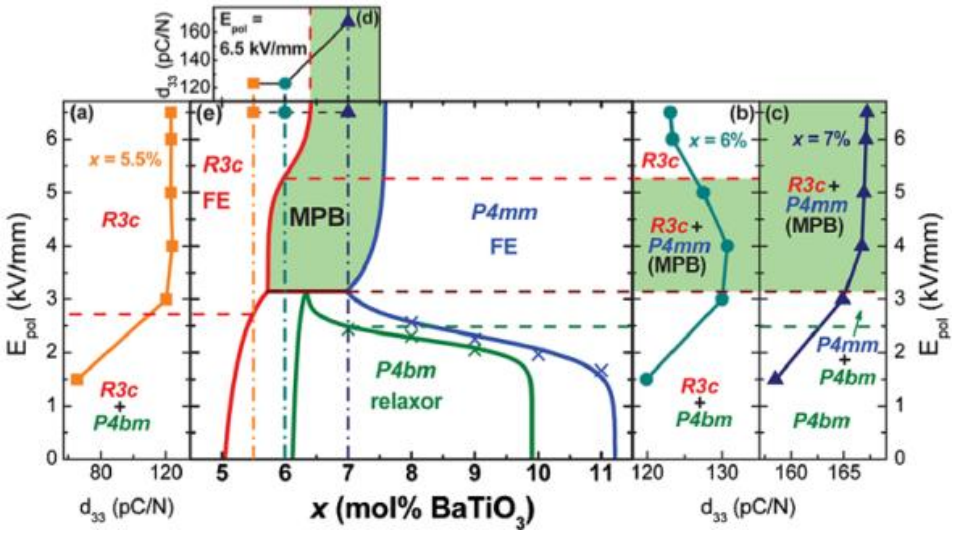

Fig.2.6.19: Phase diagram of BNBT under different electric field strengths (e). (a)-(d) show the dependence of the piezoelectric constant d_{33} on the field strength for x=0.055- 0.07.[198]

2.6.2 (iv) Effect of Poling on Local Structure: A-site Ordering

Electrical poling has the opposite effect on the local ordering of the BNBT system to that of temperature. Raman spectroscopy reveals a reduced degree of cation and octahedral disorder after application of an electric field (Fig.2.6.20).[192]

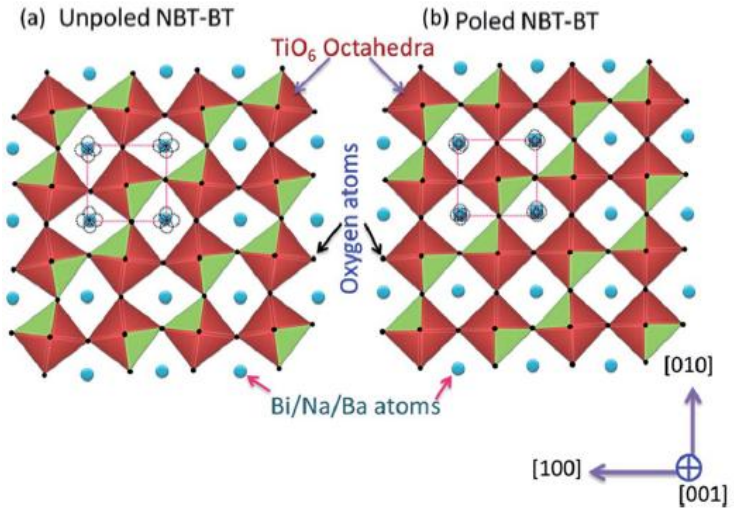

Fig.2.6.20: A schematic showing a reduction in the degree of cation and octahedral disorder after electrical poling field. The magnitude of the A-site cation displacement is shown by the circles.[192]

The local structural ordering, examined using neutron pair distribution functions (PDFs), is predominantly driven by increased correlations of the Bi/Na/Ba-O bonds. Changes in the octahedral tilt twin disorder are expected to affect these bond distances more than the O-O and Ti-O nearest neighbour distances. Octahedral tilting enhances the repulsive interaction between the Ti^{4+}-Ti^{4+} while reducing the screen effect from the negatively charged oxygen atoms. Poling decreases the free energy of the system by reducing the octahedral tilt making long-range ordering more energetically favourable. An increase in ordering of the Ti-O bonds is also observed after poling consistent with the formation of domains with a longer range tetragonal structure.[192] A similar loss of Bi-O hybridisation found in the unpoled state at T_d, is also suspected to occur at the electric-field induced phase transition[183, 186]. The only difference between the FE relaxor phase and the poled state is that the nanodomains produced by the bond weakening orient themselves along the direction of the applied field forming a more ordered lattice. Both systems exhibit a behaviour similar to that of a metastable state where only a minimal change in intrinsic energy is needed to access different states.[180] The low energy pathway enables the polarisation vector to rotate from one high symmetry direction to another, thereby exciting a high piezoelectric response in the MPB composition. In addition to the intrinsic contribution, extrinsic effects such as the motion of the domain boundaries and the boundaries separating different phases will also contribute to the piezoelectric response.[12]

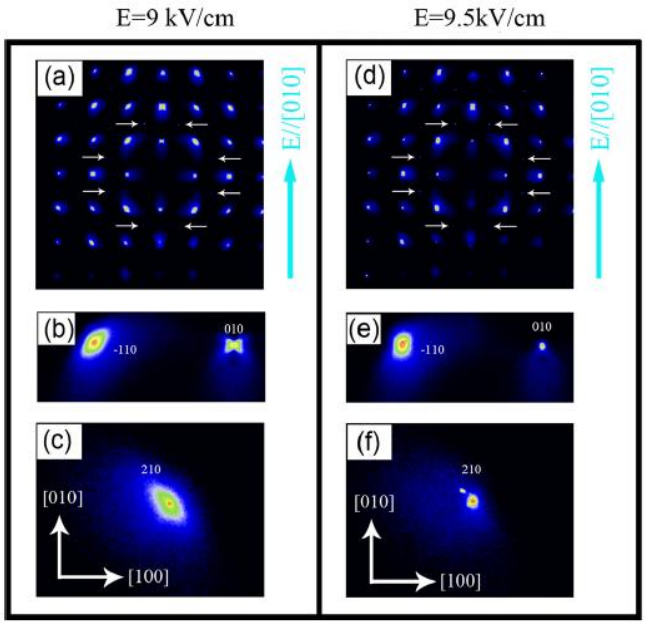

Fig.2.6.21: Room temperature XRD images of BNBT-5.6 show the diffuse scattering resulting from the local structural ordering to disappear for applied field ≥9.5 kV/cm. The diffuse scattering around the (-110), (010) and (210) Bragg peaks are enlarged in (b), (c), (e) and (f). The arrows mark the (3/2, 1/2, 0/2) superstructure reflections indicative of $a^0a^0c^+$ octahedral tilting.[124]

The XRD diffuse scattering resulting from the local structural ordering disappears on the application of a DC bias ≥9.5 kV/cm along [010], and is replaced by a splitting of the ($\bar{1}$10) and (210) Bragg peaks shown in Fig.2.6.21 for BNBT-5.6. The diffuse scattering associated with the chemical short range ordering is not affected by the applied field. An electric field induced transition occurs which enhances the $a^0a^0c^+$ tilting while suppressing the relaxor behaviour correlated with the PNRs.[124] Signatures of a monoclinic phase in the XRD scans lead Ge et al.[124] to suggest that the PNRs in BNBT-5.6 to have a local monoclinic symmetry which merge on the application of a electric field to form a long-range monoclinic structure.

2.6.3. Defining the MPB Structure in Annealed and Poled States

A detailed investigation into the structural-property correlation of ceramic BNBT ranging in composition from $0 \leq x \leq 0.11$ has been reported by Garg et al.[12]. Using powder XRD, the room temperature equilibrium structures were found to change from a mixture of monoclinic C_c and rhombohedral *R3c* symmetries to a cubiclike structure between $0.06 \leq x \leq 0.0675$ then to a cubiclike/tetragonal *P4mm* mixed structure for $0.07 \leq x < 0.10$. The C_c/*R3c* coexisting region described by Garg et al.[12] however only appears as a C_c/*R3c* 'phase boundary' between 3-4 %BT in the TEM study reported by Ma et al.[200]. TEM only probes the local structure of BNBT rather than the overall

phase structure of the system. Consequently, Ma et al.[200] acknowledge that the regions either side of the phase boundary, shown in Fig.2.6.22, may not be of a single phase and are only dominated by the C_c ($x \leq 0.03$) and *R3c* ($x \geq 0.04$) structures.

Electrical poling irreversibly transforms the coexisting C_c + *R3c* symmetries into a pure *R3c* phase.[12, 200] The cubiclike structure similarly transforms into a *R3c* + *P4mm* phase after poling.[12] Garg et al.[12] ascribe the MPB region to the composition range $0.07 \leq x < 0.10$. Poling does not lead to a complete transformation of the phase coexistence character of the MPB region ($0.07 \leq x < 0.10$), rather the tetragonal phase fraction grows slightly at the expense of the cubiclike phase retaining the MPB structure. The effect of mechanical impact and electrical poling on the structure of BNBT compositions x=0.05, 0.065 and 0.07 is demonstrated in Fig.2.6.23. A similar irreversible structural change is induced by mechanical impact, however, while high field electrical poling fully transforms the structure of the system, crushing has only a limited effect. The highest piezoelectric value is achieved in BNBT-7, however, compositions exhibiting the cubiclike structure exhibit similarly large responses. Garg et al.[12] note the importance of the electric-field induced structures over the equilibrium state in determining the MPB response of the system. The structural symmetries detected by Raman spectroscopy are identical for x>0.05. Refinement of the neutron powder diffraction spectra reveal all of the compositions (x>0.05) to exhibit the same set of superlattice reflections irrespective of the type of lattice distortion present in the system. Within the cubiclike structure, the spontaneous strain energy associated with the rhombohedral and tetragonal distortions is accommodated by creating faults of complex octahedral tilts within the otherwise orderly $a^-a^-a^-$ octahedral tilt configuration. These faults dramatically shorten the coherence length of the $a^-a^-a^-$ tilt, preventing the development of a long range FE order. The coherence length of the $a^-a^-a^-$ octahedral tilt is strongly coupled with the dipolar ordering. The development of a FE state after poling is accompanied by an increase in the coherence length of the octahedral tilt resulting in the observed phase separation and MPB-like character.[12]

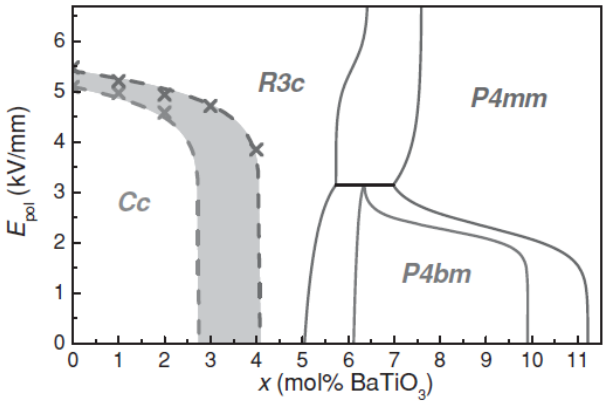

Fig.2.6.22: Phase diagram for BNBT showing the *Cc*/*R3c* phase boundary (gray band).[200]

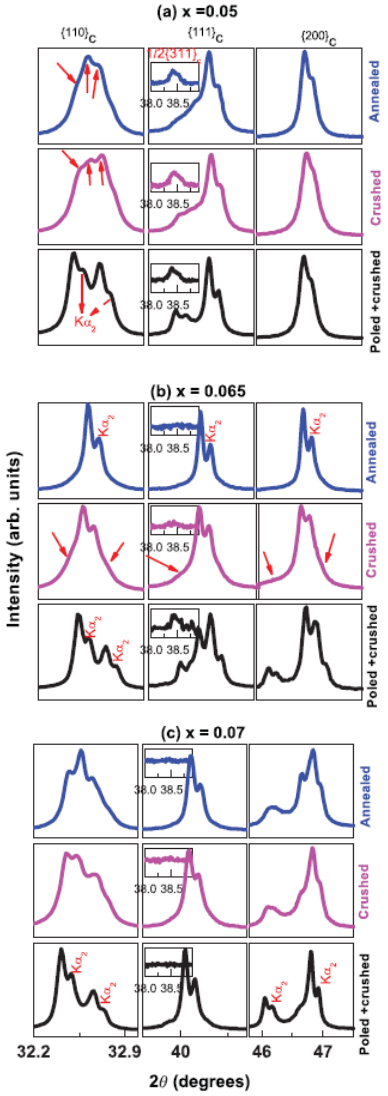

Fig.2.6.23: XRD $\{110\}_c$, $\{111\}_c$ and $\{200\}_c$ Bragg reflections for annealed, crushed and poled-crushed BNBT powdered ceramics. The unlabeled arrows mark the impact-induced structure change. These features become more clearly defined after poling in electric field of 40-50 kV/cm for 15 minutes.[12]

2.7 Grain Size Effect in Ferroelectric Materials

Grain size has been shown to have a substantial effect on the properties of many ferroic perovskites, including the position of the property enriching morphotropic phase boundary (MPB) region in lead-based solid solutions.[201],[202],[203] For example, the position of the MPB in xPb($Zn_{1/3}Nb_{2/3}$)O_3-(1-x)Pb($Zr_{0.47}Ti_{0.53}$)O_3 was found to shift from 50% to 30% PZN with the reduction of grain size.[201] Understanding how grain size influences both the intrinsic and extrinsic contributions including crystal structure and domain wall motion, respectively, will be crucial in determining the functionality of devices at increasingly smaller length scales.[204] The grain size effect on the phase transformation behaviour of ceramic capacitor $BaTiO_3$ (BT) has been extensively studied and provides a good example of how grain size may impact the properties of other perovskite materials.

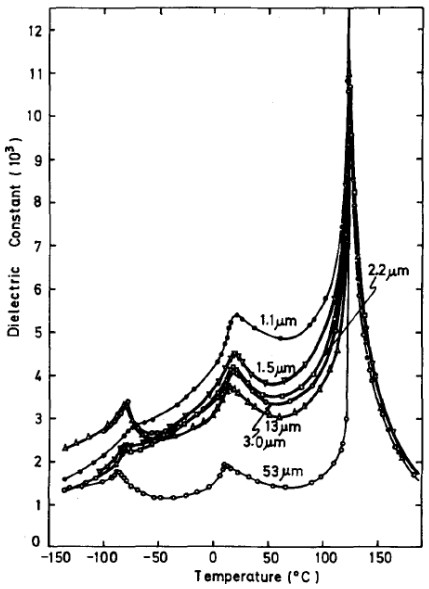

Fig.2.7.1: Temperature dependence of the dielectric constant for BT ceramics of different grain size. The dielectric constant is independent of grain size at temperatures above T_C (~120 ˚C).[84]

BT undergoes a succession of ferroelectric (FE) structural transitions from tetragonal, to orthorhombic through to rhombohedral on cooling from the high temperature paraelectric (PE) cubic phase. The effect of grain size on the properties of BT was first reported over 60 years ago by Kniepkamp and Heywang (1954)[205], who found the room temperature dielectric permittivity (ε_r) to increase when the ceramic grain size was reduced to the micron level. Temperature dependent studies revealed the dielectric permittivity to be strongly correlated with grain size in the FE state while almost

independent of grain size in the PE state (Fig.2.7.1).[84] Since these early reports, the grain size effect in BT ceramics with grains ranging in size from microns down to tens of nanometres has been extensively researched. On decreasing the grain size from 10 μm, ε_r increases reaches a maximum value of 5000, or higher, at the intermediate grain size of 1μm (Fig.2.7.2(a)).[206] Only once below this intermediate value does ε_r decrease with further reduction in grain size. The exceptionally high ε_r value achieved in ceramic BT exceeds that of the single crystal.[206],[207] Grain size however, does not have the same effect on the piezoelectric properties of BT. Rather, the piezoelectric constant d_{33} decreases continuously with decreasing grain size (Fig.2.7.2(b)). Back fields exerted by the grain boundaries oppose domain switching during electrical poling. The high density of grain boundaries in the smaller grained ceramics hinder domain alignment reducing the d_{33}.[208]

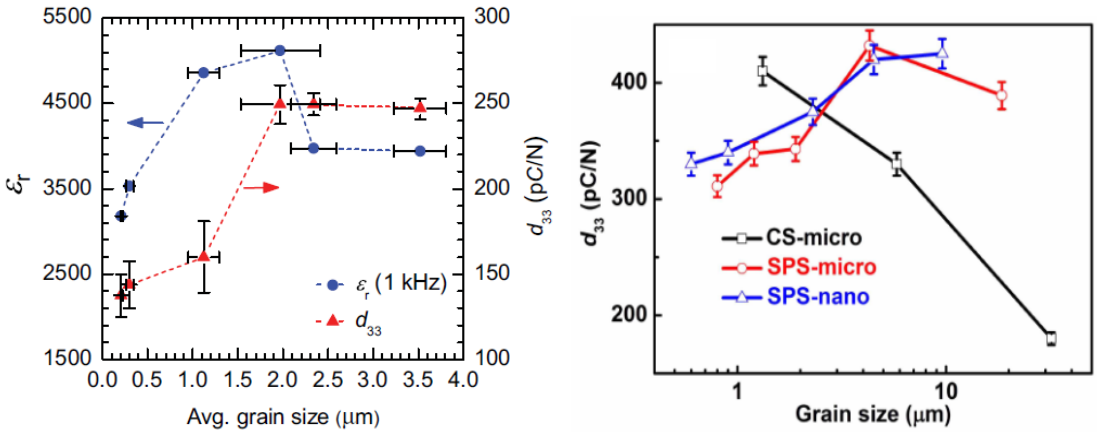

(a) (b)

Fig.2.7.2: (a) Grain size effect on the dielectric permittivity ε_r and piezoelectric constant d_{33} measured for BT at room temperature.[206] (b) d_{33} measured for BT prepared using different processing techniques: conventional sintering (CS) and SPS using nanometre and micrometre grain size powders.[208] The domain wall mobility of ceramics prepared by SPS using nano-powder is not strongly influenced by point defects. This result shows the true grain size dependence.

Two different theories based on intrinsic and extrinsic contributions have been suggested to explain the remarkable grain size effect on the dielectric properties. [206] In the earlier reports,[207],[209],[210],[211] the intermediate grains were suspected to retain a structure in close proximity to the cubic state. It was argued that the internal residual stress arising from the cubic to tetragonal phase transition at T_C could not be relived due to the absence of tetragonal 90˚ domain walls at this intermediate grain size. By suppressing the tetragonality of the lattice, the high permittivity T_C peak is effectively

shifted toward room temperature dramatically increasing ε_r. Uchino et al.[212] suggested that T_c would continue to move downwards with further reduction in grain size dropping to below room temperature at a critical particle size of 120 nm. However, this conclusion was based on the loss of tetragonality observed in powder XRD. Only a slight decrease in T_c with decreasing grain size was revealed by Kinoshite et al.[84] in the dielectric permittivity of ceramic BT putting into question this theory. All three peaks relating to the different phase transitions were observed in the dielectric permittivity (Fig.2.7.1). Only the tetragonal-orthorhombic and orthorhombic-rhombohedral transitions show a clear shift, to higher temperatures, with decreasing grain size.[84]

An alternative theory was proposed following the observation of 90˚ domain walls by Arlt et al.[213] in ceramic grains smaller than 1 μm. FE/ferroelastic tetragonal domains are expected to form below T_c, relieving the depolarisation field resulting from the space-charge layer near the surface of the grain[214] and internal residual stress arising from the structural transition[215]. The density of the domain walls increases with decreasing grain size forming a polydomain structure within the intermediate sized grains. An increased contribution to the dielectric permittivity from domain wall motion results in the enhanced response. At that time, Arlt et al.[213] assumed that the mobility of the domain walls was independent of the grain size. Calculations for the domain width dependence on the force constant showed the domain walls in fine grains more difficult to move than in coarse grains, questioning the theory.[216],[217] Arlt and Pertsev[216] reasoned that a reduction in stress in and near the grain boundary area by domain formation may soften the force constant acting as a feedback for greater domain wall motion.

The effect of internal stress and domain wall dynamics on the dielectric properties of BT has been updated by Ghosh et al.[73] using in situ high-energy XRD in applied electric fields. The origin of the enhanced permittivity is primarily from the displacement of the 90˚ domain walls, supporting Arlt et al.'s[213] theory. No significant change in the residual stress was observed and is not believed to be a dominant factor in the property enhancement.[73]

For very fine grained ceramics, both the FE transformation at T_C and the tetragonal-orthorhombic transition are suppressed.[218] The decrease in ε_r is not thought to originate from a depolarisation effect which predicts a monotonic decrease in T_C down through

room temperature[219] but rather as an effect of elastic constraint on the FE transformation.[218] The density of domain walls required to minimise the transformation stress within the grain interior and the residual tensile stress at the grain boundaries, increases with the reduction in grain size.[213] For grain sizes below 1 μm, the polydomain structure becomes too costly and the grain becomes substantially untwined, decreasing ε_r. A internal pressure has been found to substantially weaken the domain wall activity in fine-grained (700 nm) ceramics relative to coarse-grained (26 μm) ceramics.[209] Grain clamping is expected to develop when the individual grains are no longer able to achieve their full transformation strain restricting domain wall motion.[235] A single-domain state has been observed by Frey et al.[218] in fine grained ceramics with particle size of ~100 nm. However, Raman spectroscopy revealed the grains to have a locally orthorhombic structure at room temperature instead of the cubic symmetry expected for clamped grains. Further evidence for the change in symmetry was provided by differential scanning calorimetry which showed the orthorhombic-tetragonal phase transition to shift up through room temperature with decreasing grain size. The transformation stresses are expected to be more effectively minimised by the orthorhombic form of BT which has twice as many equivalent polarisation directions than the tetragonal structure, <110> and <100> respectively, stabilising the phase.[218] A brick-wall model based on FE grain cores separated by lower permittivity grain boundaries, illustrated in Fig.2.7.3, was later developed by Frey et al.[220] to explain the grain size effect on ε_r for grains smaller than 500 nm. The permittivity value of the grain cores is believed to be independent of the grain size and undergoes a normal FE transition at T_C. Instead, a dilution effect from the large number of non-FE phase boundaries, which increase with decreasing grain size, suppresses the overall permittivity.[220]

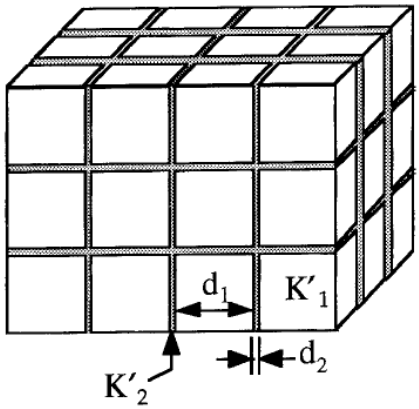

Fig.2.7.3: Schematic of the brick-wall model showing the FE grain cores with dielectric permittivity K'_1 separated by lower permittivity grain boundaries K'_2.[220]

In addition to the extrinsic effect of grain boundaries, Zhao et al.[221] reason that an intrinsic size effect from the loss of tetragonality also contributes to the reduction of ε_r with decreasing grain size (Fig.2.7.4). Ferroelectricity was predicted to be lost in fine grained BT ceramics of 10-30 nm as no cubic-tetragonal structure transition is expected to occur.[221] Evidence of a FE domain structure with polarisation switching at the local level however, has been found in ceramics with a grain size of ~30 nm using PFM.[222] A coexisting multiphase of tetragonal and orthorhombic structures has been found within ceramic grains of this size.[223] Ferroelectricity still exists within these very fine grained ceramics and is suppressed mainly by extrinsic effects exerted by the grain boundaries and is not related to the size induced stabilisation of the PE cubic structure. A 'phase transition' to a polar phase with a frozen domain structure with non-switchable polarisation is expected to occur in very small grains (< 30 nm).[222] PFM studies however, reveal local FE switching to still occurs in ceramics with 20 nm[224] and 8 nm[225] grain size (Fig.2.7.5). Petkov et al.[226] predict that no fundamental limit for ferroelectricity exists, it is only weakened intrinsically by a loss of long-range periodicity of the polar distorted Ti-O_6 octahedra. The tetragonal-type lattice atomic order is preserved to at least 3 unit-cells. The author's note that the appearance of a disordered region close to the surface of nanosized ceramic grains with a cubic structure may have prompted the discussion of a critical grain size for ferroelectricity,[212],[227] however this region is believed to be only an effect of processing and not a true grain size effect.[226]

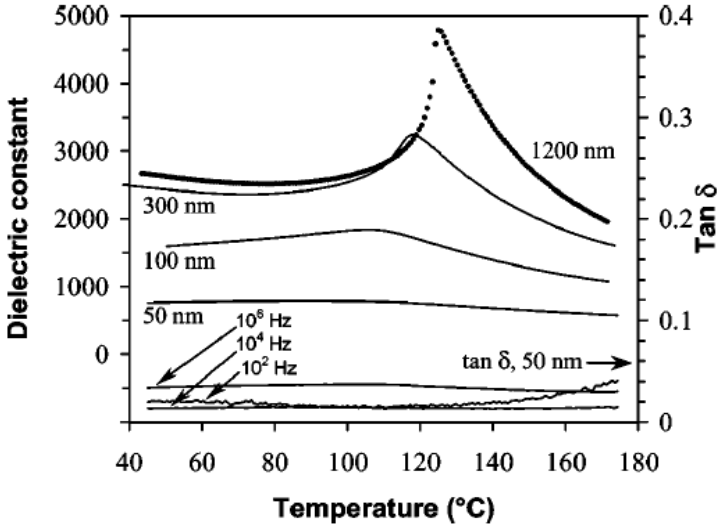

Fig.2.7.4: Temperature dependence of the dielectric constant for BT ceramics with nanometre grain size.[221]

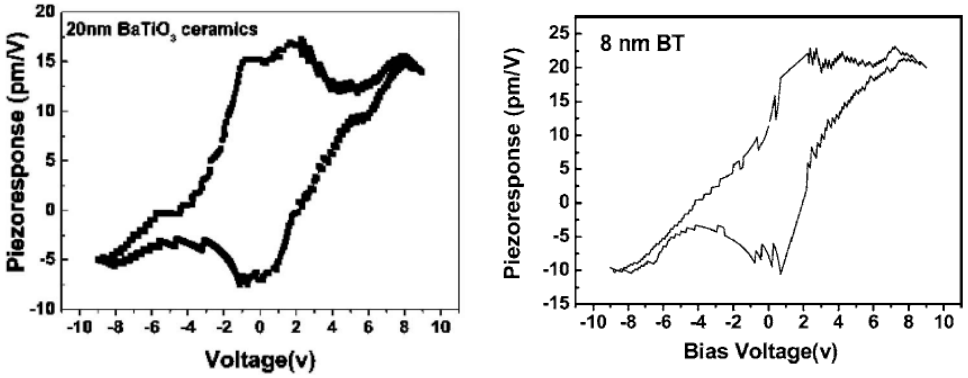

(a) (b)

Fig.2.7.5: Piezoelectric hysteresis loops showing FE switching in BT ceramics with a grain size of (a) 20 nm[224] and (b) 8 nm[225].

Grain Size has been found to influence the structure and properties of many other lead-free FEs. $Bi_{0.5}Na_{0.5}TiO_3$ (BNT) demonstrates similar grain size dependence as BT, with the maximum ε_r value occurring at a grain size of 1 μm (Fig.2.7.6). The temperature of the T_m peak in the permittivity, shown in Fig.2.7.7, however, appears nearly independent of grain size. The feature associated with the depolarisation temperature T_d shift towards higher temperature with the reduction of grain size where it then vanishes below 200 nm. Ferroelectricity is thought to disappear within this system at a critical grain size of 100 nm.[228] The low porosity of the ceramics investigated in this study however, do not allow for a meaningful comparison between the ceramics.

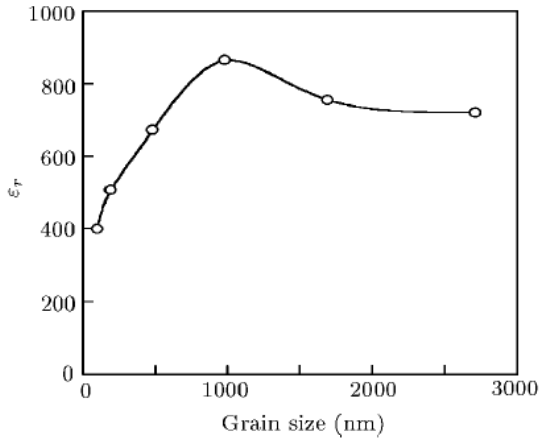

Fig.2.7.6: Grain size dependence of the dielectric permittivity ε_r in BNT.[228]

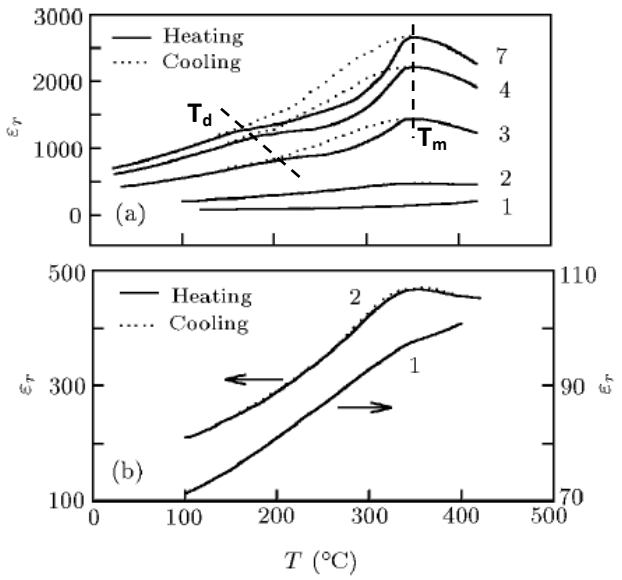

Fig.2.7.7: Temperature dependence of the dielectric permittivity ε_r of BNT ceramics with different grain size. (1: 100 nm, 2:190 nm, 3: 480 nm, 4: 980 nm and 7: 4.78 μm)[228]

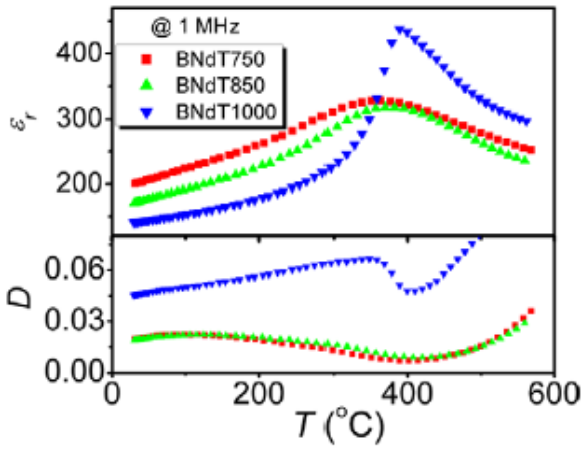

Fig.2.7.8: Dielectric response vs. temperature for BNdT ceramics with grain size 90 nm, 180 nm and 2 μm for BNdT750, BNdT850 and BNdT1000, respectively.[229]

The Aurivillius phase $Bi_{3.15}Nd_{0.85}Ti_3O_{12}$ (BNdT) shows a continuous increase in ε_r with decreasing grain size down to 90 nm (Fig.2.7.8).[229],[230] The orthorhombic distortion in this material was found to decreases with decreasing grain size. Domain wall formation was found to relieve the internal stress generated from the PE to FE transformation at T_C in the larger grain sized ceramics. However, the internal stress in the small grain ceramic is not sufficient to nucleate domain walls. Rather, a single grain single domain structure is thought to be responsible for the enhanced permittivity.[230] The internal stress forces the nano-grains back towards the tetragonal PE phase, where the dielectric permittivity is highest.[231] A similar grain size dependence was observed for the multiferroic $BiFeO_3$ (BFO).[232] Ferroelectricity was found to persist within this

materials at 40nm. The grain size effect was found to shift the temperature of T_C (*R3c→Pbnm*) from 697 ˚C[233] to 655 ˚C[232], as shown in Fig.2.7.9.

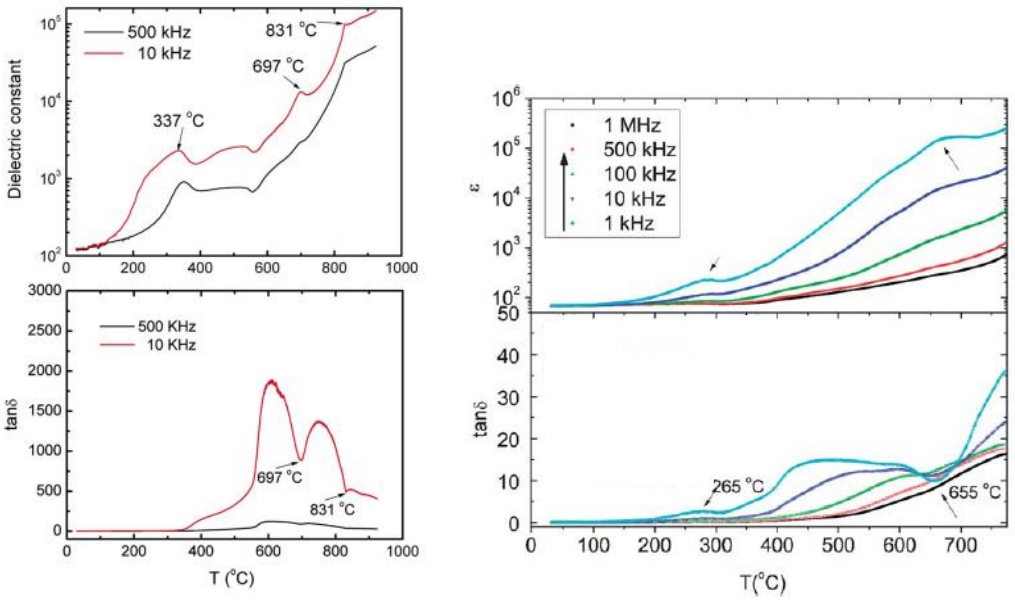

(a) (b)

Fig.2.7.9: Temperature dependence of the dielectric response for BFO with (a) micrometre[233] and (b) 40nm grain size[232]. Additives of La, Tb and Zr were added to BFO to stabilise the valence fluctuation of the iron ions which occur during processing, reducing the electrical leakage and impurities within this system.[232]

A different type of grain size effect occurs in the morphotropic phase boundary composition $Na_{0.5}K_{0.5}NbO_3$ (NKN).[234] Unlike the other lead-free ceramics evidence of a single grain-single domain structure is not observed in this material. The T_C is independent of grain size (Fig.2.7.10) and domain walls remain visible in grains as small as 200 nm. The high density of domain walls in the fine NKN grains is thought to be responsible for the increase in room temperature dielectric permittivity with decreasing grain size.[234]

Grain size has been shown to influence both the dielectric and electromechanical properties of many FE materials. The shift in the position of T_c toward lower temperatures is the result of the formation of a single grain-single domain type structure as demonstrated in $BaTiO_3$, Aurivillius phase BNdT and multiferroic BFO. The critical grain size for the formation of this domain structure is different for each composition. For example, a critical grain size has not yet been reported for the MPB composition NKN, instead the temperature of T_c remains constant for ceramics with grain size as

small at 200 nm. The nanodomain structure associated with the MPB may only be affected by grain size when it approaches that of the domain size.

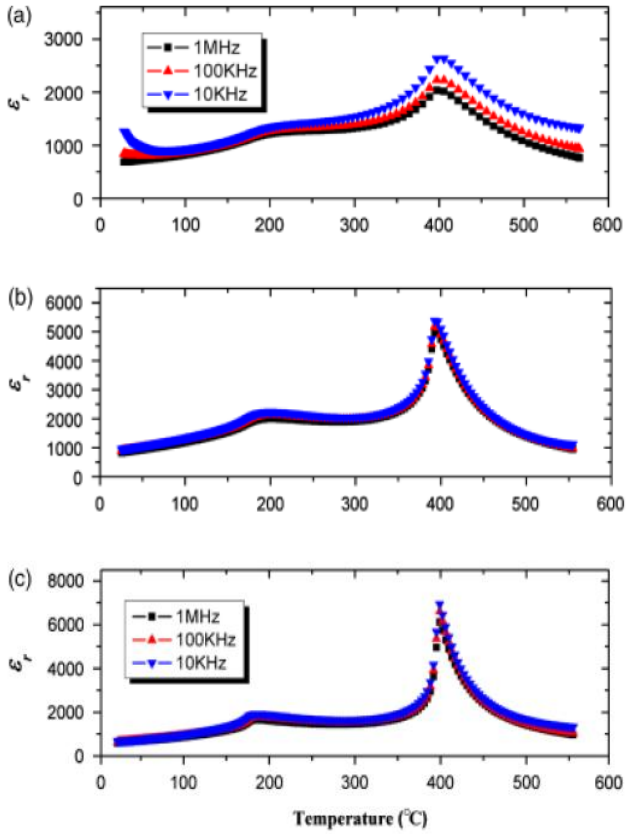

Fig.2.7.10: Dielectric permittivity vs. temperature for NKN ceramics with grain size (a) 200 nm, (b) 350 nm and (c) 980 nm.[234]

Chapter 3 Experimental Methods

In this chapter, the experimental techniques used during powder preparation, ceramic processing and characterisation are described. The methods used for crystal structure refinement and microstructure imaging are also presented as well as the techniques used to investigate the electric response of the ceramic samples.

3.1 Powder Preparation and Ceramic Processing

Polycrystalline powders were prepared by solid-state reaction using high-purity oxides and carbonates. The raw materials were weighed according to the stoichiometric formula of the selected composition. The powders were mixed in ethanol in nylon pots by planetary ball-milling (QM-3SP4, Nanjing University Instrument Plant, China) with zirconia balls of 5 mm and 10 mm diameter. The volume ratio of powder to ethanol and to milling balls is 1:2 and 1:3, respectively. The dried powder mixtures were then sieved through a 250 μm mesh to reduce the agglomeration. The powders were then calcinated in a conventional chamber furnace (Carbolit HFT 1800, UK) before further ball-milling to homogenise the particle size. Nanograin powder was prepared by high-speed planetary ball-milling using (Fritsch Pulverisette 7) with 1mm diameter zirconia balls. The same ratio of powder, solvent and milling balls was used as during regular ball-milling.

Simultaneous thermal analysis (STA) which combines thermogravimetry with differential scanning calorimetry was used to help determine the calcination temperatures of the powder mixtures. This measurement was performed using a STA1500 during heating and cooling from room temperature up to 1200 ˚C at 10 ˚C/min in an air atmosphere.

Ceramics of different grain size were prepared from the calcinated powder by two different sintering techniques: (i) from green bodies by conventional pressureless sintering using the chamber furnace and (ii) by spark-plasma sintering (SPS) in a HPD 25/1 FCT (Germany) SPS furnace.

3.1.1 Sintering by SPS

SPS is a rapid sintering method that combines high heating rates generated by a pulsed DC current with uniaxial loading for fast, low temperature densification. Graphite dies and punched lined with graphite foil were used to contain the powder samples during sintering. Schematics of the different SPS step-ups used to sinter ceramics with average grain size ranging from the nanometre to the micrometre scale are illustrated in Fig.3.1.

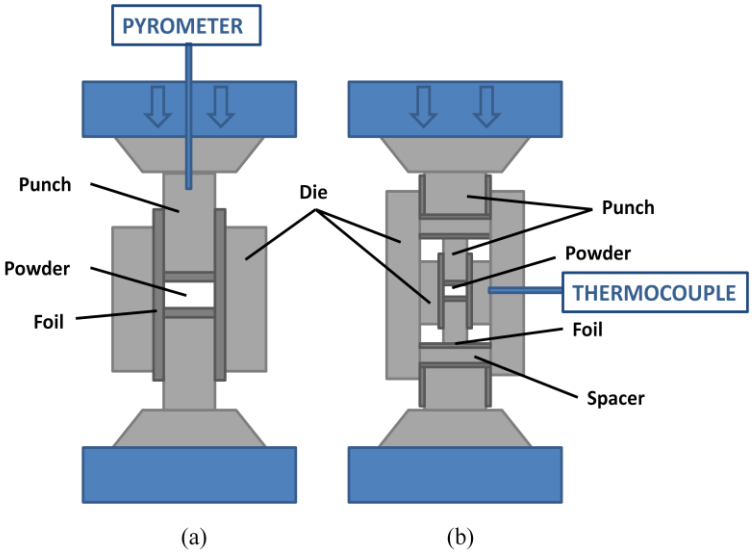

Fig.3.1: Illustration of the SPS graphite die and punch step-up used for (a) low pressure (<100 MPa), high temperature (≥800 ˚C) sintering and (b) high pressure (≥100 MPa), low temperature (< 800 ˚C) sintering. The sample diameter of step-up (a) and (b) are 20 mm and 5 mm, respectively. A thermocouple inserted into the outer die in (b) was used to monitor the temperature of the sample.

The sintering conditions can be closely monitored using this technique. For example, information about the sintering process can be gained from the SPS profile shown in Fig.3.2. The temperature of the sample is monitored by either the pyrometer in the piston or a thermocouple inserted into the middle of the graphite die, depending on the graphite die step-up. Both the relative position and speed of the piston can give information about the densification of the sample: when the force is applied by the piston on heating, the powder sample is initially compressed, once the full force is applied the position remains constant and the speed decreases to zero. As the temperature is increased sintering begins to occur and the sample shrinks. To maintain the pressure, the piston moves. Densification is comple when the piston position remains constant and the speed returns to zero. The width of the peak is dependent on the grain size range of the powder. The sintering temperature is held constant for a short period to ensure homogeneity in conditions throughout the sample. Any melting in the

sample will result in a loss of vacuum, which should remain below 0.1 hPa during this holding time.

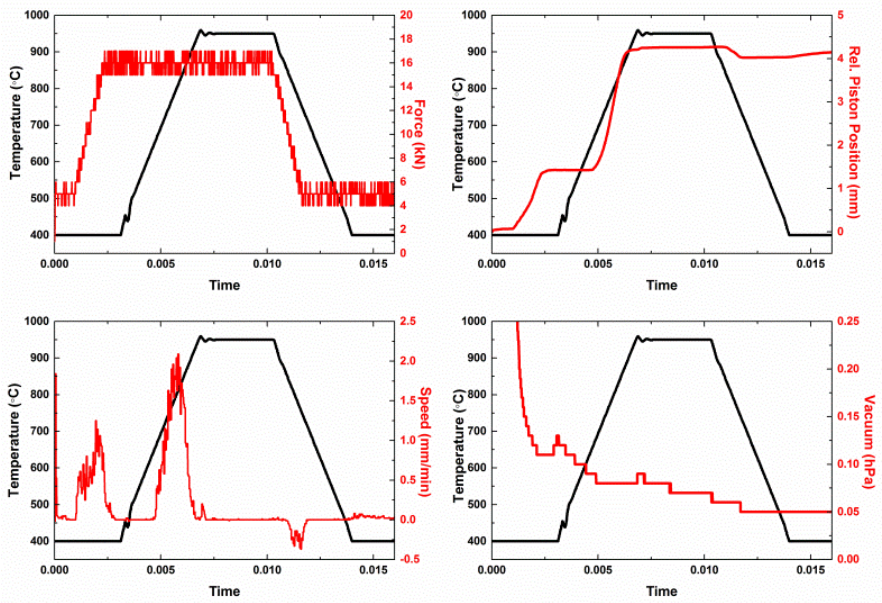

Fig.3.2: SPS sintering profile.

3.1.2 Density Measurement

The density of the sintered ceramics was measured according to the Archimedes principle:

$$\rho = \frac{m\rho_0}{m - m_w}$$

where m is the mass of the dry sample weighed in air, m_w is the mass of the sample when submerged in water and ρ_0 is the density of water. The relative density of the sample, recorded in this thesis, is determined from the expression:

$$\rho_r = \frac{\rho}{\rho_T}\ x\ 100\ \%$$

where ρ_T is theoretical density of the composition.

3.2 Determining the Crystal Structure

3.2.1 Powder X-ray Diffraction (XRD)

During powder XRD, a beam of X-rays, of wavelength λ, are applied to the surface of the crystalline material at an incident angle θ, depicted in Fig.3.3. The X-rays are scattered by the sample according to Bragg's law $n\lambda=2dsin\theta$ where n is an integer and d is the distance between the crystal planes. When there is coherent scattering from the

crystalline planes the Bragg condition is satisfied and a Bragg peak appears in the diffraction pattern.

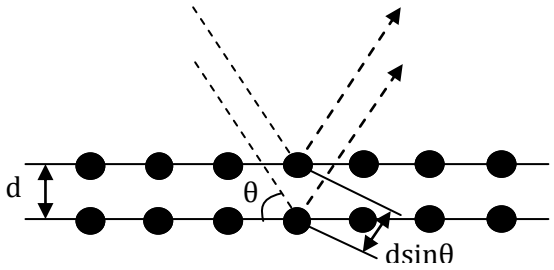

Fig.3.3: Schematic of the Bragg condition showing scattering of X-rays by atoms in a crystalline solid.

This technique was employed on numerous occasions though out the powder processing stage to check the phase formation of the calcinated powders as well as the level of ZrO_2 contamination introduced into the system by ball-milling. Rietveld refinement of the powder XRD data collected at high temperatures from the crushed ceramic was used to determine the crystal structure at different grain sizes.

XRD patterns were collected from the samples using a PANalytical X'Pert Pro X-ray diffractometer, fitted with a X'Celerator detector in θ/θ geometry using Ni filtered Cu K_α radiation (λ=1.5418 Å). For phase identification of the calcinated powders, data was collected over the 2θ range: 5-70 ˚ using a steps size of 0.0334 ˚ and a count rate of 200 seconds per step. A more detailed scan was required for Rietveld refinement of the crystal structure; in this case data was collected over the 2θ range 5-120 ˚ with 0.0167 ˚ step size and 200 seconds per step count rate. Rietveld refinement was performed on ceramics which had been lightly hand crushed using a pestle and mortar. To examine the crystal structure of the ceramics at different temperature, a thin layer of the powdered sample was mounted on a Pt plate connected to a heating filament. The temperature was monitored by a thermocouple placed close to the surface of the material. XRD data was collected at room temperature, then at 50 ˚C intervals from 100 ˚C to 700 ˚C during heating and cooling.

3.2.2 Transmission Electron Microscopy (TEM)

A JEOL 210 field-emission STEM was used to examine the room temperature crystal structure and microstructure of the ceramic samples. A thin lamella of the bulk ceramic was prepared for TEM analysis by focused ion beam machining using a FEI Quanta 3D ESEM. Using the lift-out method[236], a thin slice of the cross-section of the sample was milled out of a larger sample using a focused ion-beam then mounted on a TEM half-

grid with Pt. A protective layer of Pt was deposited on the sample surface to protect it from ion irradiation during this micromachining stage. The cross-section was then thinned to electron transparency using a low-voltage focused ion beam at grazing incident from both side of the sample. The ceramic sample was annealed at 600 ˚C for 4 h prior to TEM sample preparation to remove any mechanical stress which may have developed within the material during cutting and pre-polishing[133].

3.3 Microstructure Imaging Techniques

3.3.1 Scanning Electron Microscopy

(i) Secondary Electrons

The grain morphology of the powders and ceramics were examined using a FEI Inspect F (Hillsboro, OR) scanning electron microscope (SEM) operating in the secondary electron mode. The average grain size of the ceramics was determined from the natural and fracture surfaces. To reduce the effects from charge build up on the non-conducting surface, the materials were coated with a thin layer of gold using a sputter coater.

(ii) Back-Scattered Electrons

In the back-scattered electron mode, the domain structure of a ferroelectric can be imaged by exploiting the contrast caused by electron channelling[237]. The basic principle behind this phenomenon considers the crystal lattice to be formed of channels or paths rather than a set of atomic points, as demonstrated in Fig.3.4.[238] This channelling structure allows the electron beam to penetrate to larger depths before being scattered. Different crystal orientations will backscatter more than others, giving rise to an orientation contrast pattern. Any variation in the crystal structure either from defects such as stacking faults and dislocations, or from domain formation in the ferroelectric will alter the channels open to the electrons changing their scattering pattern. The domain contrast pattern can also be changed by tilt the crystallite as shown Fig.3.4(c).[239]

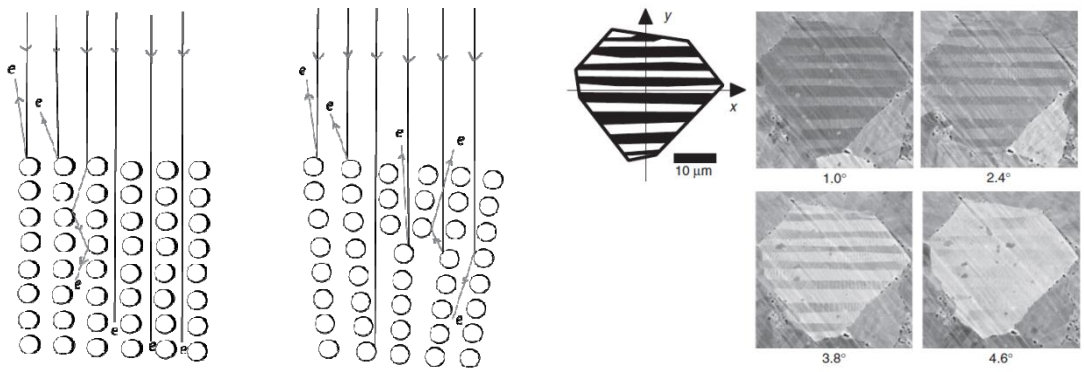

(a) (b) (c)

Fig.3.4: Schematic of the crystal lattice showing the trajectories of the incident electrons along (a) open channels and (b) closed channels formed by variations in the crystal lattice.[238] (c) Back-scattered SEM images showing the effect of tilting angle on the domain pattern in a (Na,K)NbO_3 grain.[239]

To view the ferroelectric domain structure using this technique, the ceramic surface were polished by argon ion milling[239] for 12 h under an accelerating voltage of 5 kV and an ion beam current of 0.1 mA using a JEOL SM-09010 cross-section polisher (Jeol Ltd., Tokyo, Japan). This method of polishing allows the underlying material to be exposed without significant mechanical impact. To reduce the effects of mechanical stress on the domain structure created during the pre-polishing sample preparation (i.e. cutting and grinding), the ceramics were annealed for 4 h at 600 ˚C. The electrically poled samples were not annealed prior to argon milling. This non-destructive method of sample preparation allows the ceramic to be reused for other domain imaging techniques as it does not require the sample to be chemically etched or coated in a conductive material.

SEM observations were performed using a JEOL JSM-700F field-emission SEM. The highly polished surface prepared by argon ion milling allows for high probing currents and low scan rates to be used without strongly charging the sample[239].

3.3.2 Scanning Probe Microscopy

Another imaging technique commonly used to visualise the domain structure in ferroelectric materials is scanning probe microscopy. The main instrument used in this technique is the atomic force microscope (AFM) which employs a cantilever system to probe the surface of the material. In addition to direct topographical measurements, different modes of AFM can be used to exploit the electrical nature of the ferroelectric material.[240]

(i) Piezoresponse Force Microscopy (PFM)

PFM is a contact mode technique that generates deformations in the ferroelectric by applying an AC bias-voltage to the tip of a conducting AFM probe.[241] When the tip is brought into contact with the surface, the local electromechanical response or amplitude ($d_{33}V_{AC}$) is detected as the first-harmonic component of the cantilever deflection $\Delta z = d_{33}V_{AC}cos\ (\omega t+\theta)$, where d_{33} is the 'vertical' piezoelectric coefficient and V_{AC} is the applied voltage. Information from the phase θ is used to map the local orientation of the polarisation vector. For example, the application of a positive bias to a c^- domain expands the sample and the surface oscillations are in phase with the tip voltage, θ=0, as demonstrated in Fig.3.5. Conversely, when the positive bias is applied to a c^+ domain, the sample contracts so θ=180 ˚. Information on the polarisation switching can be gained by applying a DC bias-field (V_{DC}) to the tip, so $\Delta z = d_{33}V_{DC} + d_{33}V_{AC}cos\ (\omega t+\theta)$.

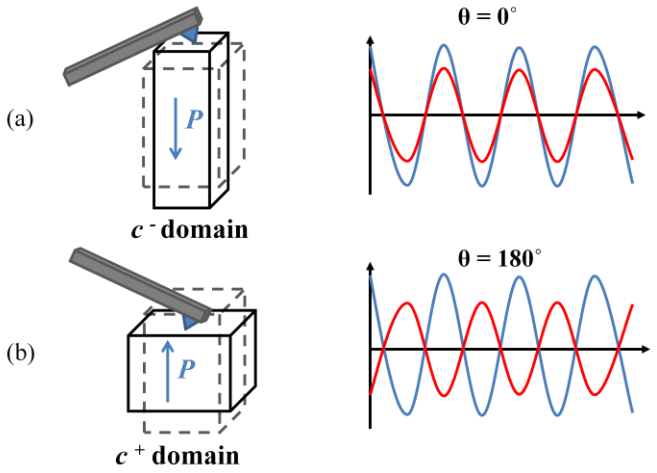

Fig.3.5: A schematic demonstrating the response of (a) c^- and (b) c^+ domains to a positive tip bias.

As the cantilever tip is in direct contact with the sample surface, any scratches or indentations from pores will distort the image of the domain pattern. To achieve high quality images, the argon ion-beam polished samples prepared for back-scattered SEM, were reused for this domain imaging technique. The PFM images were captured using a Veeco Dimension 3000 AFM.

3.4 Electrical Response

The electrical response of the material was measured from thin (<1mm) platelets, with relatively large surface area (>5 mm^2), cut from the sintered ceramic. Silver paste (Gwent Electronic Material Ltd., C2011004D5, Pontypool, UK) was fired at 600 ˚C for

10 minutes onto the large parallel faces of the ceramic to form electrodes. When required, the samples were electrically poled in silicon oil by applying a DC voltage of up to 7 kV for 5 minutes using a regulated high voltage power supply (Alpha Series II, Brandenburg).

The dielectric permittivity ε_r of the material was calculated from the measured capacitance, *C*, using the expression $C = \varepsilon_0 \varepsilon_r A/d$ where ε_0 is the permittivity of free space (8.854×10^{-12} Fm^{-1}), A is the area of the parallel electrodes and d is the distance between the electrodes. This expression requires the dielectric material, of known dimensions, to be inserted between two electrodes in the parallel plate arrangement, illustrated in Fig.3.6. The contacts made with the parallel faces of the sample act as the electrodes; the area of the electrodes is therefore the same as the area of the sample face and the distance between the electrodes is equal to the sample thickness.

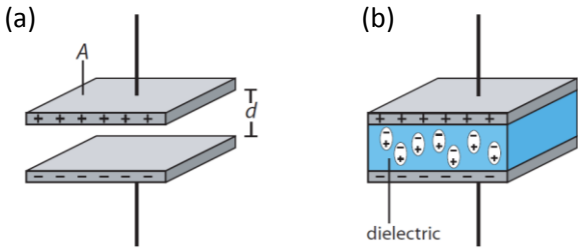

Fig.3.6: Parallel plate capacitor arrangement showing electrodes separated by (a) vacuum and (b) dielectric.

Impedance spectroscopy was performed at room temperature from 100 Hz to 1 MHz using an Agilent 4294A (Hyogo, Japan) impedance analyser. An LCR meter (Agilent, 4284A (Hyogo, Japan)) connected to a tube furnace (Lenton, LFT 16/--/180, T_{max}=1600 ˚C) was used to measure the temperature dependence of the dielectric permittivity and loss by applying an alternating voltage of 1 V at frequencies ranging from 1 kHz to 500 kHz. The measurement was performed during heating and cooling from room temperature up to 600 ˚C at a controlled rate of 3 ˚C/min. The system was tested by measuring the dielectric response of the well-known ferroelectric $BaTiO_3$. Features related to changes in the crystal structure were observed at temperatures consistent with the literature. For bias-field experiments, a DC voltage was applied to the sample using a Keithley 6517A electrometer. A schematic of the LCR equipment set-up used to measure the dielectric response in a bias-field is shown in Fig.3.7.

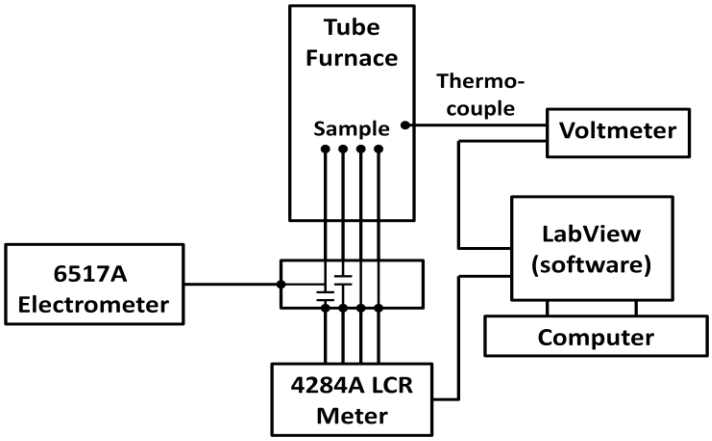

Fig.3.5: Schematic showing the LCR equipment step-up used to measure the dielectric response in a bias-field. The internal circuitry of the DC bias box is also shown.

Current-polarisation-electric field (I-P-E) loops were measured by applying triangular voltage waveforms of 5, 10 and 20 Hz to the sample using a hysteresis tester (NPL, Teddington, UK). The temperature dependence was tested by heating the sample in a silicon oil bath from room temperature up to 175 ˚C in 25 ˚C and 50 ˚C intervals.

The piezoelectric coefficient d_{33} of the samples were measured using a quasi-static ZJ-3B PIEZO (Institute of Acoustics Academia Sinica, China) d_{33} meter. X-cut quartz (d_{33}=2.3±0.1 pN) was used to calibrate the meter.

Chapter 4 Grain Size Effect in $Bi_{0.5}Na_{0.5}TiO_3$

Lead-free $Bi_{0.5}Na_{0.5}TiO_3$ (BNT) forms the basic end member of some of the most promising ferroelectric (FE) materials. Following the discovery of double hysteresis loops in Sr-doped BNT nearly 50 year ago, many papers investigating the properties of the A-site substituted perovskite BNT have been published. An antiferroelectric (AFE) phase was originally thought to exist in this material but has since been linked to a relaxor-type behaviour associated with ferrielectric *P4bm* polar nanoregions. Much uncertainty surrounding the true crystal structure still exists as distortion from the basic perovskite structure is very small in BNT, making structural refinement difficult, and no clear correlation between structure and property exists.

To gain a better understanding of this material, this chapter aims to address some of the questions that have arisen from the literature review by investigating the effect of ceramic grain size on the structure and properties of BNT. For example, research has more recently focused on the room temperature structure following the discovery of a monoclinic C_c defect structure. This chapter will consider the influence of grain size on the *R3c*/C_c structure, and whether this feature is unique to certain grain sizes. It will also examine what significance grain size has on T_d recently linked with a *R3c*-to-C_c structural transition. Much of the literature reporting the properties of ceramic BNT do not take into account the effect of grain size which is important in FE materials. To help answer these questions, crystal and domain structure analysis techniques are used to explore the defect structure in different grain size ceramics and the impact of poling fields on this structure. The nature of the FE 'transition' at T_d is tested by DC bias-field dielectric measurements, notably used to probe the relaxor behaviour of $Pb(Mg_{⅓}Nb_{⅔})O_3$[53]. The stability of the polarisation near the transition is further examined by thermal depoling experiments and hysteresis loop tests. These experiments will also help to uncover weather a critical grain size for ferroelectricity exists in the nanograin BNT ceramics.

Moving on from this the chapter will explore how grain size influences the structure of BNT at high temperature. In particular it will consider whether the dielectric peak T_m shifts to lower temperature with decreasing grain size indicating the formation of a single grain-single domain type structure as demonstrated in $BaTiO_3$[221], Aurivillius phase $Bi_{3.15}Nd_{0.85}Ti_3O_{12}$ (BNdT)[229] and multiferroic $BiFeO_3$ (BFO)[232], or whether it is

grain size independent similarly reported for the morphotropic phase boundary composition $Na_{0.5}K_{0.5}NbO_3$ (NKN)[234]. Uncovering the grain size dependence of this feature may help to understand its origin. High temperature XRD structural analysis combined with temperature dependent dielectric data will be used to help answer these questions.

This chapter will show that the model used to describe the grain size effect in other lead-free FEs can be applied, in a slightly modified form, to BNT.

4.1 Ceramic Processing

Powders of BNT were prepared by solid-state reaction from the raw materials Bi_2O_3(99.9 % Sigma-Aldrich), TiO_2(99.8 % Sigma-Aldrich) and Na_2CO_3(99.5 % Alfa Aesar). The powdered oxides and carbonate were weighed according to the stoichiometric formula $Bi_{0.5}Na_{0.5}TiO_3$ and mixed in ethanol for 2 h by planetary ball-milling at 350 rpm with zirconia balls. After drying, the powder mixture was sieved in preparation for calcination.

4.1.1 Stoichiometry

Oxygen vacancies introduced into a material by non-stoichiometry are known to alter the properties of the host system. Where a material is hydrophilic, as in the case of Na_2CO_3, particular care must be taken to insure that the mass from the absorbed water does not distort the stoichiometry of the system.

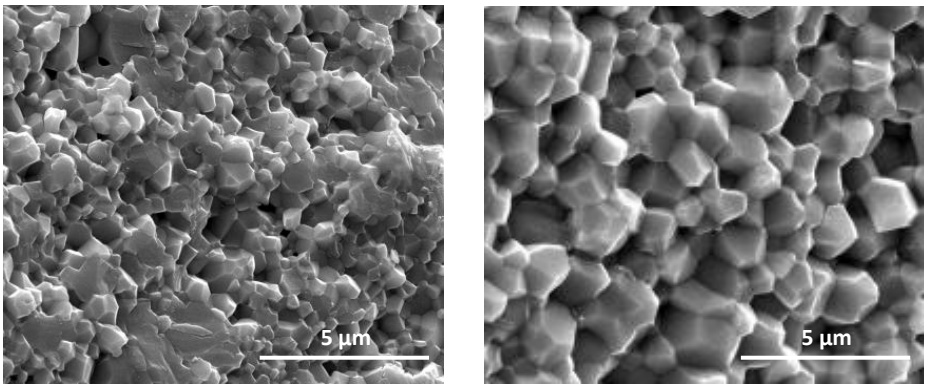

(a) (b)

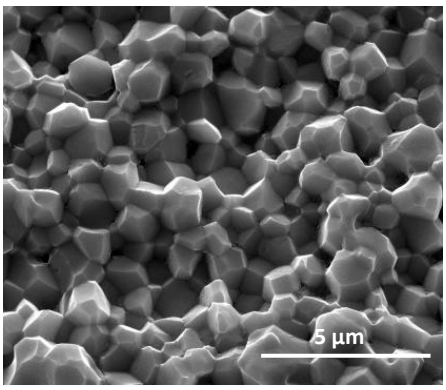

(c)

Fig.4.1: Fracture surface SEM micrographs of BNT ceramics prepared from (a) untreated, (b) dried and (c) calculated Na_2CO_3 powder. Sintered at 950 ˚C (5 mins)/50 MPa using SPS.

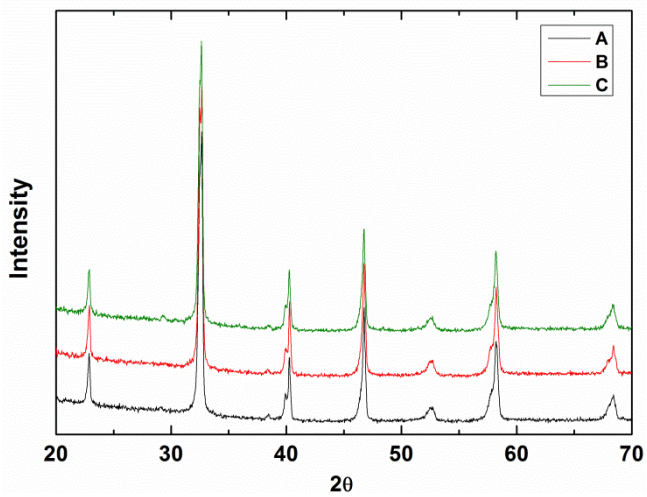

Fig.4.2: XRD pattern of BNT ceramics prepared from different batches of Na_2CO_3 powder.

A 1% change in mass was recorded for the carbohydrate after drying at 200 ˚C for 24 h. To correct for the effect of excess water and preserve the stoichiometry of the powder mixture, three batches of BNT powder were prepared: one using the raw, untreated Na_2CO_3 powder (A), another with the dried Na_2CO_3 powder weighted while hot (B) and finally one from the raw powder considered to have an additional 1 % impurity from water (C). Ceramics sintered under identical conditions by SPS [950 ˚C (5 mins)/50 MPa] were prepared from the different powder batches. Both the grain morphology, depicted in the SEM images (Fig.4.1), and structure determined from the XRD profiles of the ceramics (Fig.4.2) show very little difference between powder processing methods. However, the existence of oxygen vacancies and their effect on the conductivity of BNT is clearly illustrated in the electrical property results (Fig.4.3 and Fig.4.4). Tilting of the I-E loop and a mismatch between the coercive field (E_c) values

corresponding to the current peak in the I-E loop and P=0 in the associated P-E loop are all effects of increased conductivity[69]. Both the ceramics derived from batches A and C clearly show this behaviour. To avoid oxygen vacancies being introduced by the 'wet' starting powder, only Na_2CO_3 which had been dried and weighed while hot (batch B) would be used for future powder processing.

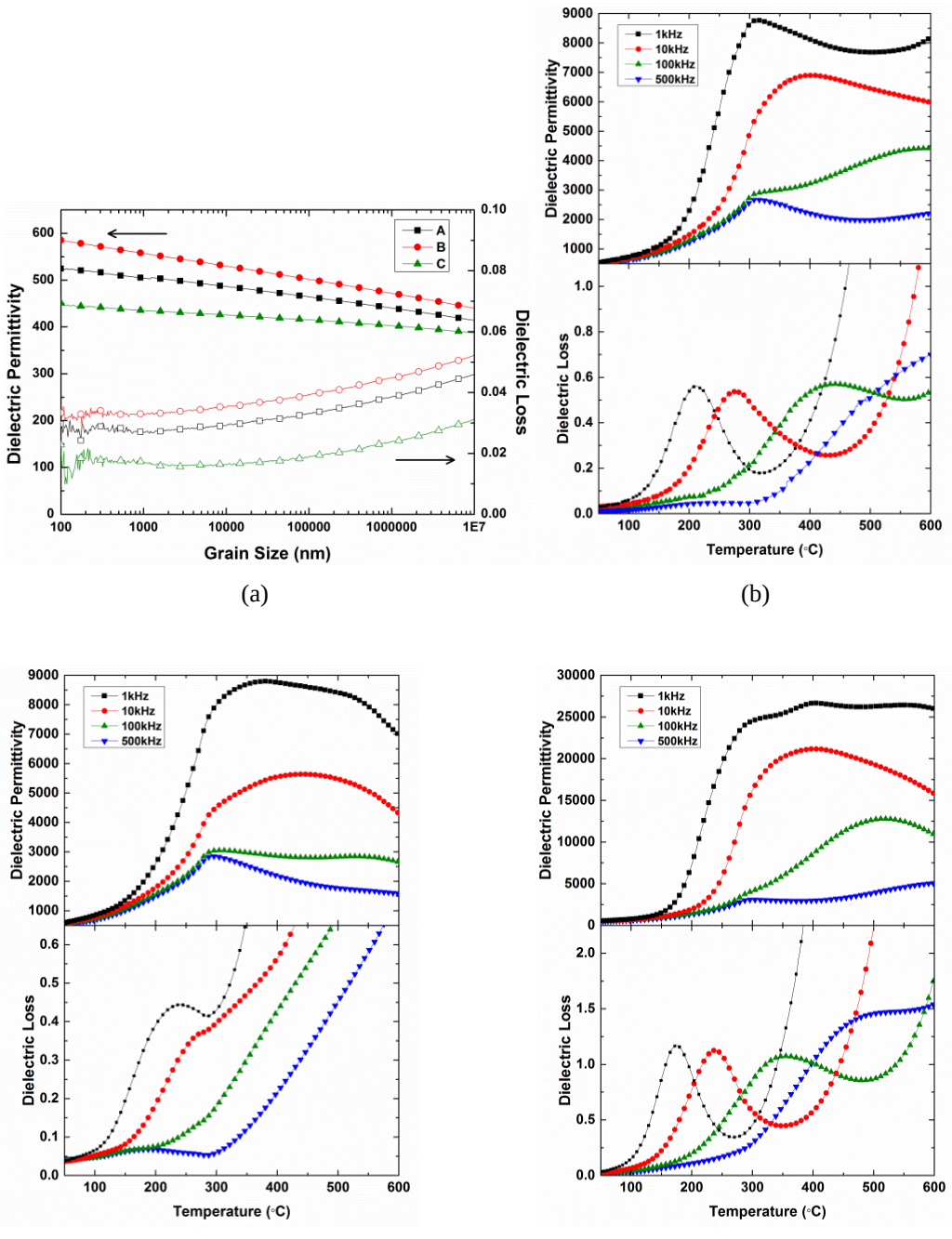

Fig.4.3: Dielectric response of the ceramics prepared by SPS [950 ˚C (5 mins)/50 MPa] from different batches of Na_2CO_3 powder: (a) frequency dependence at room temperature and temperature dependence of (b) A, (c) B and (d) C powders, measured at 1, 10, 100 and 500 kHz.

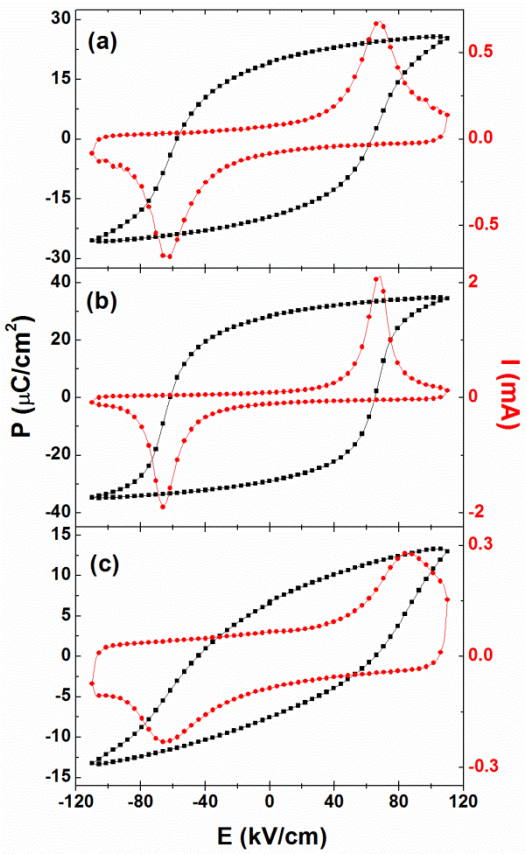

Fig.4.4: Room temperature P-E (black) and I-E (red) loops of BNT ceramics prepared by SPS [950 ˚C (5 mins)/50 MPa] using (a) A, (c) B and (c) C powder batches. Frequency:10 Hz.

4.1.2 Determining the Calcination Temperature

For solid-state powder processing, the calcination temperatures reported in the literature range from 650-900 ˚C and vary with the number of calcination steps. An in situ XRD investigation by Askel et al.[54] into the phase formation of BNT during the calcination process has shown the perovskite structure to begin to form at 500 ˚C. A transient phase, believed to originate from a secondary reaction between reactant oxides also forms at this stage however this phase disappears at 650 ˚C leaving BNT as the only phase present at 700 ˚C. [54]

The STA data obtained from the BNT powder mixture, shown in Fig.4.5, indicates a similar calcination sequence with a steep decease in mass occurring between 500 ˚C and 700 ˚C and an endothermic heat flow peak at 700 ˚C. To ensure single phase formation, a minimum calcination temperature of 800 ˚C was estimated from this data. Samples of the powder mixture were calcinated at 800 ˚C, 850 ˚C and 900 ˚C for 4 hours at a heating rate of 5 ˚C/min, and then submitted for powder XRD analyses. Single phase

formation occurs at each temperature with no additional peaks from secondary phases or unreacted starting materials (Fig.4.6). An imbalance in the elemental weight ratios of bismuth and titanium has previously been reported for BNT after calcination at 900 ˚C [142]. Starting materials Bi_2O_3 and TiO_2 have melting points of 824 ˚C and 1870 ˚C, respectively [142]. Loss of bismuth is therefore expected if any Bi_2O_3 remains present in the powder mixture as the calcination temperature approaches the Bi_2O_3 melting point. To reduce the risk of non-stoichiometry from the loss of bismuth, the lowest calcination temperature, 800 ˚C, was chosen for subsequent BNT powder processing.

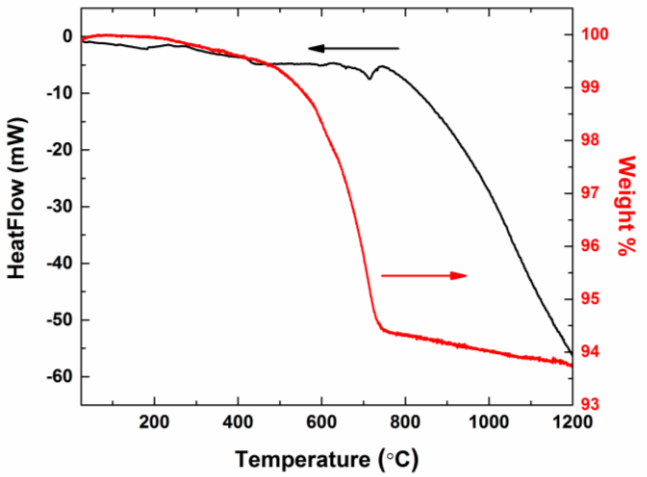

Fig.4.5: STA data for Na_2CO_3+Bi_2O_3+TiO_2 powder mixture.

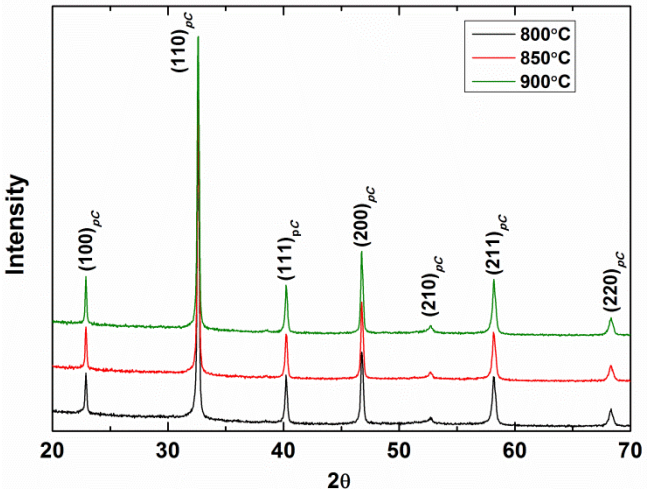

Fig.4.6: XRD patterns for BNT powders calcinated at 800, 850 and 900 ˚C, indexed using a pseudo-cubic (*pC*) unit cell.

4.1.3 Ball-Milling

Following calcination, the BNT powder was re-milled for 4 h in ethanol to break down any agglomerates formed during calcination and to reduce the overall grain size of the powders. This step is also necessary to homogenise the grain size. Ceramics sintered from powder omitting this step have a wide distribution of grain sizes as shown in Fig.4.7. The dried powders were then sieved again using a 250 µm mesh in preparation for sintering.

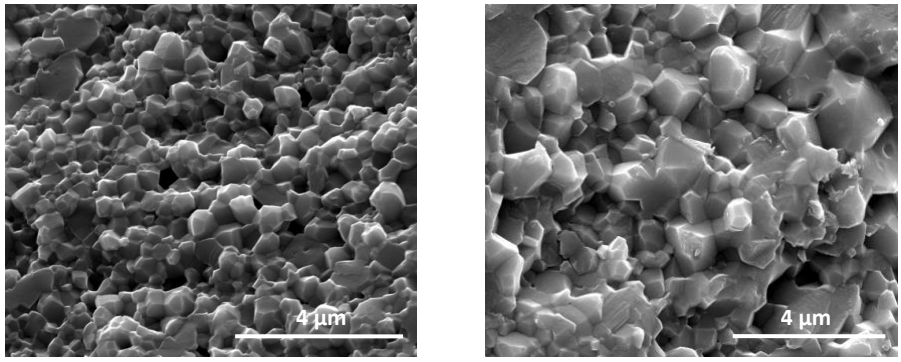

(a) (b)

Fig.4.7: Fracture surface SEM images demonstrating the importance of the post-calcination ball-milling step during powder processing. (a) A homogensous grain size is achieved in the ceramic prepared from powder with this addition ball-milling step. Grain sizes ranging from 200 nm to 2 µm can be seen in (b) for the ceramic prepared from powder omitting this step. Both ceramics were sintered using SPS under the same conditions.

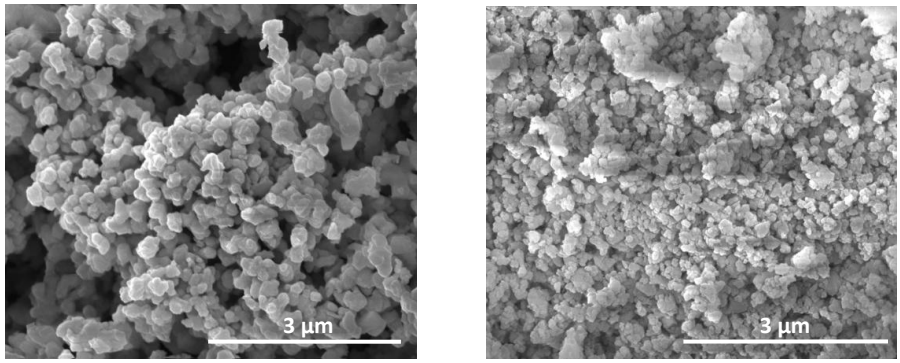

(a) (b)

Fig.4.8: SEM micrographs of BNT powder after (a) regular and (b) high-speed ball milling in ethanol.

Nano-sized BNT powder was prepared with further milling using a high-speed ball-mill. For a substantial reduction in grain size, a milling speed of 1000 rpm was used over a total period of 2 h. Initially, ethanol was used as the milling solvent. The grain sizes of the regular and high-speed milled powders were compared using the

microstructure images shown in Fig.4.8. This method of milling was found to reduce the average grain size from 200 nm to 40 nm. The level of ZrO_2 contamination from the milling balls was also monitored using XRD (Fig.4.9), as the erosion rate of the balls is much greater when milling at these high speeds.

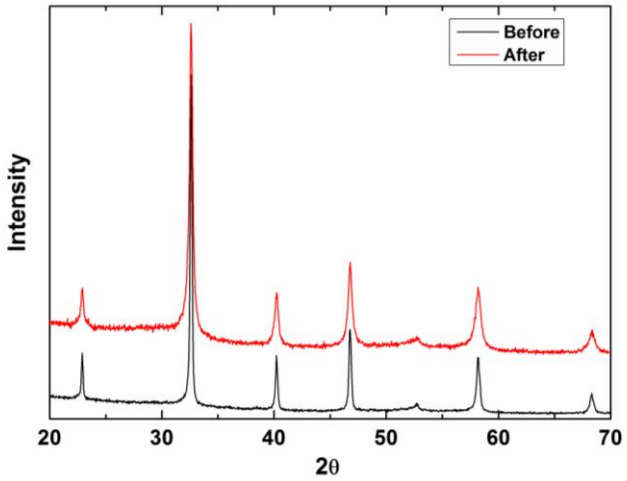

Fig.4.9: XRD patterns for BNT powders before and after high-speed ball-milling in ethanol for 2 h. No evidence of ZrO_2 impurities are observed in the powder after milling.

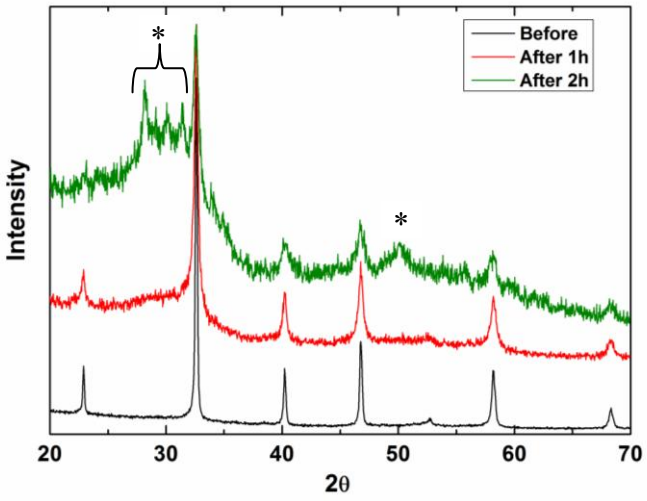

Fig.4.10: Powder XRD patterns for BNT before and after high-speed ball-milling for 1 h and 2 h in deionised water. Bragg peaks from ZrO_2 contamination are marked by *.

Due to safety concerns over the volatility of ethanol while milling at high speeds, deionised water was used to replace ethanol as the milling solvent. Under the same milling conditions, the deionised water appeared to break down the crystalline structure of the BNT powder emphasising the ZrO_2 impurity in the XRD pattern, shown in Fig.4.10. To reduce contamination from the milling media a shorter milling period of 1

h was used. This reduced the level of zirconia in the powder while still achieving nano-sized grains, evidenced in Fig.4.11. The crystalline nature of the powder was also seen to improve. Before sintering, the powder was dried for 4 h at 600 ˚C to remove any moisture remaining from the milling solvent thereby helping to improve the density of the ceramics sintered from this powder.

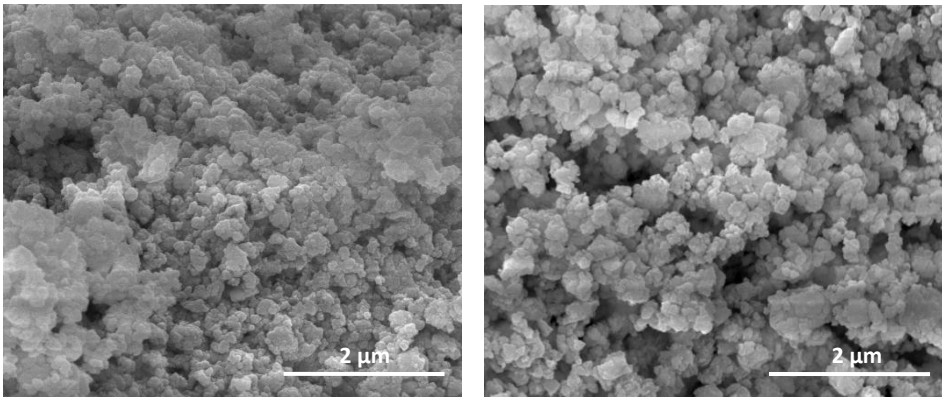

(a) (b)

Fig.4.11: SEM images of BNT powder after ball-milling for (a) 1 h and (b) 2 h in de-ionised water.

4.1.4 Chemically Prepared Powder

BNT powder prepared by sol-gel processing was used to sinter nano-grained ceramics free from zirconia contamination. This powder was supplied by Dr. Qinghui Jiang. The average grain size of the powder determined from SEM images of the microstructure, shown in Fig.4.12, was ~40 nm.

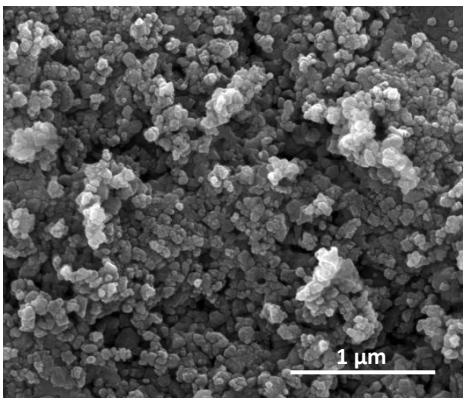

Fig.4.12: SEM image of the BNT powder prepared by sol-gel.

4.1.5 Sintering Techniques

High density ceramics with average grain size ranging from the nanometre to the micrometre scale were prepared using two different sintering techniques: spark-plasma sintering and conventional sintering. To examine the sole effect of grain size on the structure and properties of BNT, particular care was taken to ensure that the ceramics were of high density. Porosity can relieve strain resulting from structural transitions in the material which may distort the true crystal structure. The nature of the grain boundaries will also be different in materials with high porosity as gas/solid and solid/solid interfaces have different energies which will also influence the domain formation within these materials.[221] For example, low density ceramics show a sharp rise in dielectric loss at low frequencies as a result of an accumulation of charge at the interfaces between grain and pore (Fig.4.13). To guarantee a meaningful comparison between the different samples only ceramics with a porosity level <5 % were considered.

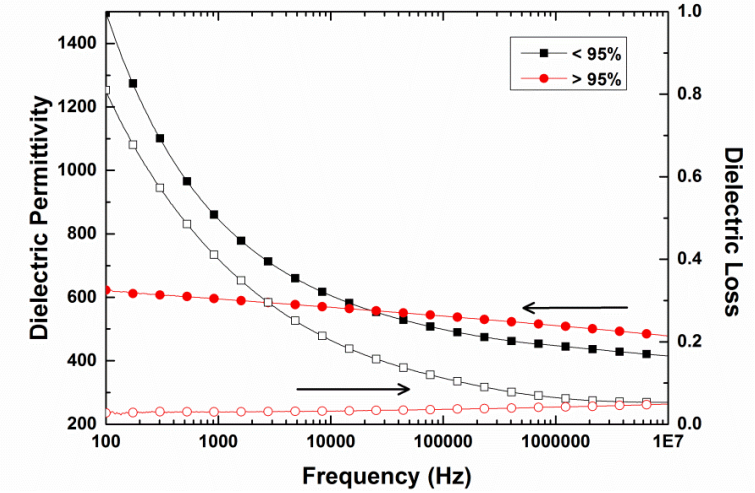

Fig.4.13: Frequency dependence of the dielectric response of low (<95 %) and high (>95 %) density ceramics with similar grain size. (solid symbols: dielectric permittivity, open symbols: dielectric loss)

(i) SPS

SPS combines high heating rates with mechanical loading for superfast densification. This technique is particularly useful for sintering ceramics with grain size below 1µm. The high pressure that can be applied during SPS enables low temperature sintering, which limits grain growth allowing the nanostructure of the powder to be retained. Powders prepared by regular and high speed ball-milling as well as the chemically prepared BNT powder were sintered using this technique.

During SPS, oxygen is partially lost from the lattice as a result of the reducing environment created by the graphite die and the atmosphere (i.e. vacuum). An annealing treatment in air was used to remove the oxygen vacancies created during sintering as well as the surface carbon contamination. To limit further grain growth, each ceramic was annealed 100-150 ˚C below the sintering temperature for 24 h. The grain size is independent of annealing time at these annealing temperatures, demonstrated in Fig.4.14. Evidence of oxygen vacancies were observed in the dielectric data of the unsuccessfully annealed ceramics (Fig.4.15) as well as their P-E loops, shown in Fig.4.16, which remain under-saturated even in very high electric fields (>9 kV/mm). When there is no restriction on grain size, annealing is typically carried out 100-200 ˚C above the sintering temperature for a much shorter time (~ 1h). The annealing process is clearly restricted by the condition used to preserve the grain size. To reduce this effect an annealing temperature closer to the sintering temperature was used for the larger grain ceramics.

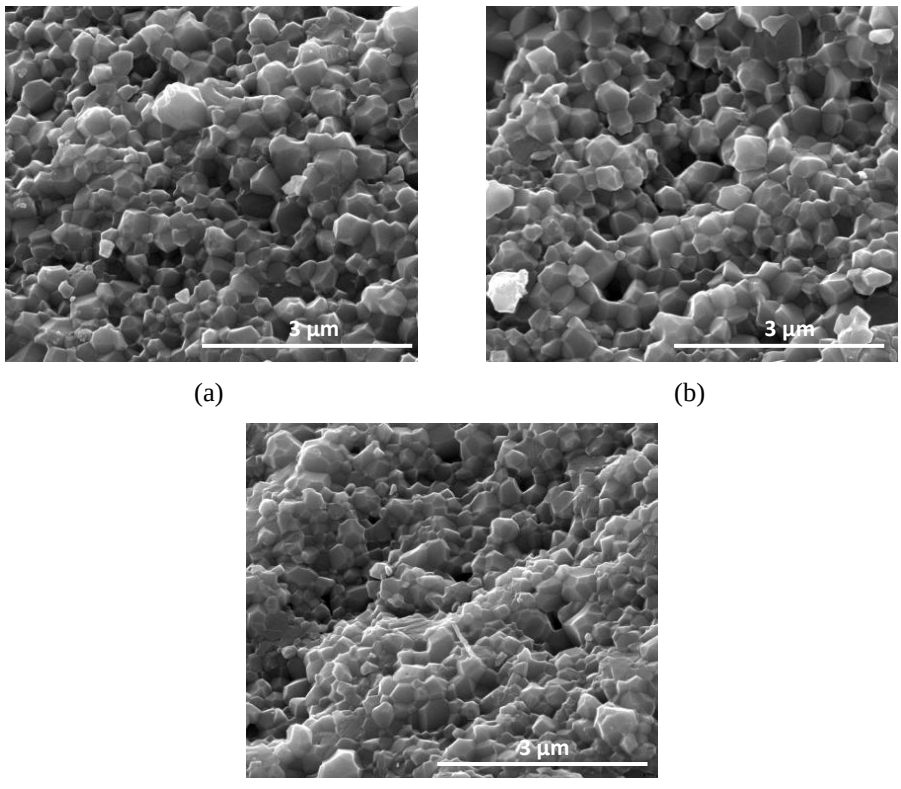

(a) (b)

(c)

Fig.4.14: Fracture surface SEM images of a BNT ceramic sintered at 900 ˚C by SPS (a) before and after annealing at 800 ˚C for (b) 12 h and (c) 24 h. The annealing time does not appear to change the average grain size of the ceramic, which remains at ~350 nm.

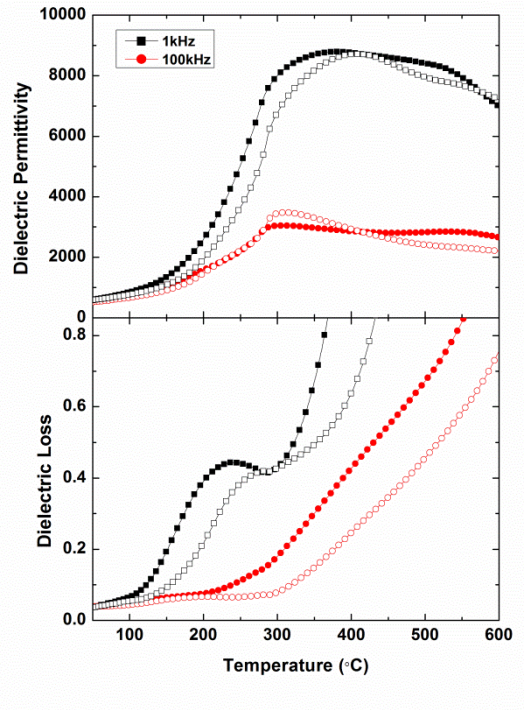

Fig.4.15: Temperature dependence of the dielectric response for the SPS ceramic sintered at 950 ˚C after annealing for 24 h at 850 ˚C (solid symbols) and 950 ˚C (open symbols). Higher temperature annealing helps to reduce the effect of point defects, particularly in the low frequency data.

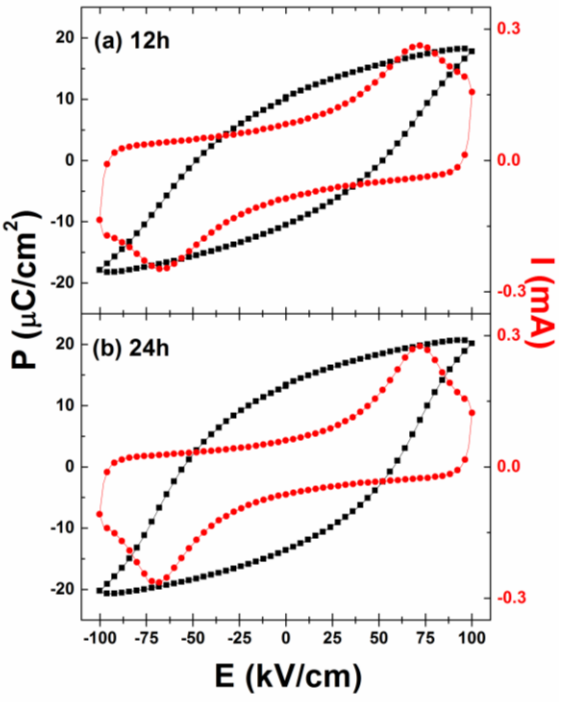

Fig.4.16: P-I-E loops of a BNT ceramic sintered at 900 ˚C by SPS after annealing at 800 ˚C for (a) 12 h and (b) 24 h.

(ii) Conventional Sintering

Conventional sintering was used to prepare ceramics with micrometre sized grains. High temperatures combined with slow sintering rates provide optimum conditions for large grain growth. Green bodies pressed from the regular ball-milled powder were sintered for 2 h in air using a conventional furnace with a slow heating rate of 3 ˚C/min. As this is a pressurless sintering technique, particular attention was given to preparing high quality, well-compacted green bodies. Initially, the SPS was used to press the powders into discs for 5 mins at 850 ˚C/50 MPa (ρ = 88 %) before high temperature sintering was carried out using the conventional furnace. Despite the large grain size (>5 μm), the density of ceramics prepared using this method were poor. Large voids were imaged in these ceramics using SEM (Fig.4.17). The temperatures required for large scale grain growth are thought to be too high for the pre-sintered disc, resulting in oversintering. Low temperatures could be applied during the second stage however a much longer sintering time would be required for adequate grain growth. Rather than using the SPS to press the green bodies, 1 % PEG 10k binder was added to the powder during the last 5 minutes of ball-milling so that disc could be prepared manually by cold pressing. A binder is traditionally added as it increases the fluidity of the powder while improving the mechanical strength of the green body. The binder was then burned out before sintering by heating the disc very slowly at 1 ˚C/min to 800 ˚C for 1 h. Ceramics prepared from these green bodies, however, appeared misshapen after sintering. Despite adding the binder during the final stage of ball-milling, the solution may not have been mixed homogenously throughout the slurry and may have separated from the powder during drying. Alternately, the binder may have been too dense. Consequently, the binder is believed to have left large vacancies within the green bodies causing the ceramic discs to become deformed during sintering. The cohesive nature of the BNT powder nevertheless allowed for further green bodies to be pressed without the need for binder.

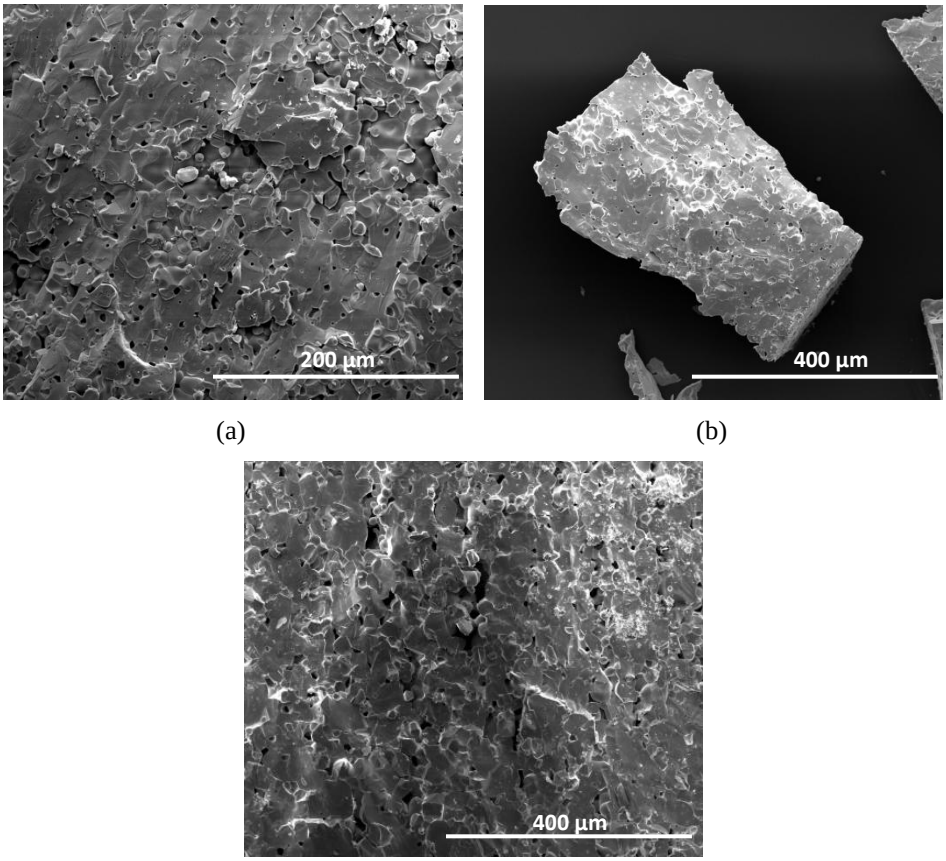

(a) (b)

(c)

Fig.4.17: SEM micrographs of conventionally sintered BNT ceramics using green bodies prepared by SPS. The sintering temperature and density of each ceramic: (a) 1150 ˚C ρ= 93 %, (b) 1200 ˚C ρ = 89 % and (c) 1250 ˚C ρ = 89 %. The images presented here only qualitatively demonstrate the high level of porosity in these ceramics.

4.1.6 Determining the Sintering Temperature

Information from the SPS output profile while sintering under minimum pressure was used to help determine the sintering temperature of the BNT powders. During sintering, the piston speed will increase as the powder begins to densify with increasing temperature. Densification occurs when there is no further shrinkage of the sample and the piston speed returns to zero. This temperature can be lowered by increasing the pressure applied during sintering. To preserve the grain size of the high-speed ball milled and chemically prepared powders, pressures of up to 500 MPa were reached. To ensure homogeneity throughout the ceramic, the sintering temperature was held constant for 5 minutes. A longer holding time of 20 minutes was used for high pressure (>100 MPa) sintering to both assist the densification process at low temperature and to take account of the temperature gradient in the large graphite die. Instead of using the pyrometer to monitor the temperature during high pressure sintering, a thermocouple

was inserted into the thicker die to ensure a more accurate temperature reading. For grain growth by SPS, temperatures higher than the minimum densification temperature were applied. However, a loss of vacuum was observed during sintering at 1000 ˚C, shown in Fig.4.18. Evidence of oxygen vacancies were observed in the electrical properties of the ceramics sintered at and above this temperature, in particular, the non-symmetry of the I-E loops shown in Fig4.19 (c) and (d). These vacancies are introduced into the composition following the volatilisation of the A-site Bi and Na ions.

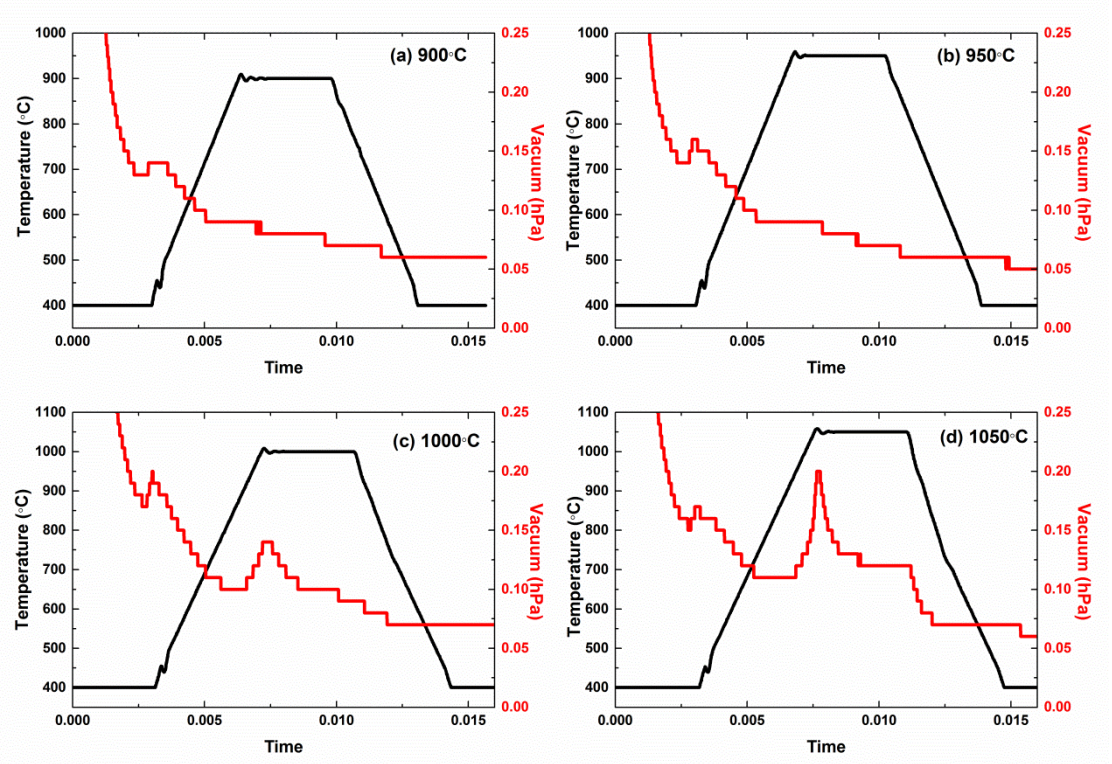

Fig.4.18: SPS sintering profiles for BNT ceramics sintered at (a) 900 ˚C, (b) 950 ˚C, (c)1000 ˚C and (d)1050˚C. A loss of vacuum (>0.1 hPa) occurs during holding (5 minutes) at temperatures higher than 950 ˚C. The full pressure of 50 MPa is applied on heating at 450 ˚C.

A minimum temperature 100 ˚C above the ‘pressureless’ SPS sintering temperature determined for the regular ball-milled powder was used for conventional sintering. Ceramics were sintered at 50 ˚C intervals above this temperature and their densities were compared. The density of the ceramics increases with increasing temperature, reaching a maximum value at 1175 ˚C, where the density then decreases. Melting occurred at 1250 ˚C. Unlike SPS, no evidence of oxygen vacancies were observed in the electrical properties of the conventional sintered ceramics.

The dependence of ceramic density on the sintering temperature for the SPS and conventional sintering techniques is shown in Fig.4.20.

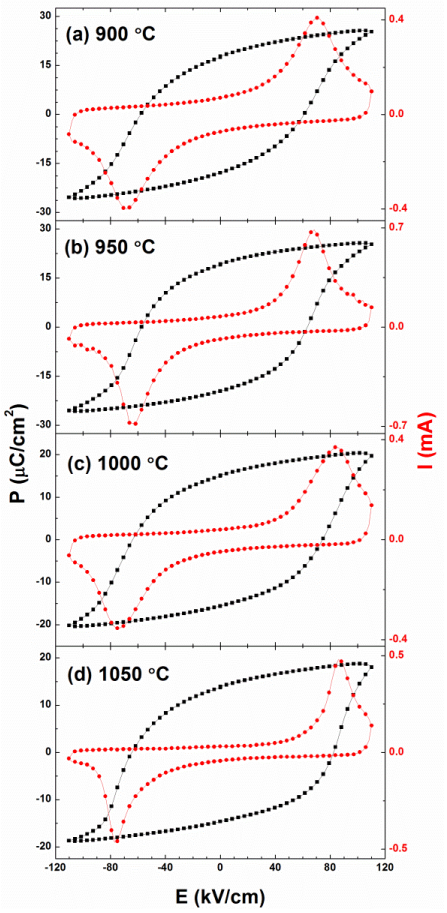

Fig.4.19: P-I-E loops of the BNT ceramics sintered by SPS at (a) 900 ˚C, (b) 950 ˚C, (c) 1000 ˚C and (d) 1050 ˚C, for 5 minutes at a pressure of 50 MPa. The non-symmetric I-E loops in (c) and (d) provide evidence of oxygen vacancies.

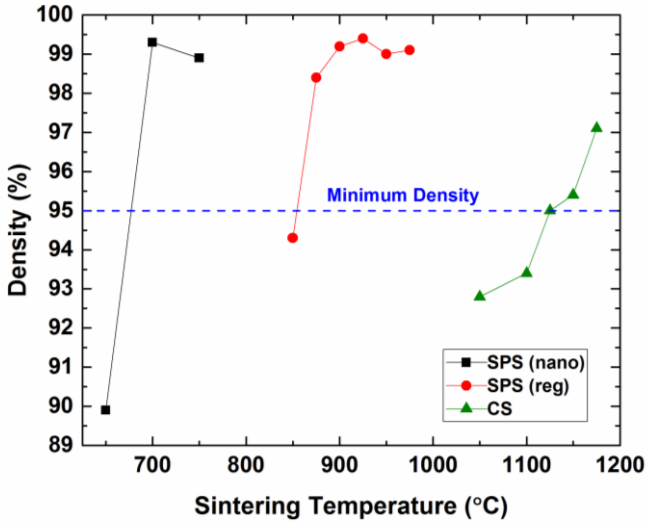

Fig.4.20: Density vs. temperature diagram for the BNT ceramics sintered using SPS and conventional sintering (CS) techniques using chemically prepared (nano) and regular ball-milled (reg) powders.

4.1.7 Determining the Grain Size

An estimate of the average grain size, taken from the SEM images of the natural surface of the conventionally sintered ceramics and the fracture surface of the annealed SPS ceramics, shown in Fig.4.21-4.23, are summarised in Fig.4.24. The grain size of the ceramic sintered at 950 ˚C is larger than the ceramic sintered at 975 ˚C. The true sintering temperature of the larger grain ceramic is thought to be higher than the temperature measured by the pyrometer in the SPS. For an accurate temperature reading, the pyrometer should be cleaned regularly. In this case, the pyrometer was not cleaned before sintering distorting the temperature reading.

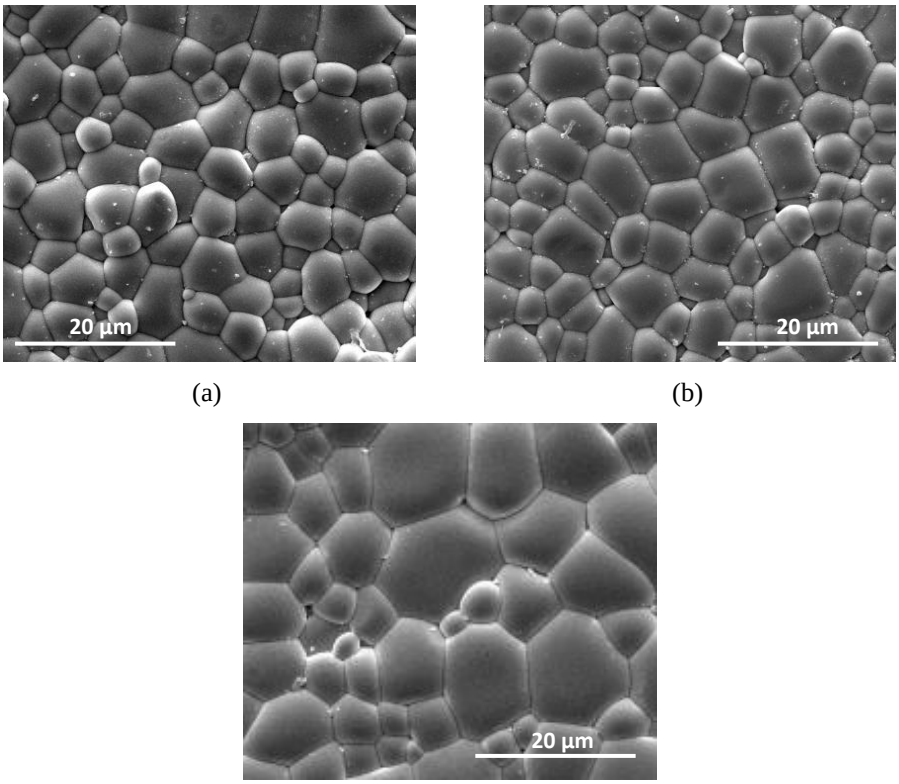

(a) (b)

(c)

Fig.4.21: SEM micrographs of the natural surface BNT ceramics sintered at (a) 1125 ˚C, (b) 1150 ˚C and (c) 1175 ˚C for 2 h using a conventional furnace.

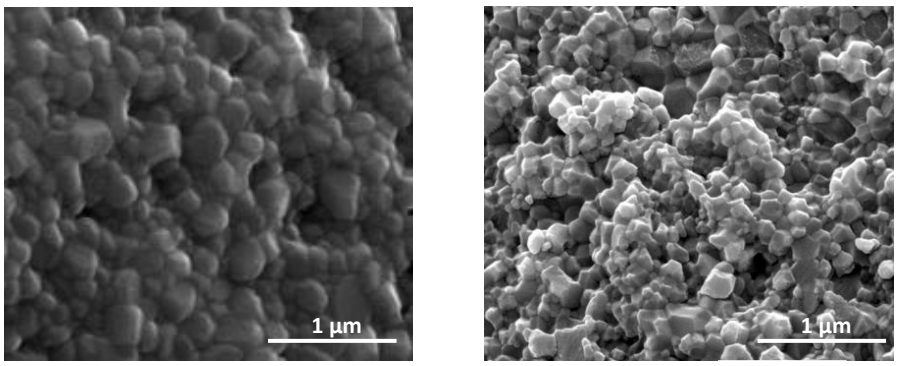

(a) (b)

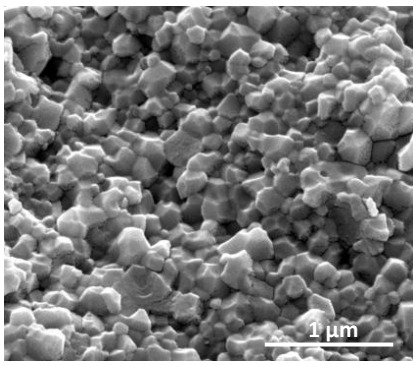

(c)

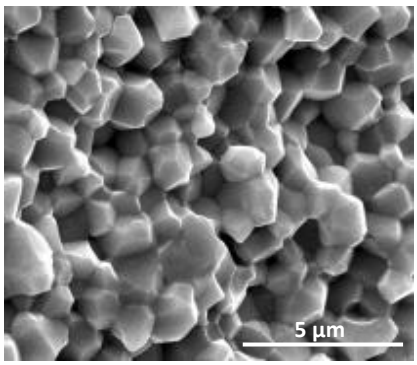

(d)

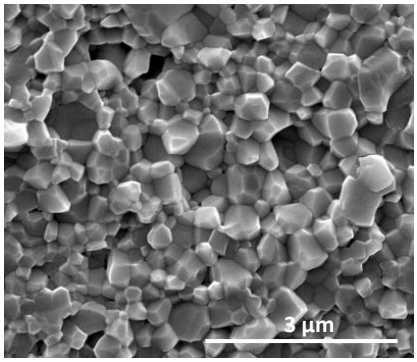

(e)

Fig.4.22: Fracture surface SEM images of SPS BNT ceramics sintered at (a) 850 ˚C/100 MPa, (b) 900 ˚C/100 MPa, (c) 925 ˚C/80 MPa, (d) 950 ˚C/50 MPa and (e) 975 ˚C/50 MPa for 5 mins with regular ball milled powder.

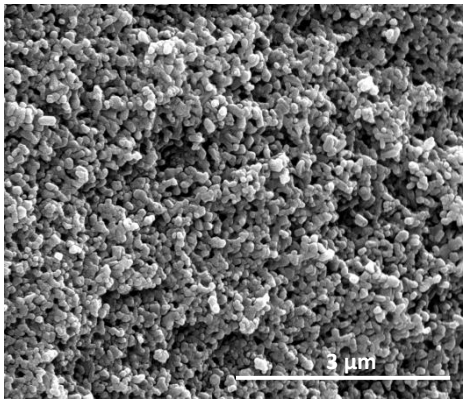

(a)

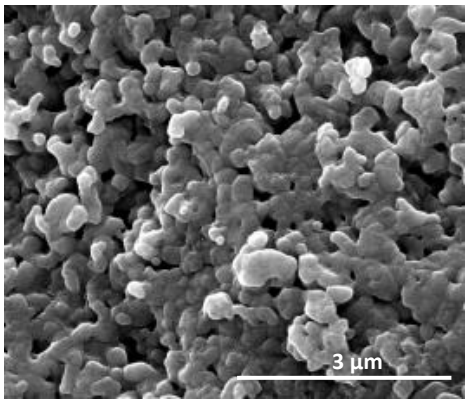

(b)

Fig.4.23: SEM images of the fracture surface of high pressure SPS-ed BNT ceramics sintered at (a) 700 ˚C/450 MPa and (b) 750 ˚C/350 MPa for 20 mins with chemically prepared powder.

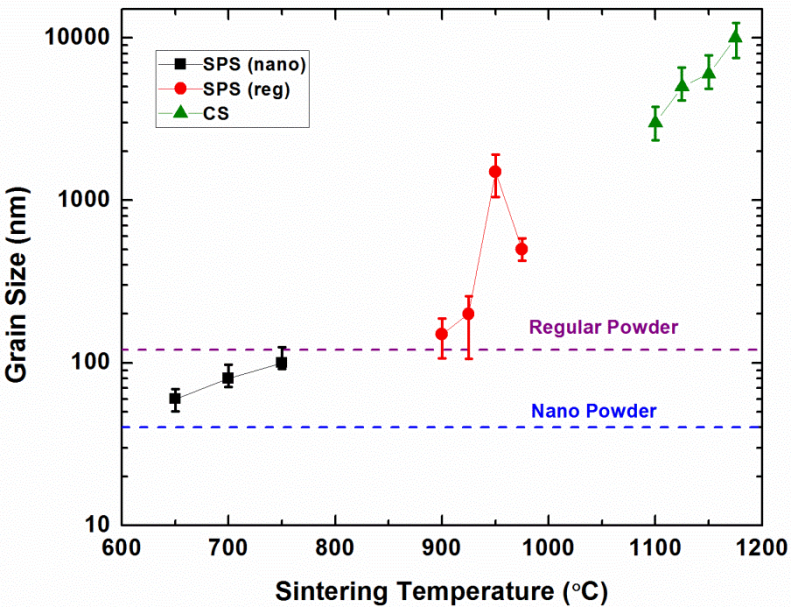

Fig.4.24: Grain size vs. temperature diagram for the BNT ceramics sintered using SPS and conventional sintering (CS) techniques. The average grain size of the regular ball-milled powder and the chemically prepared nanograin powder is marked by the dashed lines.

For structural and physical property analysis, two-three high density (>95 %) BNT ceramics were selected from each of the following grain size ranges: (i)10 nm-100 nm, (ii)100 nm- 1 µm and (iii) greater than1 µm. The processing conditions used to prepare these ceramics are summarised in Table 4.1. The sintering profiles of selected ceramics prepared using SPS are shown in Fig.4.25.

Table 4.1: Sintering conditions used to prepare selected BNT ceramics. F_{max}: temperature at which maximum force is applied.

Powder	**Sintering Method**	**Sintering Conditions** *Temperature/Duration/Pressure /Heating Rate*	**Annealing Conditions**	**Density**	**Average Grain Size**
Regular Ball-Milled	CS	1175 ˚C, 2 h, 3 ˚C/min	n/a	97.1 %	10 µm
Regular Ball-Milled	SPS	950 ˚C, 5 min, 50 MPa, 100 ˚C/min *(F_{max}= 650 ˚C)*	950 ˚C/24 h	99 %	1.5 µm
Regular Ball-Milled	SPS	975 ˚C, 5 min, 50 MPa, 100 ˚C/min *(F_{max}= 650 ˚C)*	875 ˚C/24 h	99.1 %	500 nm
Regular Ball-Milled	SPS	900 ˚C, 5 min, 100 MPa, 100 ˚C/min *(F_{max}= 650 ˚C)*	800 ˚C/24 h	99.2 %	150 nm
Sol-gel	SPS	750 ˚C (~760 ˚C), 20 min, 400 MPa, 50 ˚C/min *(F_{max}= 650 ˚C)*	650 ˚C/24 h	98.9 %	100 nm
Sol-gel	SPS	700 ˚C (~725 ˚C), 20 min, 450 MPa, 50 ˚C/min *(F_{max}= 650˚C)*	650 ˚C/24 h	99.3 %	80 nm

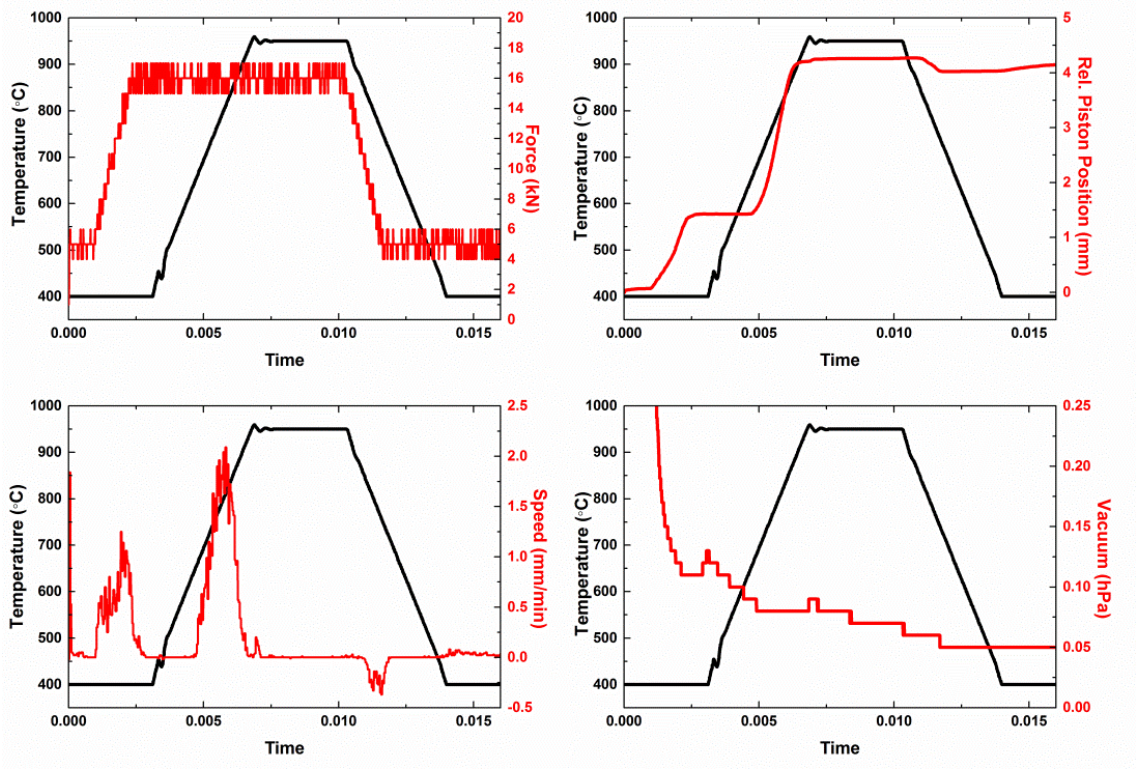

(a)

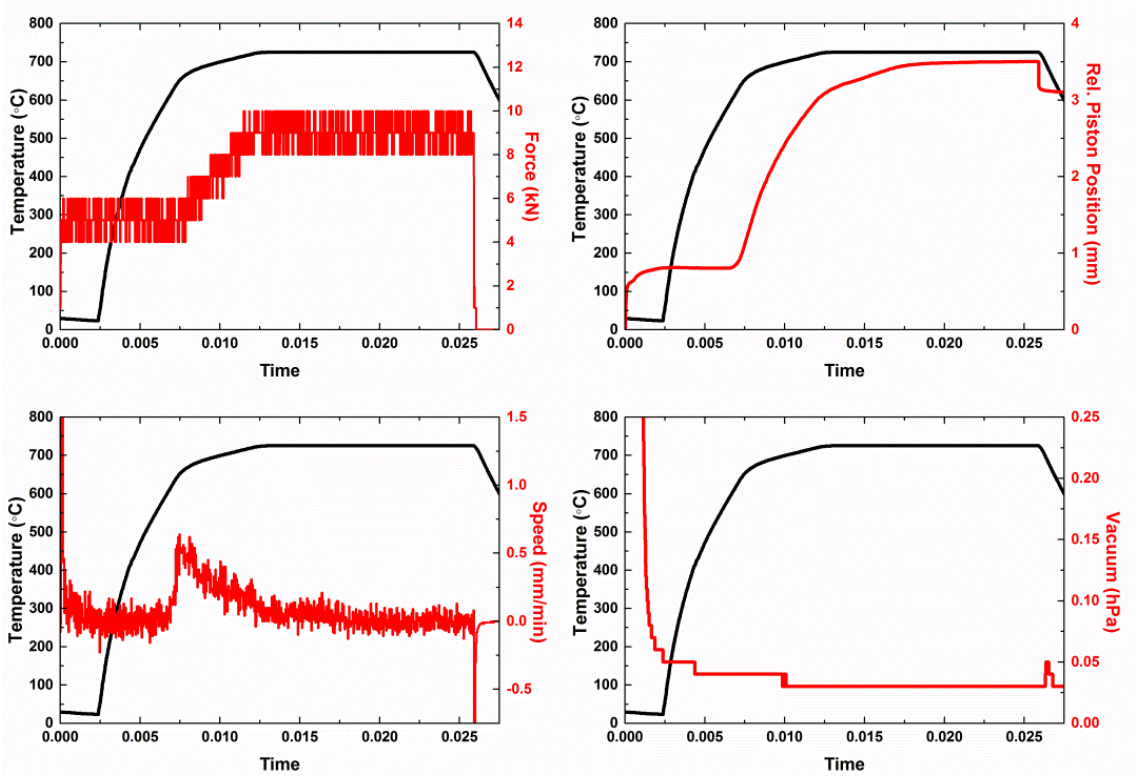

(b)

Fig.4.25: SPS sintering profiles of BNT ceramics with average grain size (a) 500 nm and (b) 80 nm, as summarised in Table 4.1.

4.1.8 Ceramics Prepared from High-Speed Ball-Milled Powder

Prior to obtaining the sol-gel BNT powder, nanograin ceramics were sintered from the high-speed ball-milled powder prepared by milling in de-ionised water for 1 h. The sintering conditions are summarised in Table 4.2, along with the density and grain size of the ceramics. SEM images of the fracture surface are shown in Fig.4.26. Despite the different sintering temperature, the average grain sizes of the ceramics are almost identical. The different permittivity values (Fig.4.27) and P_{sa} values (Fig.4.28) measured for these ceramics are thought to result from the lower density recorded for the 700 ˚C sintered ceramic. In general, the dielectric response measured for these ceramics is greatly suppressed, the permittivity peak T_m is very broad and no feature associated with T_s previously reported in the literature could be determined. The P-I-E loops show no evidence of domain switching and appear paraelectric in nature (Fig.4.28). However, a d_{33} value of 0.6 pN was measured in the 750 ˚C sintered ceramic after poling in a 65 kV/cm electric field for 5 minutes. Initially, the ZrO_2 impurity was thought to form a coating around the grains suppressing their FE properties. However, similar results were obtained for nanograin ceramics sintered from the chemically prepared powder, as demonstrated in Fig.4.29. The grain sizes of the sol-gel ceramics sintered at 700 ˚C and 750 ˚C are 80 nm and 100 nm, respectively. Although the suppression of the FE behaviour is an effect of grain size, the lower permittivity value observed for the 750 ˚C sintered high-speed ball-milled ceramic is still thought to be caused by the ZrO_2 contamination.

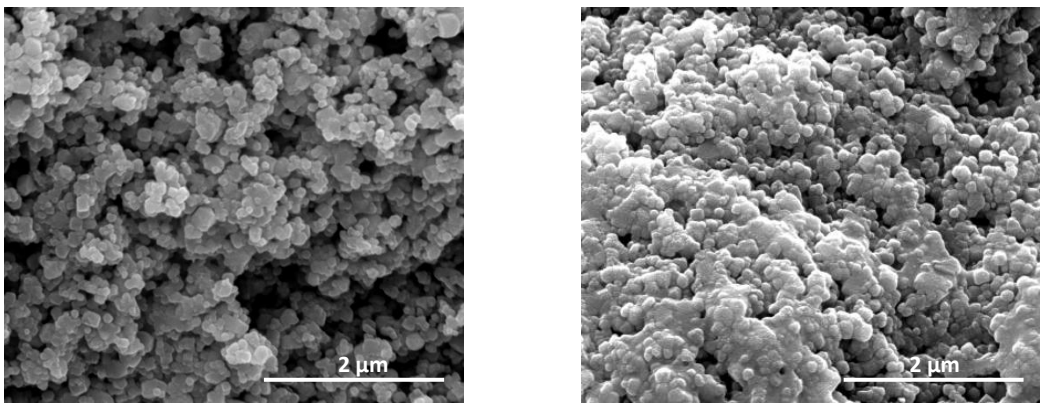

(a) (b)

Fig.4.26: Fracture surface SEM images of high pressure SPS-ed BNT ceramics sintered at (a) 700 ˚C/500 MPa and (b) 750 ˚C/500 MPa for 20 mins with high-speed ball milled powder.

Table 4.2: Sintering conditions used to prepare high-speed ball-milled BNT ceramics. F_{max}: temperature at which maximum force is applied.

Sintering Method	**Sintering Conditions** *Temperature/Duration/Pressure/Heating Rate*	**Annealing Conditions**	**Average Grain Size**	**Density**
SPS	750 ˚C, 20 min, 500 MPa, 50 ˚C/min *(F_{max}= 650 ˚C)*	650 ˚C/24 h	100 nm	98 %
SPS	700 ˚C, 20 min, 500 MPa, 50 ˚C/min *(F_{max}= 650 ˚C)*	650 ˚C/24 h	100 nm	94.5 %

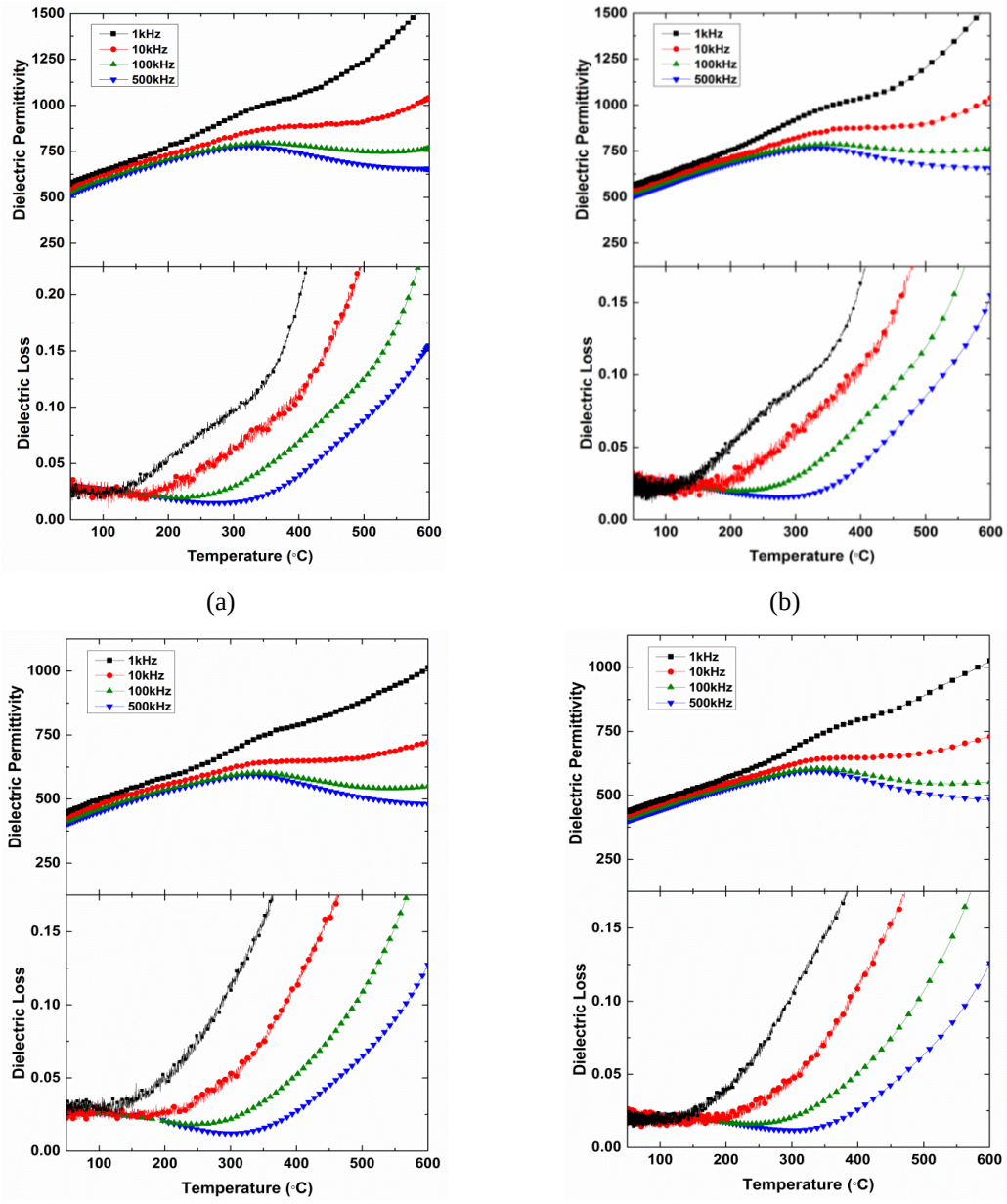

Fig.4.27: Temperature dependence of the dielectric response of the high-speed ball-milled ceramics sintered at (a), (b) 700 ˚C and (c), (d) 750 ˚C. Measured during (a), (c) heating and (b), (d) cooling at 1, 10, 100 and 500 kHz.

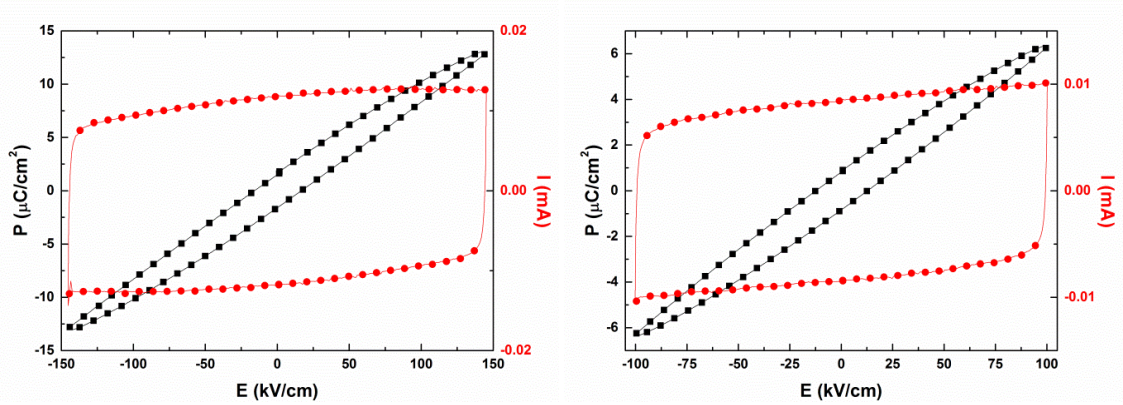

(a) (b)

Fig.4.28: Room temperature P-I-E loops measured at 10 Hz for the (a) 700 ˚C and (b) 750 ˚C sintered high-speed ball-milled ceramics.

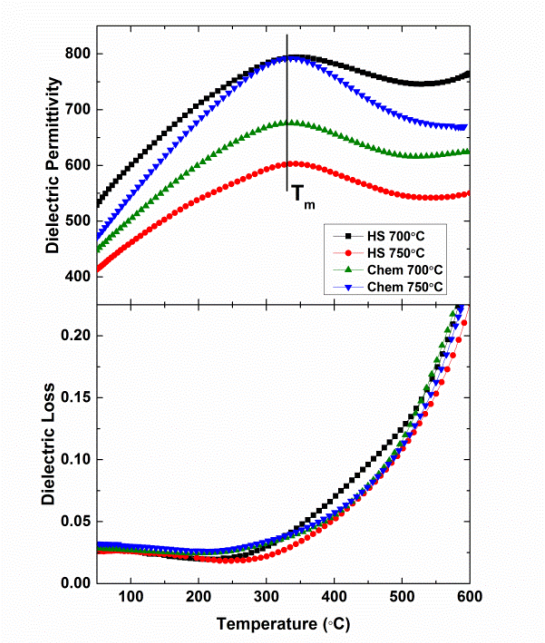

Fig.4.29: Dielectric response measured at 10 Hz of the nanograin ceramics sintered using high-speed ball-milled (HS) and sol-gel (Chem) BNT powders.

4.2 Results

4.2.1 High Temperature X-ray Diffraction (XRD)

The high temperature XRD results for the crushed 10 μm grain size BNT in its unpoled and poled states are shown in Fig.4.30 and Fig.4.31, respectively. Only the angular range demonstrating the evolution of the $(110)_{pc}$, $(111)_{pc}$, $(200)_{pc}$ and $(211)_{pc}$ Bragg reflections as a function of temperature are given. Every reflection appears twice due to the presence of the $K\alpha_2$ component in the incident beam, as noted for the poled 10 μm ceramic in Fig.4.31(a). The temperature dependent XRD patterns collected for the 1.5 μm, 500 nm and 150 nm ceramics are given in the Appendix (Fig.7.1.1 - Fig.7.1.3). The XRD data was collect at room temperature, then at 50 ˚C intervals from 100 ˚C to 700 ˚C during heating and cooling. Only the room temperature XRD data was collected for the poled 150 nm (Appendix Fig.7.1.4) and unpoled 80 nm (Appendix Fig.7.1.5) crushed ceramics. A number of different single phases were refined for the XRD data, including *R3c*, *Cc*, *P4bm*, $Pm\bar{3}m$. The lattice parameters of the structure which provided the best fit are listed in Tables 4.3-4.6. Examples demonstrating the Rietveld fit of the XRD patterns at each structural transition are given in the Appendix Fig.7.1.6-Fig.7.1.9. Additional peaks from the Pt holder can be seen in this data. As the powdered sample is heated directly by the Pt holder, only a thin layer was deposited on the plate to reduce the temperature variation across the sample. The splitting of the $(111)_{pc}$ peak observed at room temperature after poling in Appendix Fig.7.1.6, remains as a small shoulder at $2\theta=39.8$ ˚ in the high temperature data Appendix Fig.7.1.9. According to the literature, BNT is cubic at 700 ˚C[111]. This high temperature peak is not related to the crystal structure of the ceramic but from the Pt holder which overlaps with some of the BNT Bragg peaks, shown in Appendix Fig.7.1.10.

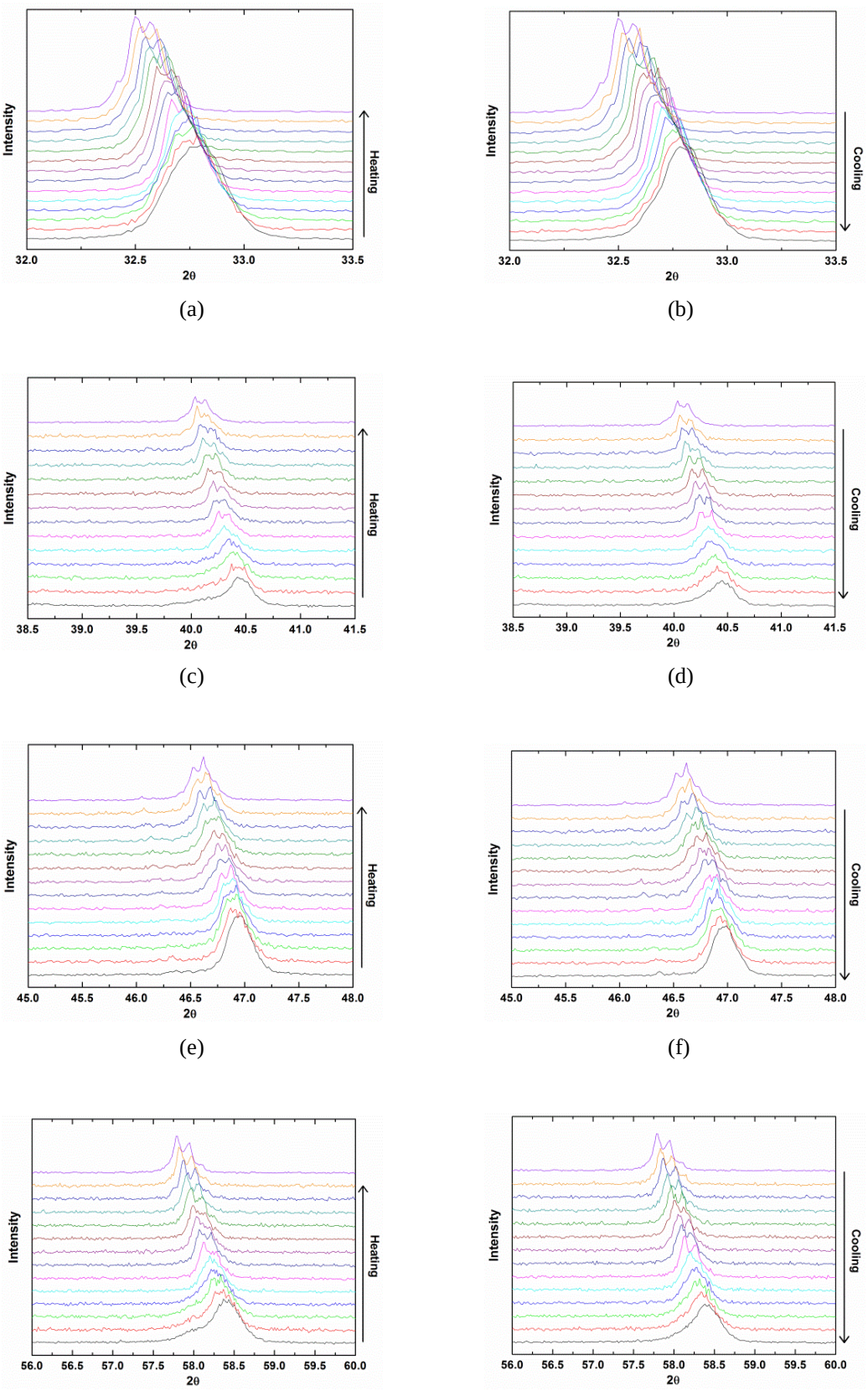

Fig.4.30: Powder XRD profiles of the crushed 10 µm grain size BNT ceramic showing the temperature evolution during heating and cooling of the Bragg reflections: (a)-(b) $(110)_{pc}$, (c)-(d) $(111)_{pc}$, (e)-(f) $(200)_{pc}$ and (g)-(h) $(211)_{pc}$.

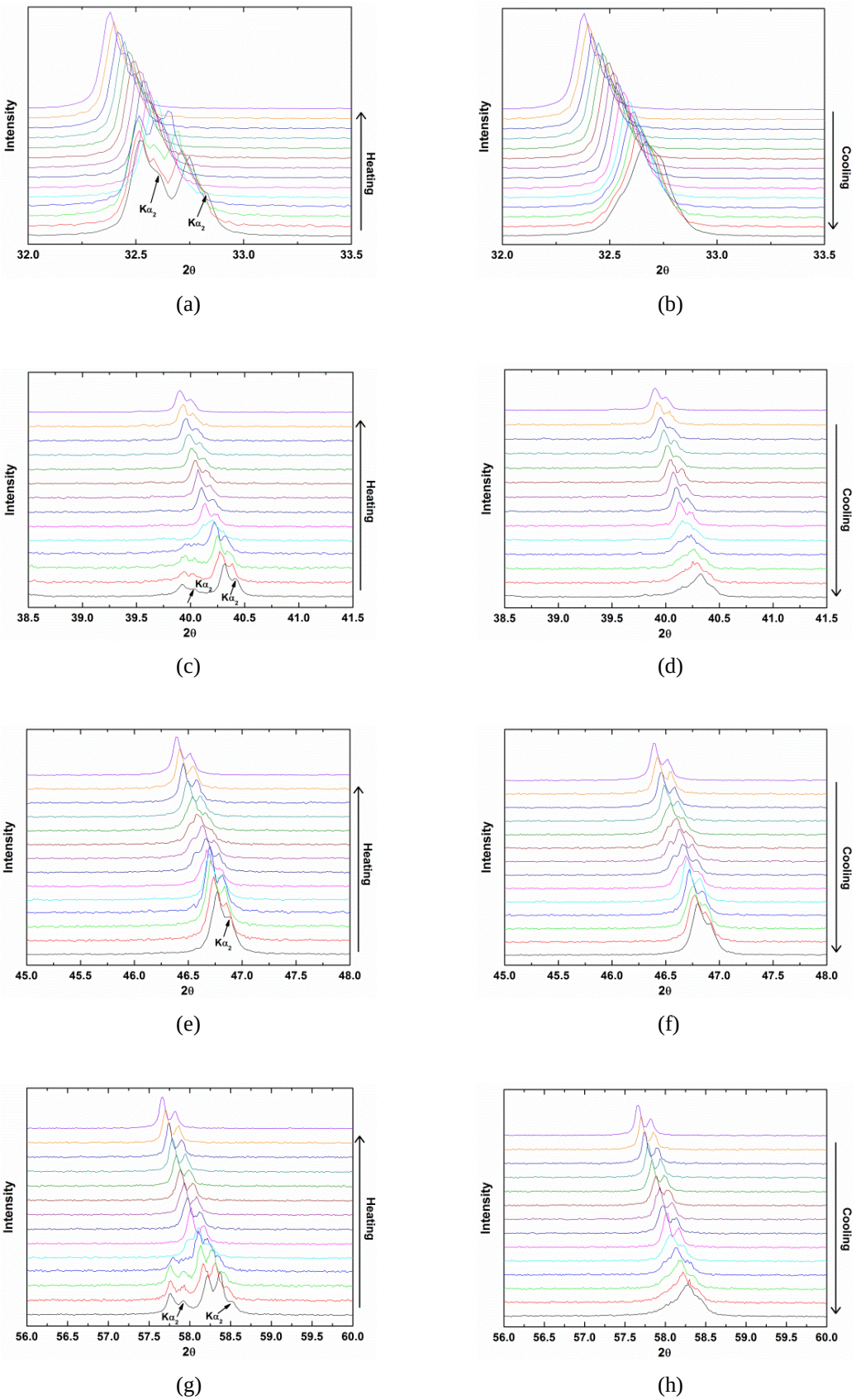

Fig.4.31: Powder XRD profiles of the electrically poled crushed 10 µm grain size BNT ceramic showing the temperature evolution during heating and cooling of the Bragg reflections: (a)-(b) $(110)_{pc}$, (c)-(d) $(111)_{pc}$, (e)-(f) $(200)_{pc}$ and (g)-(h) $(211)_{pc}$. Reflections from the $K\alpha_2$ component from the incident beam are highlighted.

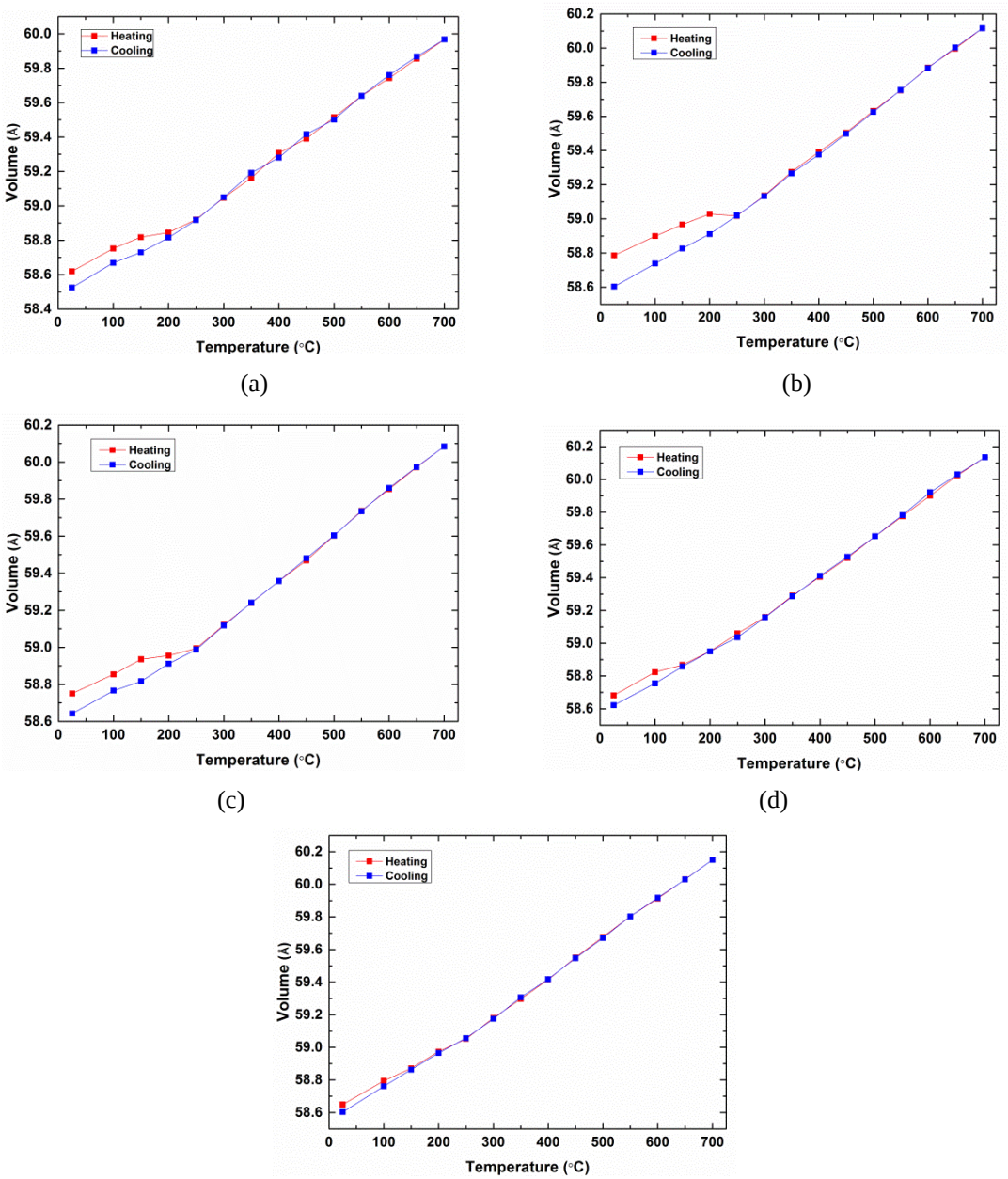

Fig.4.32: Temperature dependence of the normalised cubic unit cell volume, determined by Rietveld refinement, for the crushed (a) 10 µm, (c) 1.5 µm, (d) 500 nm, (e) 150 nm grain size ceramics. (b) shows the change in volume of the 10 µm ceramic after electrical poling. [*R3c*: Z=6, *Cc*: Z=4, *P4bm*: Z=2 and $Pm\bar{3}m$: Z=1.]

The temperature dependence of the normalised volume for each grain size during heating and cooling is shown in Fig.4.32. Below 200 ˚C, the volume of the unit cell on heating and cooling is different for all of the tested ceramics. Mechanical stress induced by crushing clearly has a similar effect on the crystal structure as electrical poling. Although the room temperature structures of the 150 nm and 500 nm grain size ceramics are refined as monoclinic for both heating and cooling runs, the refined volumes are clearly different. A mixed phase of rhombohedral *R3c* and monoclinic *Cc*

symmetries are expected to occur in all of the BNT ceramics at low temperatures, the refined structure only represents the majority phase.

A phase diagram for the grain size dependence in BNT determined by XRD is shown in Fig.4.33.

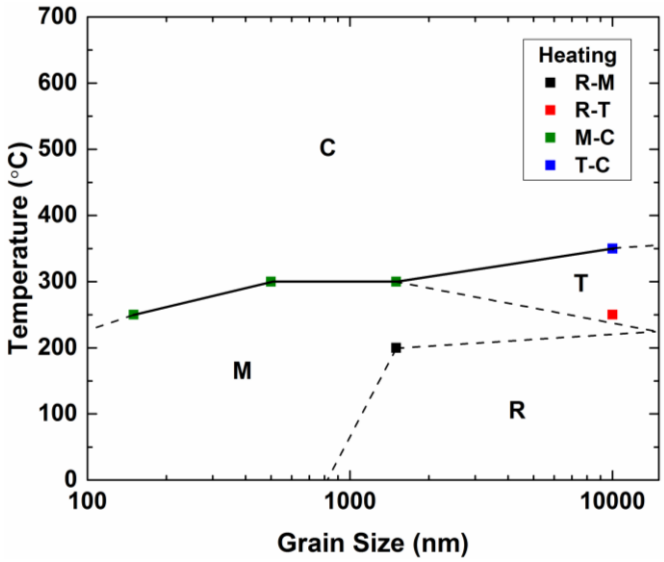

(a)

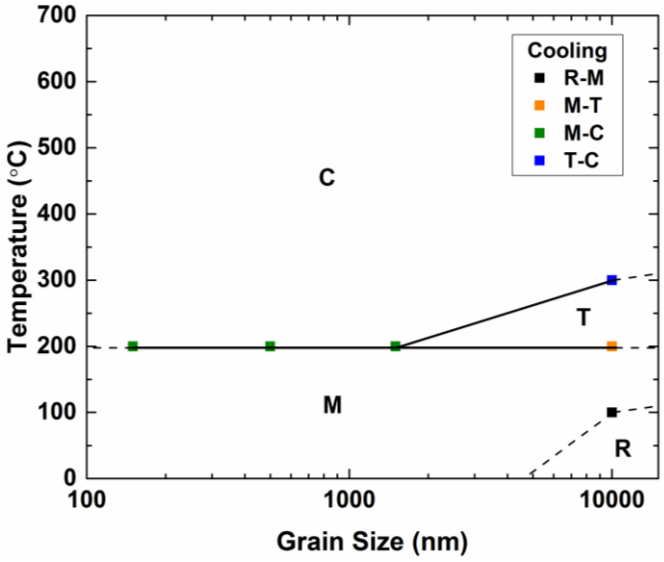

(b)

Fig.4.33: Structural phase diagram for unpoled BNT on (a) heating and (b) cooling. M: monoclinic *Cc*, R: rhombohedral *R3c*, T: tetragonal *P4bm* and C: cubic $Pm\bar{3}m$. The squares mark the temperatures were a change in structure is observed in the XRD data. The dashed lines are not obtained from structural refinement and only act as a guide.

Table 4.3: Lattice parameters calculated by Rietveld refinement of XRD data collected from crushed 10 μm unpoled and poled BNT ceramics at different temperatures.

Temp. (˚C)	10 μm Structure	10 μm cell				10 μm Poled Structure	10 μm Poled cell			
		a (Å)	*b* (Å)	*c* (Å)	β_m (˚)		*a* (Å)	*b* (Å)	*c* (Å)	β_m (˚)
25	*R3c*	5.4803(2)		13.5221(7)		*R3c*	5.4801(1)		13.5620(3)	
100		5.4859(3)		13.5252(12)			5.4856(1)		13.5609(4)	
150		5.4893(3)		13.5235(12)			5.4892(1)		13.5584(4)	
200		5.4933(3)		13.5100(14)			5.4943(1)		13.5474(5)	
250	*P4bm*	5.5016(12)		3.8933(19)		*Cc*	9.5362(6)	5.4990(2)	5.5156(2)	125.295(3)
300		5.5046(5)		3.8974(7)		*P4bm*	5.5112(2)		3.8939(2)	
350	$Pm\bar{3}m$	3.8966(2)					5.5107(1)		3.9037(1)	
400		3.8997(2)					5.5144(1)		3.9063(1)	
450		3.9016(2)					5.5183(1)		3.9081(1)	
500		3.9043(2)					5.5230(1)		3.9099(2)	
550		3.9070(2)				$Pm\bar{3}m$	3.9095(1)			
600		3.9093(2)					3.9124(1)			
650		3.9117(2)					3.9148(1)			
700		3.9142(1)					3.9174(1)			
650		3.9120(2)					3.9149(1)			
600		3.9096(2)					3.9123(1)			
550		3.9070(2)					3.9095(1)			
500		3.9040(2)				*P4bm*	5.5267(2)		3.9042(2)	
450		3.9021(2)					5.5234(2)		3.9005(2)	
400		3.8991(2)					5.5197(2)		3.8977(2)	
350		3.8972(2)					5.5163(2)		3.8953(2)	
300	*P4bm*	5.5034(4)		3.8993(5)			5.5118(2)		3.8929(2)	
250		5.5019(11)		3.8927(16)		*Cc*	9.5388(1)	5.5010(3)	5.5130(3)	125.307(8)
200	*Cc*	9.5242(31)	5.4918(13)	5.5084(14)	125.259(20)		9.5383(7)	5.4944(3)	5.5140(3)	125.367(4)
150		9.5134(18)	5.4884(7)	5.5115(7)	125.281(9)		9.5350(8)	5.4901(3)	5.5138(3)	125.389(4)
100	*R3c*	5.4872(3)		13.4995(14)			9.5346(7)	5.4851(4)	5.5134(4)	125.427(4)
25		5.4810(2)		13.4970(8)			9.5319(6)	5.4794(3)	5.5112(3)	125.473(3)

Table 4.4: Lattice parameters calculated by Rietveld refinement of XRD data collected from crushed 1.5 μm and 500 nm BNT ceramics at different temperatures.

		1.5 μm					500 nm			
Temp.	Structure	cell				Structure	cell			
(˚C)		*a* (Å)	*b* (Å)	*c* (Å)	β_m (˚)		*a* (Å)	*b* (Å)	*c* (Å)	β_m (˚)
25	*R3c*	5.4822(2)		13.5433(5)		*Cc*	9.5022(8)	5.4822(4)	5.5161(4)	125.228(3)
100		5.4872(3)		13.5426(9)			9.5132(11)	5.4876(5)	5.5184(5)	125.240(5)
150		5.4911(2)		13.5421(8)			9.5172(11)	5.4919(5)	5.5165(5)	125.249(6)
200	*Cc*	9.5221(9)	5.4926(4)	5.5187(4)	125.211(4)		9.5265(13)	5.4967(6)	5.5154(6)	125.267(7)
250		9.5331(7)	5.4989(3)	5.5141(3)	125.278(4)		9.5345(12)	5.5021(5)	5.5157(5)	125.269(7)
300	$Pm\bar{3}m$	3.8957(1)				$Pm\bar{3}m$	3.8965(1)			
350		3.8983(1)					3.8994(1)			
400		3.9009(1)					3.9019(1)			
450		3.9033(1)					3.9044(1)			
500		3.9062(1)					3.9073(1)			
550		3.9091(1)					3.9100(1)			
600		3.9117(1)					3.9127(1)			
650		3.9142(1)					3.9154(1)			
700		3.9167(0)					3.9178(1)			
650		3.9143(1)					3.9155(1)			
600		3.9118(1)					3.9131(1)			
550		3.9091(1)					3.9101(1)			
500		3.9062(1)					3.9073(1)			
450		3.9035(1)					3.9046(1)			
400		3.9009(1)					3.9020(1)			
350		3.8983(1)					3.8993(1)			
300		3.8956(1)					3.8965(1)			
250		3.8927(1)					3.8938(1)			
200	*Cc*	9.5274(7)	5.4944(3)	5.5147(3)	125.284(3)	*Cc*	9.5284(11)	5.4982(5)	5.5138(5)	125.282(6)
150		9.5179(8)	5.4887(4)	5.5156(4)	125.264(4)		9.5220(11)	5.4929(5)	5.5140(5)	125.281(6)
100		9.5105(8)	5.4855(4)	5.5164(4)	125.235(4)		9.5153(11)	5.4888(5)	5.5122(5)	125.278(5)
25		9.4999(6)	5.4801(3)	5.5147(3)	125.210(3)		9.5043(7)	5.4835(3)	5.5104(3)	125.263(3)

Table 4.5 Lattice parameters calculated by Rietveld refinement of XRD data collected from crushed 150 nm unpoled and poled BNT ceramics at different temperatures.

Temp. (˚C)	Structure	150 nm cell				Structure	150 nm Poled cell				
		a (Å)	b (Å)	c (Å)	β_m (˚)		a (Å)	b (Å)	c (Å)	V_C (Å^3)	β_m (˚)
25	*Cc*	9.5086(10)	5.4852(4)	5.5104(4)	125.287(5)	*Cc*	9.5072(8)	5.4843(3)	5.5094(3)	58.6265(40)	125.279(4)
100		9.5180(14)	5.4911(6)	5.5113(6)	125.267(8)						
150		9.5252(14)	5.4944(5)	5.5132(5)	125.299(8)						
200		9.5332(16)	5.4995(5)	5.5131(5)	125.299(10)						
250	$Pm\bar{3}m$	3.8941(1)									
300		3.8969(1)									
350		3.8995(1)									
400		3.9021(1)									
450		3.9051(1)									
500		3.9078(1)									
550		3.9106(1)									
600		3.9130(1)									
650		3.9155(1)									
700		3.9181(1)									
650		3.9155(1)									
600		3.9131(1)									
550		3.9106(1)									
500		3.9077(1)									
450		3.9050(1)									
400		3.9022(1)									
350		3.8997(1)									
300		3.8969(1)									
250		3.8942(1)									
200	*Cc*	9.5299(15)	5.5008(6)	5.5107(7)	125.270(9)						
150		9.5254(16)	5.4958(5)	5.5108(5)	125.297(9)						
100		9.5183(15)	5.4921(5)	5.5085(5)	125.290(8)						
25		9.5047(10)	5.5052(4)	5.4852(5)	125.241(9)						

Table 4.6: Lattice parameters calculated by Rietveld refinement of XRD data collected from crushed nanograin BNT ceramic at room temperature.

Temp. (˚C)	Structure	80 nm cell					wRp
		a (Å)	*b* (Å)	*c* (Å)	V_C (Å^3)	β_m (˚)	
25	*Cc*	9.5498(22)	5.4888(12)	5.4985(15)	58.791(10)	125.321(11)	10.13
	R3c	5.4945(12)		13.4842(62)	58.758(10)		10.17
	Pm$\bar{3}$*m*	3.8875(2)			58.749(9)		10.05

4.2.2 Transmission Electron Microscopy (TEM)

In addition to XRD, TEM analysis was used to further probe the room temperature structure of the nanograin BNT ceramics.

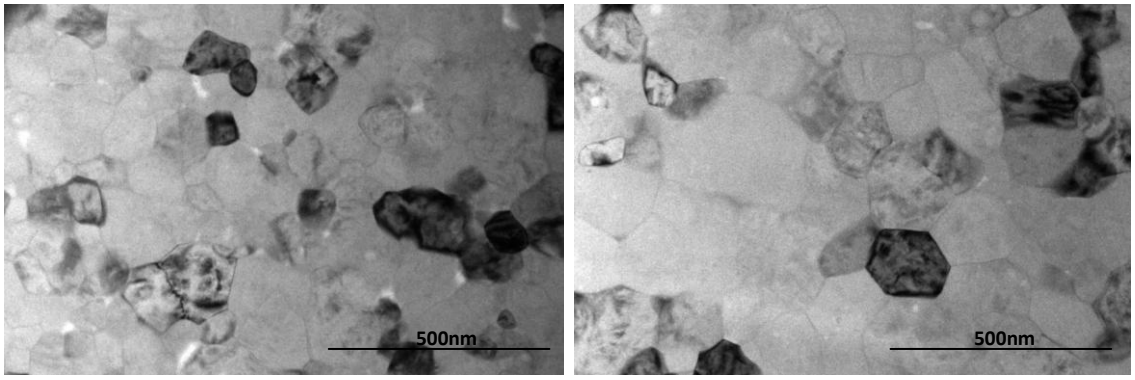

(a) (b)

Fig.4.34: (a)-(b) Bight-field TEM images of the BNT ceramic with an average grain size of 150 nm.

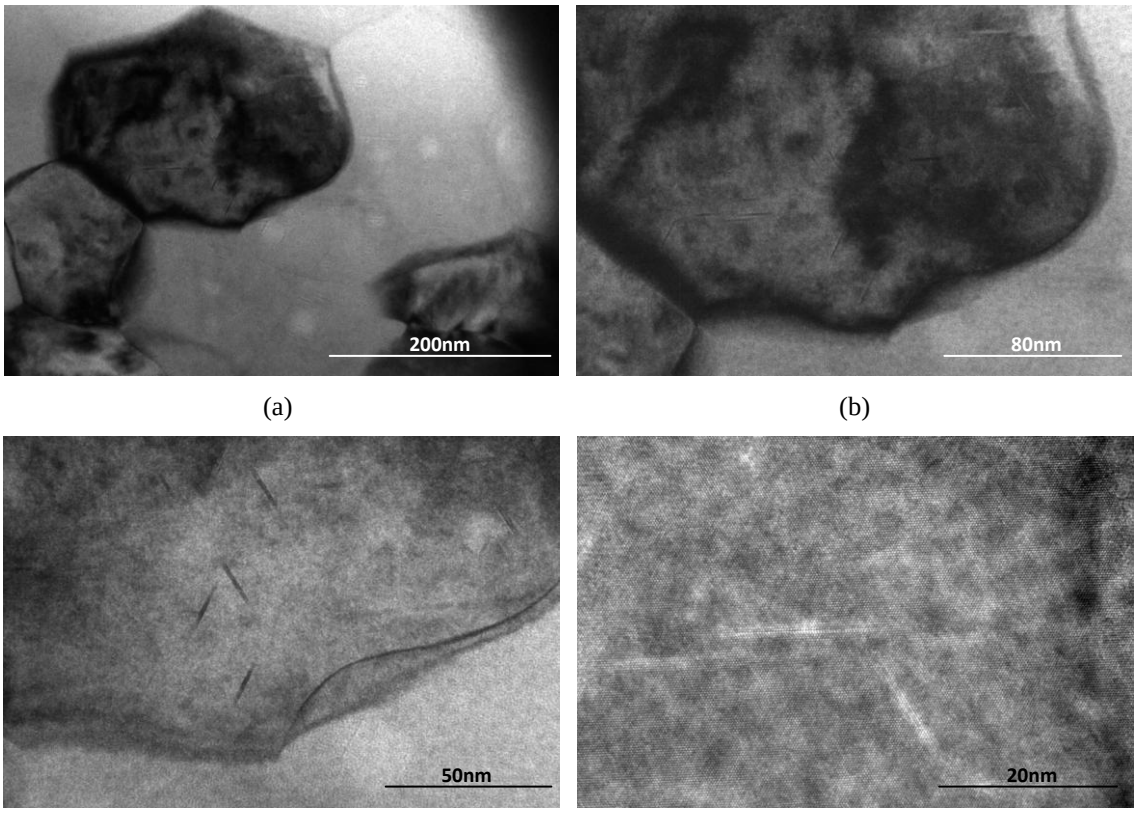

(a) (b)

(c) (d)

Fig.4.35: (a)-(c) Bight-field TEM images of a 250 nm grain with structural defects. A high resolution TEM image of the defects are shown in (d) .

Focused ion-beam machining was used to prepare a thin lamella of the 150 nm ceramic. Although the ceramic was annealed at 600 ˚C for 4 h prior to TEM sample preparation, mechanical stresses induced by the ion-beam machining may still influence the

structure. TEM images of the ceramic are shown in Fig.4.34-4.36. Although no domain walls were observed in the grains, a number of defects ranging from 10-15 nm in length were imaged though out the sample.

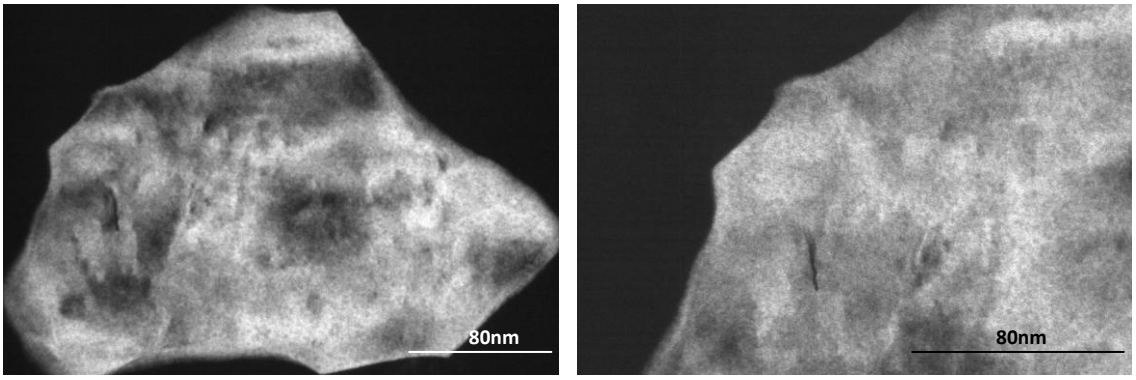

(a) (b)

Fig.4.36: (a)-(b) Dark-field TEM images of a second 250 nm grain showing similar structural defects.

4.2.3 Back-Scattered SEM

Back-scattered SEM images of the BNT ceramics collected at room temperature from the ion-beam polished surfaces are shown in Fig.4.37-4.52. Prior to ion beam polishing, all of the ceramics, except for the electrically poled samples, were annealed for 4 h at 600 ˚C to remove any mechanical stress generated in the ceramics from cutting and grinding. Two different types of domain patterns were imaged by this technique. A complex cross-hatched domain pattern was observed in a majority of the grains in the unpoled 10 μm ceramic, shown in Fig.4.37. Enlarged images showing the fine detail of the cross hatched structure are shown in Fig.4.37 (e2) and (f2). This ceramic also contains grains with a striped domain pattern shown in Fig.4.37(g). A change in domain morphology can clearly be seen in the 10 μm ceramic after electrical poling (Fig.4.38). In this case, the cross-hatch structure is replaced by a striped domain pattern seen in only a minority of the grains in the unpoled state. The domain pattern in these grains is not formed from perfect parallel stripes. Many of the domains do not stretch the length of the grain but instead force to a point randomly with the grain, while other stripes cross one another. No correlation between grain size and domain width could be made due to the complexity of the domain patterns. A cross-hatched domain structure was also imaged in the unpoled 1.5 μm ceramic, shown in Fig.4.39. The domain pattern in these images, however, are not as clear due to the uneven surface topography caused by the pore edges which scatter the Ar ions[239]. Many small pores, not detected in the fracture surface secondary electron SEM images, were observed in this sample. This

may be an effect of the higher temperatures used to anneal this ceramic. No domain patterns were imaged in either of the 500 nm (Fig.4.40) or the 150 nm (Fig.4.42) grain size BNT ceramics. However, a striped domain structure was observed in the 500nm ceramic after electrical poling, shown in Fig.4.41. This domain structure was imaged in grains as small at 200 nm (Fig.4.41(f)).

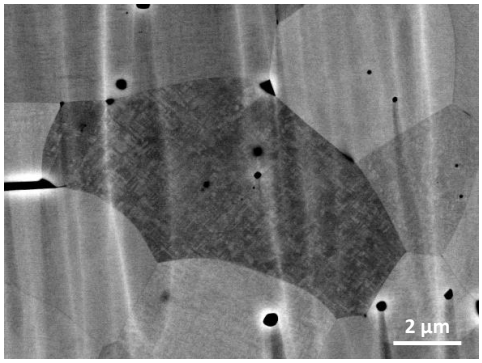

(a)

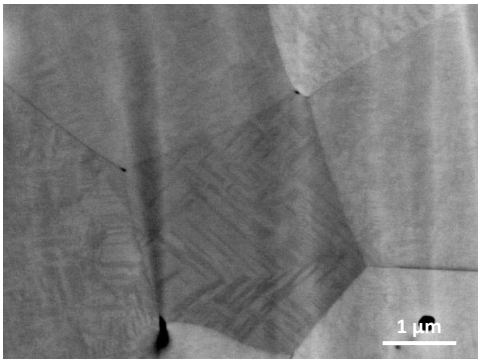

(b)

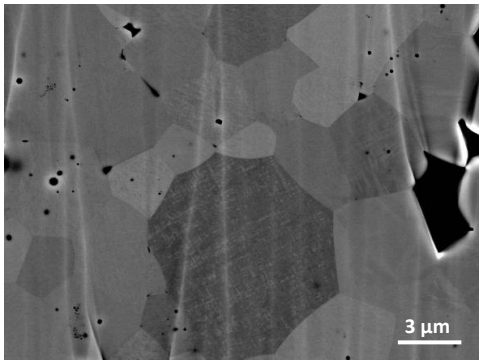

(c)

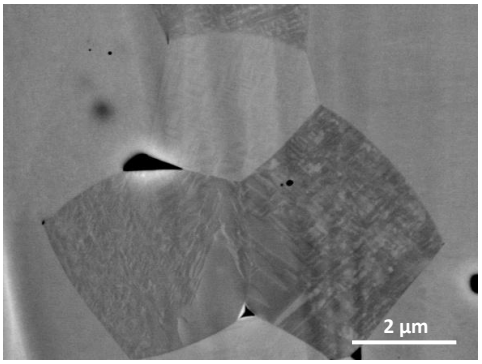

(d)

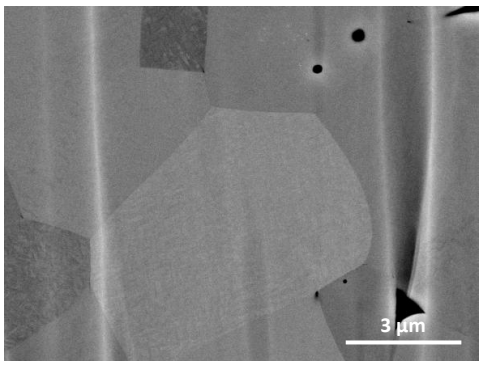

(e1)

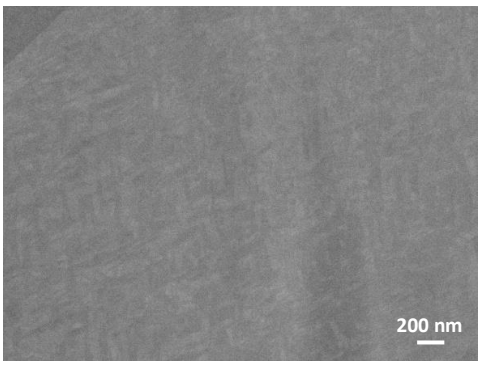

(e2)

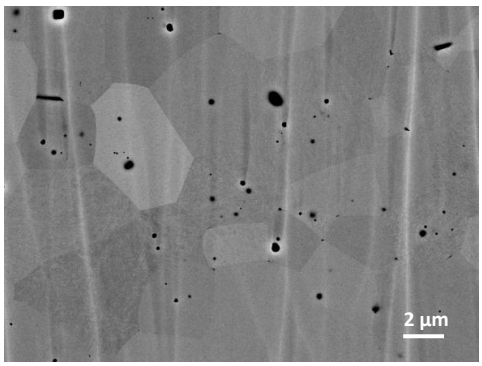

(f1)

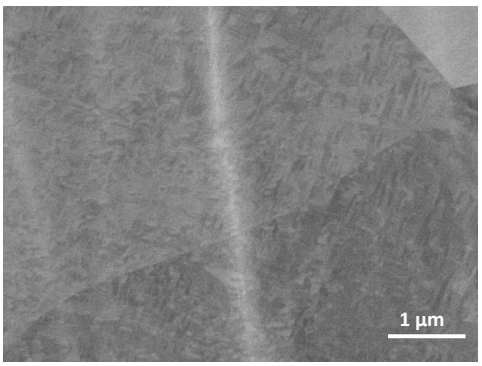

(f2)

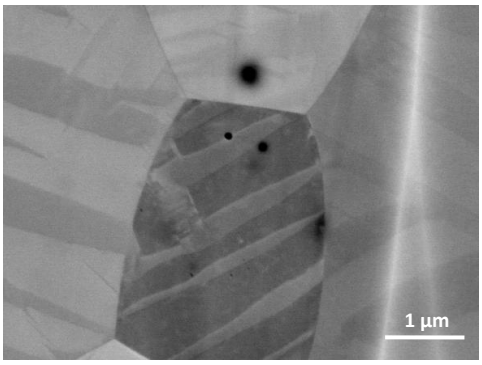

(g)

Fig.4.37: Back-scattered SEM images of the BNT ceramic with an average grain size of 10 µm. (a)-(g) Shows examples of grains containing (a)-(f) cross-hatch and (g) striped domain morphology. (e2) and (f2) are magnified areas of the domain structure shown in (e1) and (f1), respectivly.

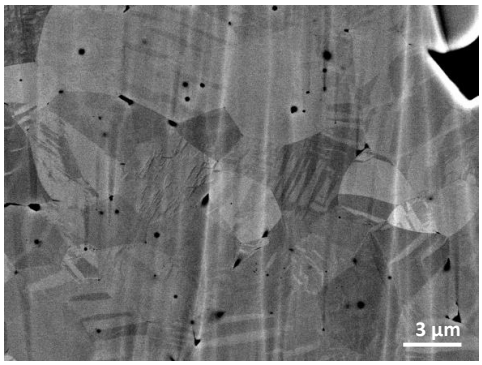

(a)

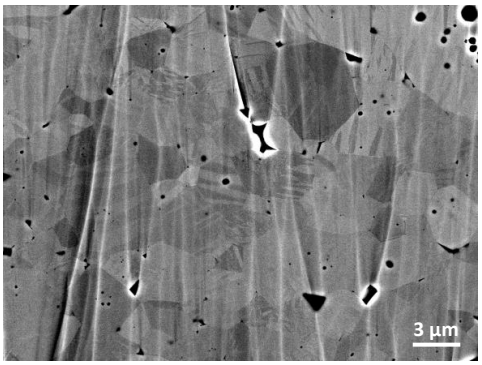

(b)

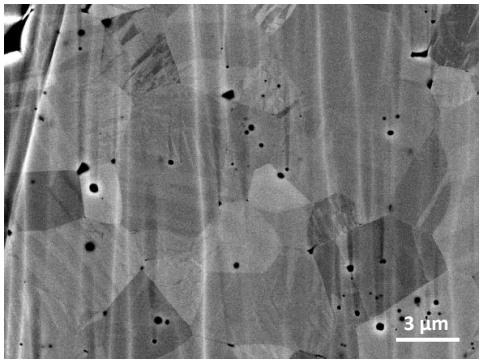

(c)

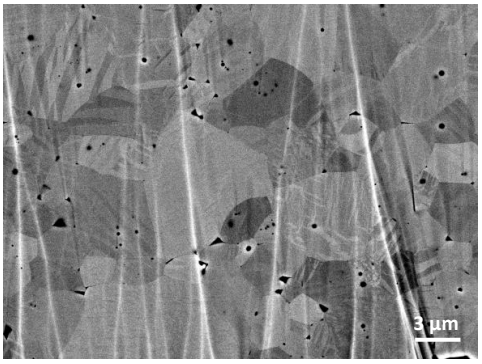

(d)

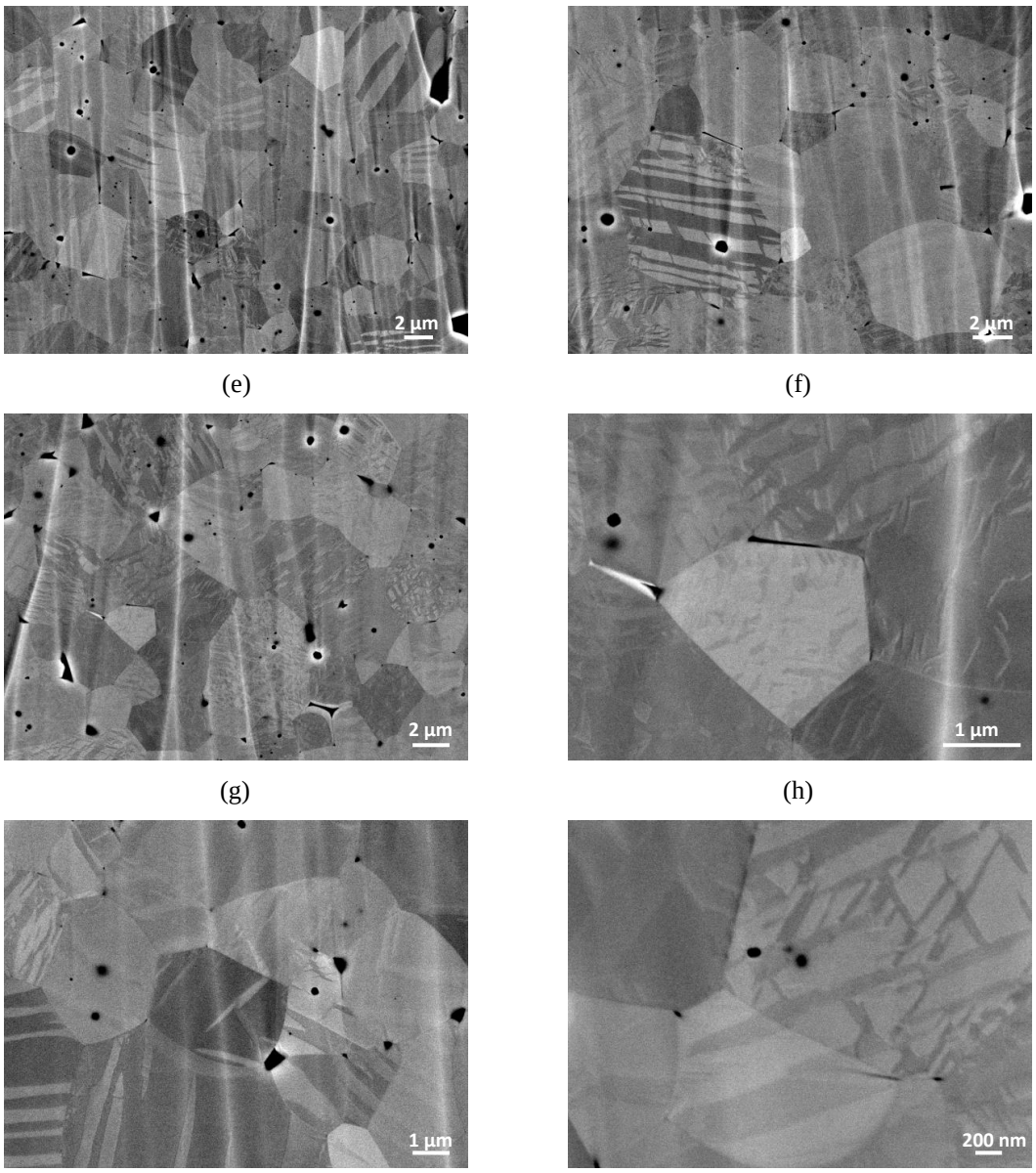

(e) (f)

(g) (h)

(i) (j)

Fig.4.38: Back-scattered SEM images of the 10 µm BNT ceramic after electrical poling. The cross-hatched domain pattern in replaced by a striped domain structure (a)-(j).

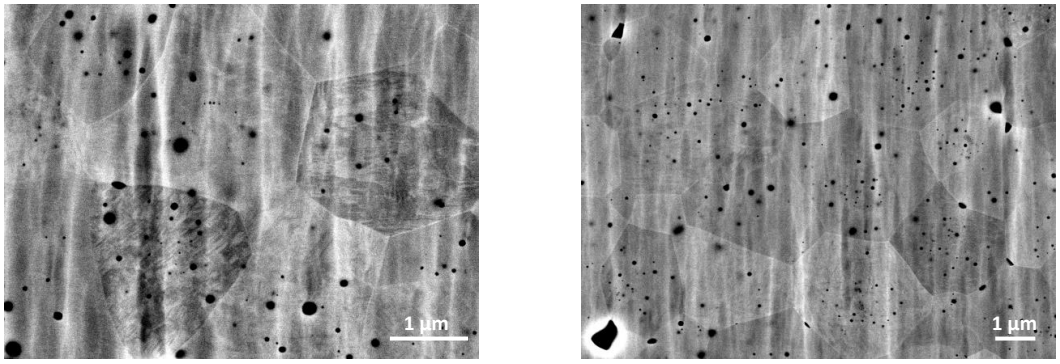

(a) (b)

Fig.4.39: (a)-(b) Back-scattered SEM images of the 1.5 µm BNT ceramic showing a cross-hatched domain structure.

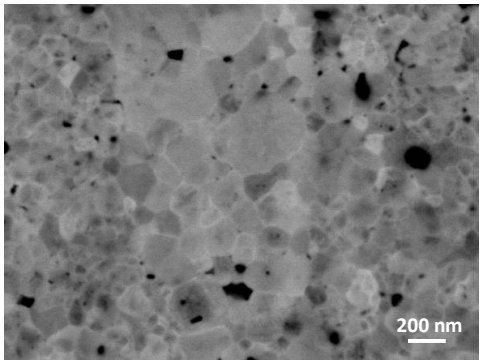

(a)

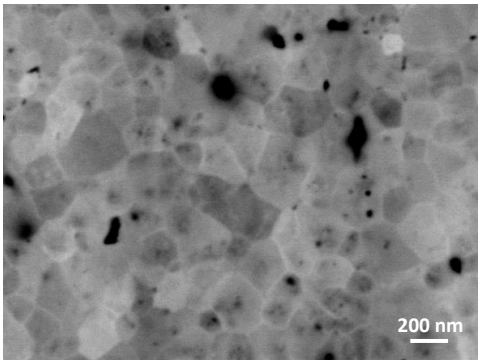

(b)

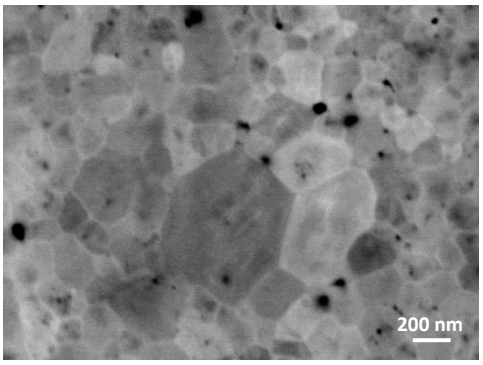

(c)

Fig.4.40: (a)-(c) Back-scattered SEM images of the 500 nm grain size ceramic showing no clear domain pattern.

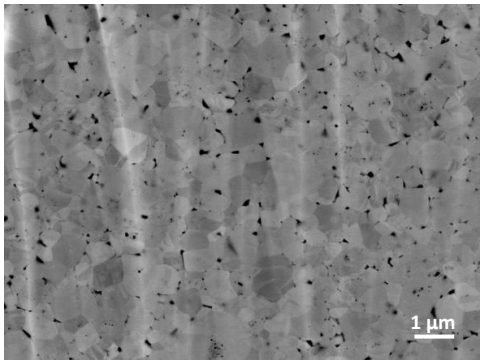

(a)

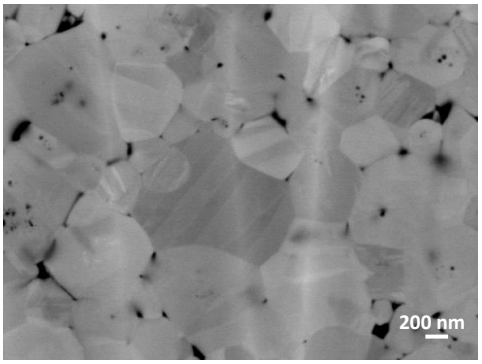

(b)

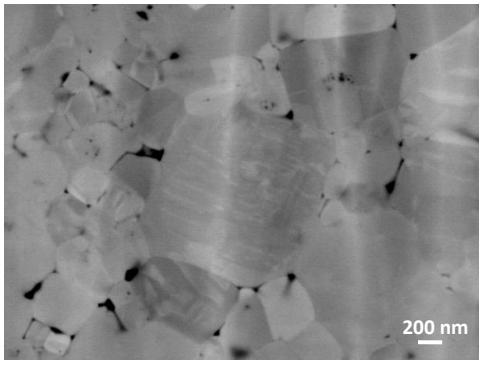

(c)

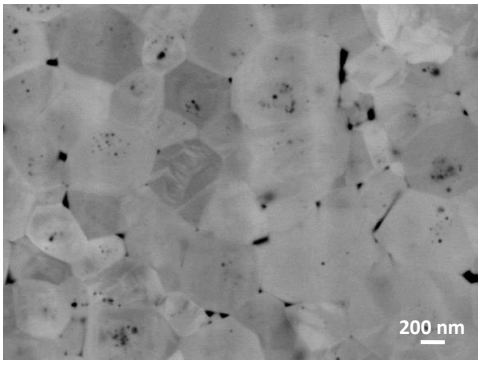

(d)

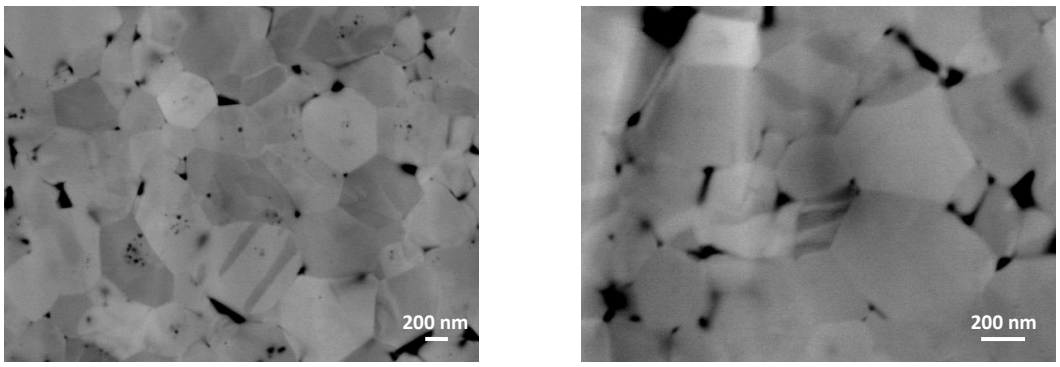

(e) (f)

Fig.4.41: (a)-(f) Back-scattered SEM images of the 500 nm BNT ceramic after electrical poling showing grains containing a striped domain pattern. (f) shows domain structure to exist in 200 nm grains.

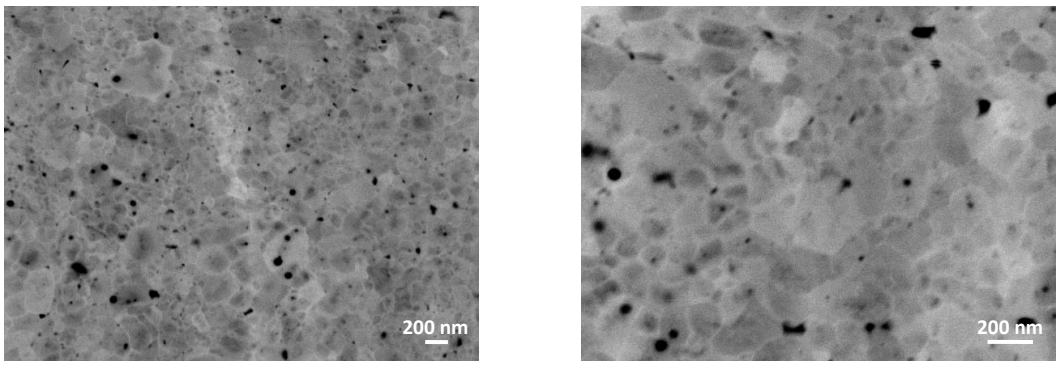

(a) (b)

Fig.4.42: (a)-(b) Back-scattered SEM images of the 150 nm ceramic showing no clear domain pattern.

4.2.4 Piezoforce Microscopy (PFM)

PFM images of the poled 10 µm, unpoled 1.5 µm and poled 500 nm BNT ceramics are shown in Fig.4.43-4.45, respectively. Piezoelectric hysteresis loops of the amplitude and phase components were also collected from the imaged areas. Fixed excitation amplitudes ranging from 5-8 V applied at 60 kHz were used to collect each image.

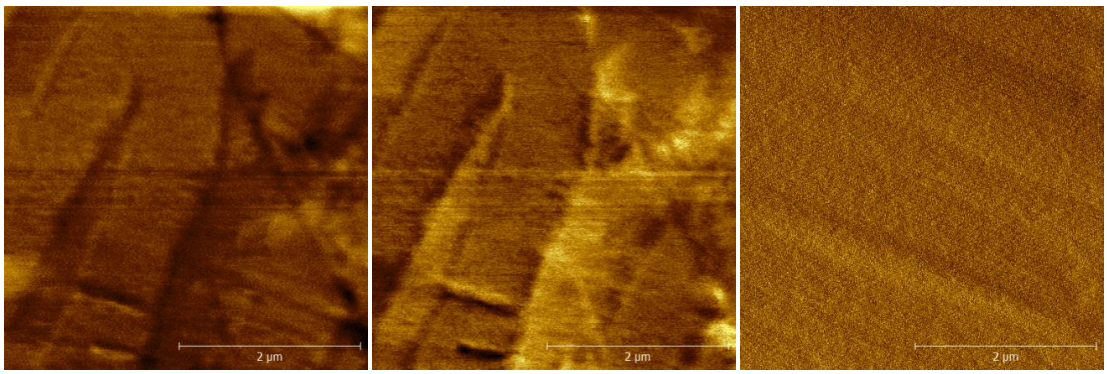

(a1) (a2) (a3)

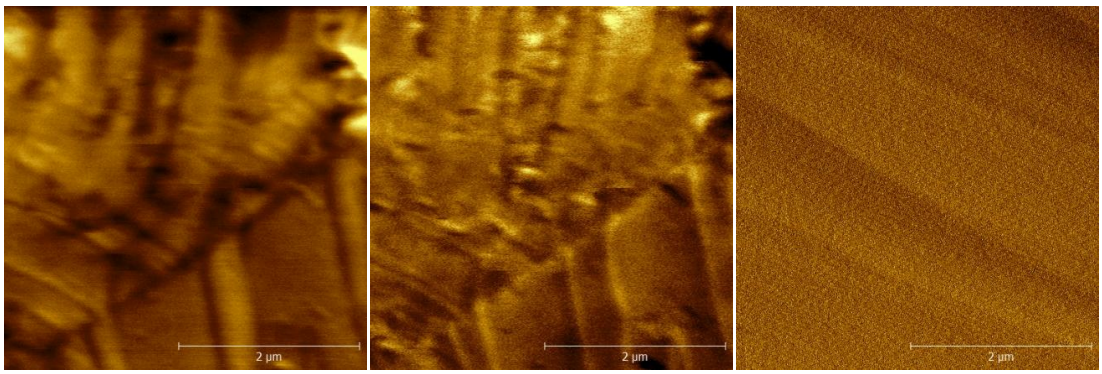

(b1) (b2) (b3)

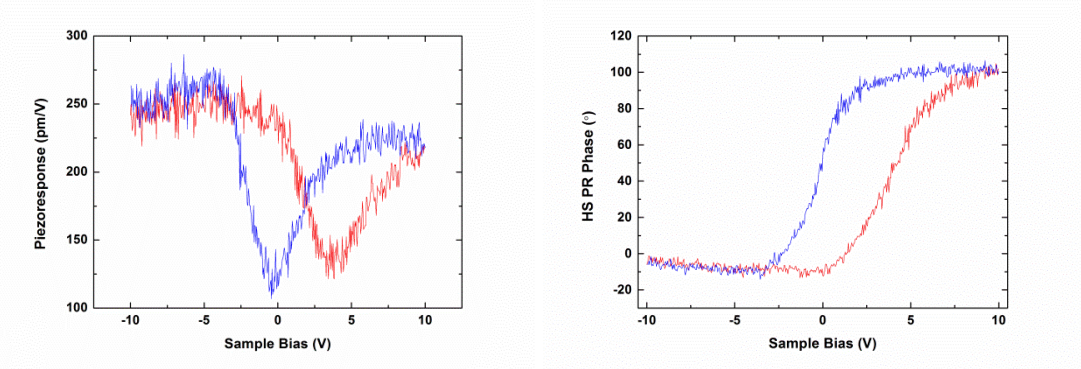

(c1) (c2)

Fig.4.43: PFM images of different areas of the poled 10 µm BNT ceramic including (a1), (b1) amplitude, (a2), (b2) phase and (a3), (b3) defelection. (c1)-(c2) Piezoelectric hysteresis loop obtained from the area imaged in (a1)-(a3). Measured with an exitation amplitude of (a1)-(a3) 5 V and (b1)-(b3) 8 V applied at 60 kHz.

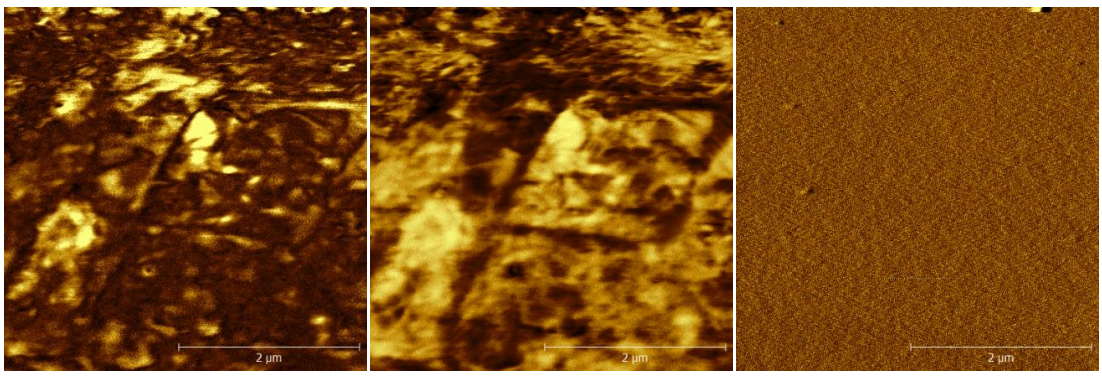

(a1) (a2) (a3)

Fig.4.44: PFM images of the 1.5 µm BNT ceramic including (a1) amplitude, (a2) phase and (a3) defelection. Measured with an exitation amplitude of 5 V applied at 60 kHz.

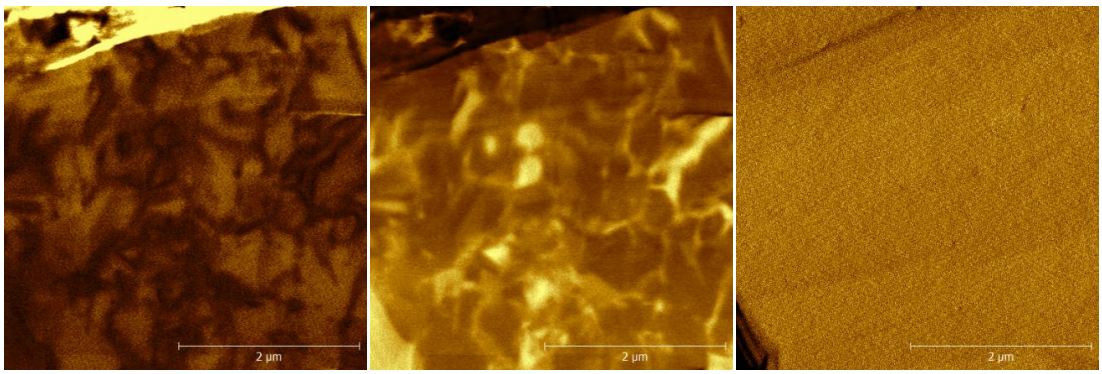

(a1) (a2) (a3)

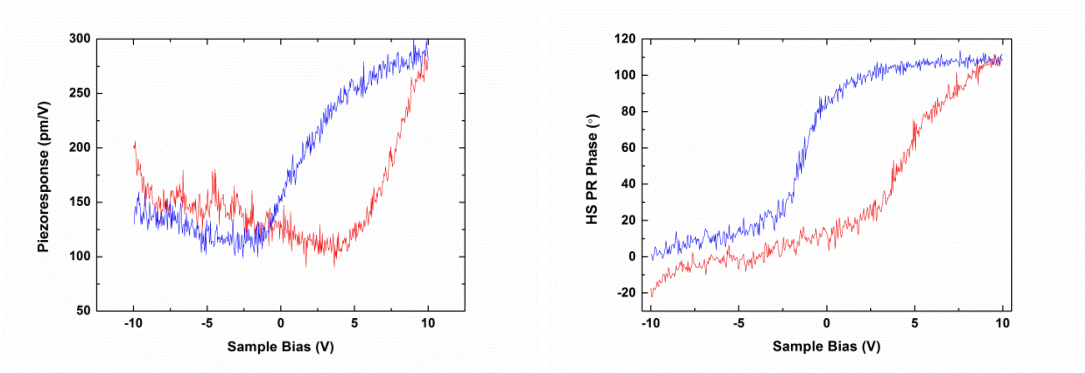

(b1) (b2)

Fig.4.45: PFM images of the poled 150 nm BNT ceramic including (a1) amplitude, (a2) phase and (a3) defelection. (b1)-(b2) Piezoelectric hysteresis loop obtained for this area . Measured with an exitation amplitude of 5 V applied at 60 kHz.

The roughness of the ceramic surface is imaged by the cantilever deflection. With the expectation of a few small pores, the surface is highly polished with no scratches that may imitate a domain structure. A striped domain pattern, previously detected by back-scattered SEM, is observed in the amplitude and phase images of the poled 10 µm grain size ceramic, shown in Fig.4.43. The domain pattern appears more complex in the unpoled state of the 1.5µm ceramic (Fig.4.44). No domain structure was observed within the grains of the poled 150 nm ceramic in Fig.4.45.

4.2.5 Dielectric Response vs. Frequency

The frequency dependence of the dielectric properties measured at room temperature is shown in Fig.4.46. In the unpoled state, all of the BNT ceramics experience a decrease in dielectric permittivity with increasing frequency. Within the measured frequency range, extrinsic contributions from domain wall motion dominate the polarisation. Intrinsic properties including the polar response of the electronic, ionic and dipolar structures also contribute to the permittivity however their response to the applied

electric field remains effectively constant at these low frequencies. Rather, the decrease in permittivity is a result of a relaxation of the domain wall motion. At high frequency, the domain walls are unable to respond to the applied electric field reducing their contribution to the permittivity.

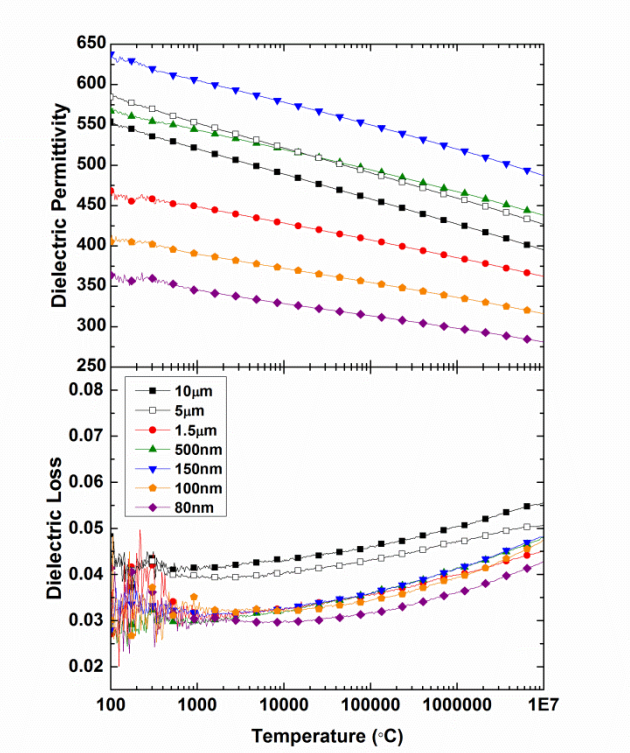

Fig.4.46: Frequency dependence of the dielectric response of the BNT ceramics with different grain size.

The dielectric loss measured for all of the ceramics was observed to increase with increasing frequency. Dielectric loss is a measure of the delay in response of the electric flux density to the applied electric field. The long relaxation time associated with the domain wall motion increases the lag at higher frequencies resulting in this increase in loss.

Electrical poling was found to decrease the values of both the dielectric permittivity and loss in all the BNT ceramics, shown in Fig.4.47. Domain size typically increases on poling, reducing the number of domain walls and their contribution to the polarisation.

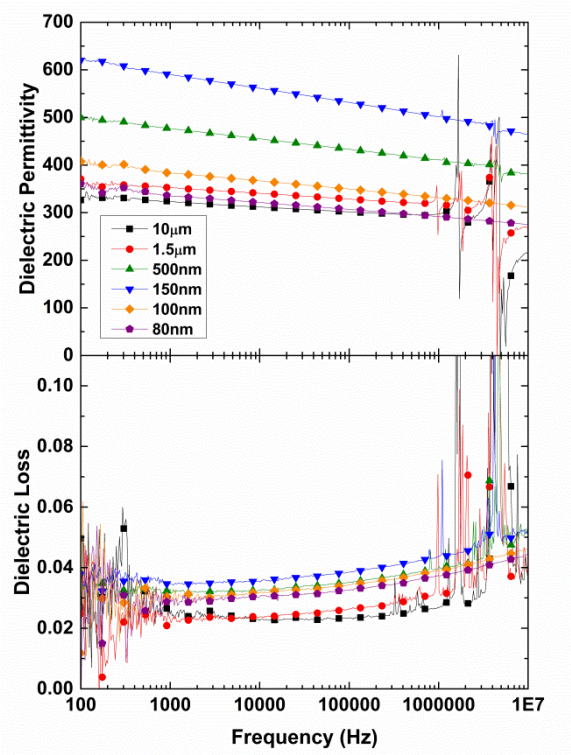

Fig.4.47: Dielectric response vs. frequency of the poled BNT ceramics with different grain size.

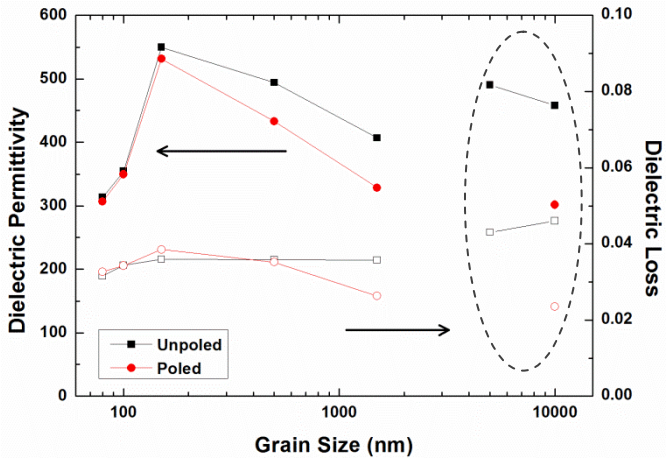

Fig.4.48: Grain Size dependence of the dielectric response in the unpoled and poled states at 100 kHz. Conventionally sintered samples are separated from those prepared by SPS by the dashed circle.

The effect of grain size on the dielectric response of BNT at 100 kHz is summarised in Fig.4.48. The dielectric permittivity typically decreases with increasing grain size, however the lowest permittivity value was measured for the 1.5 μm ceramic rather than the largest grain size. The different sintering techniques used may explain this result. All of the ceramics sintered using the SPS follow the general trend of decreasing permittivity with increasing grain size. When the permittivity values of ceramics formed

using conventional sintering are compared, for example the 5 and 10 μm ceramics, they also follow the same trend. Dielectric loss remains relatively constant with increases grain size, except for the conventionally sintered ceramics which have the highest loss values. This difference is thought to be a product of point defects.

4.2.6 Dielectric Response vs. Temperature

(i) Unpoled

The temperature dependent dielectric response of each BNT ceramic measured at frequencies 1, 10,100 and 500 kHz from room temperature up to 600 ˚C (3 ˚C/min) is shown in Fig.4.49. A number of features previously reported in the literature were identified in the dielectric data. In the unpoled state, BNT typically exhibits three anomalies: T_S, T_{RE} and T_M, highlighted in Fig.4.49(a1). A broad shoulder T_S appears in the dielectric permittivity with increasing temperature before reaching a maximum at T_M. T_S appears as a broad peak on the shoulder of the dielectric loss which decreases sharply with increasing temperature until T_M where it finally increases disproportionally due to effects from conductivity. The frequency distribution in the dielectric response increases with increasing temperature above T_S before vanishing at T_{RE} then increasing once again at T_M.

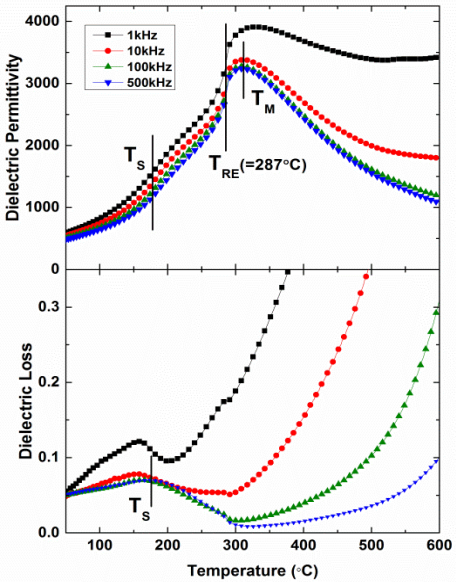

(a1)

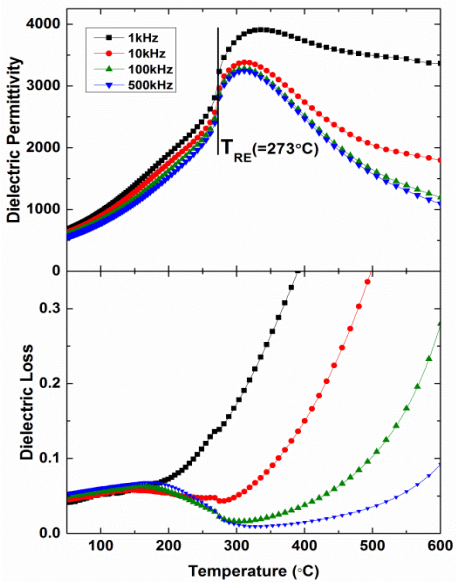

(a2)

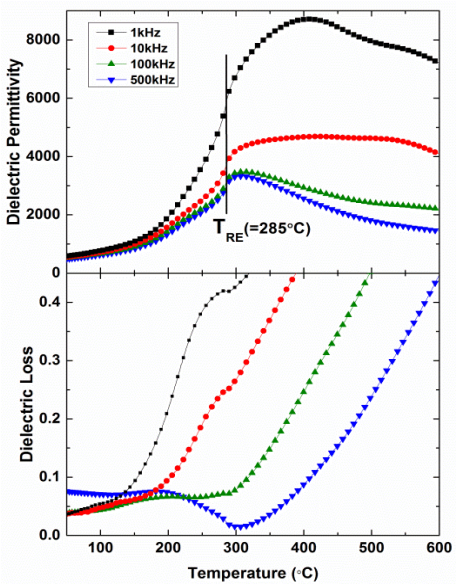

(b1)

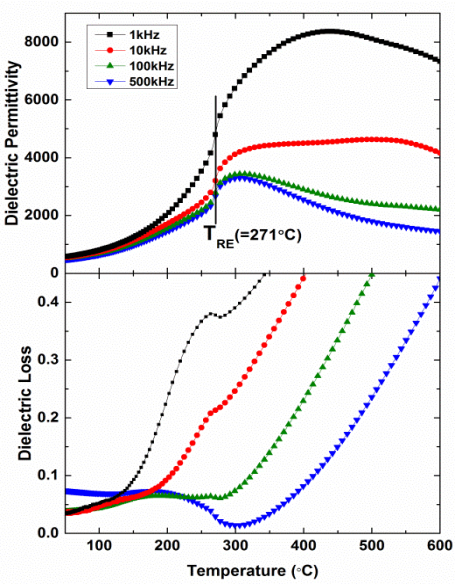

(b2)

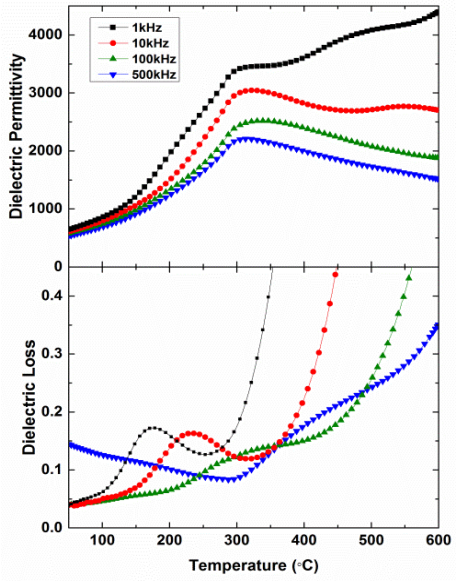

(c1)

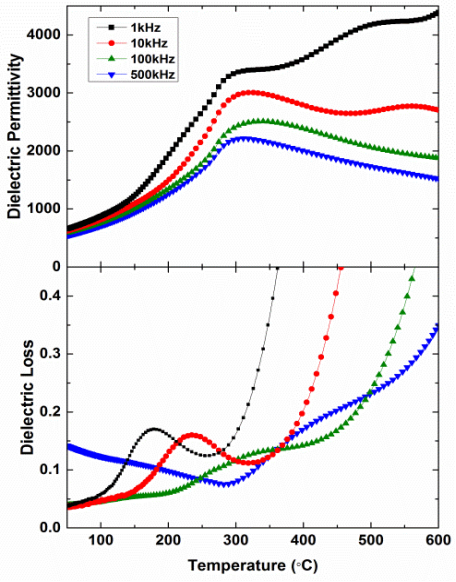

(c2)

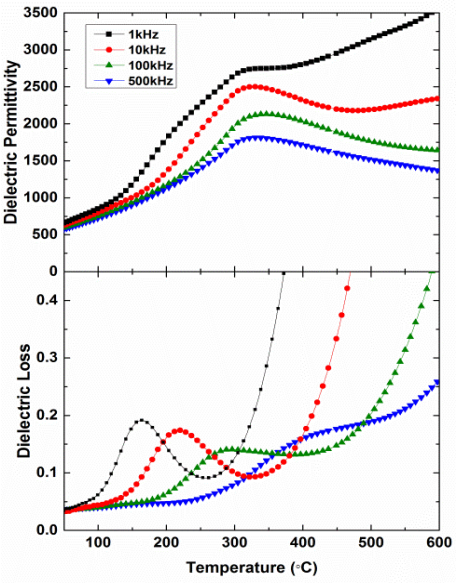

(d1)

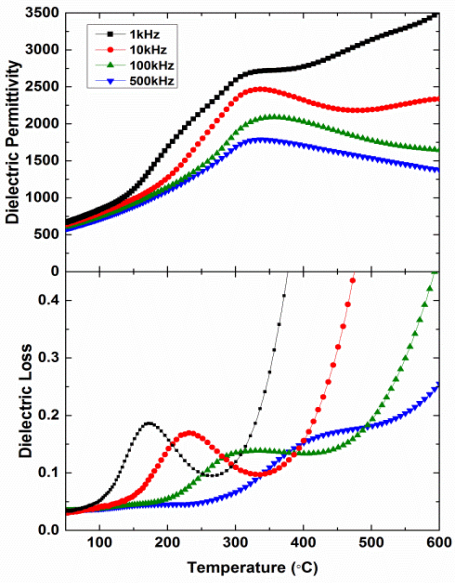

(d2)

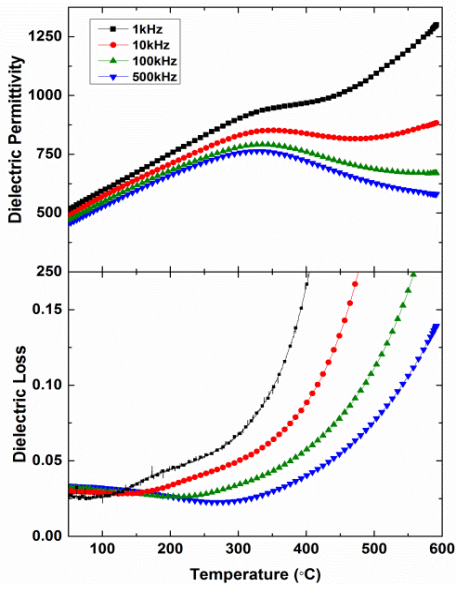

(e1)

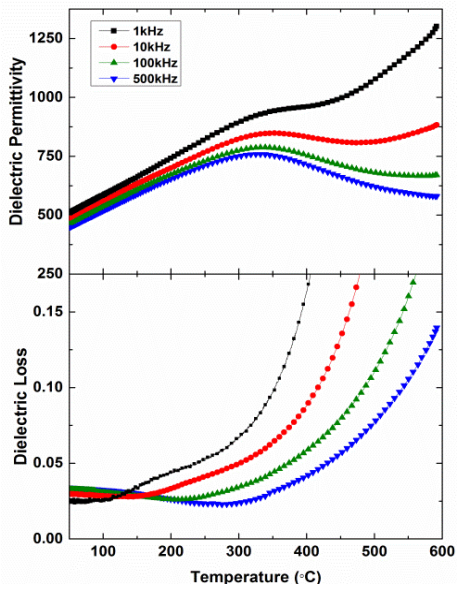

(e2)

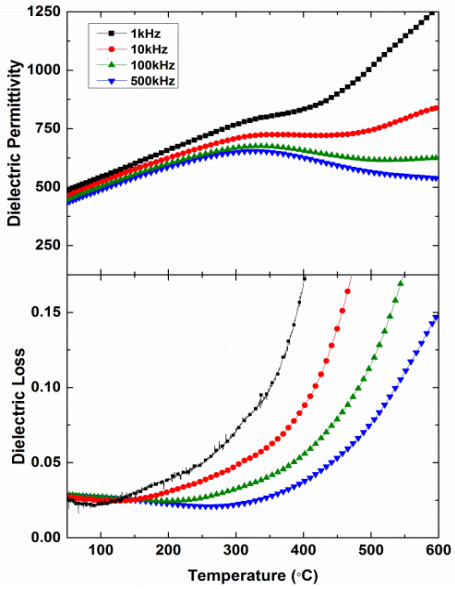

(f1)

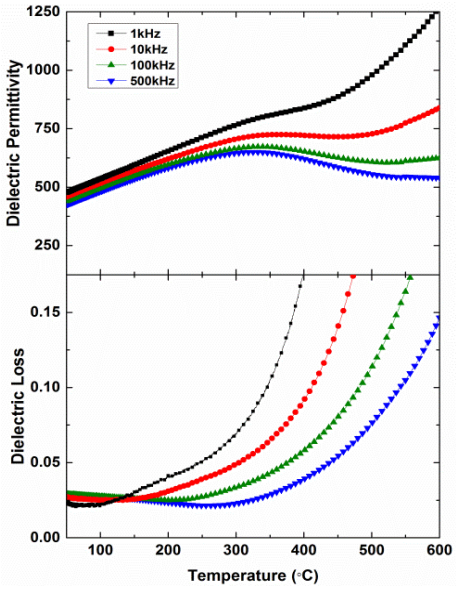

(f2)

Fig.4.49: Temperature dependence of the dielectric response measured during (a1)-(f1) heating and (a2)-(f2) cooling at 1, 10, 100 and 500 kHz for each grain size: (a1)-(a2)10 µm, (b1)-(b2) 1.5 µm, (c1)-(c2) 500 nm, (d1)-(d2) 150 nm, (e1)-(e2) 100 nm and (f1)-(f2) 80 nm.

Not all of the features could be identified in the dielectric response at each grain size. For ceramics with a grain size of 500 nm and below, neither T_S nor T_{RE} could be determined whereas T_M was observed for all of the tested ceramics. T_S is most prominent in the heating run of the ceramics with largest grain size, however this feature vanishes on cooling. A discrepancy in the temperature of T_{RE} also exists between heating and cooling, where T_{RE} occurs at a higher temperature on heating. No such temperature hysteresis is observed for T_M.

As the grain size decreases, the peak in the permittivity broadens and shifts to higher temperatures, as shown in Fig.4.50 and summarised in Table 4.9. The permittivity value is also reduced, decreasing from ~3300 for micrometre grain size ceramics to ~2000 for the 150 nm grain size sample when measured in a 100 kHz applied field.

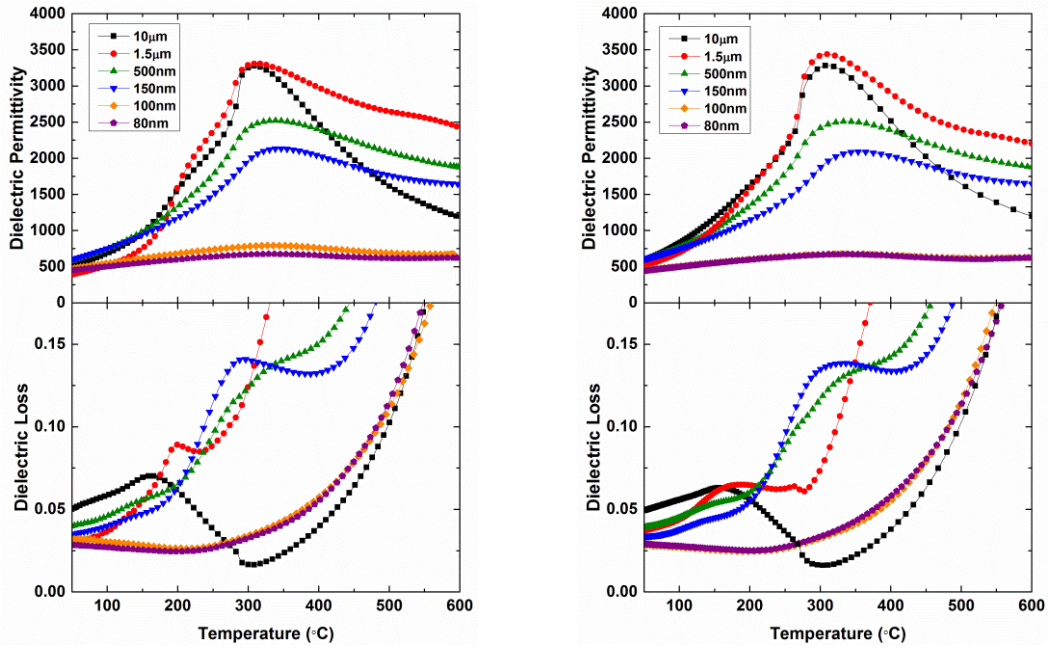

(a) (b)

Fig.4.50: Grain size dependence of the dielectric response measured during (a) heating and (b) cooling at 100 kHz.

Table 4.9: The temperature T_M of the peak in the dielectric permittivity measured at 100 kHz.

Grain Size	T_m (˚C)
10 µm	310
1.5 µm	310
500 nm	338
150 nm	345
100 nm	334
80 nm	334

The shoulder in the dielectric loss is observed on both heating and cooling however it becomes less pronounced with decreasing grain size. For ceramics with grain size of 150 and 500 nm, the shoulder is replaced by peaks which shift to higher temperatures with increasing frequency. These peaks do not appear to correspond to any features in the dielectric permittivity and are thought to be caused by point defects that were not removed by annealing.

(ii) Poled (65 kV/cm)

The effect of poling on the temperature dependence of dielectric response of BNT measured at frequencies 1, 10,100 and 250 kHz is shown in Fig.4.51. The dielectric response was measured on heating and cooling from room temperature up to 600 ˚C at a rate of 3 ˚C/min. Each BNT ceramic was poled in an applied field of 65 kV/cm for 5 minutes.

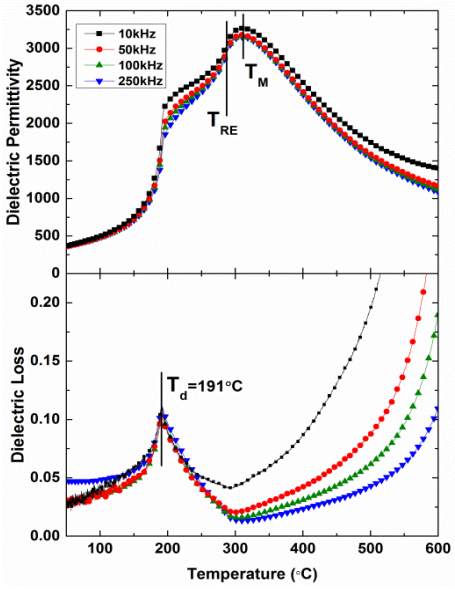

(a1)

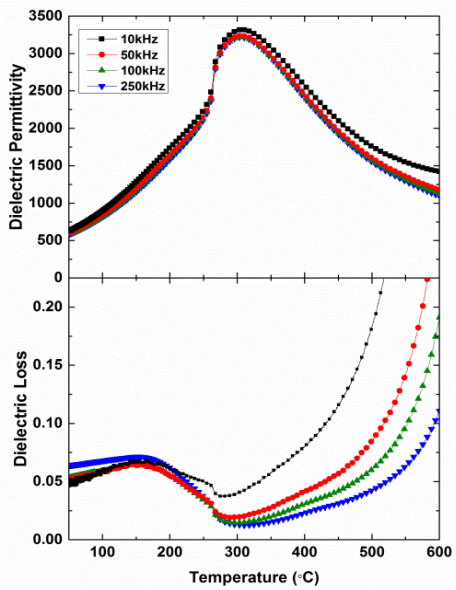

(a2)

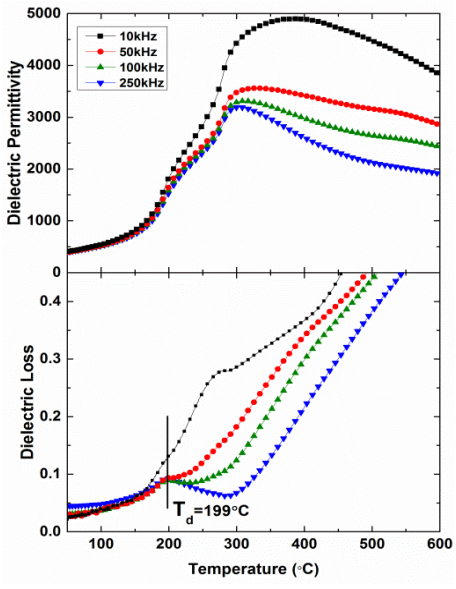

(b1)

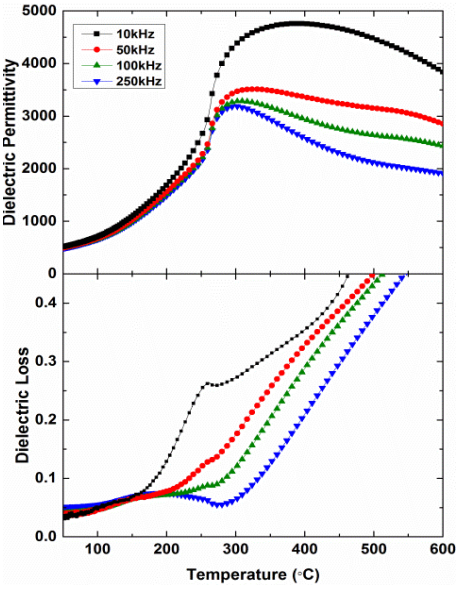

(b2)

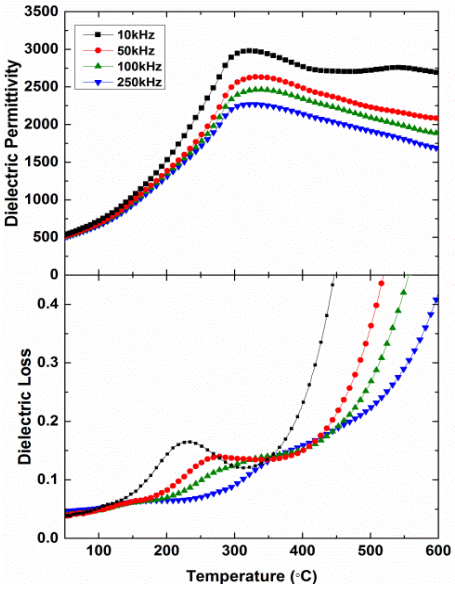

(c1)

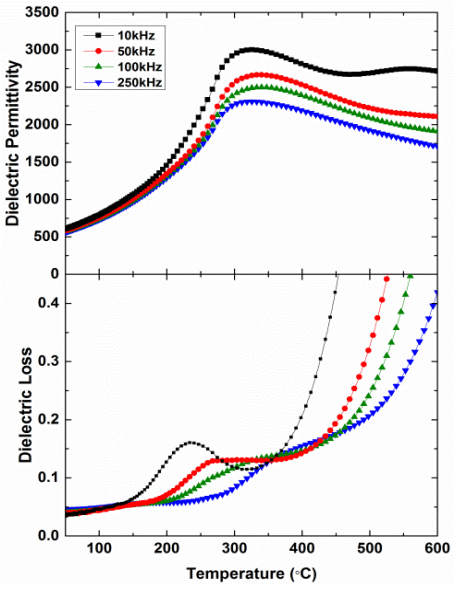

(c2)

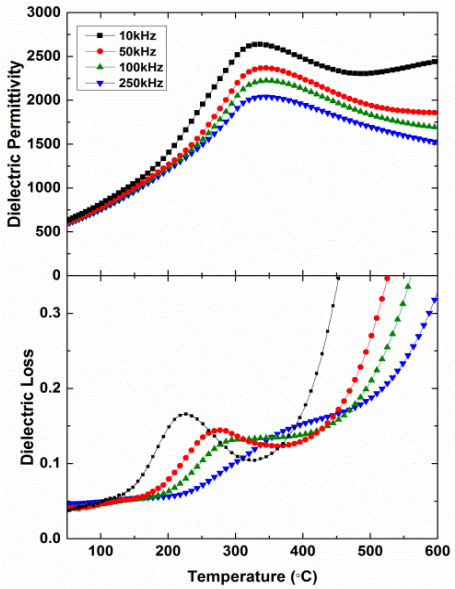

(d1)

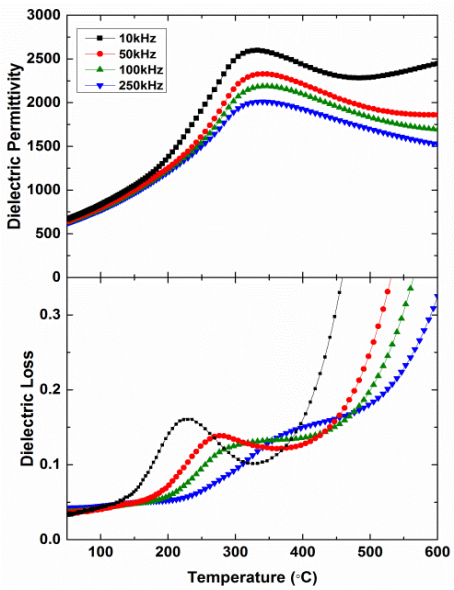

(d2)

Fig.4.51: Dielectric response vs. temperature for each grain size (a1)-(a2) 10 µm, (b1)-(b2) 1.5 µm, (c1)-(c2) 500 nm and (d1)-(d2) 150 nm after electrical poling. Measured during (a1)-(d1) heating and (a2)-(d2) cooling at 1, 10, 100 and 250 kHz.

In the poled state, T_S is replaced by a sharp feature T_d which appears in both the dielectric permittivity and loss as shown in Fig.4.51(a1). The frequency distribution of the dielectric response is minimal below T_d and only increases above this temperature. Poling does not appear to induce a distinct feature at T_d in the small grain ceramics however the shoulder in the dielectric loss becomes more pronounced and shifts to higher temperatures. T_{RE} also shifts to higher temperatures on poling however T_m remains unchanged.

Poling lowers the dielectric permittivity value below T_d for all of the grain sizes. The permittivity value at T_M is also lowered but only in ceramics with a grain size greater than 150 nm, shown in Fig.4.52. Cooling after poling is similar to the cooling run in the unpoled state where T_d disappears because of depoling.

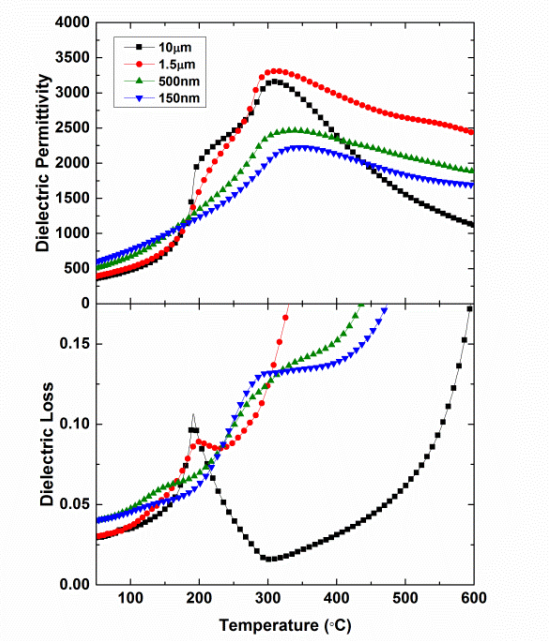

Fig.4.52: Grain size dependence of the dielectric response measured at 100 kHz after electrical poling.

(iii) Weak Bias-Field (3 kV/cm and 5 kV/cm)

To understand the nature of the transition at T_d, the influence of a DC bias-field on the dielectric properties of BNT was investigated. The dielectric response was measured at frequencies 10, 50, 100 and 250 kHz between 25 ˚C and 250 ˚C (3 ˚C/min) after various electrical and thermal treatments: 1. Field Cooling (FC), 2. Zero Field Heating after Field Cooling (ZFH af. FC), 3. Field Heating after Field Cooling (FH af. FC), 4. Field Heating (FH) and 5. Zero Field Cooling after Field Heating (ZFC af. FH). To eliminate the possibility of remanent macropolar regions influencing the results, the samples were thermally annealed at 600 ˚C before each measurement. The results were also compared with the dielectric data collected for the unpoled (ZFH/ZFC) and poled (ZFH Poled) states.

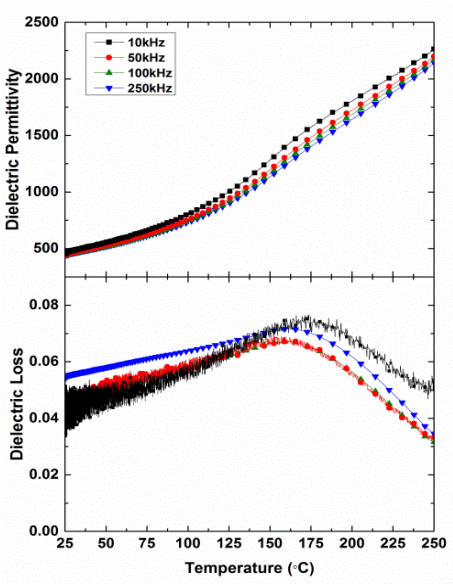

(a) FC (3 kV/cm)

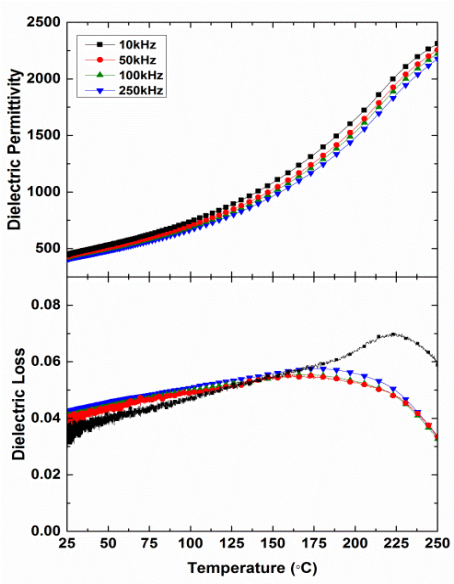

(b) FC (5 kV/cm)

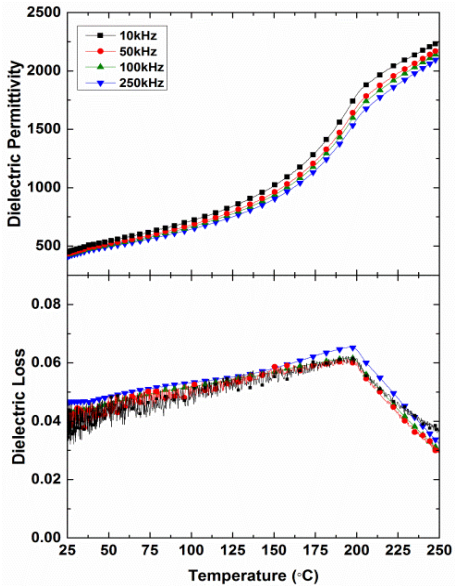

(c) ZFH af. FC (3 kV/cm)

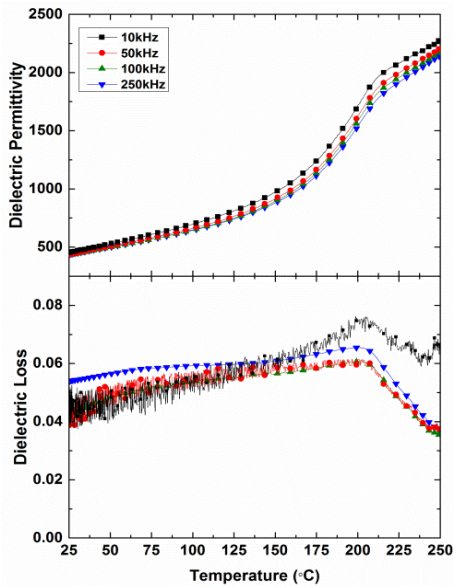

(d) FH af. FC (3 kV/cm)

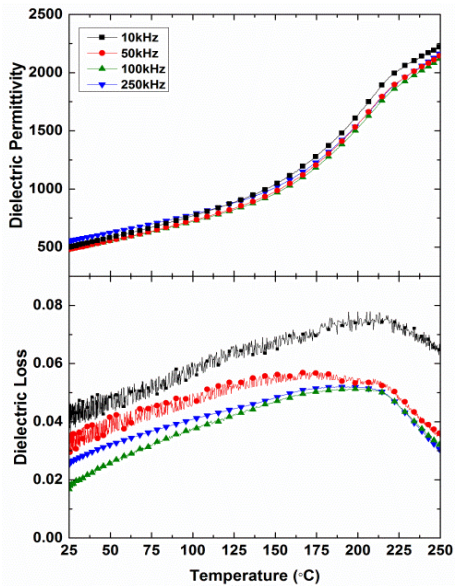

(e) FH (3 kV/cm)

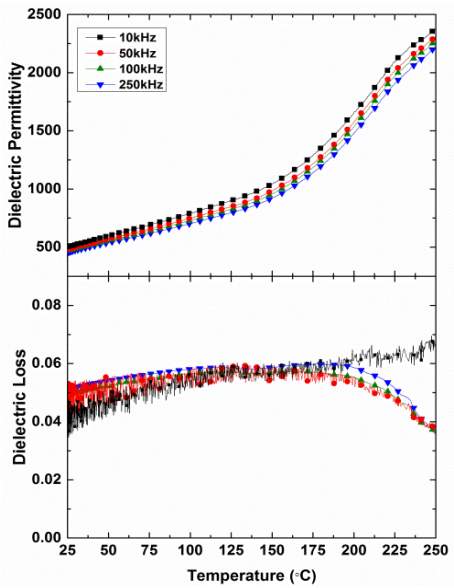

(f) FH (5 kV/cm)

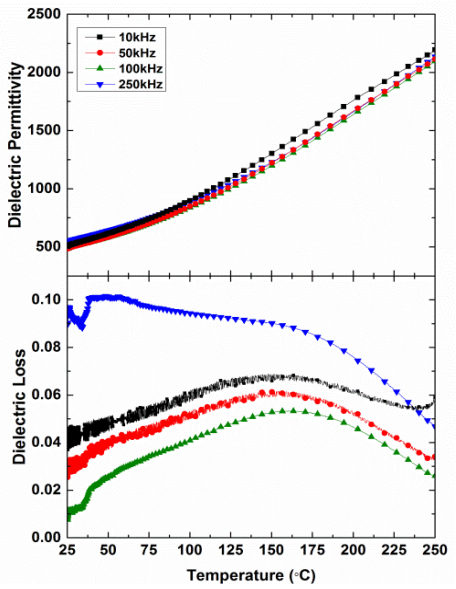

(g) ZFC af. FH (3 kV/cm)

Fig.4.53: The dielectric response of the 10µm ceramic measured at frequencies 10, 50, 100 and 250 kHz after various electrical and thermal treatments, as summarised in the text.

The dielectric results for the 10 µm grain size BNT ceramic are shown in Fig.4.53. The thermal depolarisation temperatures determined from the peak in the dielectric loss after each measurement are summarised in Table 4.10. T_{do} occurs at the same temperature for ZFH Poled and ZFH af. FC (Fig.4.54 (a)). The depoling temperature of the polar state induced by either poling the ceramic at room temperature or during cooling is independent of the initial poling field strength. A bias field applied during heating helps to retain the polar state shifting T_{db} to higher temperatures during FH and FH af. FC. FH with a 5 kV/cm bias-field however does not appear to further increase the temperature of T_{db}. The dielectric permittivity of the FH af. FC is lower than the FH runs, below T_{do}, as cooling in an applied field has a greater poling effect. Above T_{do}, the permittivity during FH af. FC increases, whereas the permittivity only becomes dependent on the strength of the bias during FH at T_{db}. The frequency dispersion in the bias-field measurements remains relatively constant over the measured temperature range, unlike ZFH Poling which shows a dramatic increase above T_{do}. The dielectric response of ZFC and ZFC af. FH are identical with both measurements showing a broad peak in the dielectric loss similar to ZFH at T_S, shown in Fig.4.54 (b). Neither of these measurements show a feature associated with T_S in the permittivity curve. FC in a 3 kV/cm bias-field does not appear to change the dielectric loss however, a broad shoulder is observed in the permittivity curve at T_s. The temperature of this feature shifts to T_{db} when the cooling bias-field is increased to 5 kV/cm, shown in Fig.4.54 (c).

Table 4.10: The thermal depolarisation temperatures determined from the peak in the dielectric loss of the 10µm grain size BNT ceramic measured at 100 kHz. T_d: depoling after high field poling at room temperature, T_{do}: depoling after cooling in a bias-field, T_{db}: depoling in a bias-field.

T_S	T_d	T_{do}	T_{db}
162 ˚C	191 ˚C	191 ˚C	213 ˚C

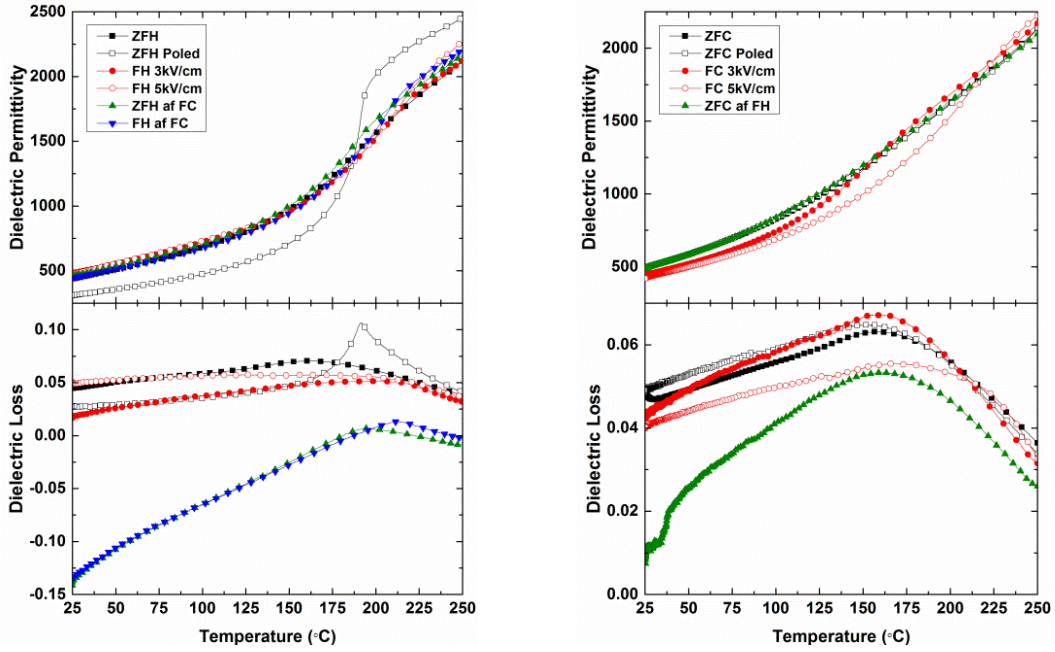

(a) (b)

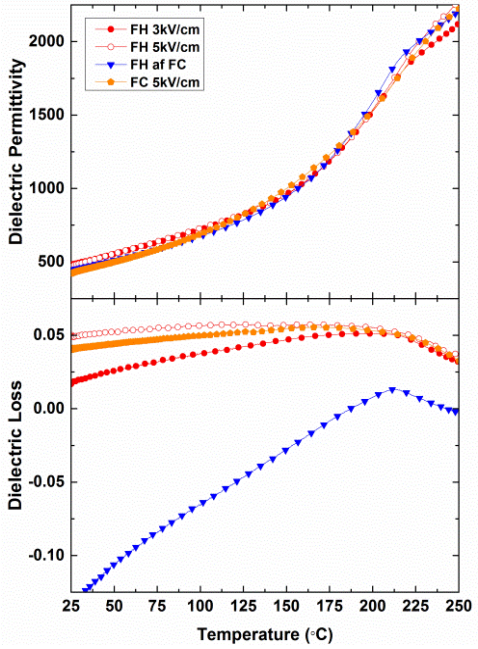

(c)

Fig.4.54: Dielectric response of the 100 kHz data collected from the 10 µm ceramic during (a) heating and (b) cooling, (c) shows the bias-field measurements with the same T_{bd}.

The effect of a bias-field on the dielectric properties of the 1.5 µm and 500 nm ceramics was also measured (Fig.4.55). However, the bias-field appears to be too weak to induce a clear change in response at the depoling temperature.

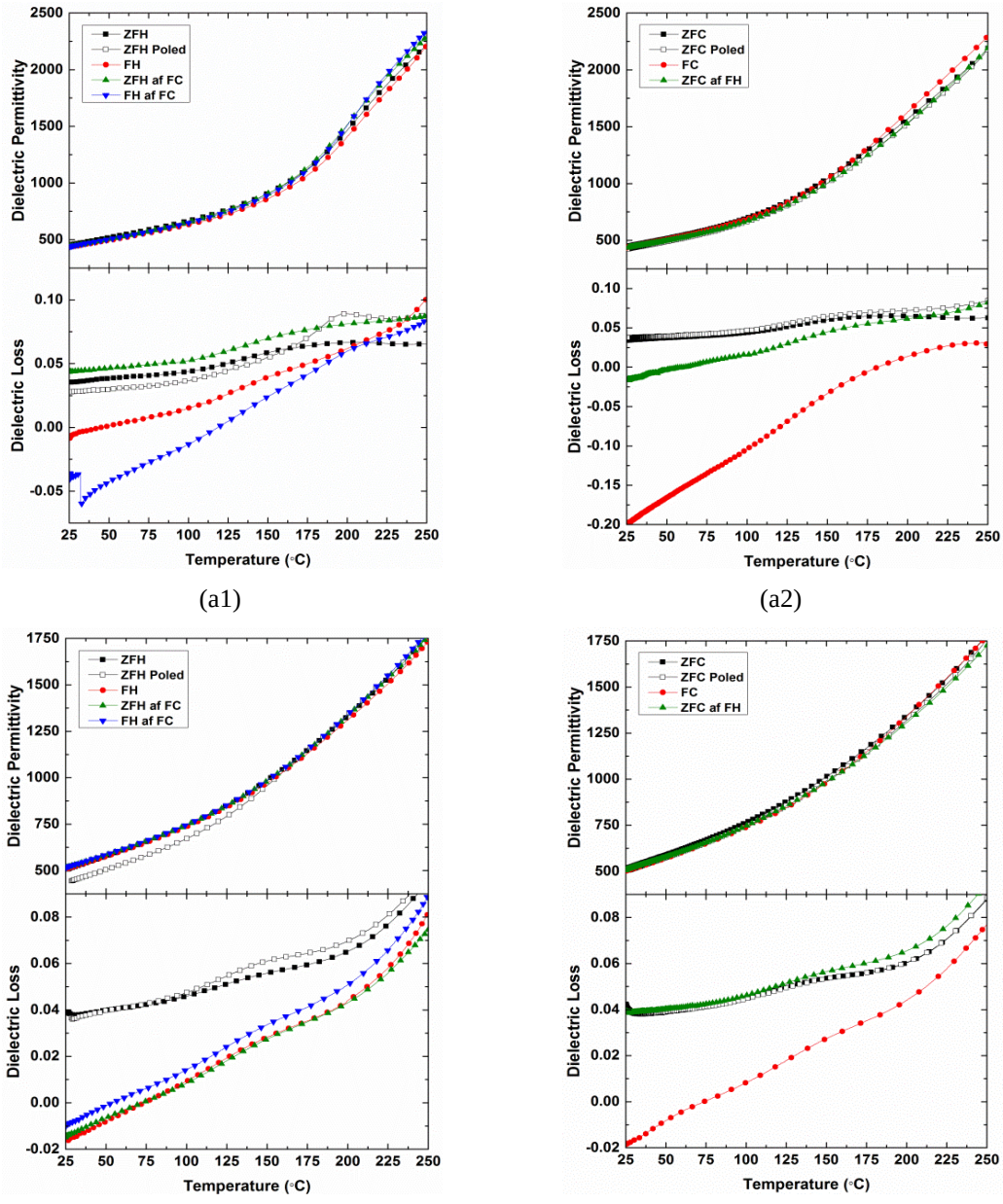

Fig.4.55: The dielectric response of the (a1)-(a2) 1.5 µm and (b1)-(b2) 500 nm BNT ceramics measured during (a1), (b1) heating and (a2), (b2) cooling at 100 kHz after various electrical and thermal treatments, as summarised in the text.

4.2.7 Polarisation and Current vs. Electric Field

The temperature dependence of the P-E/I-E loops for each ceramic is shown in Fig.4.56. The temperatures were selected with reference to the dielectric response of the ceramics.

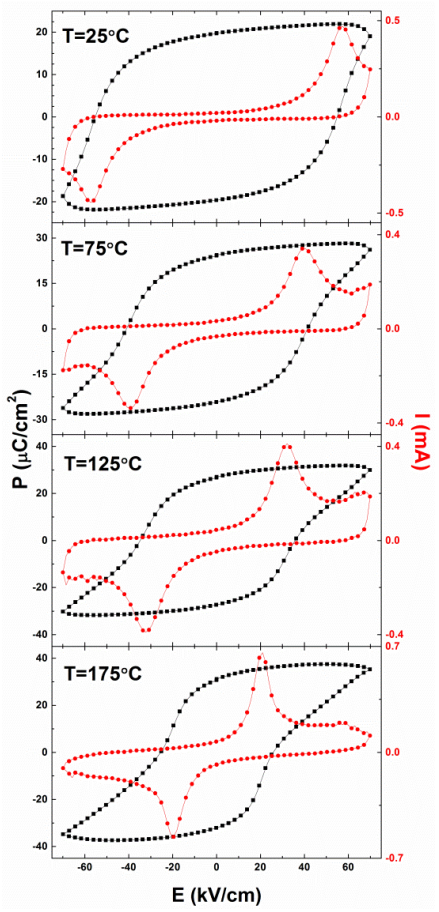
T=25°C
T=75°C
T=125°C
T=175°C
P (μC/cm²)
I (mA)
E (kV/cm)

(a)

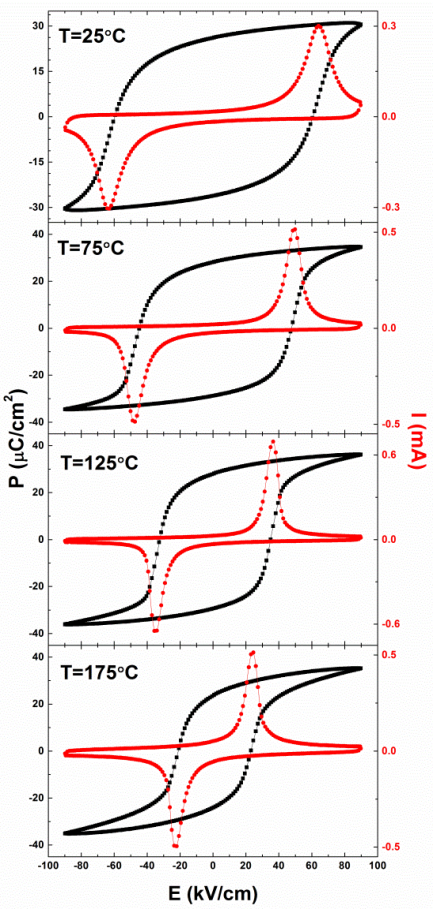
T=25°C
T=75°C
T=125°C
T=175°C
P (μC/cm²)
I (mA)
E (kV/cm)

(b)

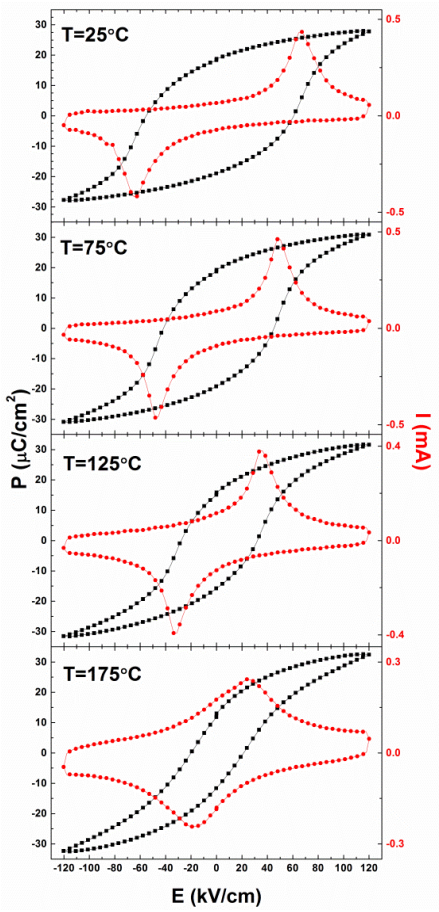
T=25°C
T=75°C
T=125°C
T=175°C
P (μC/cm²)
I (mA)
E (kV/cm)

(c)

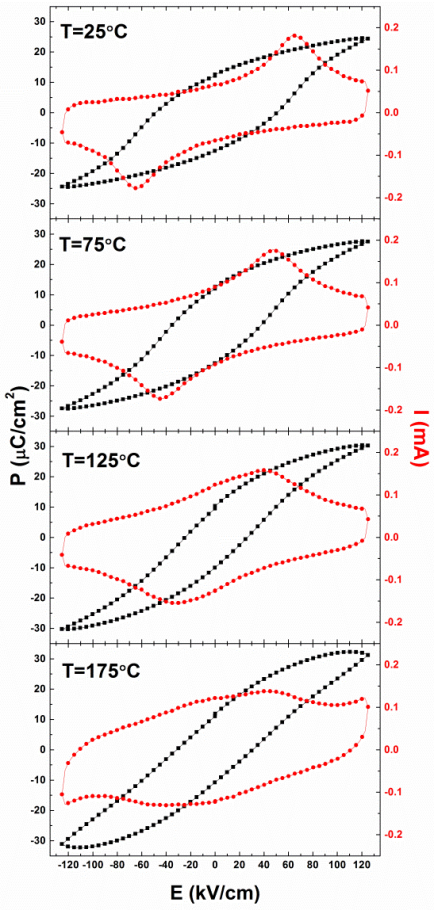
T=25°C
T=75°C
T=125°C
T=175°C
P (μC/cm²)
I (mA)
E (kV/cm)

(d)

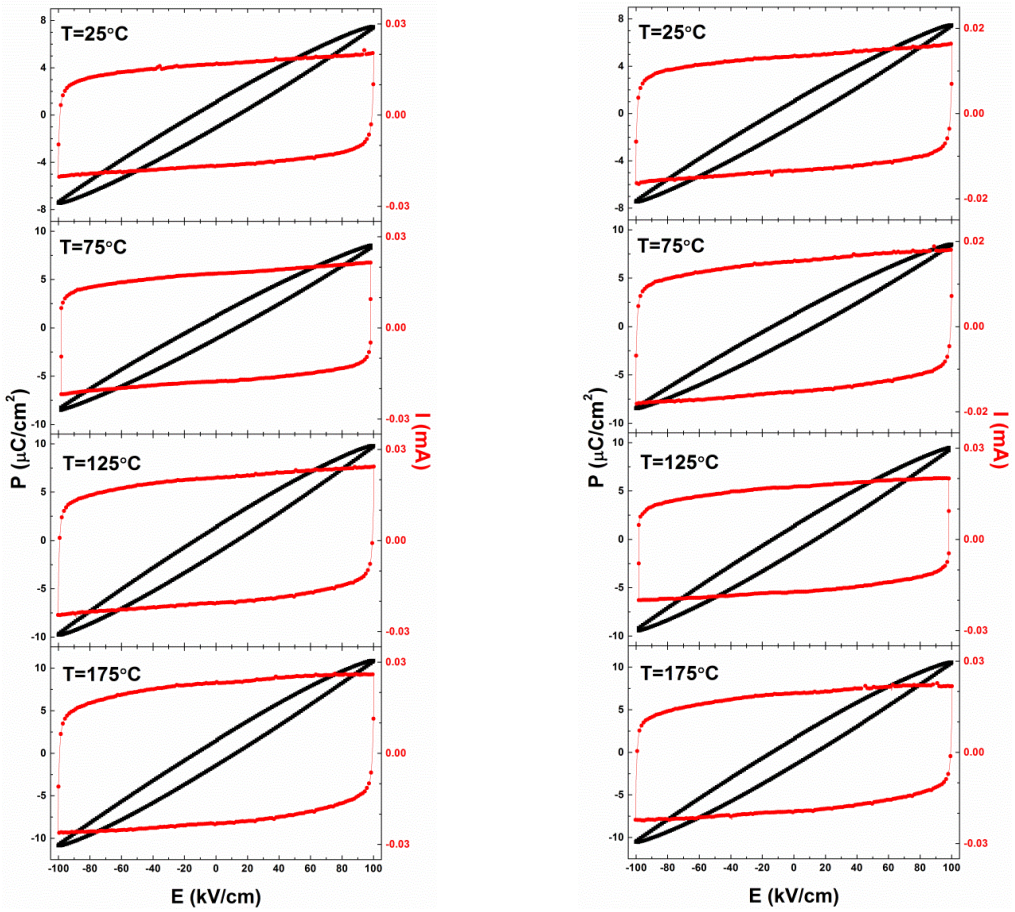

(e) (f)

Fig.4.56: Temperature dependence of the P-I-E loops of measured at 10Hz for each BNT ceramics with grain size (a) 10 μm, (b) 1.5 μm, (c) 500 nm, (d) 150 nm, (e) 100 nm and (f) 80 nm.

Evidence of ferroelectricity is provided by the domain switching current peaks which are observed for all ceramics over the studied temperature range (25-175 ˚C), except for the ceramics with grain size <100 nm. The temperature dependence of the remnant polarisation (P_r), saturation polarisation (P_{sa}) and coercive field (E_c) values, collected from the P-E/I-E loop measured at 10 Hz, are summarised in Fig.4.57. To successfully saturate the P-E loop, a high electric field (>>E_c) must be applied to the ceramic. BNT however, has a low breakdown field which can make poling difficult. Although poling becomes easier at elevated temperatures, the breakdown field decreases due to increased conductivity in the ceramic. The effect of high conductivity can clearly be seen in the I-E loops, which become slanted at high temperature. A higher breakdown field can be achieved in ceramics with smaller grain size. However, the E_c value is also higher for smaller grain size ceramics. This hinders saturation making it impossible to obtain an accurate P_{sa} value.

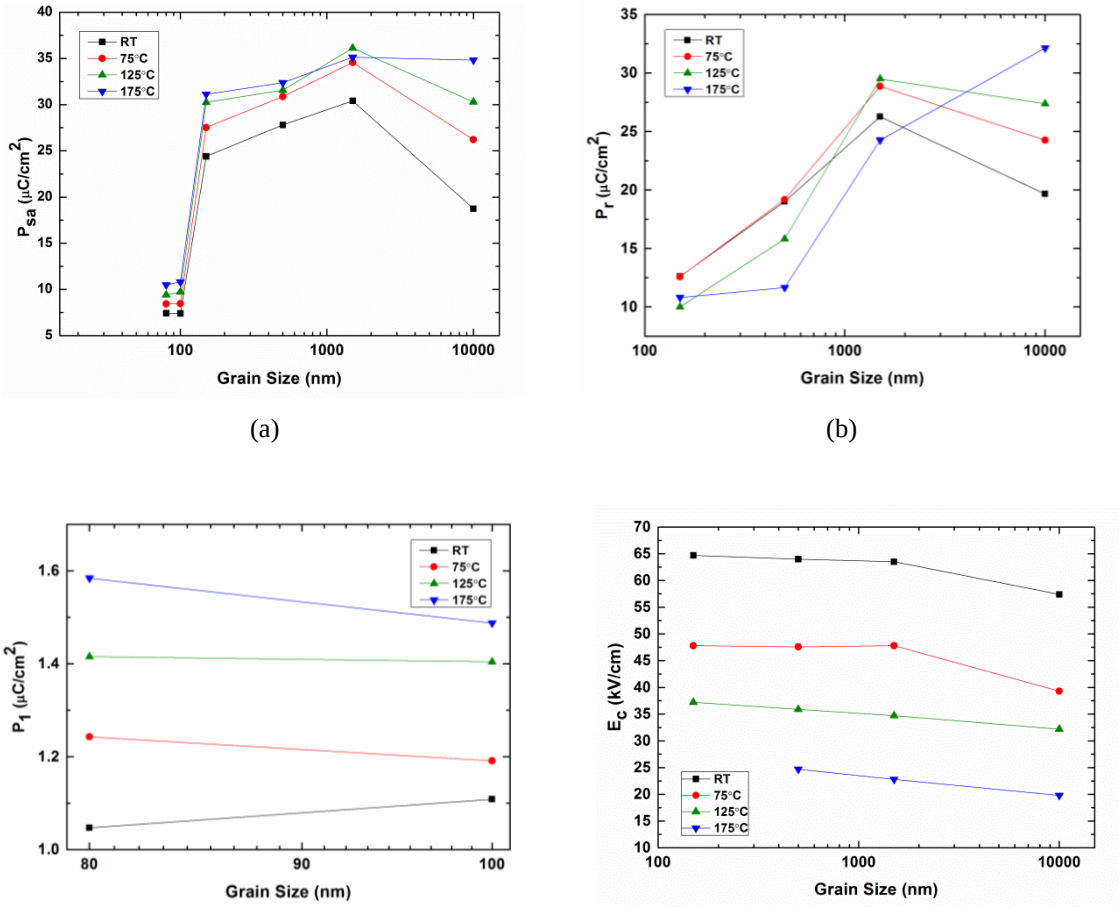

Fig.4.57: Grain size dependence of the (a) saturation polarisation (P_{sa}), (b) remnant polarisation (P_r), (c) zero electric field polarisation (P_1) and (d) coercive field (E_c) values, collected from the P-I-E loops measured at 10 Hz.

The values of both P_{sa} and P_r decrease as the grain size of the BNT ceramic is reduced. During poling, internal stresses are created at the grain boundaries. The re-orientation of non-180 ° domains involves the re-orientation of the spontaneous strain which can change the dimension of the individual grains. As the grain boundary density is higher for the smaller grain size ceramics, the intergranular stress will be larger in these ceramics. Back fields exerted by the grain boundaries suppress the domain reversal reducing P_{sa}. The high intergranular stress will also force the domains to switch back when the field is removed, decreasing P_r.

For all grain sizes, P_{sa} increases with increasing temperature. Greater domain reversal is expected to occur at these elevated temperatures as the domain walls become more active. Any long-range FE order induced by the applied electric field will be easily broken by these active domain walls as the field is removed. The P-E loops are therefore expected to become slimmer with increasing temperature as P_r is reduced, however, this

not true for all of the grain sizes. Instead, P_r increases with increasing temperature for the largest grain size ceramic. As the grain size is reduced, P_r which initially increases with increasing temperature begins to decrease at 125 ˚C and 75 ˚C for the 1.5 µm and 500 nm ceramics, respectively. P_r only decreases with increasing temperature at a grain size of 150 nm. At high temperatures, conductivity can become a problem as the ceramics become lossy, distorting the shape of the hysteresis loops and in particular the value of P_r. This is clearly the case in the 150 nm grain size ceramic at 175 ˚C, where P_r diverges from the trend. Although, high conductivity clearly affects the 10 µm ceramic, the 1.5 µm ceramics also shows an increase in P_r value with temperature but does not appear to be effected by conductivity. In this case, the inability to fully saturate the sample at lower temperatures is thought to result in an increase rather than a decrease in P_r below 175 ˚C.

For grain sizes ≤ 100 nm, the non-zero polarisation at zero electric field P_1, shown in Fig.4.57 (c), is related to conductivity rather than domain switching.

The electric field E_c is the external field required to switch the macroscopic polarity of the FE domains by the growth of existing domain parallel to the applied field, the nucleation and growth of new parallel domains and by domain wall motion[146]. The value of E_c is therefore dependent on the domain structure and the mobility of the domain walls in the ceramic. E_c can be seen to decrease with increasing grain size. As grain size is reduced, the increase in grain boundary density is expected to restrict the movement of the domain walls, hindering polarisation switching. For each grain size, E_c clearly shift to lower fields with increasing temperature, as shown in Fig.4.57 (c). As temperature increases, the thermal motion of the atoms in the lattice increases, lowering the energy barrier for polarisation reversal and domain wall reorientation.

(i) Frequency Dependence

For each grain size, E_c increases with increasing frequency while both P_{sa} and P_r decrease. This frequency dependence can be related to the relaxation time of the domain walls. At high frequencies, fewer domain walls can follow the applied electric field hindering the growth in size and number of domains parallel to the applied field. A higher strength field is required to force more of the domain walls that can still follow the field to switch the polarisation. The frequency dependence of the E_c, P_{sa} and P_r values is demonstrated in Fig.4.58.

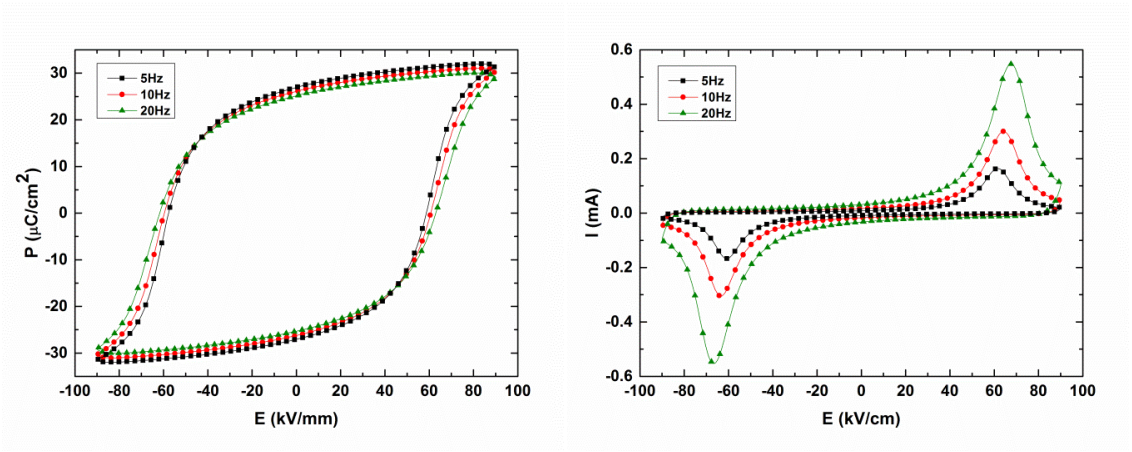

(a) (b)

Fig.4.58: Room temperature (a) P-E and (b) I-E loops for 1.5 μm grain size BNT ceramic, measured at 5, 10 and 20 Hz.

4.2.8 *Piezoelectric Response (d_{33}) vs. Temperature*

The d_{33} in BNT is grain size dependent: as the grain size is reduced the d_{33} decreases. During electrical poling, the stress at the grain boundary increases as the non-180 ˚ domains orientate themselves with the applied field. Back fields exerted by the grain boundaries oppose this domain switching. The high density of grain boundaries in the smaller grain size ceramics hinders domain alignment reducing the d_{33}.

The temperature dependence of the d_{33} measured during heating for each ceramic after poling in a 65 kV/cm electric field for 5 minutes is shown in Fig.4.59. The d_{33} remains relatively constant for the large micro-grain ceramics during heating. Between 150 and 175 ˚C, the d_{33} value decreases sharply from 64 to 17 pN and from 56 to 20 pN, for 10 μm and 1.5 μm ceramics respectively. The relatively high d_{33} value for the 500 nm ceramic is only maintained until 75 ˚C, where it then decreases more rapidly with increasing temperature. Whereas, the sharpest decrease in d_{33} value of the 150 nm ceramic occurs between 25 and 50 ˚C. None of the ceramics are fully depoled at 200 ˚C.

Room temperature d_{33} values of 1.9 pN and 1.6 pN were recorded for the 80 nm and 100 nm grain size BNT ceramics, respectively, after poling in a 65 kV/cm electric field for 10 minutes.

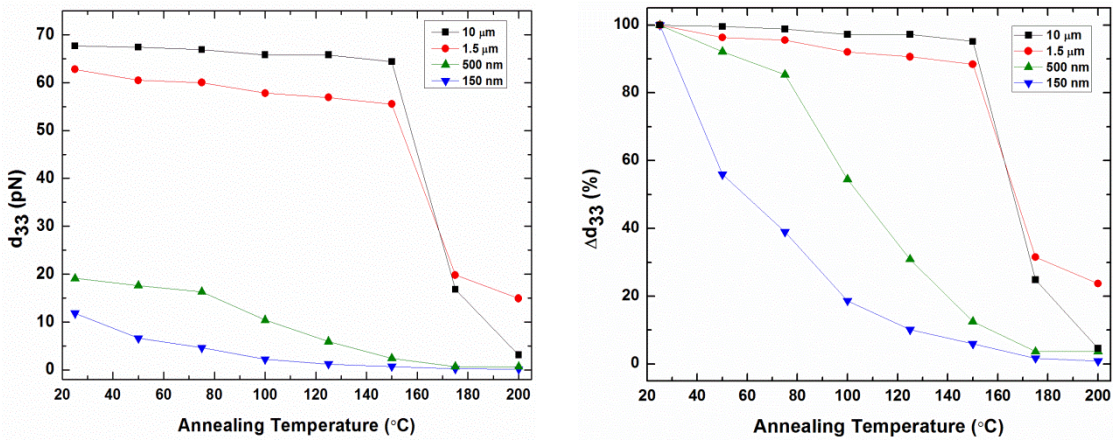

(a) (b)

Fig.4.59: (a) d_{33} and (b) Δd_{33} measured for each BNT grain size during depoling, after heating in silicon oil for 5 minutes at each temperature.

4.3 Discussion

4.3.1 Room Temperature

According to the literature, the crystal structure of BNT is rhombohedral *R3c* at room temperature. This structure was ascribed by Beanland and Thomas[157] after examining a defect free area of single crystal BNT using TEM. A defect structure of tetragonal $a^0a^0c^+$ platelets (TPs) and planer boundaries, including antiphase boundaries (APB), nanotwins (NTs) and domain walls with locally different symmetries were observed in the single crystal. NTs are expected to form at the point where a domain wall passes through either an APB or TP. Deactivation of the domain walls and pinning is likely to occur when a large number of NTs decorate the APBs and TPs. In order to maintain the structural continuity of the oxygen octahedra, the local tilt system surrounding the planer defect is expected to differ from that of the bulk in the form of a transitional region with local symmetry $a^-a^-c^-$. An average monoclinic *Cc* structure will be assigned to BNT by large-scale diffraction techniques when it has a high density of defects. This structure is largely reported for materials which have undergone a thermal annealing process.[150] High poling fields are expected to remove the defect structure in BNT causing the irreversible change in symmetry from *Cc* to *R3c*, observed by Rao et al.[149] using XRD.

The room temperature XRD results for the crushed BNT ceramics (Fig.4.33) show a clear transition in average crystal structure from rhombohedral *R3c* to monoclinic *Cc* with decreasing grain size. Both crystal symmetries could be fitted to the XRD data, however the structure with the better quality of fit was assigned to each grain size. A mixed structure of *R3c* and *Cc* symmetries may equally well exist in this material.

Grinding and crushing is known to have a similar effect as a weak poling field on the crystal structure of BNT.[150] Mechanical and electrical stresses induced in the system is known to increase the volume fraction of rhombohedral phase by reducing the density of NTs.[157] The powdered ceramics submitted for XRD were not annealed after crushing. The structures determined from these ceramics are therefore not in an equilibrium state. Electrical poling becomes difficult with decreasing grain size as the increased density of grain boundaries restricts the movement of the domain walls. A higher electric field is required for polarisation reversal as demonstrated by the increased coercive field (E_c) measured for the smaller grain ceramics (Fig.4.57). The

decrease in dielectric permittivity induced by electrical poling is lessened by the decrease in grain size (Fig.4.48), as fewer grains are able to expel the defect structure, retaining the *Cc* symmetry. The mechanical stress induced by crushing is unable to reduce the multi-domain structure and remove the high density of NTs in ceramics with nanometre grain size.

The largest grain ceramics are best described by the *R3c* structure in the mechanically stressed state after crushing. Thermal annealing however, does not fully transform the average structure of the largest grain ceramic (10 μm) back to the equilibrium *Cc* structure. While the dielectric permittivity of each ceramic increases after annealing (Fig.4.50), the value follows the same trend with changing grain size. Grain size is therefore thought to have a real influence on the defect structure in BNT. Back-scattered SEM, preformed at room temperature, revealed two types of domain morphology in the micrometre grain BNT ceramic: a striped and a cross-hatched domain structure. In the unpoled state, where the ceramic was thermally annealed prior to ion-beam polishing, both domain structures exist. The cross-hatched pattern (Fig.4.37) was found to transform on electrical poling to the striped domain structure (Fig.4.38). A decrease in both dielectric permittivity and loss were also observed for each grain size (Fig.4.48). Poling is expected to reduce the number of domain walls and therefore NTs by increasing the size of the domains aligned with the applied field transforming the crystal structure to rhombohedral. Grains with a high density of NTs are thought to have a cross-hatched domain pattern with *Cc* crystal structure. As demonstrated by Beanland and Thomas [157], a NT forms when a domain wall passes through an APB (or TP). Grains which contain a large number of NTs are therefore expected to have a high density of mobile domain walls, and/or APBs and TPs. An increase in domain wall density may account for the increase in dielectric permittivity measured in the BNT ceramics with reducing grain size. The saturation polarisation (P_{sa}) was found to decrease with decreasing grain size (Fig.4.57). While the NTs do not appear to hinder domain wall vibration, they may well pin the domain walls preventing the growth of large domains. A domain structure could not be clearly seen in the BNT ceramics with average grain size ≤ 500 nm using back-scattered SEM (Fig.4.40), however a small number of grains with a striped domain structure were observed in these ceramics after electrical poling (Fig.4.41). A domain structure must therefore exist in these small grains. A fine cross-hatched domain pattern is expected to form in these small grain size ceramics but because of the low resolution of the SEM detector at high magnification it

remains hidden. No domain walls were observed during TEM analysis of the nanometre BNT ceramic. The sample prepared for this technique however was extremely thin. In BNT, mobile domain walls are known to be expelled from very thin areas of material (t<~50 nm)[157] and may help to explain their absence from the TEM images. Small defects of ~10-15 nm in length, were observed in the TEM images of a 250 nm grain (Fig.4.35). These defects are reminiscent of the NTs previously reported by Beanland and Thomas[157].

For ceramics with a grain size ≤ 100 nm, the room temperature dielectric permittivity begins to decrease with further reduction in grain size. No evidence of domain reversal was observed in the I-E loops of these ceramics. However, ferroelectricity is still expected to occur at this grain size following the observation of features associated with T_m in the dielectric response and the detection of a small d_{33}. A single grain-single domain type structure, similarly reported for fine-grain $BaTiO_3$, is expected to occur. The relatively high permittivity values measured for these ceramics arise from the increase in internal stress within the single domain grains. The crystal structure of these ceramics should now be rhombohedral. The NT defect structure responsible for the *Cc* symmetry is no longer expected to form within these grains due to a loss of domain walls. The true crystal structure however could not be refined from the XRD data collected for the crushed nanograin ceramic (Appendix Fig.7.1.5). All of the tested structures (i.e. *Cc*, *R3c*, $Pm\bar{3}m$) provided an equally good fit. Alternatively, the C_c defect structure may still occur and instead the reduction in dielectric permittivity results from a dilution effect caused by the high density of grain boundaries.

4.3.2 Elevated Temperatures ≤ T_d

The high temperature XRD results show the rhombohedral *R3c* structure, refined for the unpoled and poled large micro-grain ceramics, to transform to monoclinic *Cc* with increasing temperature (Fig.4.33). The *Cc* symmetry best describes the unpoled 1.5 µm and poled 10 µm BNT ceramics at 200 ˚C and 250 ˚C, respectively. The monoclinic structure, however, could not be refined for the unpoled 10 µm grain ceramic. This structural transition is still expected to occur as the monoclinic symmetry appears within this system at 200 ˚C on cooling. The XRD data was collected at temperature intervals of 50 ˚C. It is likely that the *R3c*-to-*Cc* transition occurs above 200 ˚C but is not detected before the system transforms to a tetragonal *P4bm* structure near 250 ˚C.

The depolarisation temperature T_d of the poled 10μm ceramic lies within the temperature range of the *R3c*-to-*Cc* structural transition (Fig.4.51(a)). The frequency distribution of the dielectric response is minimal below T_d and only increases above this temperature. Electrical poling is thought to preserves the long-range FE order associated with the defect-free structure, shifting the structural transition to higher temperatures. The domain wall density is expected to increase with the loss of long-range FE order at T_d resulting in a sharp increase in permittivity. NTs develop where these domain walls pass through APBs or TPs forming the monoclinic defect structure.

High poling fields are expected to remove the defect structure in BNT causing the irreversible change in symmetry from *Cc* to *R3c* at room temperature. This transition is only observed in the large micro-grain ceramics. The loss of long-range polar order coincides with the reversal of this transition which appears as a sharp peak in the dielectric loss at T_d. Electrical poling is also expected to reduce the defect structure in the smaller micro-grain ceramics however not enough to transform the average structure. As the structure remains monoclinic for these ceramics, T_d does not appear as a sharp feature. The frequency distribution in the dielectric response does however show some variation between the different grain sizes, where the large micro-grain ceramics retain a minimal frequency distribution to higher temperatures.

A long-range FE order is less likely to be retained at these elevated temperatures when the grain size is reduced. This is evident in the temperature dependent d_{33} data (Fig.4.59).The domain walls in the smaller grains are expected to be more active at breaking the order when the temperature is increased. Back fields exerted by the high density of grain boundaries in the smaller grain size ceramics aid the switch back of the domains when the field is removed, reducing the piezoelectric response of these ceramic.

4.3.3 High Temperatures ≥ T_d

According to the literature, the TPs detected by TEM analysis in the room temperature structure of BNT form from a local disorder in the perovskite structure caused by the mixed A-site.[157] These platelets act as nucleation sites for polar nanoregions (PNRs) which are believed to be responsible for the relaxor behaviour in BNT.[132] Neutron diffraction analysis shows the *P4bm* symmetry to coexist with the *R3c*/*Cc* structure at 230 ˚C in poled BNT. The *P4bm* symmetry however, is not detected by XRD analysis

below 300 ˚C. The diffraction peaks appear singlet in nature at 300 ˚C and fits well with a single phase cubic $Pm\bar{3}m$ model. This cannot be real as neutron diffraction patterns exhibit prominent ½$\{ooe\}_c$-type superlattice peaks corresponding to a *P4bm* phase at this temperature. Tetragonal splitting of the pseudocubic $\{200\}_c$ Bragg peak only becomes noticeable above 300 ˚C. Rao et al.[151] note a complete disappearance of the *R3c* phase above 300 ˚C. This observation disagrees with the neutron study by Jones and Thomas[110],[111] for unpoled BNT, who report the *R3c* and *P4bm* phases to coexist up to 397 ˚C. At 520 ˚C, the structure appears cubic with $Pm\bar{3}m$ symmetry. Neutron diffraction however, show the ½$\{ooe\}_c$-type superlattice peaks to persist beyond this temperature.[151]

The high temperature XRD patterns collected for the BNT ceramics of different grain size share similarities to the XRD results reported by Rao et al.[151]. The ceramics with grain size below 10 µm could not be fitted with the *P4bm* structure. Both the 150nm and 500 nm ceramics remain monoclinic up to 250 ˚C and 300 ˚C respectively, where the structure then transforms to a cubic $Pm\bar{3}m$ symmetry. The same *Cc*-to- $Pm\bar{3}m$ structural transition also occurs for the 1.5 µm ceramic near 300 ˚C. The absence of the *P4bm* symmetry in these ceramics may be a result of the short coherence length of the in-phase tilts which remain hidden to XRD. Evidence of a structural transition to the *P4bm* phase was found in the XRD patterns collected from the largest micro-grain size ceramic. In the unpoled state, the *P4bm* symmetry was found to fit well with the data collected at 250 and 300 ˚C, before transforming to the cubic structure at 350 ˚C. In the poled state, the structure remains monoclinic at 250 ˚C, but then transforms to the tetragonal structure with further increase in temperature. The *P4bm* symmetry fits the structure up to 500 ˚C, before changing to cubic at 550 ˚C.

According to the literature, in-phase tilts associated with the tetragonal symmetry first appear near the depolarisation temperature T_d (~150 ˚C). The long range coherence length of the field-stabilised rhombohedral phase is thought to suddenly decrease at this temperature with the growth of the incompatible in-phase tilted *P4bm* regions.[151] These observations led Rao et al.[151] to associate the monoclinic distortion observed by bulk diffraction techniques specifically with the strain generated by localised in-phase $a^0a^0c^+$ tilted regions in the rhombohedral matrix. Thomas et al.[157] have since linked the monoclinic distortion with a defect structure of NTs which form when a domain wall passes through either an APB or TP.

The *R3c*-to-*Cc* structural transition associated with T_d is more likely to result from a loss of long-range FE order due to thermal fluctuations rather than from sudden growth of *P4bm* regions. If this were the case, the depoling temperatures of the polar state induced by either poling the ceramic at room temperature (T_{do}) or in a bias field applied during heating (T_{db}) should be the same. The bias field applied during heating instead helped to retain the polar state shifting the depoling temperature to higher temperatures ($T_{db} > T_{do}$) (Fig.4.54). This does not mean that *P4bm* regions do not grow at this transition. The TPs form from a local disorder that could increase with the loss of the field ordered state. The NT defect structure may well form from an increase in both the number of domain walls and TPs. The dielectric permittivity of the BNT ceramics was found to increase with increasing grain size at these elevated temperatures (Fig.4.52). A higher density of domain walls from either the rhombohedral phase or the tetragonal PNRs is expected to occur in the larger grains.

The TPs grow in size and number at the expense of the *R3c* phase, forming *P4bm* PNRs with increasing temperature. XRD refinement shows a shift in the *Cc*-to-*Pm*$\bar{3}$*m* transition towards lower temperatures with decreasing grain size (Fig.4.33). Rao et al.[151] note the coherence length of the tetragonal $a^0a^0c^+$ tilted regions to decrease with applied field. Fewer TPs are therefore expected to be present in the larger grains of BNT below T_d. As a long-range polar order is not observed in the micro-grain size ceramics below 1.5 µm, a larger number of PNRs may well exist in these smaller grains at lower temperatures. The relaxor behaviour associated with these PNRs may account for the significant frequency dispersion in the dielectric response above room temperature (Fig.4.50). For the large micro-grain size ceramics, the stabilised, defect-free rhombohedral phase increases the temperature of both the *R3c*-to-*Cc* and *Cc*-to-*P4bm* structural transitions (Fig.4.33). The influence of the long-range ordered structure on the transition temperatures can be clearly seen by comparing the XRD results for the 10 µm ceramics in the unpoled and poled state.

The dielectric response of the 10 µm ceramic shows a sharp increase in permittivity as well as a decrease in the frequency dispersion at T_{RE} in both unpoled and poled states (Fig. 4.49(a) and Fig.4.51(a), respectively). This feature coincides with the *P4bm* structure. The coherence length of the *P4bm* distortion is expected to increase at this temperature, becoming large enough to be detected by XRD. In a typical relaxor, the

PNRs grow with decreasing temperature. A dynamic slowing of their fluctuations occurs below T_m and the system enters an isotropic relaxor state where the polar domains are randomly oriented.[52] The PNRs in BNT are also expected to grow with decreasing temperature towards T_m. However, larger *P4bm* microdomains are thought to percolate the grains causing the frequency dispersion to vanish between T_{RE} and T_M. Below T_{RE}, the system enters a dispersive relaxor state where the microdomains break into randomly oriented, slowed down nanodomains. If BNT behaved as a typically relaxor, the PNRs would be expected to grow with continued decrease in temperature, however this is unlikely as the structure transforms to *R3c*/*Cc*. Above T_m, thermal fluctuations break up the larger domains reforming the smaller PNRs. The decrease in size of the *P4bm* regions may account for this change in structure detected at 350 ˚C in the unpoled ceramic. Poling is thought to influence the size of the *P4bm* nanodomains, which remain detectable by XRD up to 550 ˚C. The frequency distribution in the dielectric permittivity at temperatures above T_m is also greatly reduced after room temperature poling. T_{RE} is also observed in the 1.5 μm ceramic, however the tetragonal symmetry is not detected by XRD for this grain size. None of the ceramics with grain size ≤ 500 nm show this feature in their dielectric permittivity.

Grain size affects both the temperature and the permittivity value of the T_m peak in BNT. T_m broadens and shifts to higher temperatures as the grain size is reduced (Fig.4.50). Similar grain size dependence is observed for the permittivity peak at the orthorhombic-to- tetragonal structural transition in $BaTiO_3$. The effect of grain size on this transition has been explained in terms of transformation strain energies and twinning mechanisms. The simple ability of the orthorhombic structure in $BaTiO_3$ to spontaneously polarise along twice as many equivalent directions as the tetragonal phase makes it more effective at minimising the transformation stresses than the tetragonal phase, stabilising the lower temperature structure in the smaller grains. The same theory could be applied to T_m in BNT. Although no static structural transition takes place at T_m, a gradual change in structure occurs as the *P4bm* phase increases at the expense of the *R3c*/*Cc* structure. The phase below T_m may be more stress accommodating than the phase above T_m. The rhombohedral FE structure has eight possible domain states compared to six for the tetragonal structure.[146]

The temperature of the *Cc*-to-*Pm*$\bar{3}$*m* structural transitions determined by XRD do not match the grain size effect observed in the dielectric response at T_m. If the same theory

applies to T_m as the orthorhombic-to- tetragonal transition in $BaTiO_3$, the lower temperature *R3c*/*Cc* structure would be expected to be more stable in the nano-grain size ceramics than the *P4bm* phase. As a greater proportion of the nano-grains are of *R3c*/*Cc* phase, T_m will shift to higher temperatures. However, XRD analysis show the *Cc*-to- *Pm*$\bar{3}$*m* structural transition to occur at lower temperatures in the smaller grain ceramics, implying that a greater proportion of *P4bm* phase is present in smaller grains at lower temperatures. This XRD result may be misleading. A greater fraction of the *P4bm* phase could occur in the larger grains than the smaller grain however, the absolute volume of *R3c*/*Cc* phase would still be greater than in the smaller grains. This could result in the XRD detector continuing to see *R3c*/*Cc* phase in the larger grains up to higher temperatures.

As the grain size is reduced, the permittivity value of the peak decreases (Fig.4.50). The increased stress exerted at the grain boundaries of the smaller grains hinders the domain wall motion suppressing the permittivity.

4.3.4 Cooling

The influence of electrical and mechanical stresses on the structural transitions can be clearly seen when comparing the heating and cooling runs of the XRD results (Fig.4.33). Despite the different transition temperatures for the 150 nm, 500 nm and 1.5 µm ceramics during heating, all the ceramics undergo a *Pm*$\bar{3}$*m*-to-*Cc* structural transition near 200 ˚C. No feature associated with T_s/T_d is observed in the dielectric permittivity of these ceramics on cooling (Fig.4.49 and 4.51). Below T_{RE}/T_m, the frequency distribution decreases smoothly with decreasing temperature.

The *Cc*-to-*P4bm* and *P4bm*-to- *Pm*$\bar{3}$*m* structural transitions refined for the 10 µm ceramic in both the unpoled and poled states show no temperature hysteresis between the heating and cooling runs. Yet, the dielectric response at these elevated temperatures is not the same as T_{RE} occurs at higher temperatures on heating. The temperature difference between $T_{RE\text{-}Heating}$ and $T_{RE\text{-}Cooling}$ is less than 50 ˚C and occurs within the temperature interval between XRD measurements so is not detected. The *Cc* -to-*R3c* transition however, occurs at lower temperatures on cooling. No feature associated with T_d is observed in the dielectric response on cooling. The dielectric response on cooling is the same for the unpoled and poled samples as heating to 600 ˚C anneals the material destabilises the long-range FE order associated with the *R3c* phase. A feature T_{db}

appears in the dielectric permittivity when the ceramic is cooled in a bias-field (Fig.4.54). The bias-field is thought to stabilise the long-range FE order, which appears at higher temperatures when the bias-field strength is increased from 3 kV/cm to 5 kV/cm.

The temperature of the $Pm\bar{3}m$-to-*P4bm* transition refined from the cooling XRD data is very different for the unpoled and poled states of the 10 µm ceramic. The *P4bm* phase is expected to occur in both samples up until temperatures of 550 ˚C. However, the coherence length of the *P4bm* PNRs is only long enough to be seen by XRD in the poled sample. Similarly, the frequency distribution in the dielectric permittivity above T_m remains minimal on cooling for the poled sample. Heating to 700 ˚C does not completely remove the effects of the poling on the domain structure of the BNT ceramic. Remnants of the FE structure are still expected to exist within the high temperature cubic phase.

4.4 Summary

High density ceramics of lead-free BNT, ranging in grain size from 80nm to10µm, were successfully sintered from nanometre and micrometre grain size powders by SPS and conventional sintering techniques. Crystal and domain structure analysis was combined with dielectric and electromechanical measurements to reveal the grain size effect in ceramic BNT.

Grain size was shown to influence the room temperature defect structure, transforming the average crystal structure from rhombohedral *R3c* to monoclinic C_c with reducing grain size. The increase in dielectric permittivity with decreasing grain size is caused by high domain wall density linked with a cross-hatched domain pattern. This finding is consistent with the literature which identifies interactions between domain walls and APB or TPs as the source of the C_c NT defect structure. High grain boundary density was found to restrict the electric field induced C_c-to-*R3c* transition, maintaining the multi-domain defect structure. The depoling temperature T_d associated with the *R3c*-to-C_c transition occurs at higher temperatures for larger micrograin size ceramics but is independent of electric field strength. Grain boundaries are expected to have less impact on the structure of these ceramics allowing the long-range *R3c* FE order to be retained

to higher temperatures. Evidence of a critical grain size for ferroelectricity was not found within the investigated grain size range, however a decrease in dielectric permittivity with further reduction in grain size for ceramics with nanometer ($\leq$ 100 nm) grains suggest a grain size limit may exist for the C_c defect structure. Alternatively, the C_c defect structure may still occur and instead the reduction in dielectric permittivity results from a dilution effect caused by the high density of grain boundaries.

Grain size affects both the temperature and the permittivity value of the high temperature T_m peak, measured at 100 kHz, in BNT. T_m broadens and shifts to higher temperatures as the grain size is reduced while the increased stress exerted at the grain boundaries of the smaller grains hinders the domain wall motion suppressing the permittivity value. Similar grain size dependence is observed in $BaTiO_3$ but at the orthorhombic-to- tetragonal structural transition rather than T_c. Although no static structural transition takes place at T_m in BNT, a gradual change in structure occurs as the *P4bm* phase increases at the expense of the *R3c*/*Cc* structure. A larger number of domain states are thought to be offered by the phase below T_m making it more stress accommodating.

While the grain boundary density in BNT has similar influence on domain wall motion and polarisation reversal as other lead-free FEs, the grain size effect in BNT is different because of the C_c defect structure and the effect of the NTs on the FE domain structure and associated properties.

Chapter 5 Grain Size Effect in 94%$Bi_{0.5}Na_{0.5}TiO_3$-6%$BaTiO_3$

The morphotropic phase boundary (MPB) solid-solution (1-*x*)$Bi_{0.5}Na_{0.5}TiO_3$-*x*$BaTiO_3$ was discovered nearly 30 years ago[13] during the search for a new group of lead-free piezoelectric ceramics to replace the popular piezoelectric ceramic Pb (Zr_xTi_{1-x})O_3 (PZT). Despite the considerable attention paid to this group of materials, the exact position of the MPB is still under question due to the weak correlation between structure and property. Further, structural analysis of this system is restricted because of the ambiguity surrounding the crystal structure of the basic end-member BNT. As demonstrated in the literature review, the nature of the synthesis and characterisation method used clearly influence the MPB range reported by different groups. Ceramic grain size is similarly expected to influence the properties of this material, as demonstrated in other ferroelectric (FE) materials. Furthermore, electrical poling irreversibly alters the phase structure of the solid-solution changing the morphotropic phase from a boundary ($0.05 \leq x \leq 0.06$) in the equilibrium state to a wide region ($0.06 \leq x \leq 0.10$) in the poled state.[187]

The effect of grain size on the structure and electrical properties of the MPB composition 0.94$Bi_{0.5}Na_{0.5}TiO_3$-0.06$BaTiO_3$ (BNBT-6) is examined in this chapter. While the MPB is expected to cover a range of compositions, a concentration of 6% $BaTiO_3$ was chosen as it exhibits the most enhanced dielectric and piezoelectric properties in the poled state[13]. The different phase diagrams proposed for the equilibrium and poled states outlined in the literature review raises the question of how grain size will affect the position of the boundary. Particularly in the case of BNBT-6 which is believed to undergo a field-induced phase separation of its equilibrium cubiclike structure formed of *R3c*/*P4bm* nanodomains to a MPB structure of cubiclike/ tetragonal *P4mm* phases which was observed in annealed BNBT-7.[12] This field-induced phase is also field strength dependent, transforming to a *R3c* long-range FE order in high applied fields (≥ 6 kV/cm).[198] To help answer this question crystal and domain structure analysis techniques are used to explore the grain size dependence of the MPB as well as the impact of poling fields on the structure. The field-strength dependence of different grain size ceramics will also be tested by DC bias-field dielectric measurements, thermal depoling experiments and hysteresis loop tests.

Temperature dependent dielectric measurements will be used observed the effect of grain size on the dielectric features T_d and T_m to help determine whether or not BNBT-6 adopts the same grain size model as other MPB compositions, for example $Na_{0.5}K_{0.5}NbO_3$, or other lead-free FEs such as $BaTiO_3$, Aurivillius phase $Bi_{3.15}Nd_{0.85}Ti_3O_{12}$ and multiferroic $BiFeO_3$.

5.1 Ceramic Processing

Powders of BNBT-6 were prepared by solid-state reaction. Oxides and carbonates of the raw materials Bi_2O_3(99.9% Sigma-Aldrich), TiO_2(99.8% Sigma-Aldrich), Na_2CO_3(99.5% Alfa Aesar) and $BaCO_3$ (99.8% Alfa Aesar) were weighed according to the stoichiometric formula $Bi_{0.5}Na_{0.5}TiO_3$-0.06$BaTiO_3$. To correct for the effect of excess water and preserve the stoichiometry of the powder mixture, the hydrophilic Na_2CO_3 and $BaCO_3$ powders were weighted while hot after drying for 24 h at 200 °C. The powders were then mixed in ethanol for 2 h by planetary ball-milling at 350 rpm with zirconia balls. After drying, the powder mixture was sieved in preparation for calcination.

5.1.1 Determining the Calcination Temperature

The calcination temperatures reported in the literature for the solid-state reaction of BNBT, range from 800-1100 ˚C and vary with the number of calcination steps.

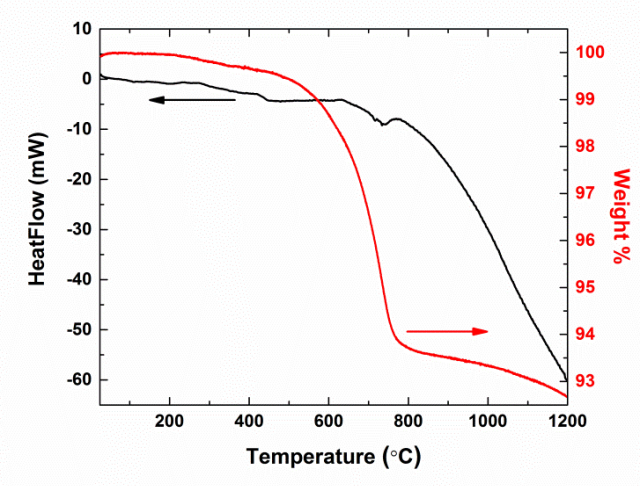

Fig.5.1: STA data for Na_2CO_3+Bi_2O_3+$BaCO_3$+TiO_2 powder mixture

The STA data obtained from the BNBT-6 powder mixture shows a similar calcination sequence to BNT with a steep decease in mass occurring between 500 ˚C and 800 ˚C

and an endothermic heat flow peak at 750 ˚C (Fig.5.1). A minimum calcination temperature of 800 ˚C was estimated from this data.

Samples of the powder mixture were initially calcinated at 800 ˚C, 850 ˚C and 900 ˚C for 4 hours at a heating rate of 5 ˚C/min, and then submitted for powder XRD analyses. In addition to the pseudo-cubic perovskite pattern, peaks from a secondary $BaTiO_3$ phase were observed in the XRD profiles, shown in Fig.5.3. The intensity of the secondary peaks, however decrease with increasing calcination temperature. Higher calcinations temperatures of 925 ˚C, 950 ˚C, 1000˚C and 1050 ˚C were then applied to the powder mixture. Single phase formation occurred with the disappearance of the secondary $BaTiO_3$ peaks at 1000 ˚C and 1050 ˚C. From these results, it was concluded that BNT and $BaTiO_3$ form separately during calcination before combining to form BNBT-6 as the temperature is increased. The melting point of the raw material Bi_2O_3 (T_{mp}= 824 ˚C) is lower than the single phase formation temperature of BNBT-6.[142] Precipitation of bismuth is expected to occur if any Bi_2O_3 is present in the powder mixture as the calcination temperature approaches the Bi_2O_3 melting point. To reduce the risk of non-stoichiometry from the loss of bismuth, a two-step calcination method was applied to BNBT-6, depicted in Fig.5.2.

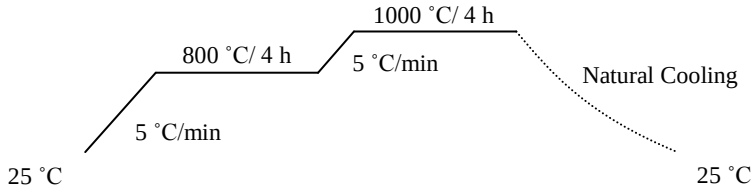

Fig.5.2: Schematic demonstrating the two-step calcination method used to prepare BNBT-6 powder.

By allowing BNT to form at 800 ˚C before increasing the temperature to 1000 ˚C, the amount of Bi_20_3 present in the powder at the elevated temperature is reduced. The XRD data collected from powder calcinated by this two-step method is shown in Fig.5.4.

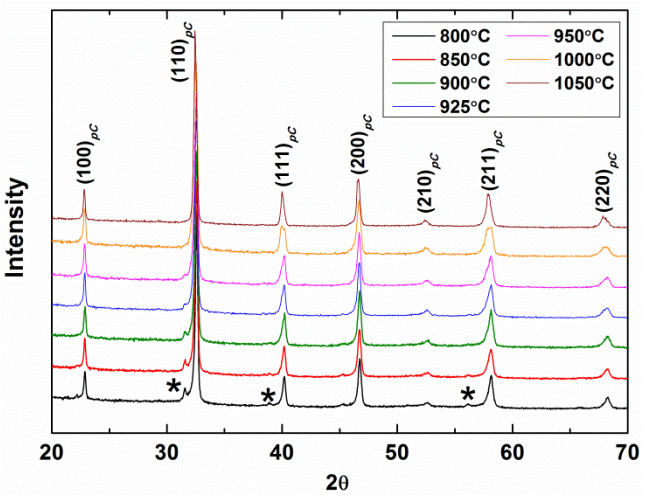

Fig.5.3: Powder XRD patterns for BNBT-6 powders calcinated at temperatures ranging from 800 to 1050 ˚C, indexed using a pseudo-cubic (*pC*) unit cell. Bragg peaks from secondary $BaTiO_3$ phase are marked by *.

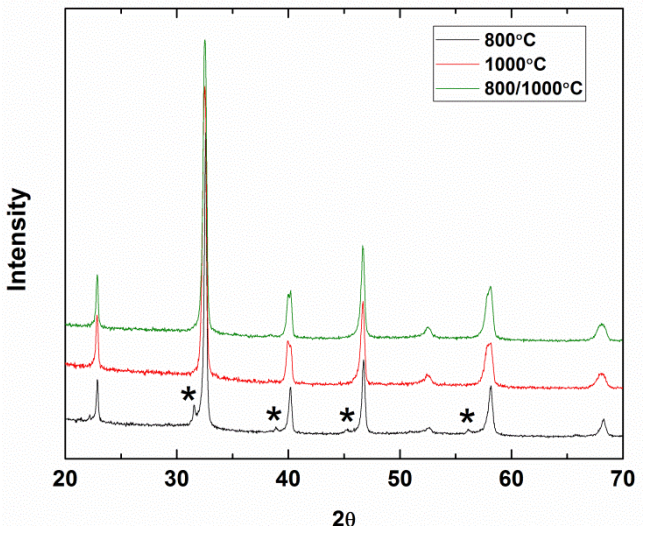

Fig.5.4: Powder XRD pattern after calcination using the two-step method. The profile is compared with single step calcinations at 800 ˚C and 1000 ˚C.*: peaks from secondary $BaTiO_3$ phase.

5.1.2 Ball-Milling

Following calcination, the BNBT-6 powder was re-milled for 4h in ethanol to break down any agglomerates formed during calcination and to reduce the overall grain size of the powders. However, a milling period of 4 h was not sufficient to homogenise the grain size. Although the powder appeared at first to be homogeneous, ceramics sintered from this powder show a range of grain sizes from tens to hundreds of nanometres in each sample. SEM images of the powder and ceramic are shown in Fig.5.4. Longer milling periods of 6, 8 and 12 h were then tested. A slower milling speed of 250 rpm

was applied when milling for 12 h to reduce the risk of contamination from the nylon milling pot. Both the ceramics sintered from the 8 h/350 rpm and 12 h/250 rpm milled powders have a relatively narrow grain size distribution (Fig.5.5). To avoid the risk of agglomerates forming in the fine powder during long periods of ball-milling[142], the shorter milling period of 8 h was selected for future powder processing. The dried powders were then sieved again using a 250 μm mesh in preparation for sintering.

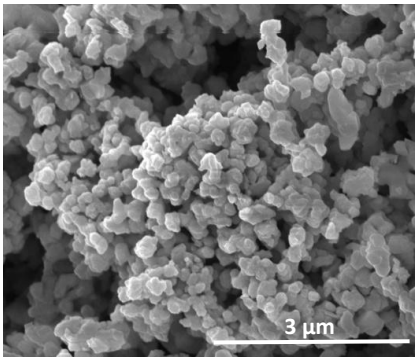

(a1)

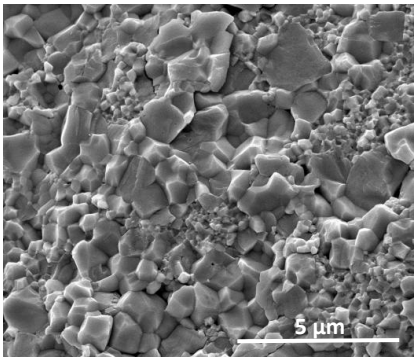

(a2)

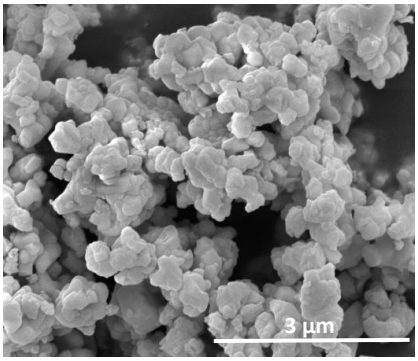

(b1)

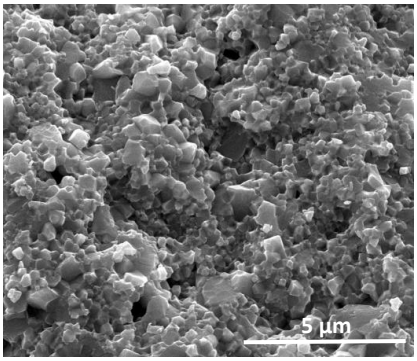

(b2)

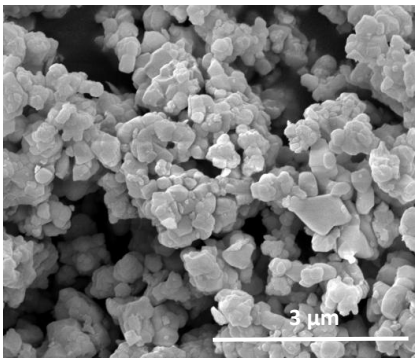

(c1)

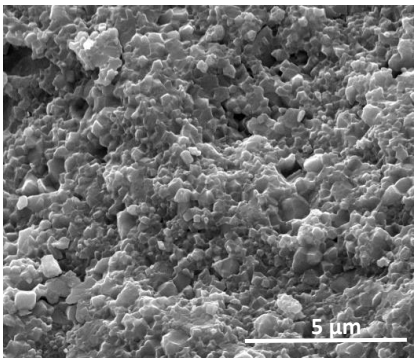

(c2)

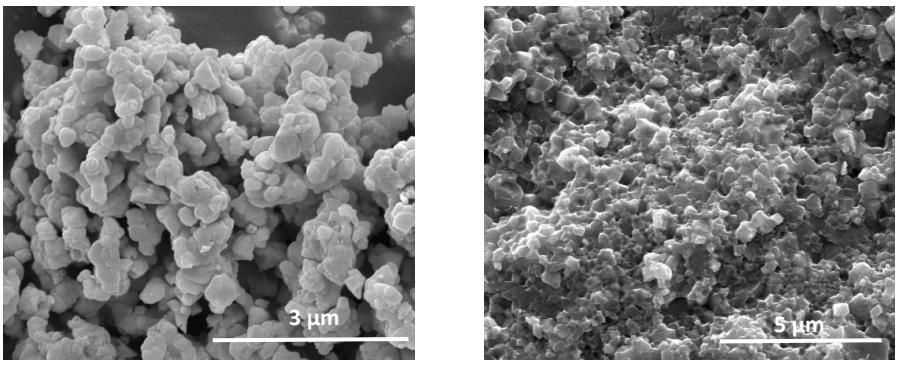

(d1) (d2)

Fig.5.5: SEM images of (a1)-(d1) powder and fracture surface of the corresponding (a2)-(d2) ceramic sintered by SPS at 975 ˚C(5 min)/60 MPa. The different milling duration and speeds used to prepare each powder are as follows: (a1)-(a2) 4 h/350 rpm, (b1)-(b2) 6 h/350 rpm, (c1)-(c2) 8 h/350 rpm and (d1)-(d2) 12 h/250 rpm.

Nano-sized BNBT-6 powder was prepared with further milling using a high-speed ball-mill. Initially, ethanol was used as the milling solvent however this had to be replaced with deionised water due to concerns over the volatility of ethanol while milling at high speeds. To reduce the ZrO_2 contamination from the milling media, a milling period of 1 h was used. This method of milling was found to reduce the average grain size from 230 nm to 75 nm.SEM images of the high-speed ball-milled powders are shown in Fig.5.6. Before sintering, the powder was dried for 4 h at 600 ˚C to remove any moisture remaining from the milling solvent thereby helping to improve the density of the ceramics sintered from this powder.

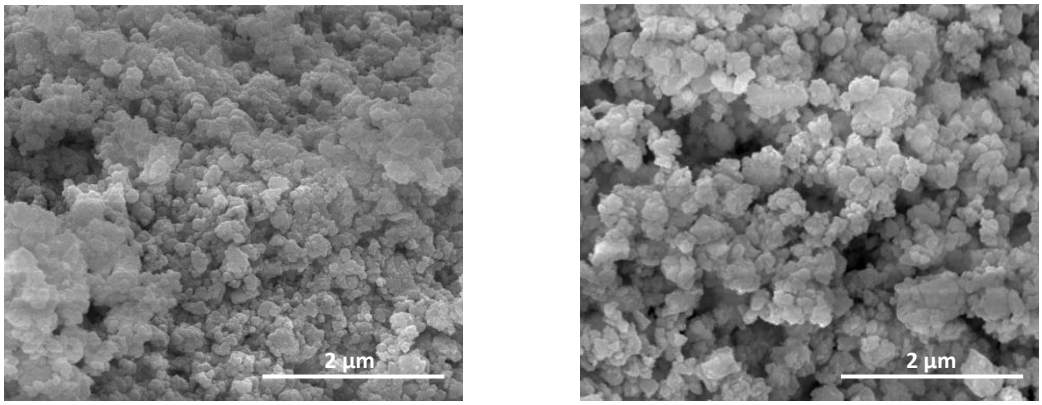

(a) (b)

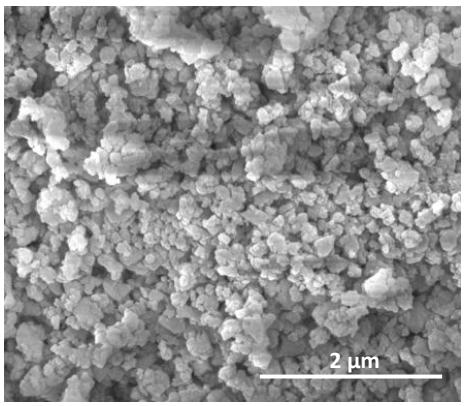

(c)

Fig.5.6: SEM images of BNBT-6 powder after ball-milling for (a) 1 h and (b) 2 h in de-ionised water and (c) 2 h in ethanol.

5.1.3 Chemically Prepared Powder

Nano-grained BNBT-6 powder free from zirconia contamination was prepared using sol-gel processing by Dr. Qinghui Jiang. The average grain size of this powder determined by SEM (Fig.5.7) is 60 nm.

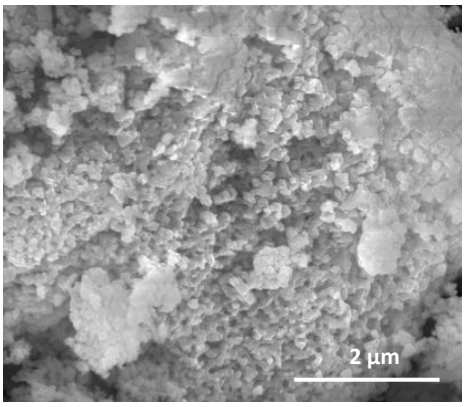

Fig.5.7: SEM image of the BNBT-6 powder prepared by sol-gel.

5.1.4 Sintering Techniques

Two different sintering techniques: spark-plasma sintering and conventional sintering were used to prepare high density ceramics of different average grain size. Particular care was taken to ensure that the ceramics sintered using these methods were of a density greater than 95 % of the theoretical density to guarantee a meaningful comparison between the different grain size samples.

(i) SPS

SPS is particularly useful for sintering ceramics with grain size below 1µm as it combines high heating rates with mechanical loading. Fast, low temperature densification allows the nanostructure of the powders prepared by regular and high speed ball-milling and chemically by sol-gel processing to be retained using this sintering technique.

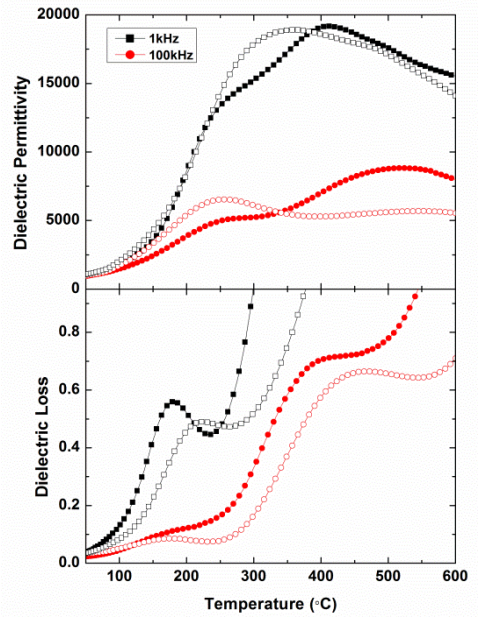

Fig.5.8: Temperature dependence of the dielectric response for the SPS ceramic sintered at 1000 ˚C after annealing for 24 h at 900 ˚C (solid symbol) and 950 ˚C (open symbol). Higher temperature annealing helps to reduce the effect of point defects, particularly in the low frequency data.

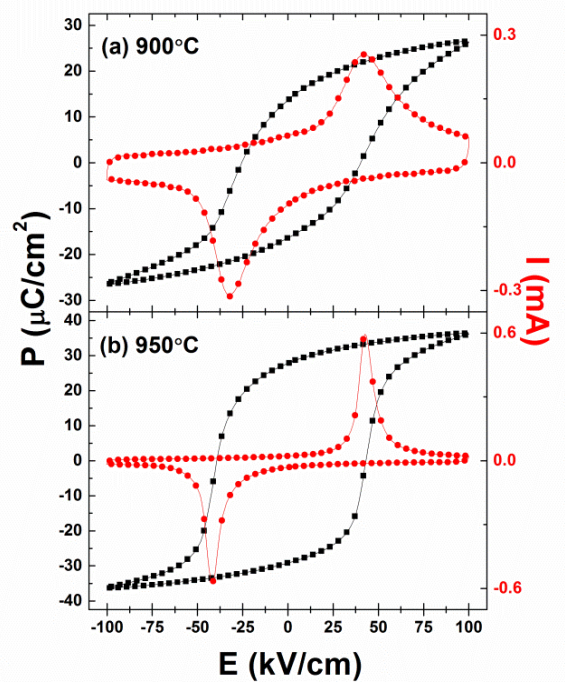

Fig.5.9: P-I-E loops measured for the SPS ceramic sintered at 1000 ˚C after annealing for 24 h at (a) 900 ˚C and (b) 950 ˚C.

To remove the oxygen vacancies created during SPS as well as the surface carbon contamination from the graphite paper surrounding the samples, the BNBT-6 ceramics were annealed in air for 24 h at 100 ˚C below their sintering temperature. As was also the case for BNT, the condition used to preserve the grain size was found to restrict the annealing process, particularly for the ceramics sintered at high temperature. Evidence of oxygen vacancies was observed in the dielectric response (Fig.5.8) and P-E loops (Fig.5.9). Higher annealing temperatures closer to their sintering temperature were then applied to these ceramic.

(ii) Conventional Sintering

Conventional sintering was used to prepare ceramics with micrometre sized grains. Green bodies cold-pressed from the regular ball-milled powder were sintered for 2 h in air using a conventional furnace with a slow heating rate of 3 ˚C/min. The cohesive nature of the BNBT-6 powder allowed for the green bodies to be pressed without the need for binder.

5.1.5 Determining the Sintering Temperature

The minimum sintering temperature of the BNBT-6 powder was determined from the SPS output profile of the piston speed while sintering under minimum pressure. Low temperature, high pressure conditions were used when sintering the high-speed ball milled and chemically prepared powders. Different holding times of 5 to 20 minutes were used during low and high pressure sintering, respectively, to ensure a homogeneous temperature was applied throughout the sample. For grain growth by SPS, temperatures higher than the minimum densification temperature were applied. Melting and a loss of vacuum were observed during sintering at temperatures above 1000 ˚C (Fig.5.10). A-site vacancies introduced into the composition following the volatilisation of the Bi and Na ions are thought to be responsible for the non-symmetry in the I-E loops of these ceramics, shown in Fig.5.11.

A minimum temperature 100 ˚C above the ‘pressureless’ SPS sintering temperature determined for the regular ball-milled powder was used as a minimum sintering temperature for conventional sintering. Ceramics were sintered at 50 ˚C intervals above this temperature and their densities were compared. The density of the ceramics increases reaching a maximum value at 1200 ˚C before decreases with further increase of temperature. Melting occurred at 1300 ˚C. No evidence vacancies induced by

volatilisation of the A-site ions were observed in the electrical properties of the conventional sintered ceramics.

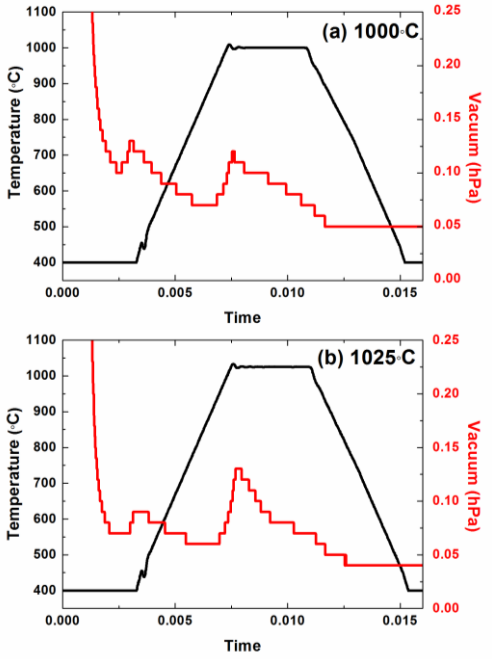

Fig.5.10: SPS sintering profiles for BNBT-6 ceramics sintered at (a) 1000 ˚C and (b) 1025 ˚C. A loss of vacuum (>0.1 hPa) occurs during holding (5 minutes) at temperatures higher than 1000 ˚C.

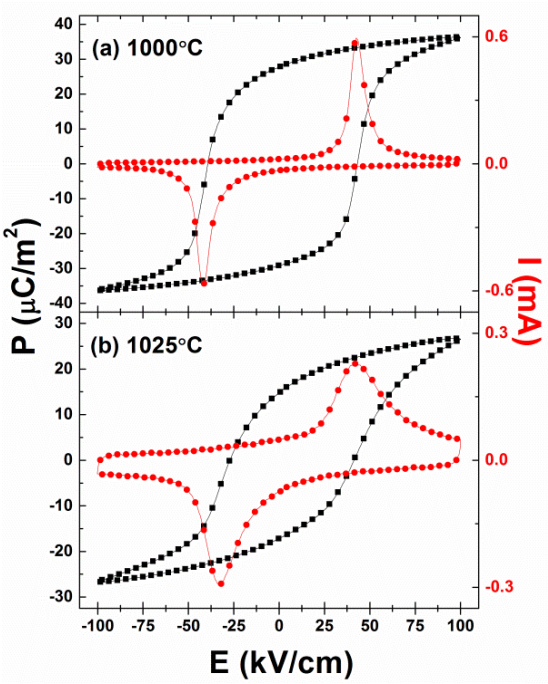

Fig.5.11: P-I-E loops of the BNBT-6 ceramics sintered by SPS at (a) 1000 ˚C and (b) 1025 ˚C for 5 minutes at a pressure of 60 MPa. The non-symmetric I-E loops in (b) provide evidence of oxygen vacancies.

The dependence of ceramic density on the sintering temperature for the SPS and conventional sintering techniques is shown in Fig.5.12.

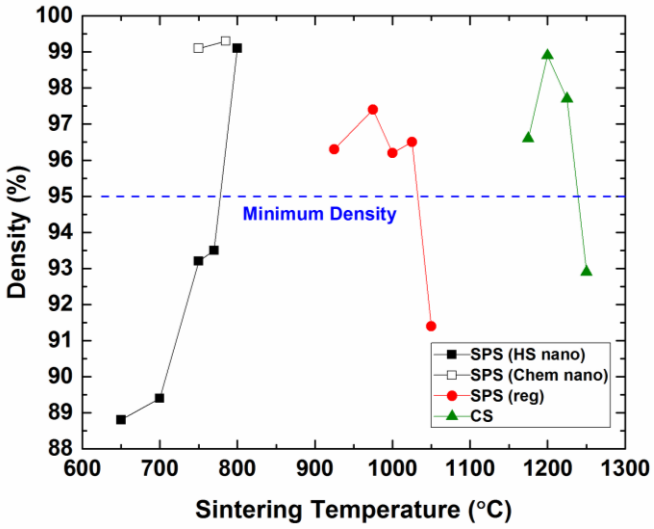

Fig.5.12: Density vs. temperature diagram for the BNBT-6 ceramics sintered using SPS and conventional sintering (CS) techniques from chemically prepared (Chem nano), high-speed ball-milled (HS nano) and regular ball-milled (reg) powders.

5.1.6 Determining the Grain Size

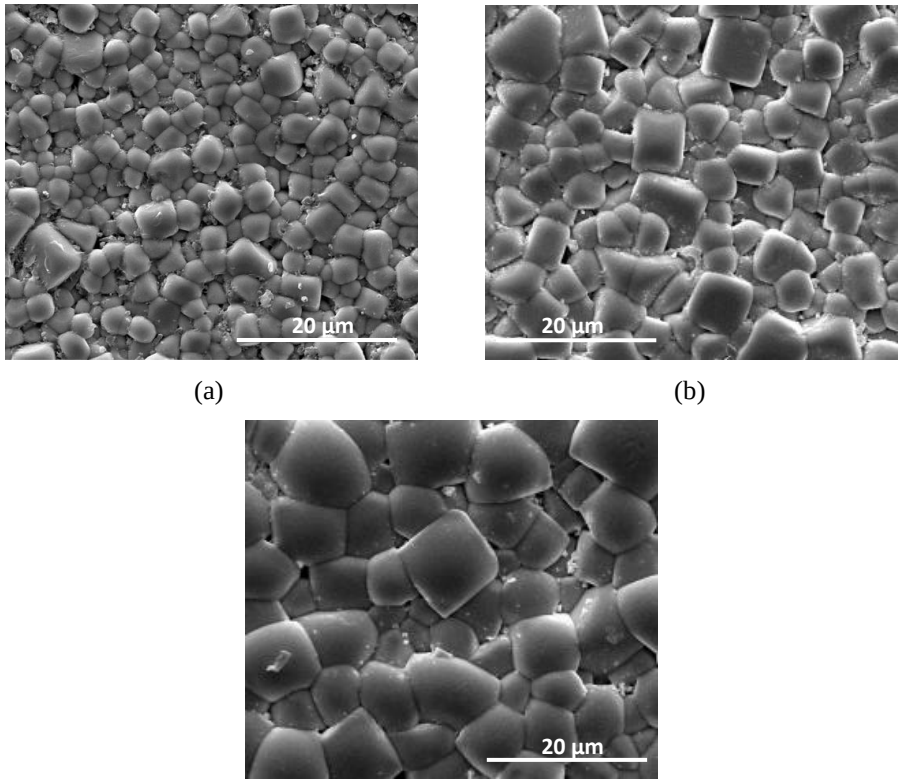

(a) (b)

(c)

Fig.5.13: SEM micrographs of the natural surface BNBT-6 ceramics sintered at (a) 1175 ˚C, (b) 1200 ˚C and (c) 1225 ˚C for 2 h using a conventional furnace.

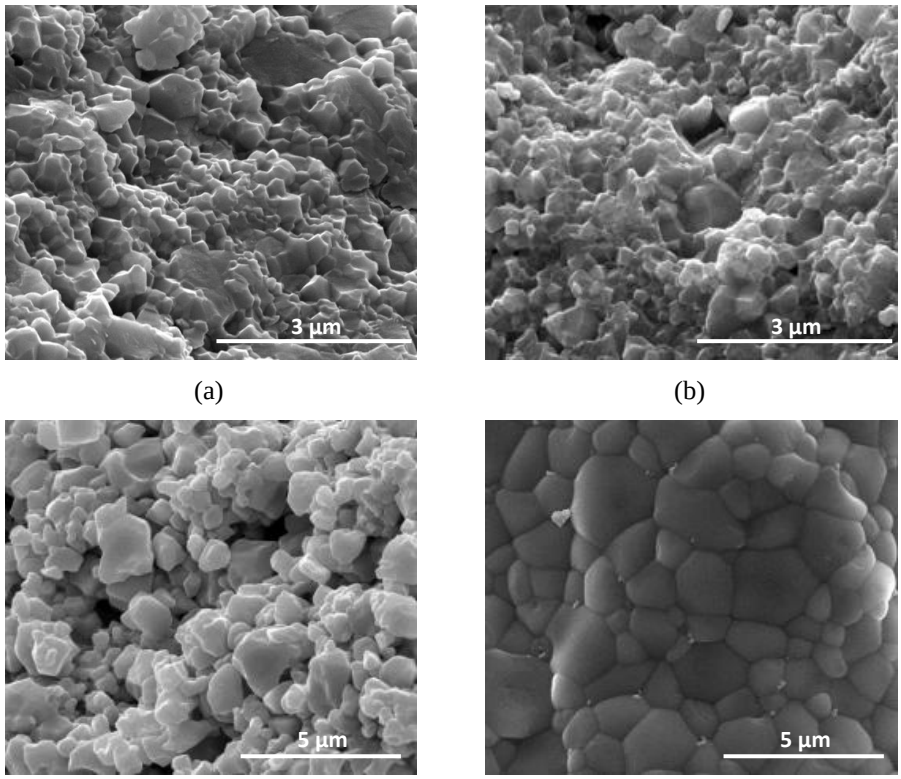

(a) (b)

(c) (d)

Fig.5.14: Fracture surface SEM images of SPS BNBT-6 ceramics sintered at (a) 925 ˚C/80 MPa, (b) 975 ˚C/60 MPa, (c) 1000 ˚C/60 MPa and (d) 1025 ˚C/60 MPa for 5 mins with regular ball milled powder.

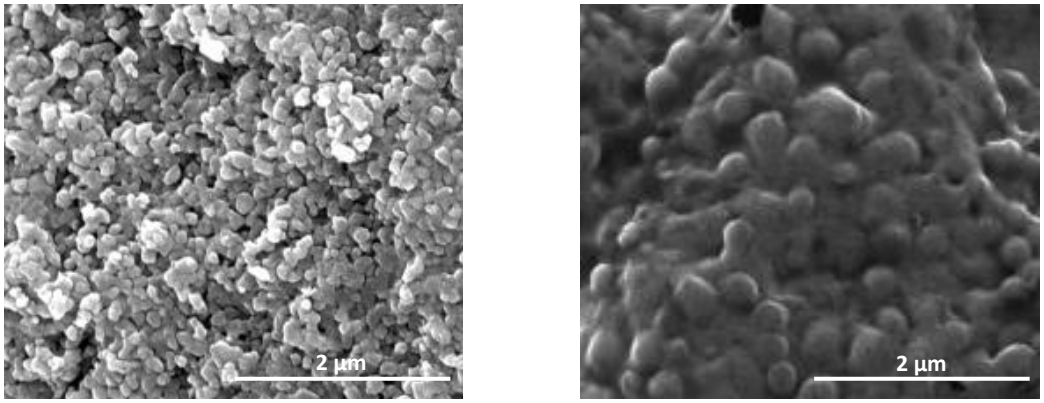

(a) (b)

Fig.5.15: SEM images of the fracture surface of high pressure SPS-ed BNBT-6 ceramics sintered at (a) 750 ˚C/450 MPa and (b) 785 ˚C/350 MPa for 20 mins with chemically prepared powder.

An estimate of the average grain size, taken from the SEM images of the natural surface of the conventionally sintered ceramics and the fracture surface of the annealed SPS ceramics shown in Fig.5.13-5.15, are summarised in Fig.5.16.

For structural and physical property analysis, two-three high density (>95 %) BNT ceramics were selected from each of the following grain size ranges: (i)10 nm-100 nm, (ii)100 nm- 1 µm and (iii) greater than1 µm. The processing conditions used to prepare these ceramics are summarised in Table 5.1. The sintering profiles of the ceramics prepared using SPS are shown in Fig.5.17.

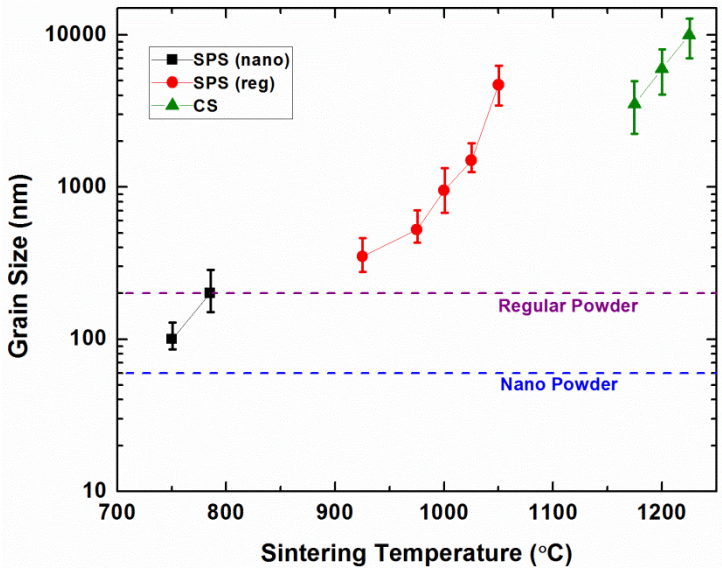

Fig.5.16: Grain size vs. temperature diagram for the BNBT-6 ceramics sintered using SPS and conventional sintering (CS) techniques. The average grain size of the regular ball-milled powder and the chemically prepared nanograin powder is marked by the dashed lines.

Table 5.1: Sintering conditions used to prepare selected BNBT-6 ceramics. F_{max}: temperature at which maximum force is applied.

Powder	**Sintering Method**	**Sintering Conditions** *Temperature/Duration/Pressure /Heating Rate*	**Annealing Conditions**	**Density**	**Average Grain Size**
Regular Ball-Milled	CS	1200 ˚C, 2 h, 3 ˚C/min	n/a	98.9 %	6 µm
Regular Ball-Milled	CS	1175 ˚C, 2 h, 3 ˚C/min	n/a	96.6 %	3.5 µm
Regular Ball-Milled	SPS	1000 ˚C, 5 min, 60 MPa, 100 ˚C/min *(F_{max}= 650 ˚C)*	950 ˚C/24 h	96.2 %	950 nm
Regular Ball-Milled	SPS	925 ˚C, 5 min, 80 MPa, 100 ˚C/min *(F_{max}= 650 ˚C)*	825 ˚C/24 h	96.3 %	350 nm
Sol-gel	SPS	785 ˚C, 20 min, 450 MPa, 50 ˚C/min *(F_{max}= 650 ˚C)*	700 ˚C/24 h	99.3 %	200 nm
Sol-gel	SPS	750 ˚C, 20 min, 450 MPa, 50 ˚C/min *(F_{max}= 650 ˚C)*	700 ˚C/24 h	99.1 %	100 nm

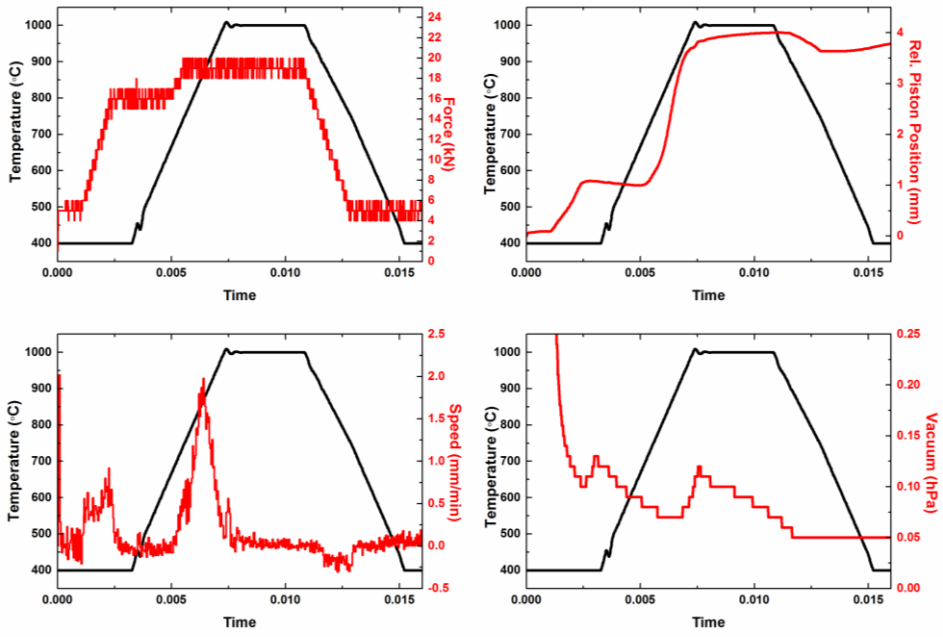

(a)

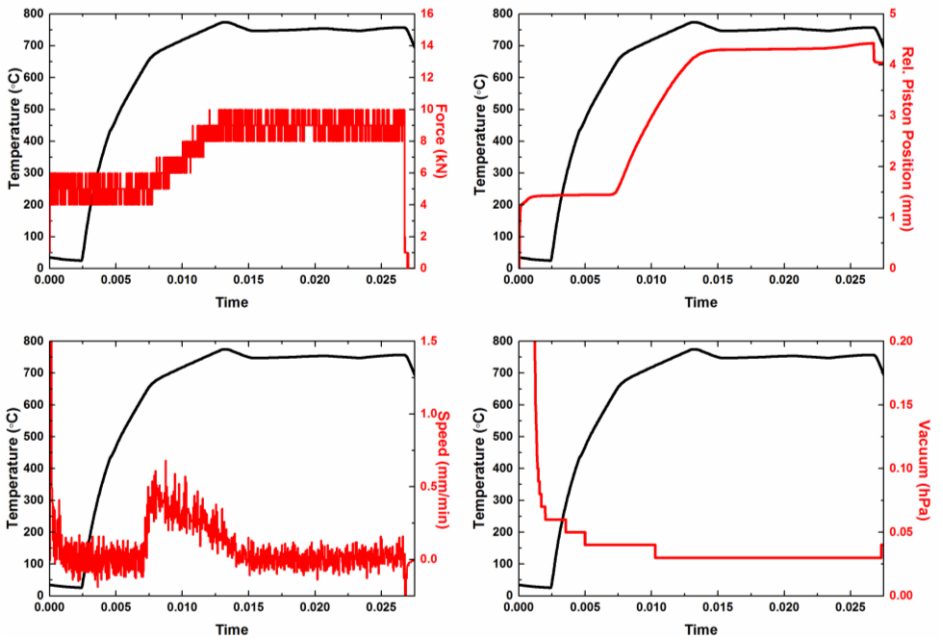

(b)

Fig. 5.17: SPS sintering profiles of BNBT-6 ceramics with average grain size (a) 950 nm and (b) 100 nm, as summarised in Table 5.1.

5.1.7 Ceramics Prepared from High-Speed Ball-Milled Powder

The high-speed ball-milled powder was initially used to sinter the ceramics within the grain size range of 10-100 nm. The sintering conditions are summarised in Table 5.2, along with the density and grain size measured from the SEM images of the fracture surface shown in Fig.5.18.

Table 5.2: Sintering conditions used to prepare high-speed ball-milled BNBT-6 ceramics. F_{max}: temperature at which maximum force is applied.

Sintering Method	**Sintering Conditions** *Temperature/Duration/Pressure/Heating Rate*	**Annealing Conditions**	**Average Grain Size**	**Density**
SPS	850 ˚C, 20 min, 500 MPa, 50 ˚C/min *(F_{max}= 650 ˚C)*	750 ˚C/24 h	200 nm	99.4 %
SPS	800 ˚C, 20 min, 500 MPa, 50 ˚C/min *(F_{max}= 650 ˚C)*	700 ˚C/24 h	150 nm	99.1 %

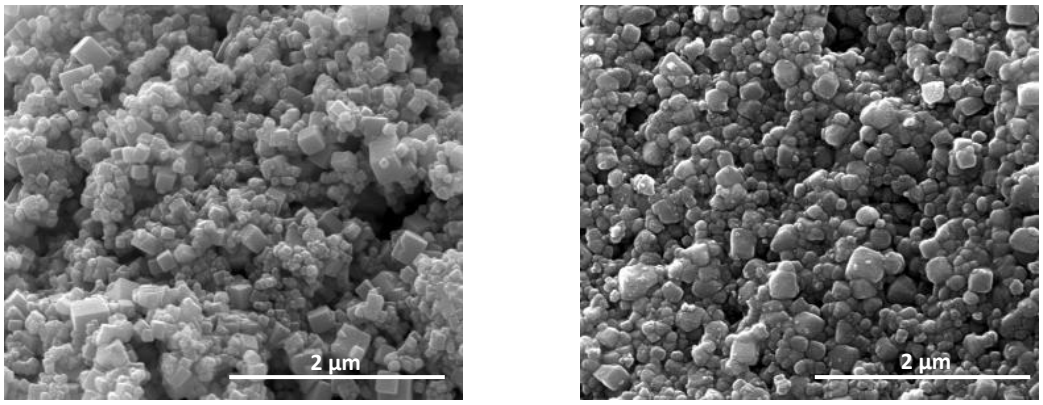

(a) (b)

Fig.5.18: Fracture surface SEM images of high pressure SPS-ed BNBT-6 ceramics sintered at (a) 800 ˚C/500 MPa and (b) 850 ˚C/500 MPa for 20 mins with high-speed ball milled powder.

Impurities from the ZrO_2 milling media were thought to hinder the FE properties of these ceramic resulting in the low permittivity, shown in Fig.5.19, and the absence of current switching peaks in the I-E loops (Fig.5.20). d_{33} values 2.3 pN and 2.6 pN were measured for the 800 ˚C and 850 ˚C sintered ceramic, respectively, after poling in a 60 kV/cm electric field for 10 minute. To avoid contamination from ZrO_2, nanograin size powder prepared by sol-gel rather than ball-milling was used to sinter the final samples. However, similar results were obtained for nanograin ceramics sintered from the chemically prepared powder, as demonstrated in Fig.5.21. Consequently, the suppression of the FE nature is not thought to be caused by the ZrO_2 contamination. Although the grain sizes of the ceramics range from 100-200 nm, the permittivity values are very different. This may still be related to the effect of ZrO_2 in the high-speed ball milled ceramics.

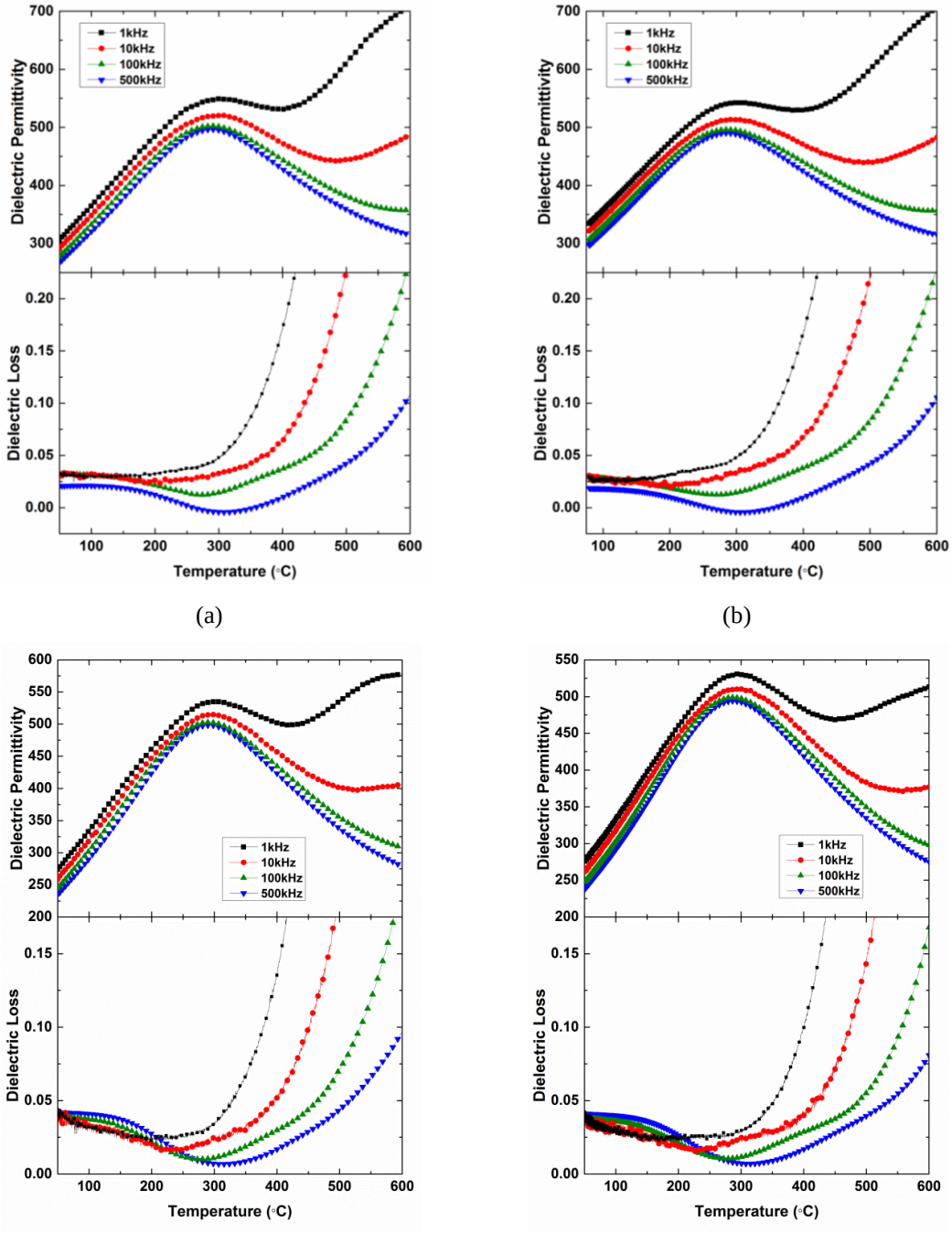

(a) (b)

(c) (d)

Fig.5.19: Temperature dependence of the dielectric response of the high-speed ball-milled ceramics sintered at (a), (b) 800 ˚C and (c), (d) 850 ˚C. Measured during (a), (c) heating and (b), (d) cooling at 1, 10, 100 and 500 kHz.

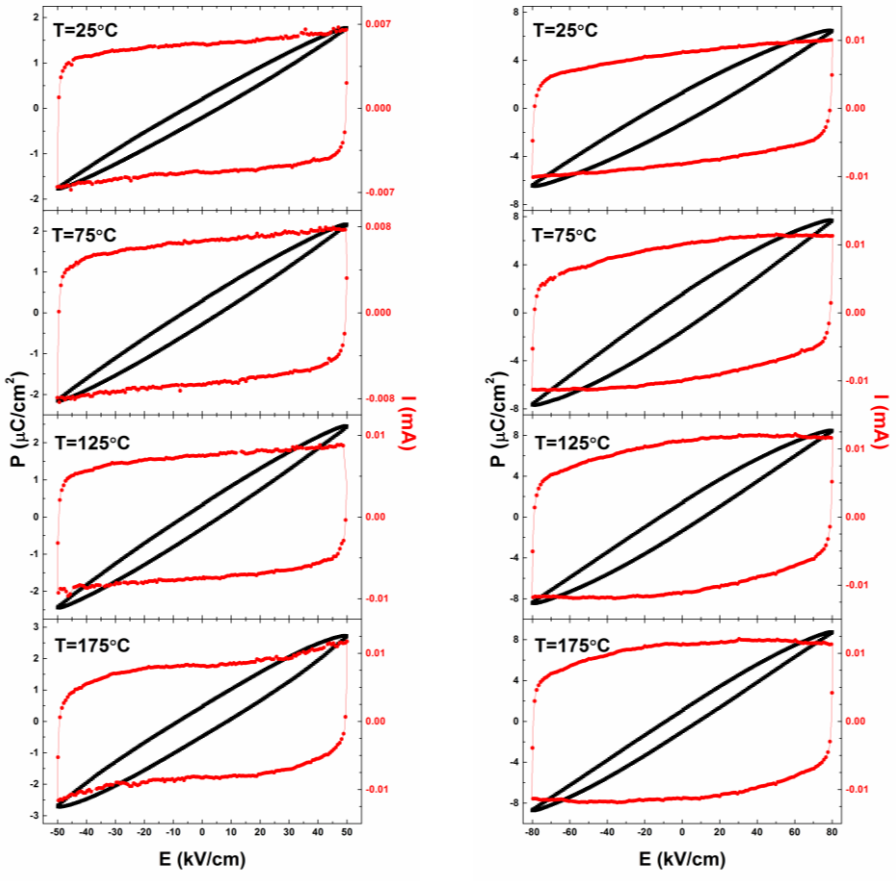

(a) (b)

Fig.5.20: Room temperature P-I-E loops measured at 10 Hz for the (a) 800 ˚C and (b) 850 ˚C sintered ceramics.

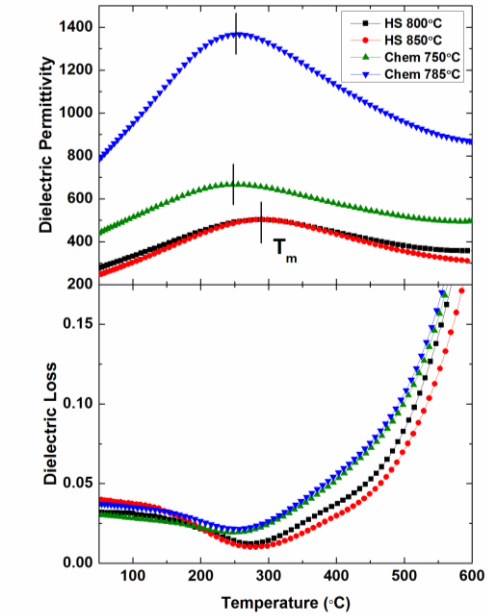

Fig.5.21: Dielectric response measured at 10 Hz of the nanograin ceramics sintered using high-speed ball-milled (HS) and sol-gel (Chem) BNBT-6 powders.

5.2 Results

5.2.1 High Temperature X-ray Diffraction (XRD)

The high temperature XRD results for the crushed 6 μm BNBT-6 ceramics in its unpoled and poled states are shown in Fig.5.21 and Fig.5.22, respectively. Only the $(110)_{pc}$, $(111)_{pc}$, $(200)_{pc}$ and $(211)_{pc}$ Bragg peaks are shown. XRD data was collect at room temperature, then at 50 ˚C intervals from 100 ˚C to 700 ˚C during heating and cooling. Every reflection appears twice due to the presence of the $K\alpha_2$ component in the incident beam, as noted for in Fig.5.21 (a). The temperature dependent XRD collected from the 350 nm, 950 nm and 3.5 μm ceramics are given in Appendix Fig.7.2.1-Fig.7.2.3. Only the room temperature XRD data was collected for the 100 nm BNBT-6 ceramic shown in Appendix Fig.7.2.4. The lattice parameters of the structures which provided the best fit are listed in Table 5.3-5.8. The temperature dependence of the normalised volume for each grain size during heating and cooling is shown in Fig.5.23. Examples demonstrating the Rietveld fit of the XRD patterns for each structure are shown in Appendix Fig.7.2.5-Fig.7.2.7. As was also the case for BNT, peaks from the Pt holder appear in the diffraction patterns of some of the ceramics, as demonstrated in Appendix Fig.7.2.8. Single phase structures were only used to fit the XRD data collected from the poled 6 μm grain size ceramic and the unpoled 350 nm ceramics, while only the *R3c/P4bm* structure was fitted for the unpoled 950 nm ceramic below 200 ˚C. However, mixed phases of *R3c/P4bm* and $Pm\bar{3}m$/*P4bm* symmetries are also expected to occur within these materials, as demonstrated by the Rietveld fits in Appendix Fig.7.2.9. Further support for this mixed phase structure, is provided by the XRD data collected from the 100 nm ceramic, which is refined as a mixed phase of $Pm\bar{3}m$/*P4bm* symmetries at room temperature (Appendix Fig.7.2.4).

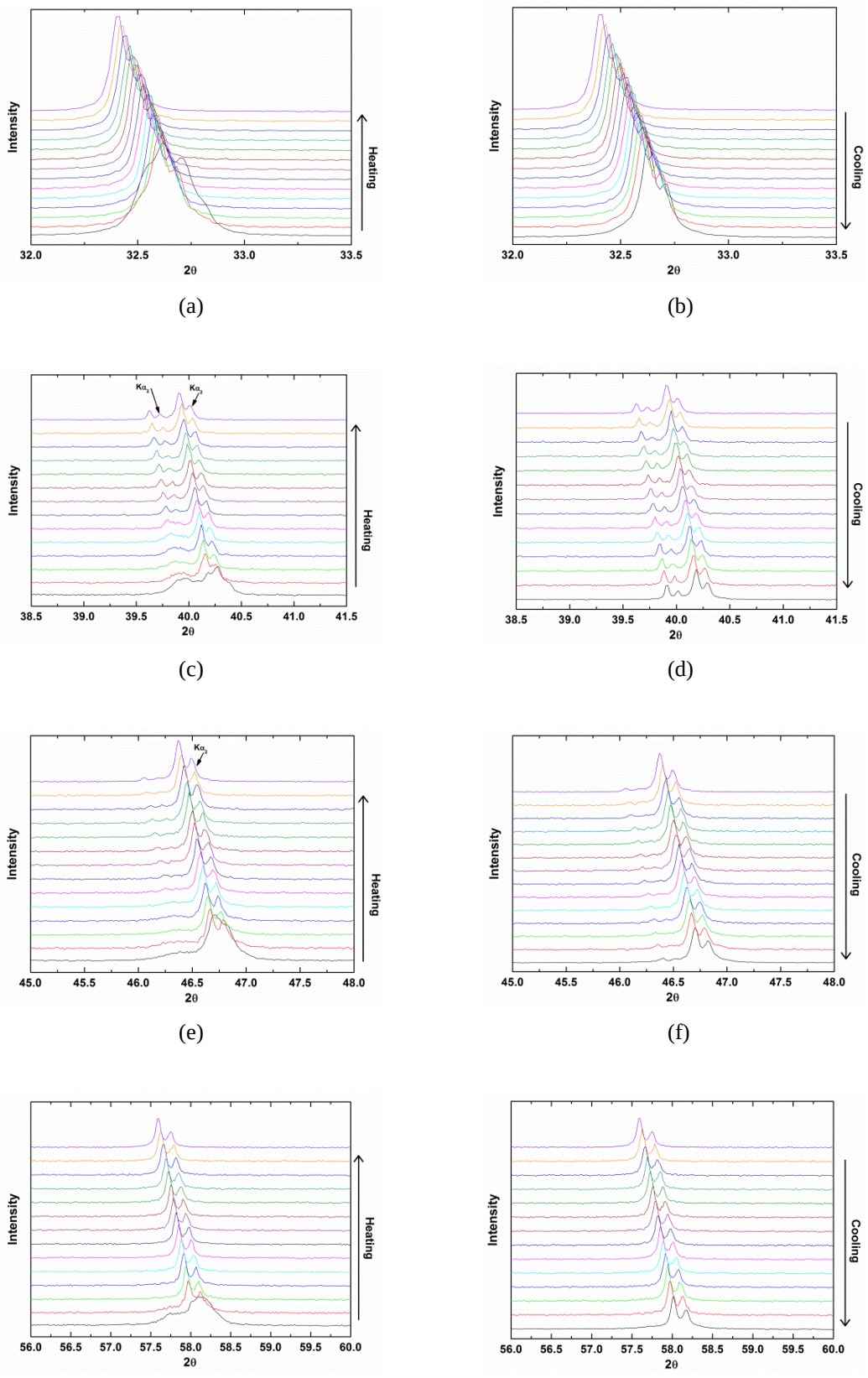

Fig.5.21: Powder XRD profiles of the crushed 6 µm grain size BNBT-6 ceramic showing the temperature evolution during heating and cooling of the Bragg reflections: (a)-(b) $(110)_{pc}$, (c)-(d) $(111)_{pc}$, (e)-(f) $(200)_{pc}$ and (g)-(h) $(211)_{pc}$. Reflections from the $K\alpha_2$ component from the incident beam are highlighted.

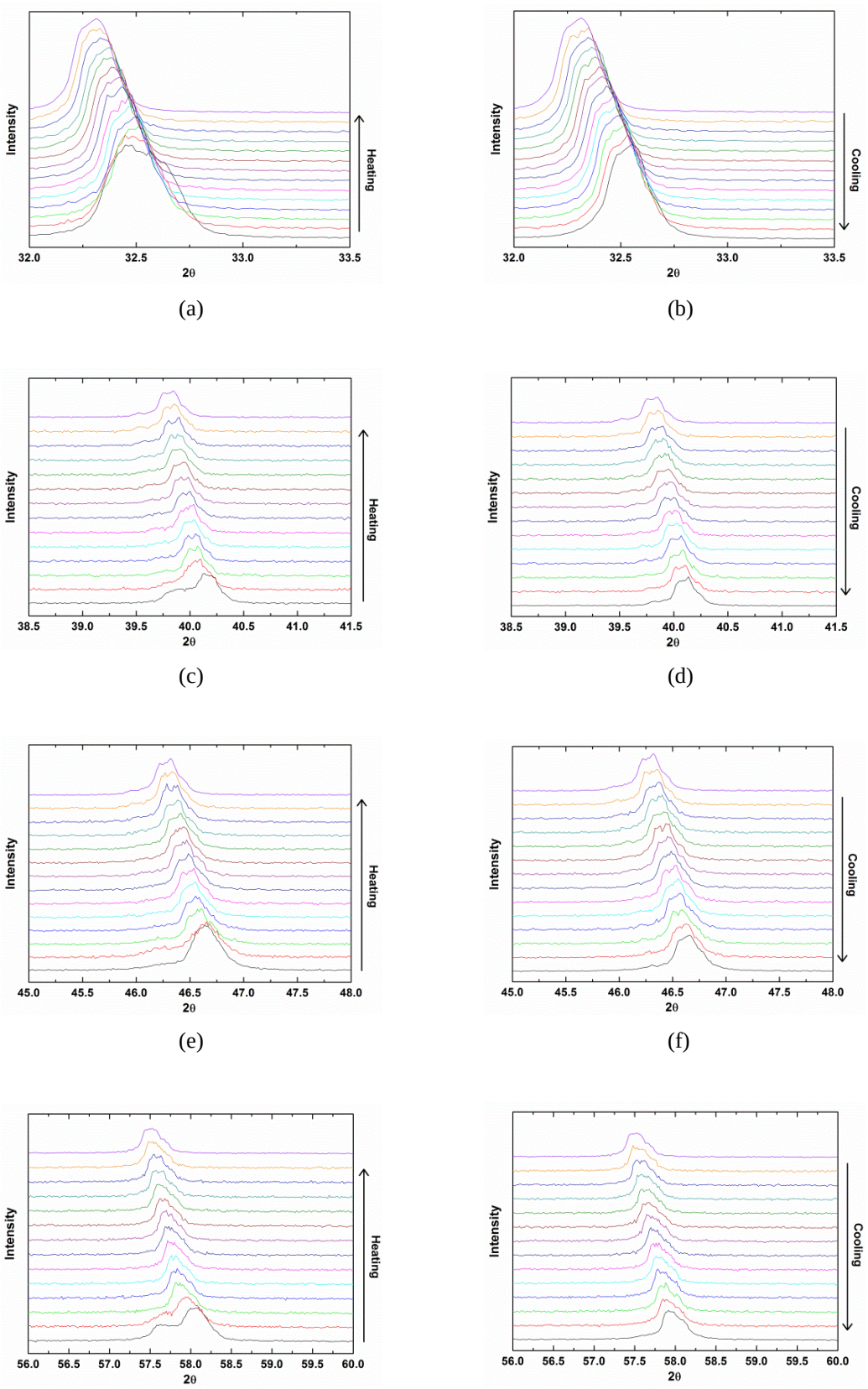

(a) (b)

(c) (d)

(e) (f)

(g) (h)

Fig.5.22: Powder XRD profiles of the electrically poled crushed 6 µm grain size BNBT-6 ceramic showing the temperature evolution during heating and cooling of the Bragg reflections: (a)-(b) $(110)_{pc}$, (c)-(d) $(111)_{pc}$, (e)-(f) $(200)_{pc}$ and (g)-(h) $(211)_{pc}$.

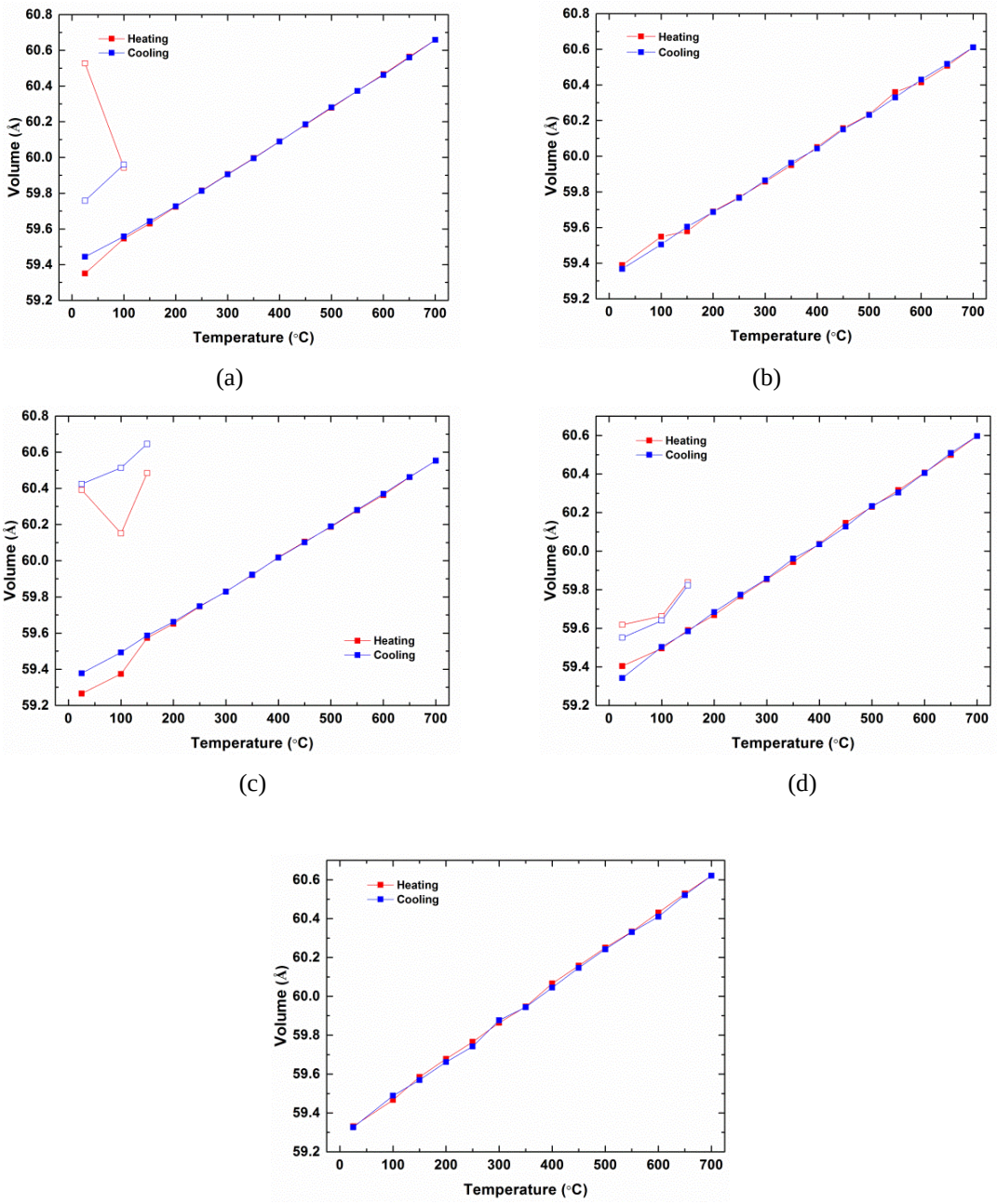

Fig.5.23: Temperature dependence of the normalised cubic unit cell volume, determined by Rietveld refinement, for the crushed (a) 6 µm, (c) 3.5 µm, (d) 950 nm, (e) 350nm grain size ceramics. The data for the poled 6 µm BNBT-6 ceramic is given in (b). For mixed phase refinement, Phase 1: solid symbols and Phase 2: open symbols (see Tables 5.3-5.5). [*R3c*: Z=6, *Cc*: Z=4, *P4bm*: Z=2 and $Pm\bar{3}m$: Z=1.]

A phase diagram for the grain size dependence in BNBT-6 determined from the XRD data is shown in Fig.5.24.

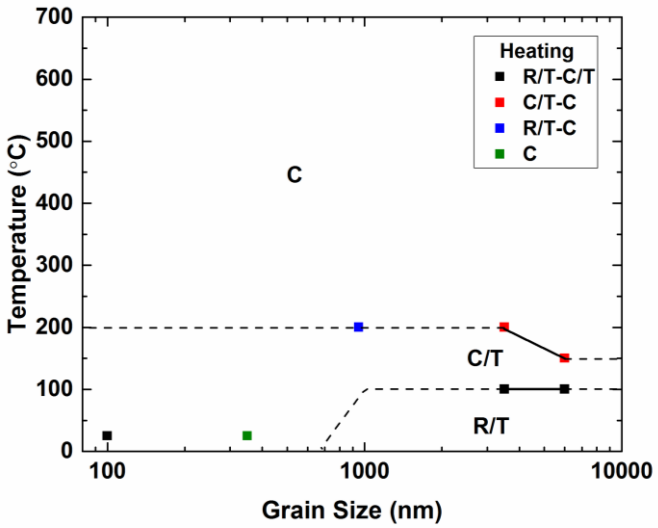

(a)

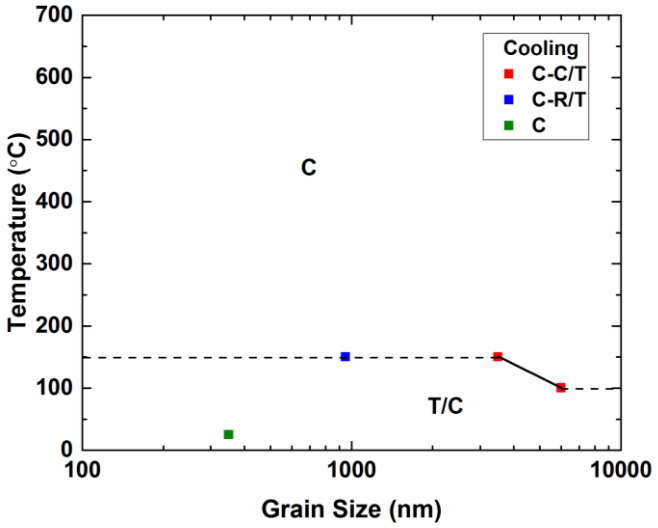

(b)

Fig.5.24: Structural phase diagram for unpoled BNBT-6 on (a) heating and (b) cooling. R: rhombohedral *R3c*, T: tetragonal *P4bm* and C: cubic $Pm\bar{3}m$. The squares mark the temperatures were a change in structure is observed in the XRD data. The dashed lines are not obtained from structural refinement and only act as a guide.

Table 5.3: Lattice parameters calculated by Rietveld refinement of XRD data collected from crushed 6 μm unpoled and poled BNBT-6 ceramics at different temperatures.

		6 μm					6 μm Poled	
Temp.	Structure	Phase 1: Cell		Structure	Phase 2: Cell		Structure	Cell	
(˚C)		*a* (Å)	*c* (Å)		*a* (Å)	*c* (Å)		*a* (Å)	*c* (Å)
25	*R3c*	5.5052(2)	13.5676(9)	*P4bm*	5.5429(6)	3.9401(6)	*R3c*	5.5026(2)	13.5892(7)
100	$Pm\bar{3}m$	3.9050(1)			5.5504(16)	3.8916(17)		5.5166(8)	13.5566(37)
150		3.9068(1)					$Pm\bar{3}m$	3.9057(2)	
200		3.9088(1)						3.9081(2)	
250		3.9108(1)						3.9099(2)	
300		3.9128(1)						3.9117(2)	
350		3.9148(1)						3.9138(2)	
400		3.9168(1)						3.9160(2)	
450		3.9189(1)						3.9183(2)	
500		3.9209(1)						3.9199(2)	
550		3.9230(1)						3.9227(2)	
600		3.9250(1)						3.9239(2)	
650		3.9271(1)						3.9259(2)	
700		3.9291(0)						3.9281(1)	
650		3.9270(0)						3.9261(2)	
600		3.9249(1)						3.9242(2)	
550		3.9230(1)						3.9220(2)	
500		3.9210(1)						3.9199(2)	
450		3.9189(1)						3.9181(2)	
400		3.9168(1)						3.9158(2)	
350		3.9148(1)						3.9141(2)	
300		3.9128(1)						3.9119(2)	
250		3.9108(1)						3.9098(2)	
200		3.9089(1)						3.9080(2)	
150		3.9071(1)						3.9062(2)	
100		3.9052(1)		*P4bm*	5.5529(18)	3.8891(20)		3.9041(2)	
25		3.9027(0)			5.5120(7)	3.9338(11)		3.9011(1)	

Table 5.4: Lattice parameters calculated by Rietveld refinement of XRD data collected from crushed 3.5 μm and 950 nm BNBT-6 ceramics at different temperatures.

	3.5 μm					950 nm				
Temp.	Structure	Phase 1: Cell		Structure	Phase 2: Cell		Structure	Phase 1:Cell		Structure	Phase 2:Cell	
(˚C)		*a* (Å)	*c* (Å)		*a* (Å)	*c* (Å)		*a* (Å)	*c* (Å)		*a* (Å)	*c* (Å)
25	*R3c*	5.5009(2)	13.5692(8)	*P4bm*	5.5397(8)	3.9359(8)	*R3c*	5.5040(2)	13.5859(8)	*P4bm*	5.5064(6)	3.9325(5)
100	$Pm\bar{3}m$	3.9012(2)			5.5613(12)	3.8898(16)		5.5131(5)	13.5616(23)		5.5062(5)	3.9358(5)
150		3.9056(1)			5.5440(1)	3.9357(11)		5.5167(10)	13.5656(46)		5.5155(8)	3.9341(7)
200		3.9073(1)					$Pm\bar{3}m$	3.9076(2)				
250		3.9094(1)						3.9098(2)				
300		3.9112(1)						3.9117(2)				
350		3.9131(1)						3.9136(2)				
400		3.9153(1)						3.9157(2)				
450		3.9172(1)						3.9181(2)				
500		3.9189(1)						3.9199(2)				
550		3.9209(1)						3.9217(2)				
600		3.9227(1)						3.9237(2)				
650		3.9249(1)						3.9257(2)				
700		3.9269(1)						3.9278(1)				
650		3.9249(1)						3.9259(2)				
600		3.9229(1)						3.9236(2)				
550		3.9210(1)						3.9215(2)				
500		3.9190(1)						3.9199(2)				
450		3.9171(1)						3.9176(2)				
400		3.9152(1)						3.9156(2)				
350		3.9132(1)						3.9140(2)				
300		3.9111(1)						3.9118(2)				
250		3.9094(1)						3.9099(1)				
200		3.9075(1)						3.9080(1)				
150		3.9059(1)		*P4bm*	5.5478(9)	3.9409(11)		5.5243(5)		*P4bm*	5.5198(8)	3.9268(6)
100		3.9038(1)			5.5426(8)	3.9396(10)		5.5245(13)			5.5078(6)	3.9320(6)
25		3.9013(1)			5.5394(5)	3.9383(7)		5.5137(6)			5.5005(4)	3.9366(4)

Table 5.5: Lattice parameters calculated by Rietveld refinement of XRD data collected from crushed 350 nm and 100 nm BNBT-6 ceramics at different temperatures.

	350 nm		100 nm					
Temp.	Structure	Cell	Structure	Phase 1: Cell		Structure	Phase 2: Cell		
(˚C)		*a* (Å)		*a* (Å)	V_C (Å^3)		*a* (Å)	*c* (Å)	V_C (Å^3)
25	$Pm\bar{3}m$	3.9003(2)	$Pm\bar{3}m$	3.8993(2)	59.287(10)	*P4bm*	5.5624(22)	3.9708(20)	61.428(45)
100		3.9032(3)							
150		3.9058(3)							
200		3.9079(3)							
250		3.9098(3)							
300		3.9119(2)							
350		3.9137(2)							
400		3.9163(2)							
450		3.9183(2)							
500		3.9203(2)							
550		3.9221(2)							
600		3.9242(2)							
650		3.9263(2)							
700		3.9283(1)							
650		3.9262(2)							
600		3.9238(2)							
550		3.9220(2)							
500		3.9201(2)							
450		3.9181(2)							
400		3.9159(2)							
350		3.9137(2)							
300		3.9122(2)							
250		3.9092(2)							
200		3.9075(2)							
150		3.9055(3)							
100		3.9037(3)							
25		3.9002(2)							

5.2.2 Back-Scattered SEM

Back-scattered SEM was used to image the domain structure of the BNBT-6 ceramics shown in Fig.5.25-5.31. Mechanical stresses generated in the ceramics from cutting and grinding were removed by annealing the samples at 600 ˚C for 4 h prior to polishing. A complex microstructure of fine and broad striped domains was imaged in all of the ceramics with average grain size greater than 350 nm. Instead of filling the whole grain, the striped domains are often broken up and occasionally form a herringbone-type structure. Electrical poling does not appear to induce a noticeable change in domain structure in Fig.5.27 and Fig.5.30. No clear domain pattern was imaged in the grains of either the unpoled and poled 350nm ceramics (Fig.5.31), expect for a single, larger grain (>350 nm) shown in Fig.5.31(c).

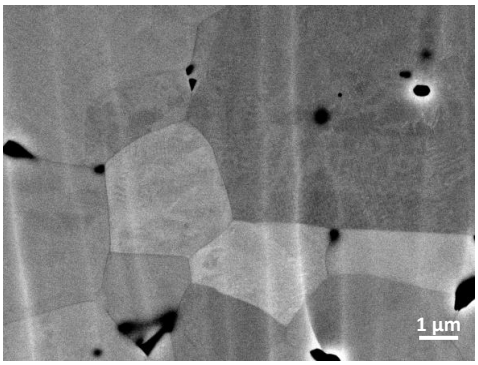

(a)

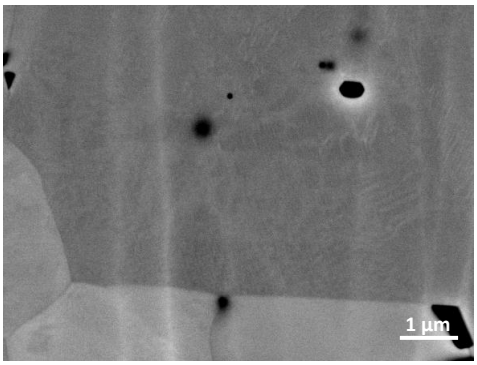

(b)

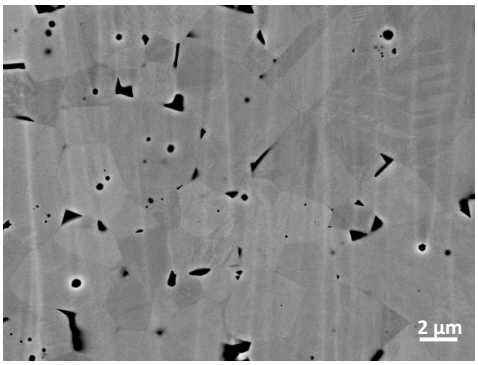

(c)

Fig.5.25: (a)-(c) Back-scattered SEM images of the BNBT-6 ceramic with an average grain size of 10µm.

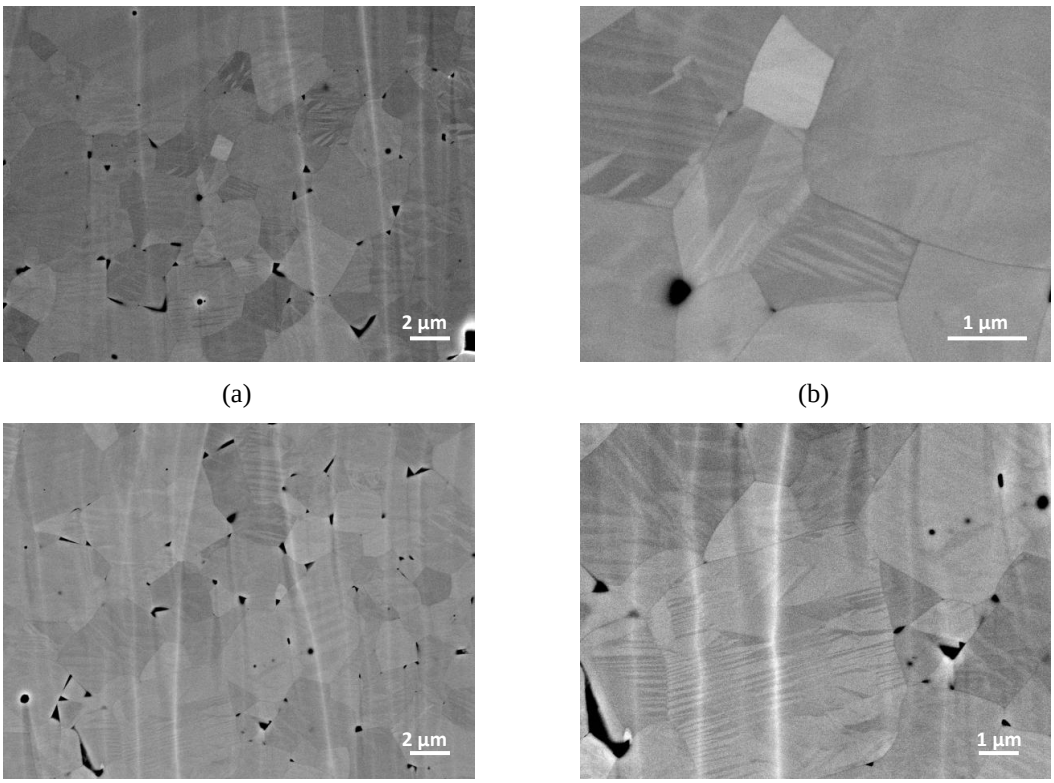

(a) (b)

(c) (d)

Fig.5.26: (a)-(c) Back-scattered SEM images of the 6µm grain size BNBT-6 ceramic.

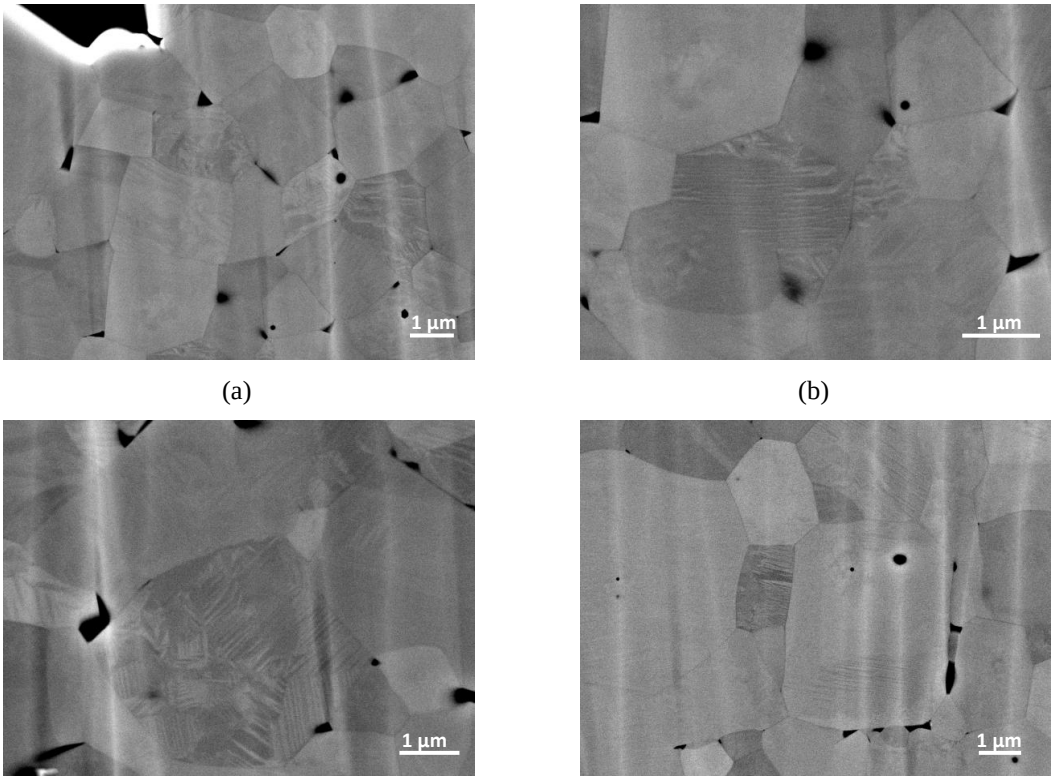

(a) (b)

(c) (d)

Fig.5.27: (a)-(d) Back-scattered SEM images of the 6µm BNBT-6 ceramic after electrical poling.

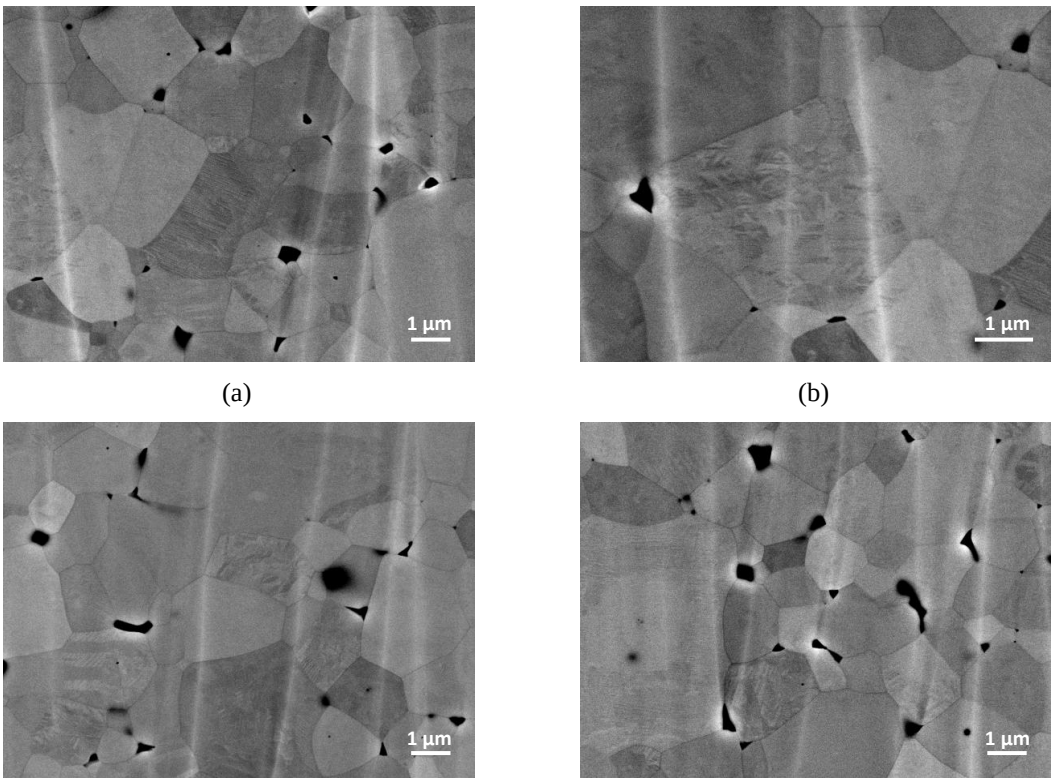

(a) (b)

(c) (d)

Fig.5.28: (a)-(d) Back-scattered SEM images of the 3.5µm BNBT-6 ceramic.

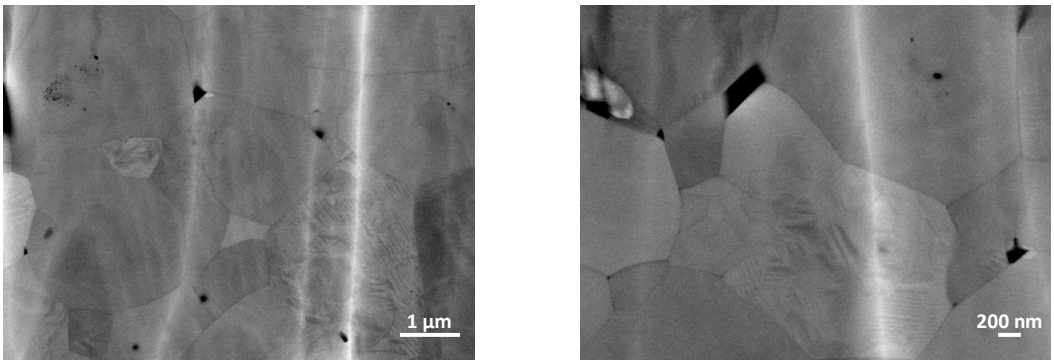

(a) (b)

Fig.5.29: (a)-(b) Back-scattered SEM images of the 950nm BNBT-6.

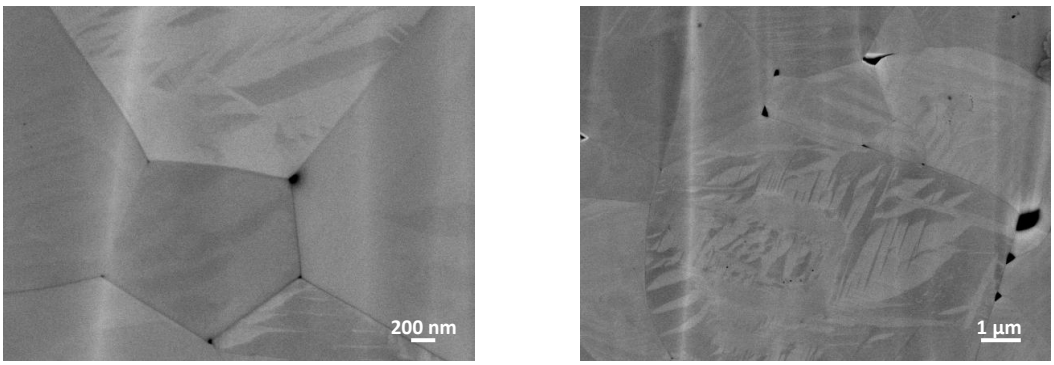

(a) (b)

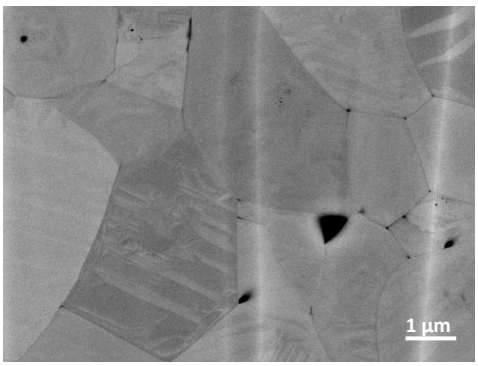

(c)

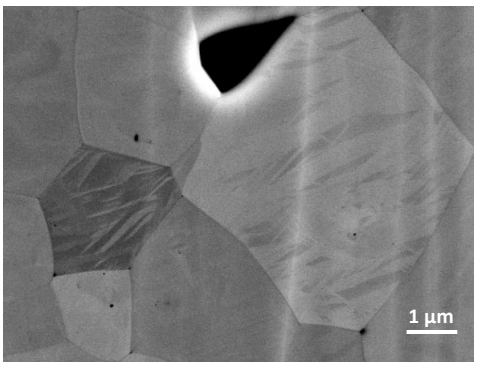

(d)

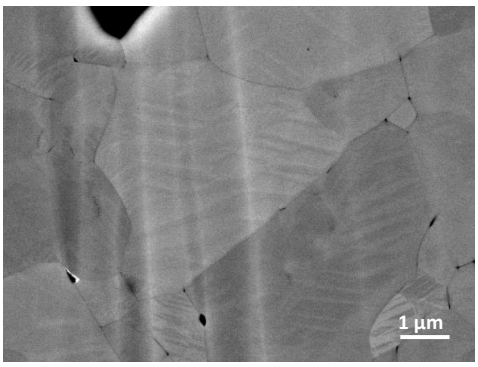

(e)

Fig.5.30: (a)-(e) Back-scattered SEM images of the 950nm BNBT-6 ceramic after electrical poling.

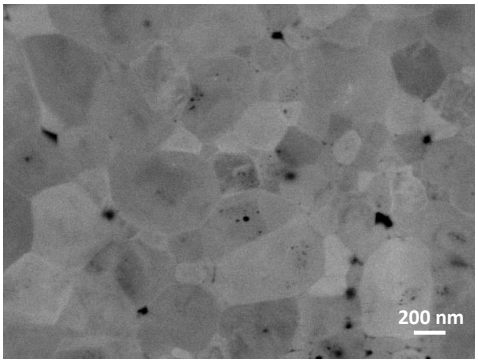

(a)

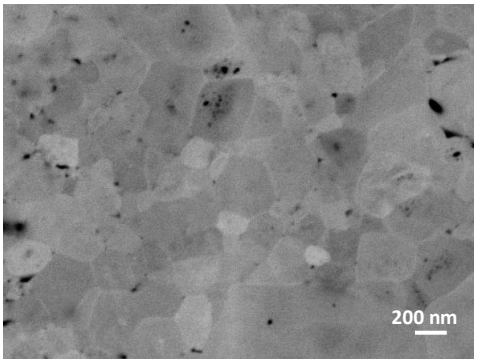

(b)

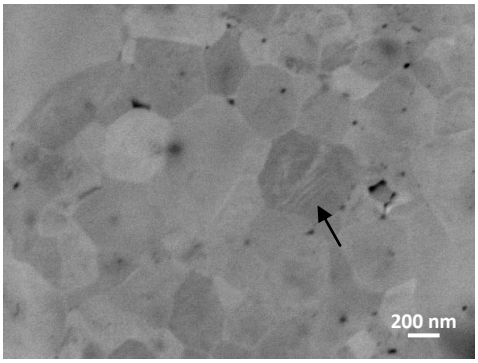

(c)

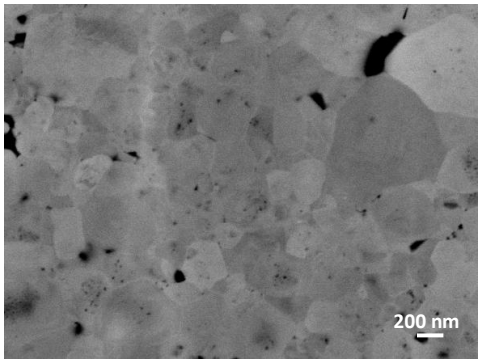

(d)

Fig.5.31: Back-scattered SEM images of the 350nm BNBT-6 ceramic (a)-(c) before and (d) after electrical poling. In (c) the striped domain pattern is marked by an arrow.

5.2.3 Piezoforce Microscopy (PFM)

Fig.5.32-5.36 show the PFM images and piezoelectric hysteresis loop collected from a selection of the BNBT-6 ceramics at fixed excitation amplitudes of 1- 8 V applied at a driving frequency of 60 kHz.

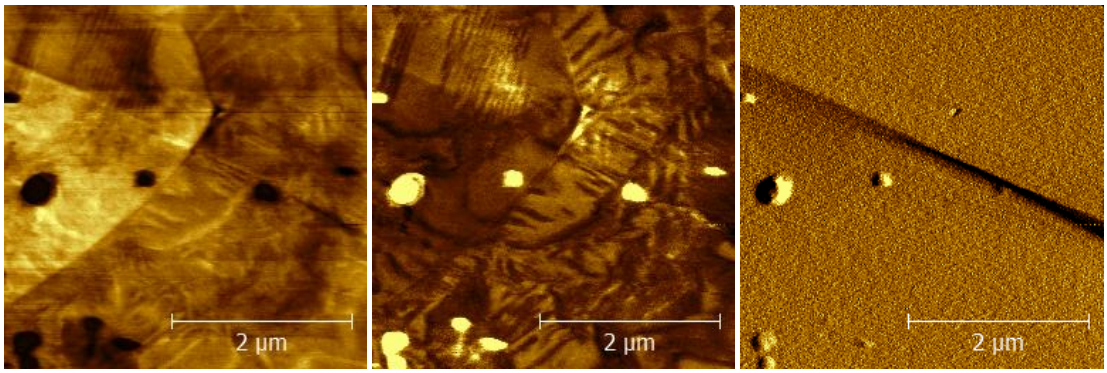

(a1) (a2) (a3)

Fig.5.32: PFM images of the 10µm BNBT-6 ceramic including (a1) amplitude, (a2) phase and (a3) defelection. Measured with an exitation amplitude of 5V applied at 60 kHz.

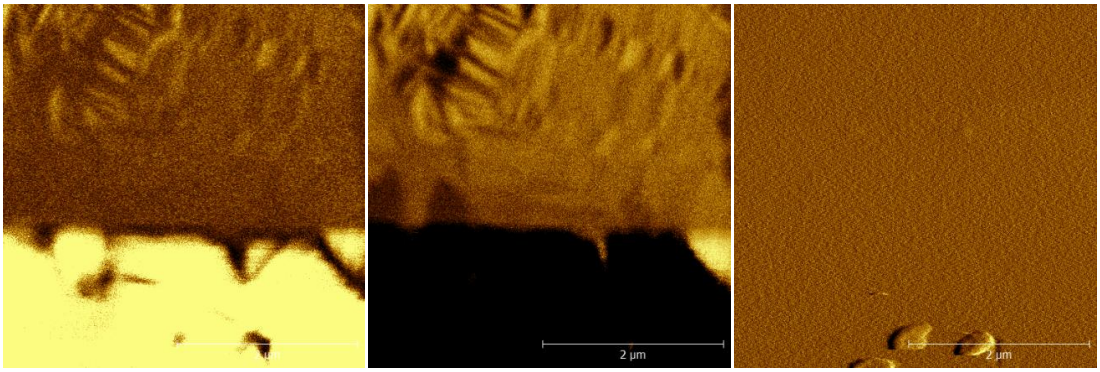

(a1) (a2) (a3)

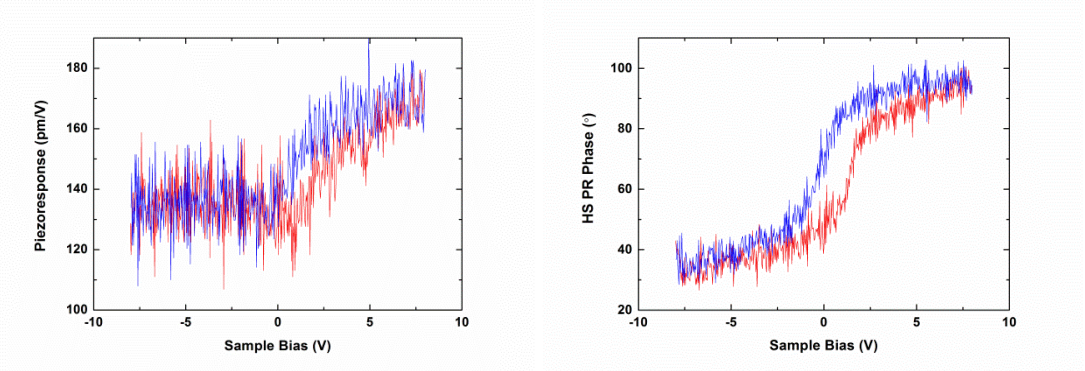

(b1) (b2)

Fig.5.33: PFM images of the 6µm BNBT-6 ceramic including (a1) amplitude, (a2) phase and (a3) defelection. (b1)-(b2) Piezoelectric hysteresis loop obtained for this area . Measured with an exitation amplitude of 2 V applied at 60 kHz.

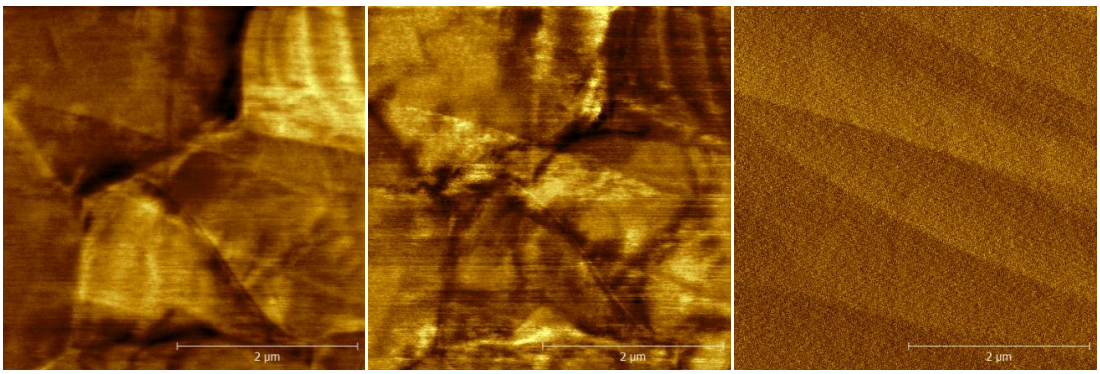

(a1) (a2) (a3)

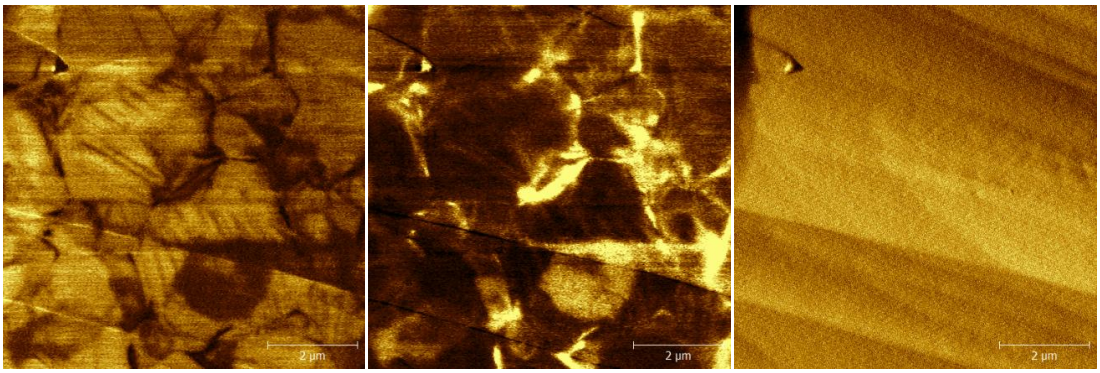

(b1) (b2) (b3)

Fig.5.34: PFM images of different areas of the poled 950 nm BNBT-6 ceramic including (a1),(b1) amplitude, (a2), (b2) phase and (a3), (b3) defelection. Measured with an exitation amplitude of (a1)-(a3) 5 V and (b1)-(b3) 2.5 V applied at 60 kHz.

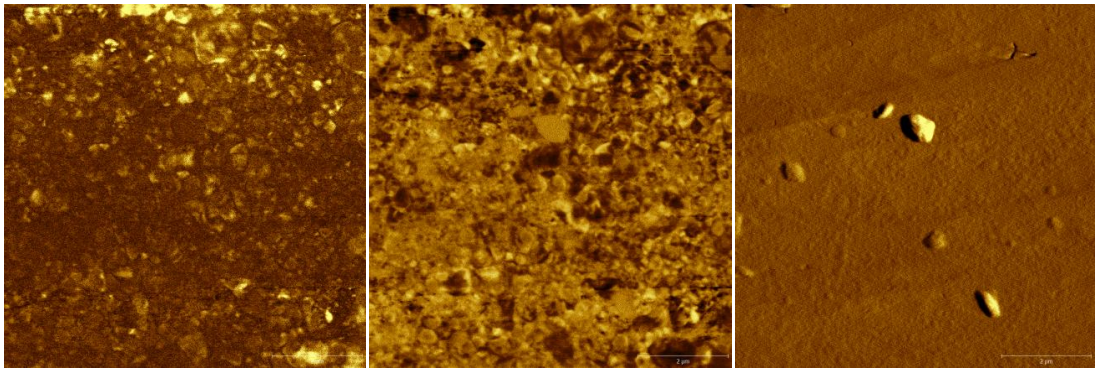

(a1) (a2) (a3)

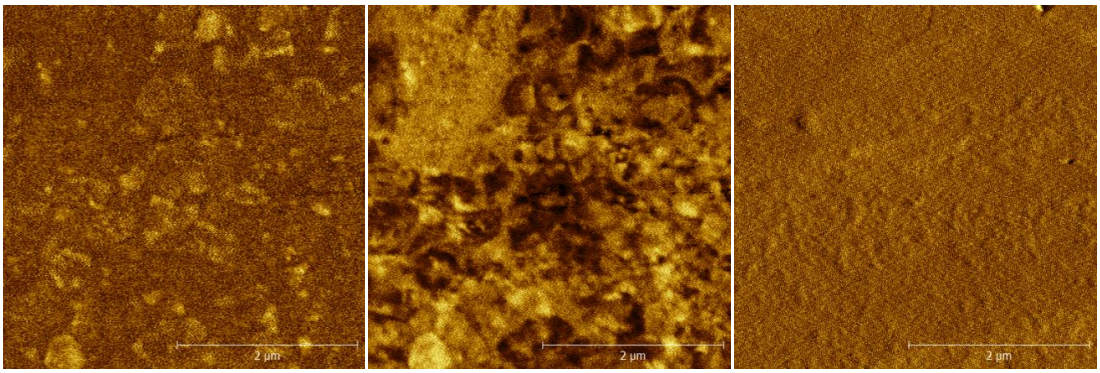

(b1) (b2) (b3)

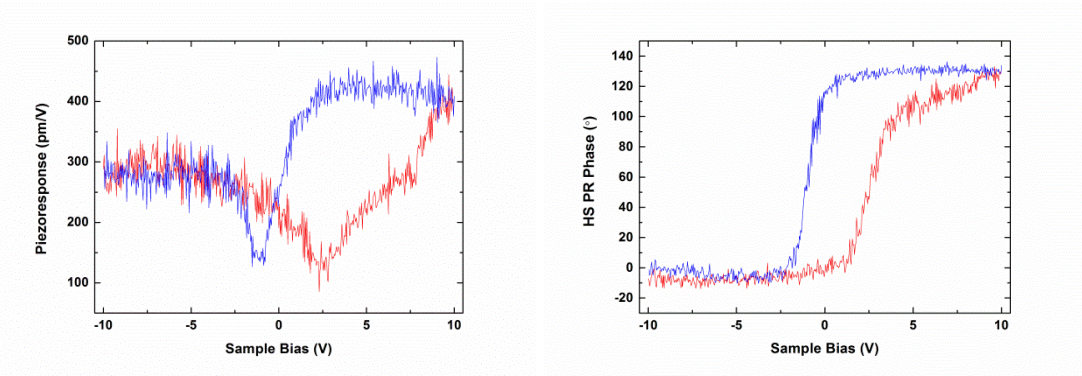

(c1) (c2)

Fig.5.35:PFM images of different areas of the 350 nm BNBT-6 ceramic including (a1),(b1) amplitude, (a2), (b2) phase and (a3), (b3) defelection. (c1)-(c2) Piezoelectric hysteresis loop obtained from the area imaged in (b1)-(b3). Measured with an exitation amplitude of (a1)-(a3) 2.5 V and (b1)-(b3) 2 V applied at 60 kHz.

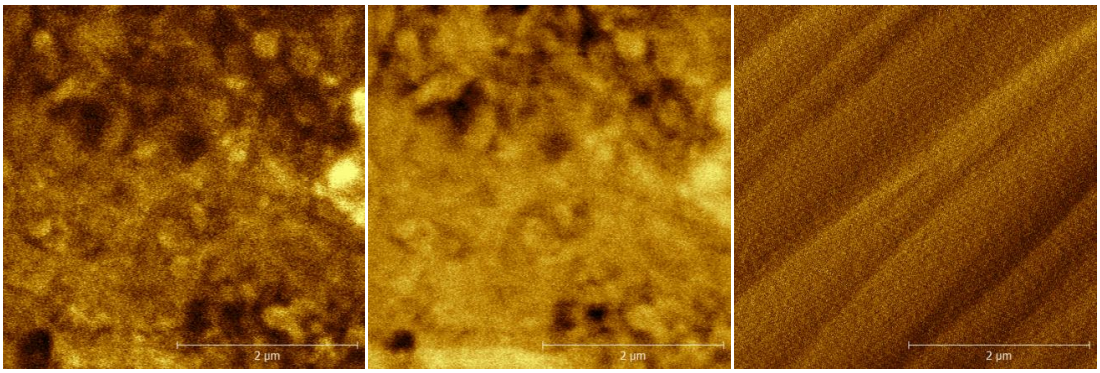

(a1) (a2) (a3)

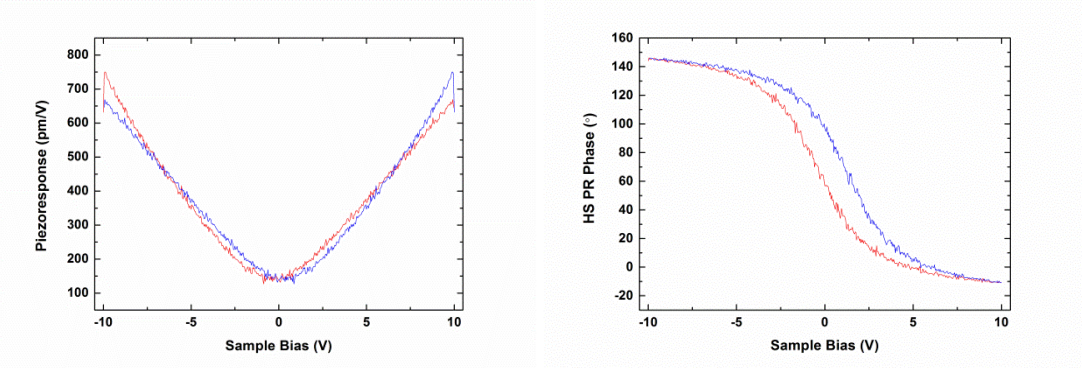

(b1) (b2)

Fig.5.36: PFM images of the poled 350 nm BNBT-6 ceramic including (a1) amplitude, (a2) phase and (a3) defelection. (b1)-(b2) Piezoelectric hysteresis loop obtained for this area. Measured with an exitation amplitude of (a1)-(a3) 8 V and (b1)-(b2) 1 V applied at 60 kHz.

The domain structure captured by PFM mimics that observed by back-scattered SEM. A complex domain structure of fine lamellar domains, distinct from any areas of uneven surface such as pores or scratches detected in the deflection, was observed in the

amplitude and phase images of the large grain ceramics (Fig.5.32-5.34). No domain structure was observed within the grains of the 350 nm ceramic in either the unpoled (Fig.5.35) or poled (Fig.5.36) state; however piezoelectric hysteresis were obtained for both of these samples confirming the ferroelectric nature of the material at this small grain size.

5.2.4 Dielectric Response vs. Frequency

The room temperature frequency dependence of the dielectric properties measured for the BNBT-6 ceramics is shown in Fig.5.37. The dielectric permittivity shows a clear decrease in value with increasing frequency for each grain size. Within the measured frequency range, the polarisation is dominated by the relaxation effects of the domain wall motion. As the frequency is increased, fewer domain walls are unable to respond to the applied electric field reducing their contribution to the permittivity. Similarly, the long relaxation time associated with the domain wall motion increases the dielectric loss with increasing frequency.

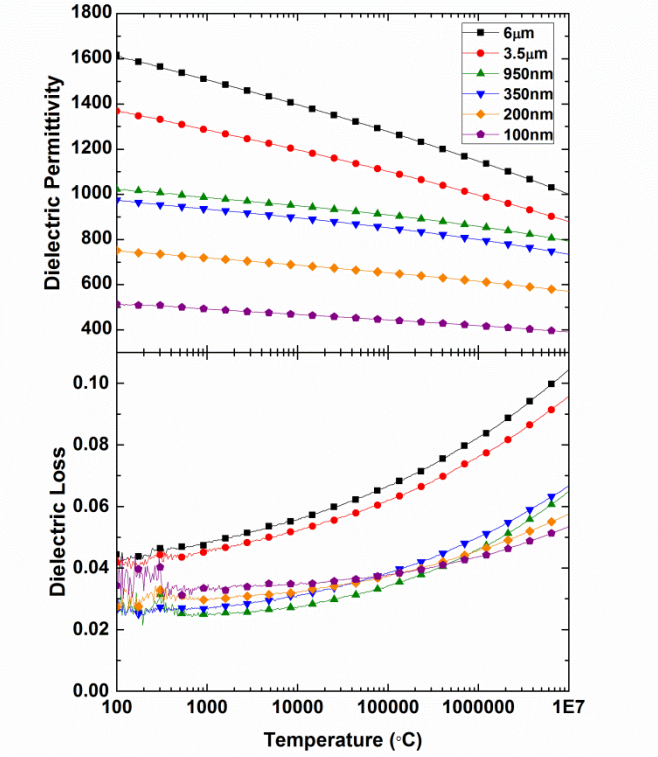

Fig.5.37: Dielectric response vs. frequency of the BNBT-6 ceramics with different grain size.

The effect of grain size on the dielectric response of BNBT-6 is summarised in Fig.5.38 for the 100 kHz data. The dielectric permittivity typically decreases with decreasing

grain size. The density of domain walls required to minimise the transformation stress within the grain interior and the residual tensile stress at the grain boundaries are expected to increase with the reduction in grain size. This polydomain structure is expected to become too costly. As a result, the degree of twining in the smaller grains is reduced and the permittivity decreasing. Dielectric loss remains relatively constant with decreasing grain size, except for the conventionally sintered ceramics which have the highest loss values, which is likely to be caused by point defects.

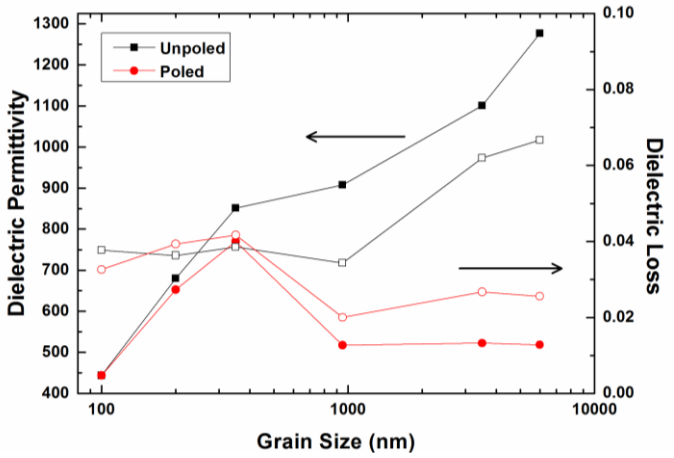

Fig.5.38: Grain Size dependence of the dielectric response in the unpoled and poled states at 100 kHz. (solid symbol: dielectric permittivity, open symbol: dielectric loss)

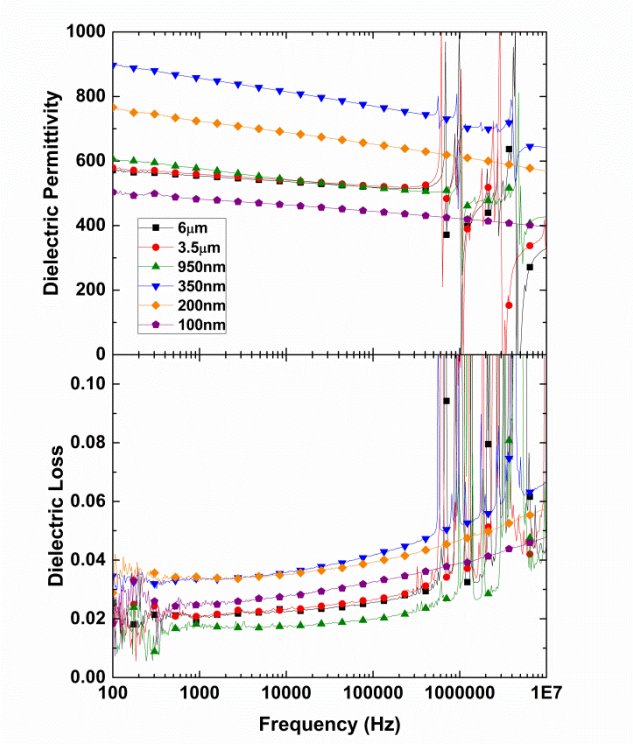

Fig.5.39: Dielectric response vs. frequency of the poled BNBT-6 ceramics with different grain size.

The dielectric permittivity and loss values of all the BNBT-6 ceramics decrease after electrical poling, shown in Fig.5.39. Fewer domain walls are expected to contribute to the polarisation due to the growth of the domain size on poling.

5.2.5 Dielectric Response vs. Temperature

(i) Unpoled

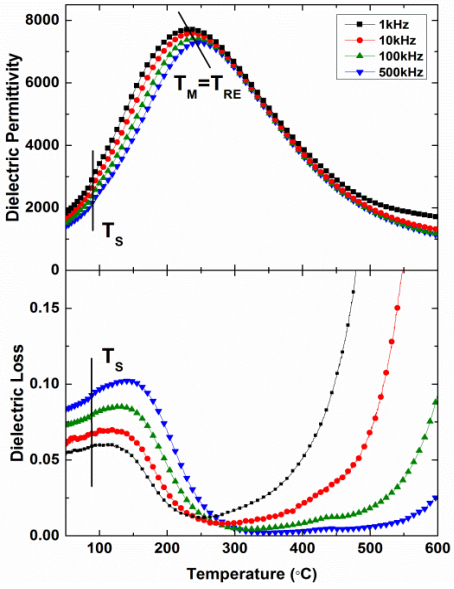

(a1)

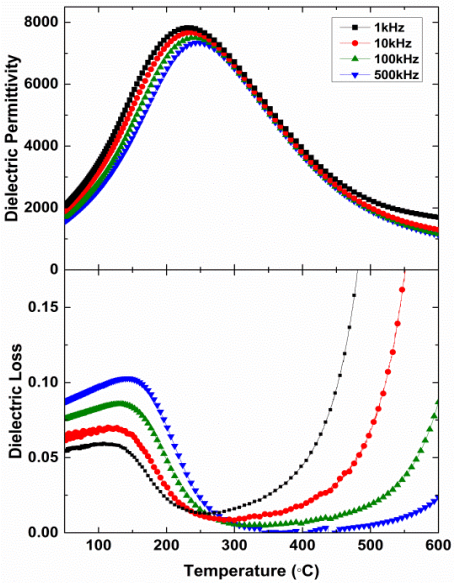

(a2)

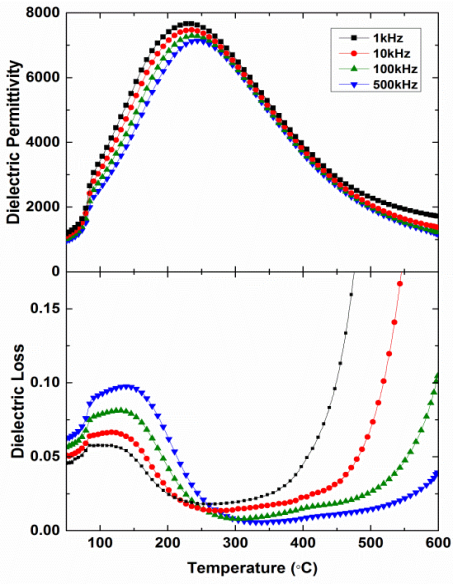

(b1)

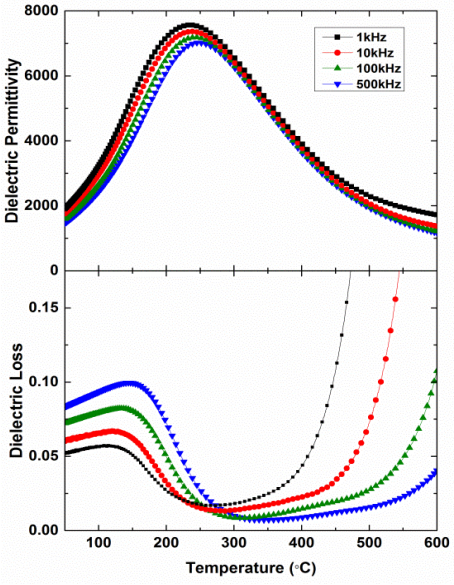

(b2)

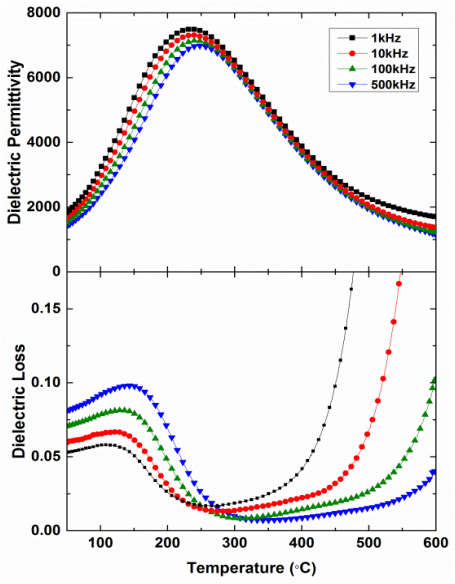
1kHz
10kHz
100kHz
500kHz
Dielectric Permittivity
Dielectric Loss
Temperature (°C)

(b3)

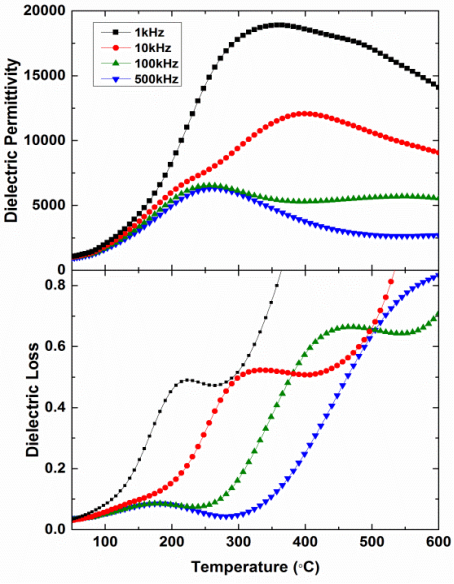
1kHz
10kHz
100kHz
500kHz
Dielectric Permittivity
Dielectric Loss
Temperature (°C)

(c1)

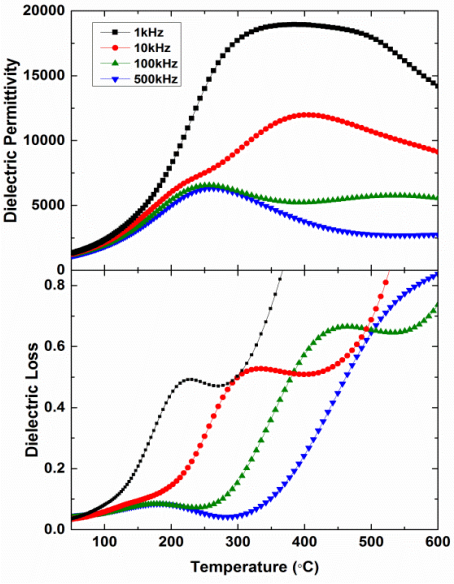
1kHz
10kHz
100kHz
500kHz
Dielectric Permittivity
Dielectric Loss
Temperature (°C)

(c2)

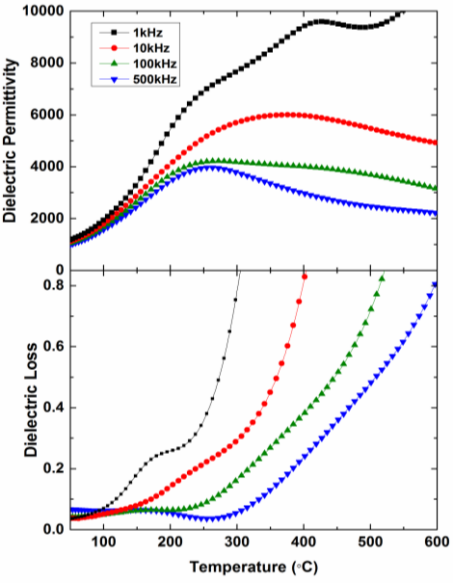
1kHz
10kHz
100kHz
500kHz
Dielectric Permittivity
Dielectric Loss
Temperature (°C)

(d1)

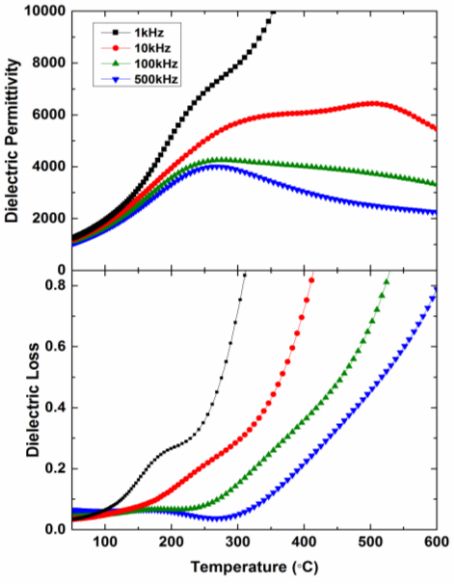
1kHz
10kHz
100kHz
500kHz
Dielectric Permittivity
Dielectric Loss
Temperature (°C)

(d2)

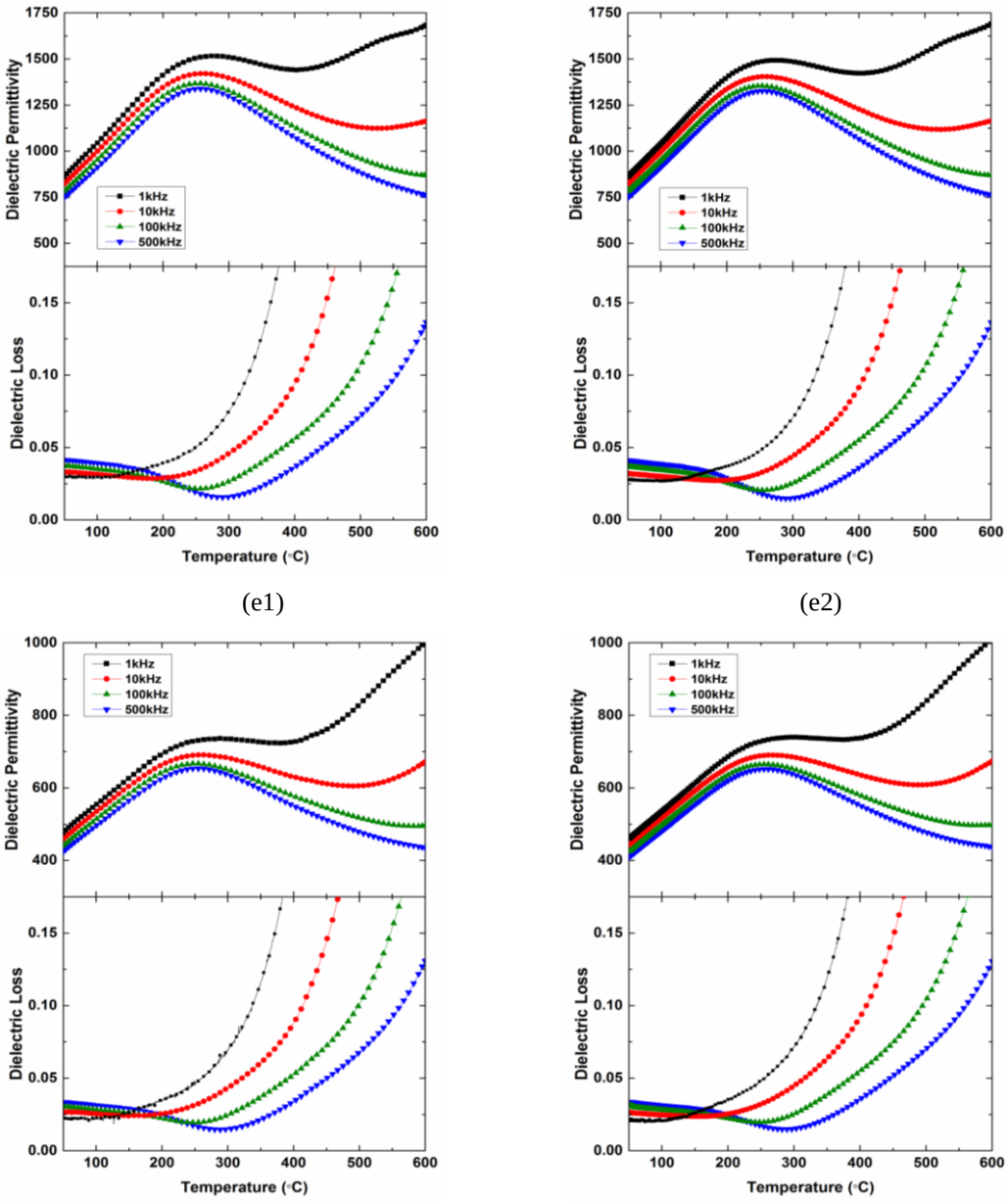

Fig.5.40: Temperature dependence of the dielectric response measured during (a1)-(f1) heating and (a2)-(f2) cooling at 1, 10, 100 and 500 kHz for each grain size: (a1)-(a2) 6 µm, (b1)-(b3) 3.5 µm, (c1)-(c2) 950 nm, (d1)-(d2) 350 nm, (e1)-(e2) 200 nm and (f1)-(f2) 100 nm. The dielectric response of the 3.5 µm grain size ceramic measured during heating after annealing at 600 ˚C for 4 h is shown in (b3).

Fig.5.40 shows the temperature dependence of the dielectric permittivity and loss of each BNBT-6 ceramic measured at frequencies of 1, 10,100 and 500 kHz during heating and cooling from room temperature up to 600 ˚C at a rate of 3 ˚C/min. BNBT-6 typically exhibits three anomalies in the unpoled state: $T_{S,}$ T_{RE} and T_M. These features, highlighted in Fig.5.40(a), are similar to those identified in BNT and are consistent with the dielectric studies reported in the literature[163]. The temperature T_m for each grain size is summarised in Table 5.9. Unlike BNT, the BNBT-6 ceramics exhibit a classical-

type of relaxor behaviour where T_{RE} coincides with T_M. This is clearly demonstrated in the ceramics prepared by conventional sintering were the frequency distribution vanishes at T_{RE}/T_M and remain minimal up to 500 ˚C were conductivity begins to distort the data.

Not all of the features could be identified in the dielectric response at each grain size. For ceramics with a grain size of 350 nm and below, T_S could not be clearly determined whereas T_M was observed for all of the tested ceramics. T_S is most prominent in the heating run of the ceramics with largest grain size, however this feature disappears on cooling. T_M on the other hand shows no temperature hysteresis and occurs at the same temperature on heating and cooling. T_{RE} could not be determined for any of the ceramics prepared by SPS. The frequency distribution in the permittivity measured for these ceramics continues to increase with increasing temperature; this is most prominent in the ceramics which show multiple peaks in their dielectric loss. Point defects, not removed by annealing, are thought to occur within these ceramics distorting the low frequency data.

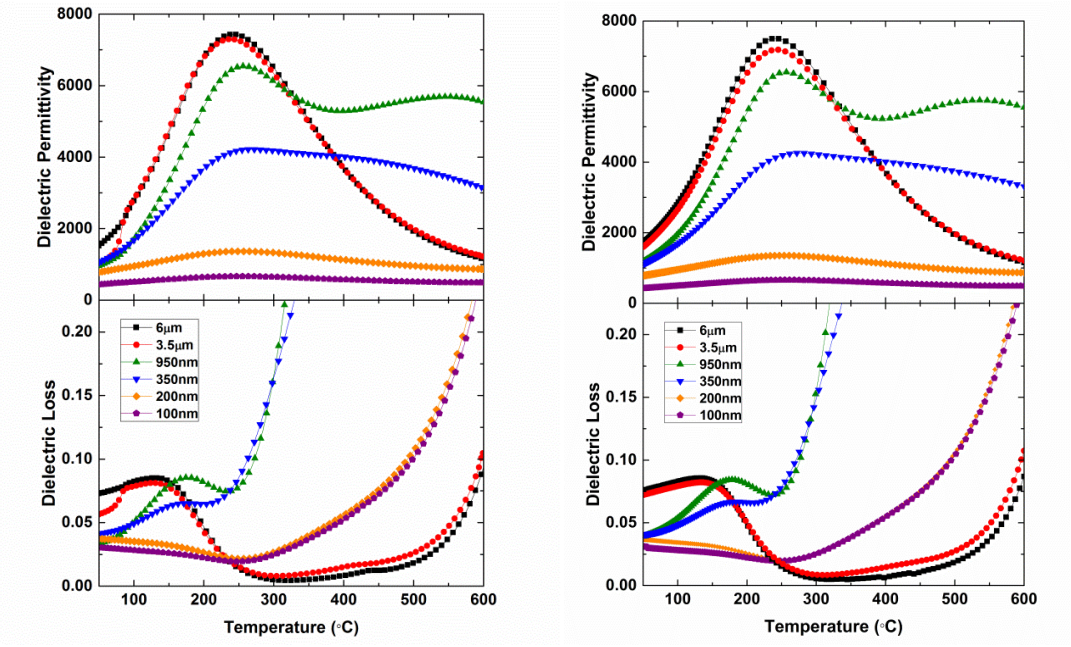

Fig.5.41: Grain size dependence of the dielectric response measured during (a) heating and (b) cooling at 100 kHz.

Table 5.9: The temperature T_M of the peak in the dielectric permittivity measured at 100 kHz.

Grain Size	**T_m (˚C)**
6 µm	242
3.5 µm	244
950 nm	256
350 nm	268
200 nm	254
100 nm	251

As shown in Fig.4.41, the peak in the permittivity T_M broadens, shifting only slightly to higher temperatures with decreasing grain size. The permittivity value is also reduced, decreasing from ~7400 for micrometre grain size ceramics to ~4200 for the 350 nm grain size sample when measured in a 100 kHz applied field.

(ii) Poled (60kV/cm)

Fig.5.42 shows the temperature dependence of the dielectric permittivity and loss after electrical poling. Each BNBT-6 ceramic was poled in an applied field of 60 kV/cm for 5 minutes before measuring the dielectric response at frequencies 10, 50,100 and 250 kHz on heating and cooling from room temperature up to 600 ˚C at a rate of 3 ˚C/min.

In the poled state, T_S is replaced by a sharp feature T_d which appears in both the dielectric permittivity and loss. Rather than appearing as a peak, as is the case for BNT, a shoulder-like feature, similar to that observed in the permittivity curve, appears in the dielectric loss data at T_d. The frequency distribution of the dielectric response is minimal below T_d and only increases above this temperature. Poling does not appear to induce a distinct feature at T_d in the smallest grain ceramics however the frequency distribution is dramatically reduced after poling. The temperature of T_m remains generally unchanged by poling however the reduction in the frequency distribution shifts the permittivity peak in the lower frequency data towards higher temperatures.

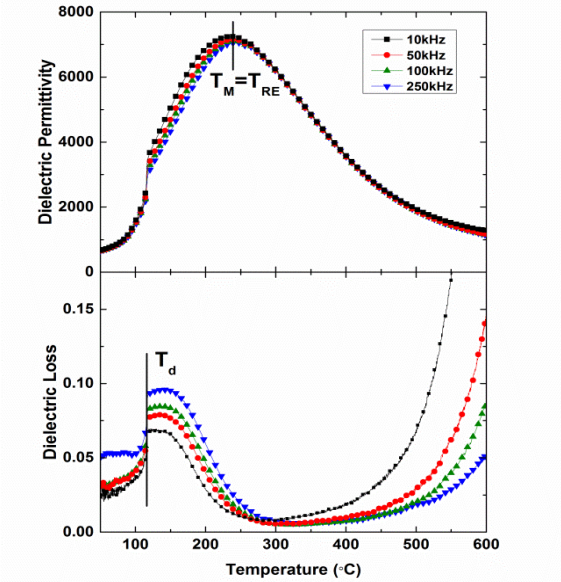
Dielectric Permittivity
Dielectric Loss
Temperature (°C)
10kHz
50kHz
100kHz
250kHz
T_M=T_RE
T_d

(a1)

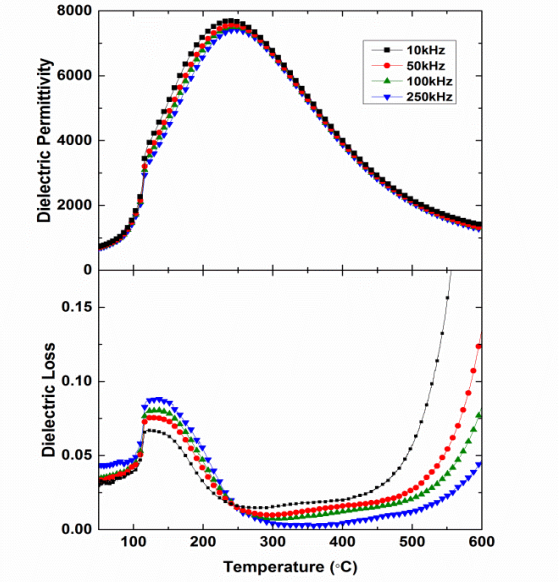
Dielectric Permittivity
Dielectric Loss
Temperature (°C)
10kHz
50kHz
100kHz
250kHz

(b1)

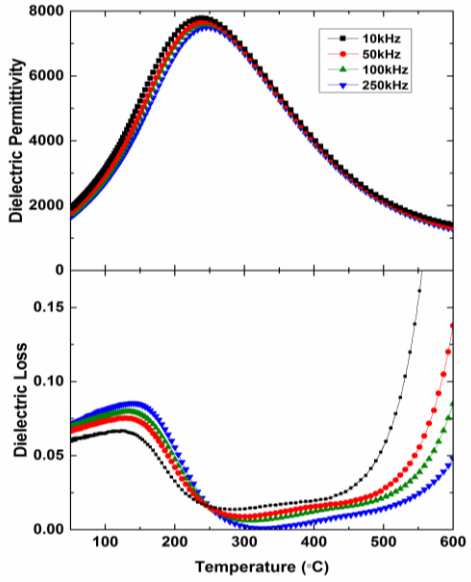
Dielectric Permittivity
Dielectric Loss
Temperature (°C)
10kHz
50kHz
100kHz
250kHz

(b2)

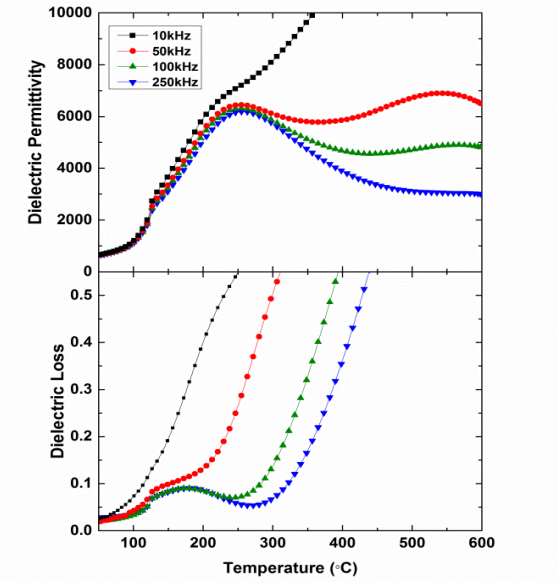
Dielectric Permittivity
Dielectric Loss
Temperature (°C)
10kHz
50kHz
100kHz
250kHz

(c1)

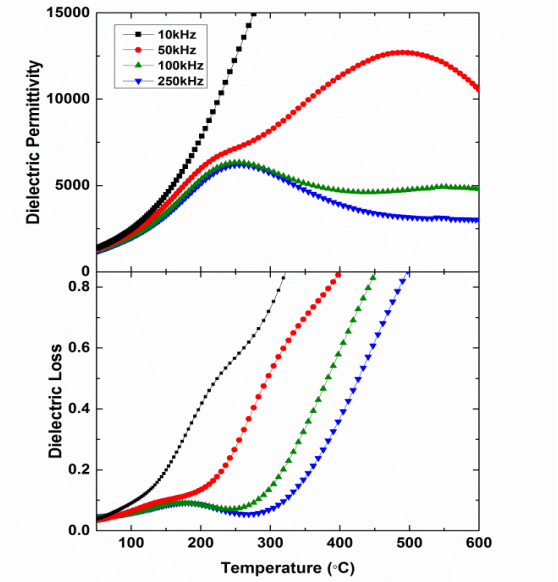
Dielectric Permittivity
Dielectric Loss
Temperature (°C)
10kHz
50kHz
100kHz
250kHz

(c2)

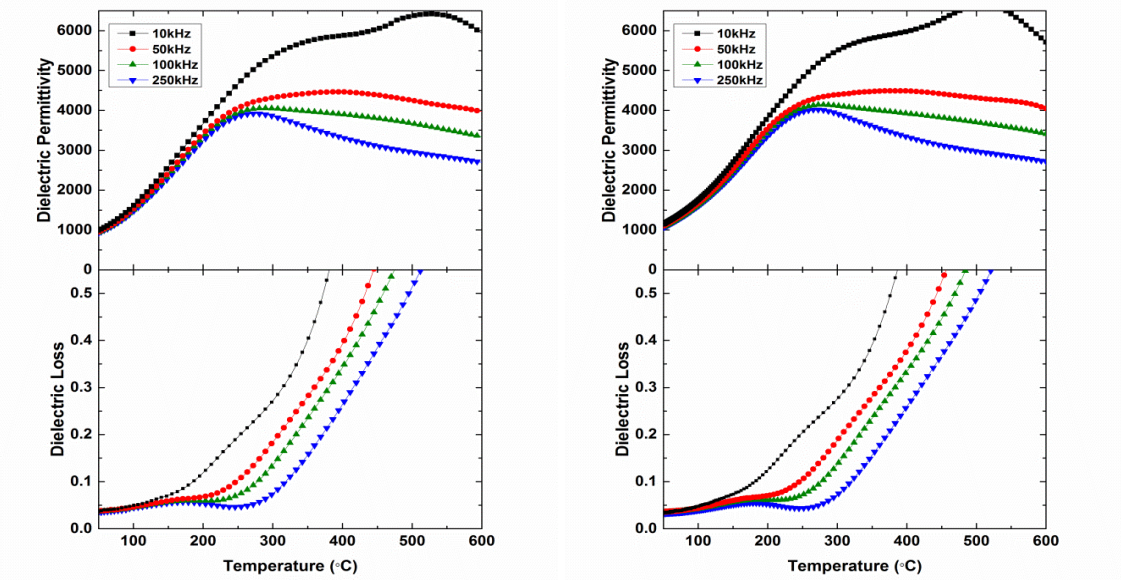

(d1) (d2)

Fig.5.42: Dielectric response vs. temperature for each grain size (a1) 6 µm, (b1)-(b2) 3.5 µm, (c1)-(c2) 950 nm and (d1)-(d2) 350 nm after electrical poling. Measured during (a1)-(d1) heating and (b2)-(d2) cooling at 1, 10, 100 and 250 kHz.

Poling lowers the dielectric permittivity value below T_d for all grain sizes, shown in Fig.5.43, as well as the permittivity value at T_M. Cooling after poling is similar to the cooling run in the unpoled state where T_d vanishes.

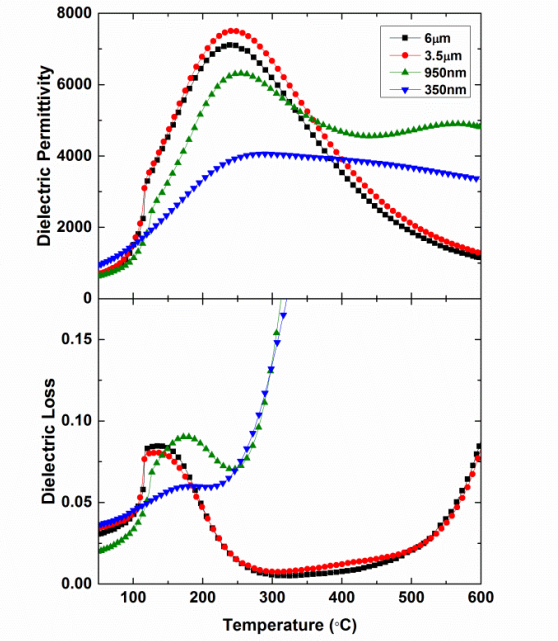

Fig.5.43: Grain size dependence of the dielectric response measured at 100 kHz after electrical poling.

(iii) Weak Bias-Field (3 kV/cm and 5 kV/cm)

The influence of a DC bias-field on the dielectric properties of BNBT-6, in particular on the transition at T_d, was investigated. The dielectric response was measured at frequencies 10, 50, 100 and 250 kHz between 25 ˚C and 180 ˚C (3 ˚C/min) after various electrical and thermal treatments: 1. Field Cooling (FC), 2. Zero Field Heating after Field Cooling (ZFH af. FC), 3. Field Heating after Field Cooling (FH af. FC), 4. Field Heating (FH) and 5. Zero Field Cooling after Field Heating (ZFC af. FH). A bias-field of 3 kV/cm was applied to each ceramic. A higher strength field of 5 kV/cm was also applied to the largest grain size ceramic. The samples were thermally annealed at 600 ˚C before each measurement to help eliminate the possibility of remanent macropolar regions influencing the results.

The dielectric results for each BNBT-6 ceramic are shown in Fig.5.44-5.50. The different thermal depolarisation temperatures determined from the shoulder in the dielectric response after each measurement are summarised in Table 5.10. In Fig.5.45, 5.47, 5.49 and 5.50 the dielectric results measured at 100 kHz for each grain size are compared with the dielectric data collected from their respective unpoled (ZFH/ZFC) and poled (ZFH Poled) states.

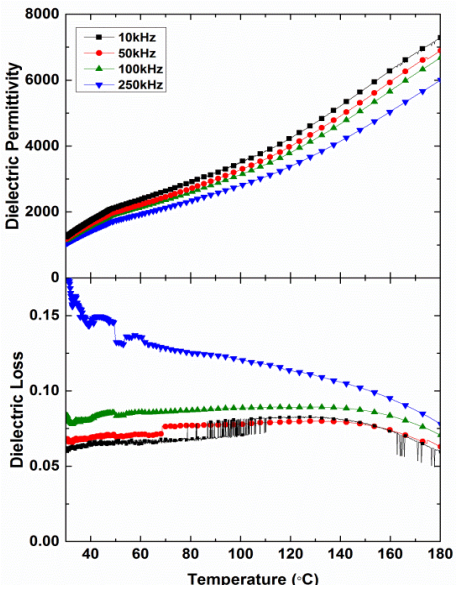

(a) FC (3 kV/cm)

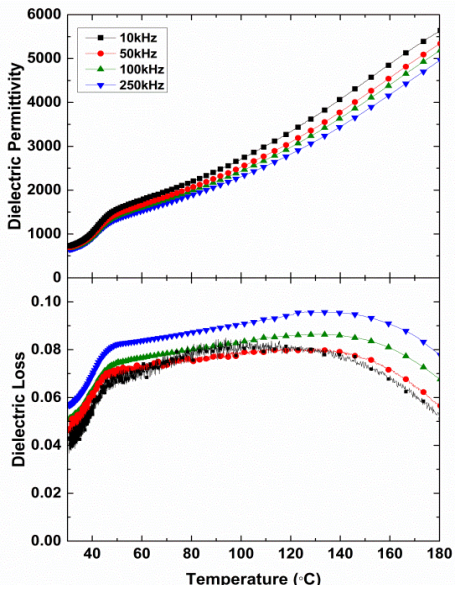

(b) FC (5 kV/cm)

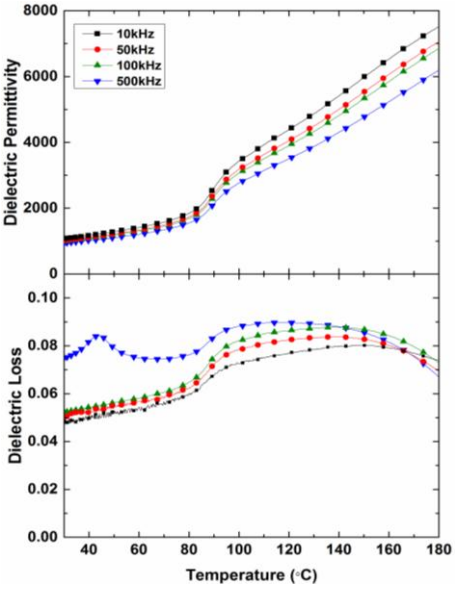

(c) ZFH af. FC (3 kV/cm)

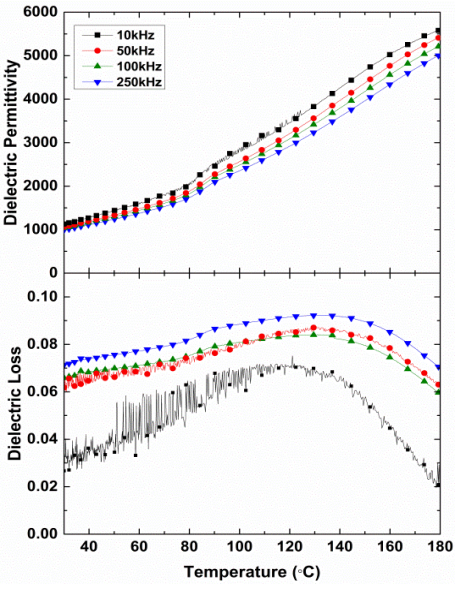

(d) ZFH af. FC (5 kV/cm)

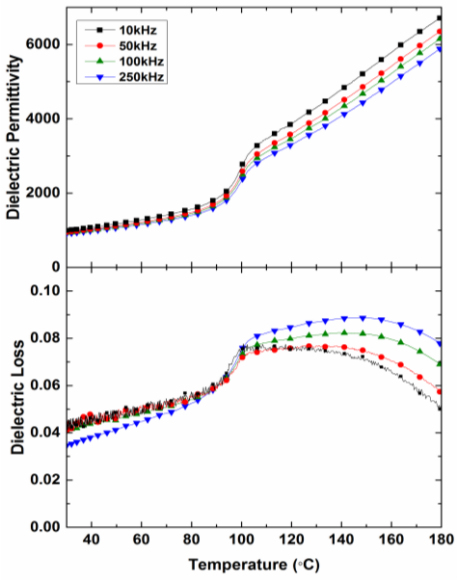

(e) FH af. FC (3 kV/cm)

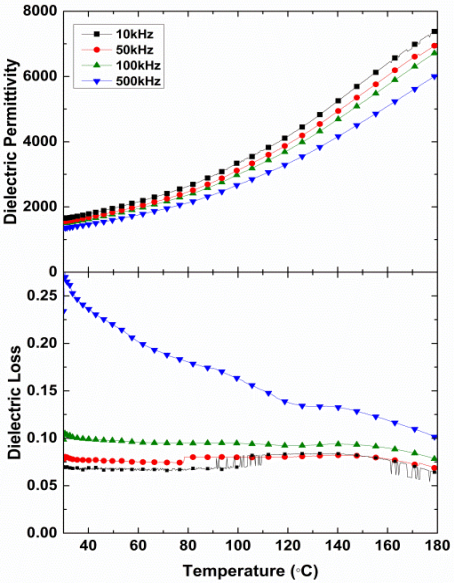

(f) FH (3 kV/cm)

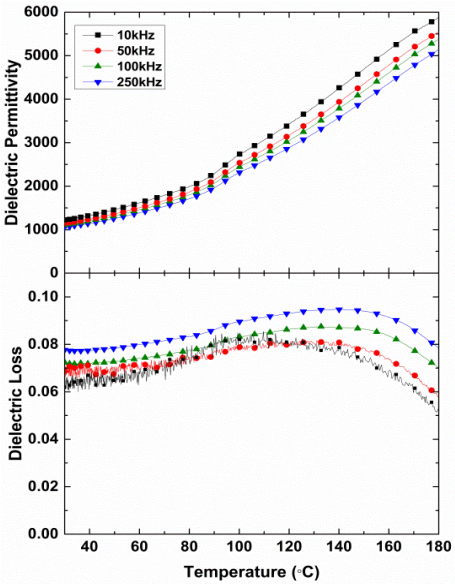

(g) FH (5 kV/cm)

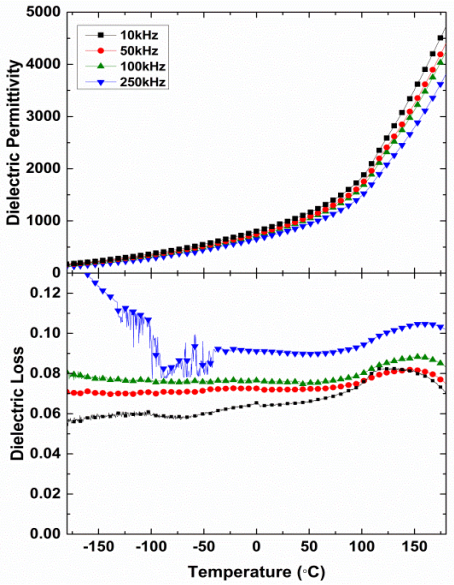

(h) FH (5 kV/cm) at LT

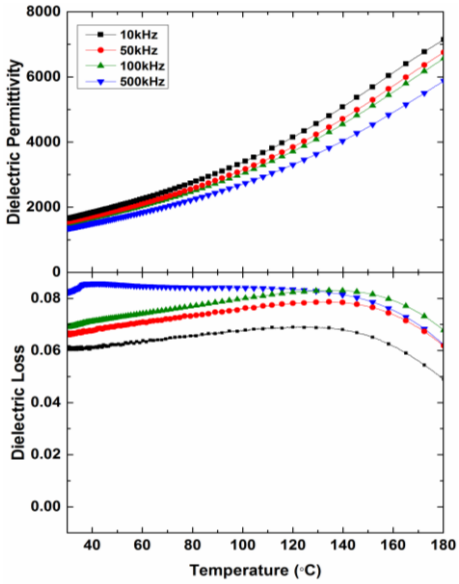

(i) ZFC af. FH (3 kV/cm)

Fig.5.44: The dielectric response of the 6 µm ceramic measured at frequencies 10, 50, 100 and 250 or 500 kHz after various electrical and thermal treatments, as summarised in the text. LT: bias-field applied at -180 ˚C.

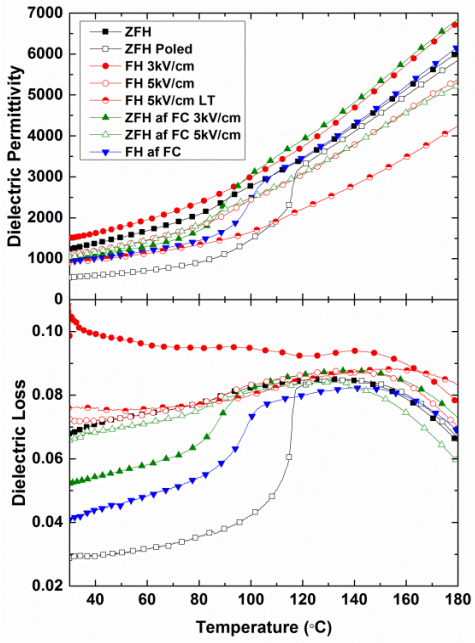

(a)

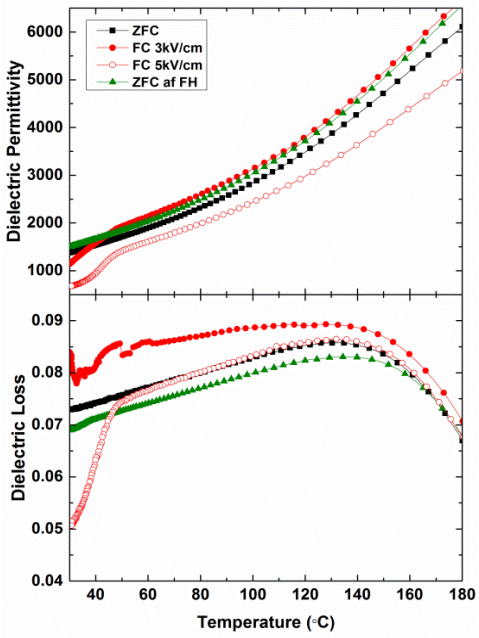

(b)

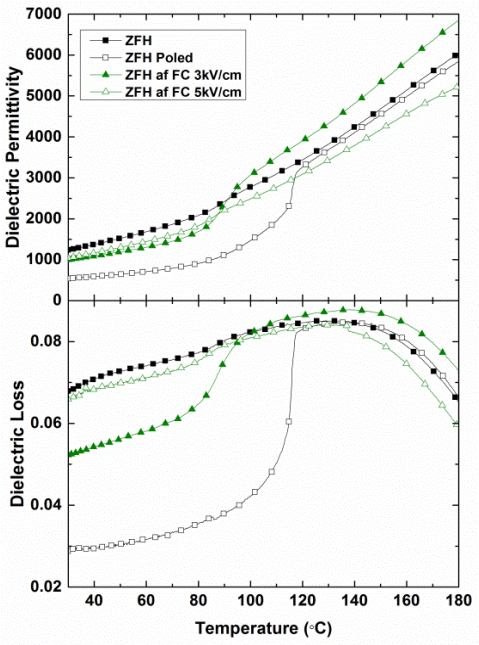

(c)

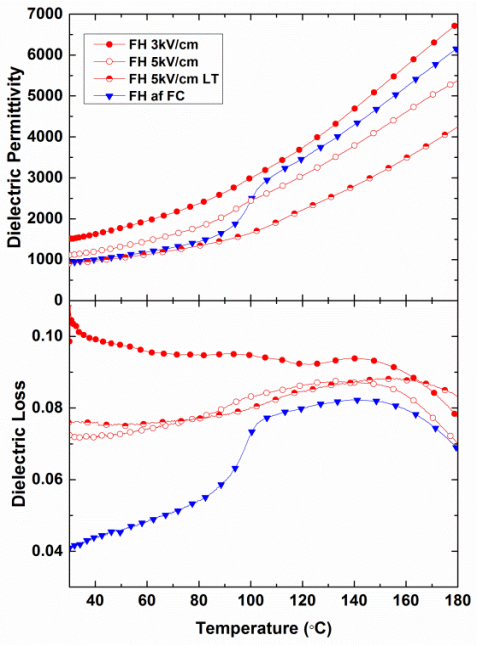

(d)

Fig.5.45: Dielectric response of the 100 kHz data collected from the 6 µm ceramic during (a) heating and (b) cooling. (c) and (d) show the bias-field measurements with different T_d and T_{bd}, respectively. LT: bias-field applied at -180 ˚C.

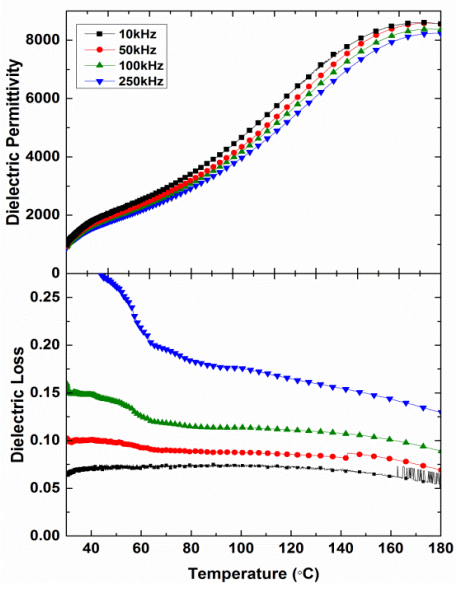

(a) FC (3 kV/cm)

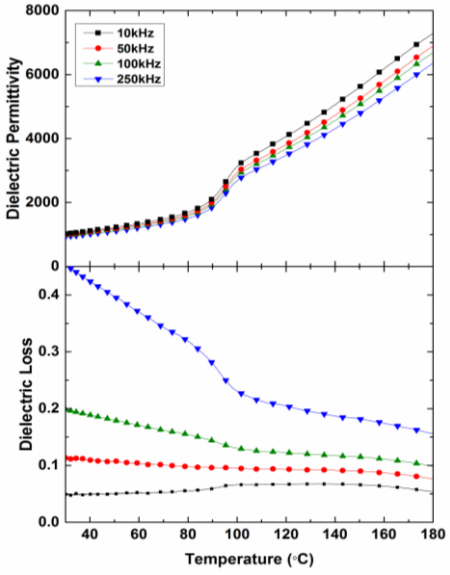

(b) ZFH af. FC (3 kV/cm)

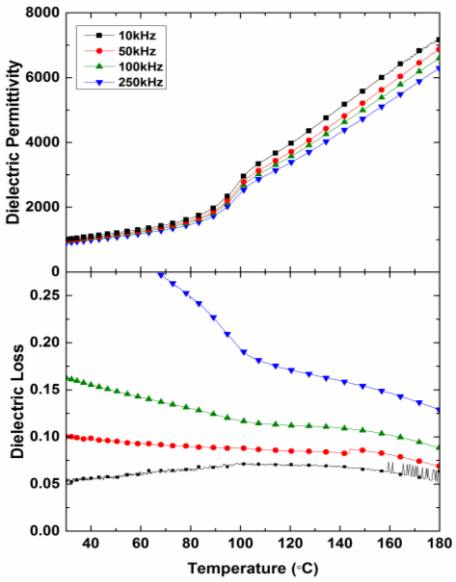

(c) FH af. FC (3 kV/cm)

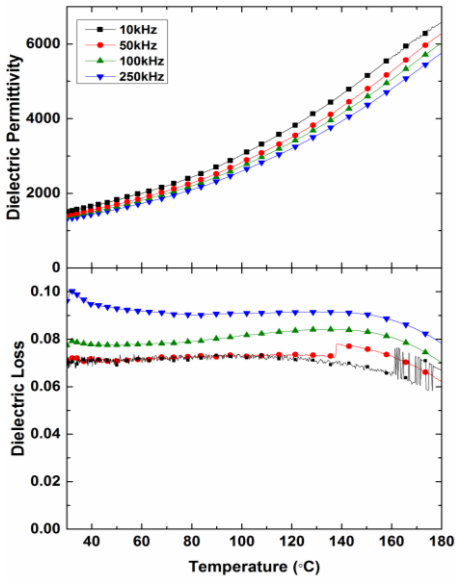

(d) FH (3 kV/cm)

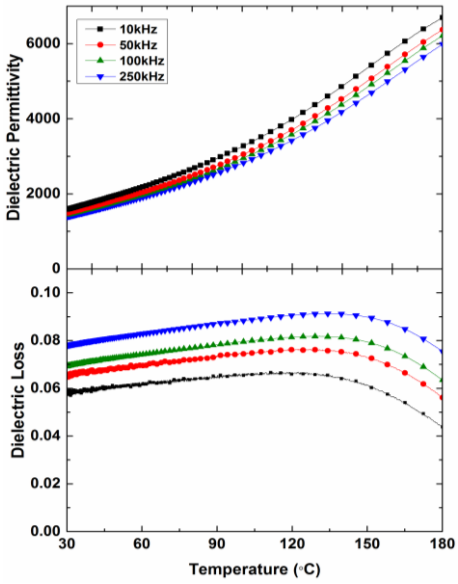

(e) ZFC af. FH (3 kV/cm)

Fig.5.46: The dielectric response of the 3.5 µm ceramic measured at frequencies 10, 50, 100 and 250 kHz after various electrical and thermal treatments, as summarised in the text.

The bias-field has the greatest influence on the dielectric response of the largest grain size ceramics. The 6 µm (Fig.5.45) and 3.5 µm (Fig.5.47) ceramics show the same dependence for the various electrical and thermal treatments. The depoling temperatures for these ceramics determined from T_s for ZFH and T_{do} for ZFH af. FC in a 3 kV/cm and a 5 kV/cm bias field are the same. Consequently, the polar states promoted by either mechanical stress from processing or from cooling in a weak-field are thought to be identical. The depoling temperature T_d of the polar state induced by poling in a high electric field however, occurs at a substantially higher temperature. The same sequence,

$T_d > T_s = T_{do}$ was observed for the 950 nm ceramic (Fig.5.49). The polar states created in BNBT-6 are clearly dependent on the initial poling field strength.

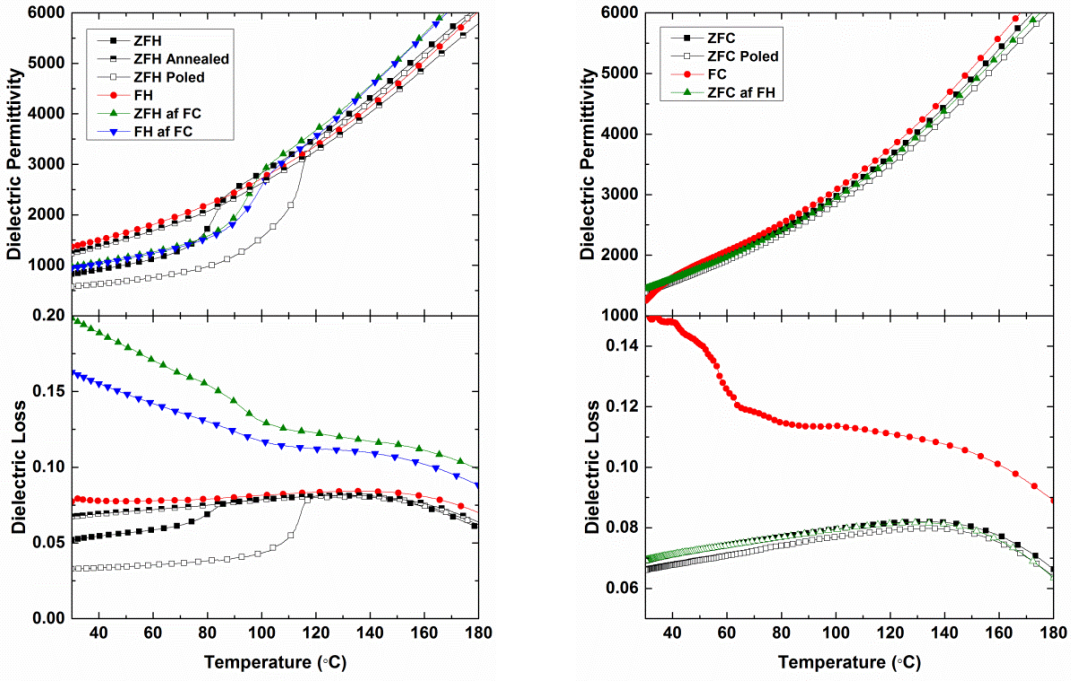

(a) (b)

Fig.5.47: Dielectric response of the 100 kHz data collected from the 3.5 µm ceramic during (a) heating and (b) cooling.

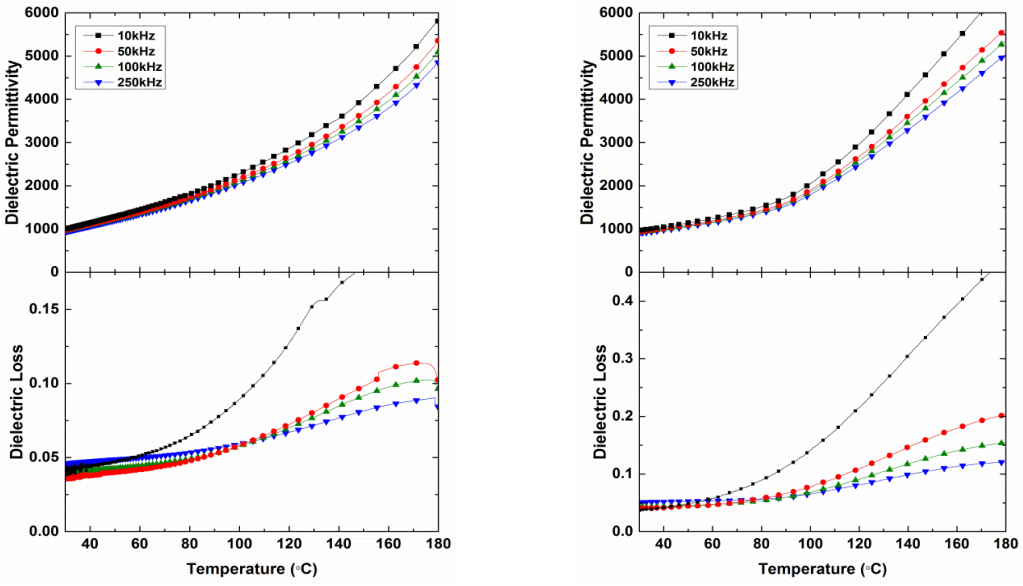

(a) FC (3 kV/cm) (b) ZFH af. FC (3 kV/cm)

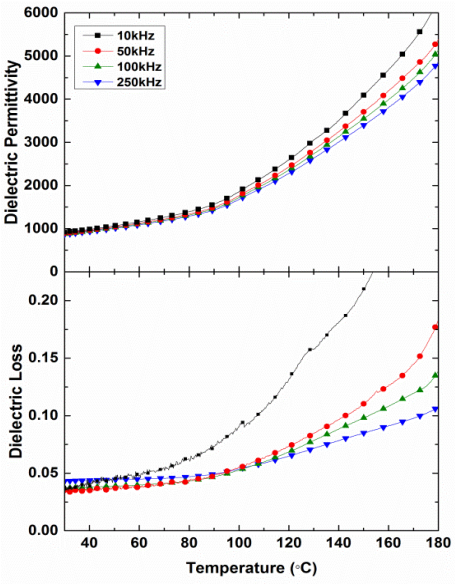

(c) FH af. FC (3 kV/cm)

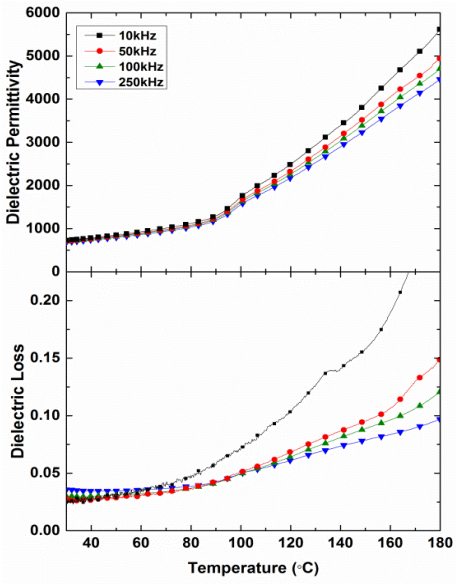

(d) FH (3 kV/cm)

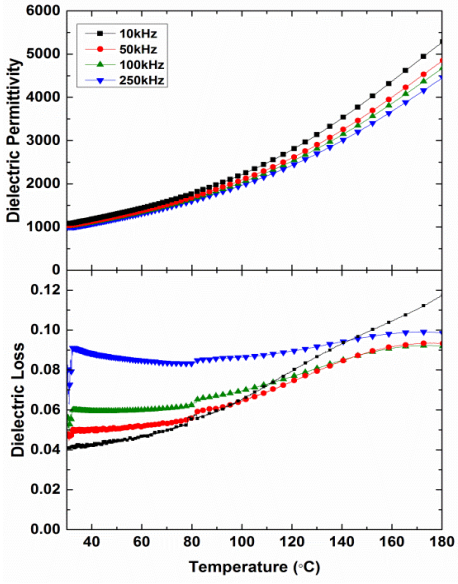

(e) ZFC af. FH (3 kV/cm)

Fig.5.48: The dielectric response of the 950 nm ceramic measured at frequencies 10, 50, 100 and 250 kHz after various electrical and thermal treatments, as summarised in the text.

The application of a bias field during heating helps to retain the polar state induced by the weak field shifting the depoling temperature T_{db} to higher temperatures during FH (5 kV/cm) and FH af. FC, as demonstrated Fig 5.45 (d). Although, the field is not strong enough to increase T_{db} to temperatures above T_d(Fig.5.45 (a)). T_{db} for FH in a 3 kV/cm bias-field could not be determined. This field is thought to be too weak to change the polar ordering of the annealed state. However, T_{db} for FH af. FC in a 3 kV/cm bias occurs at a slightly higher temperature than FH in a 5 kV/cm. Heating in a 5 kV/cm bias-field from low temperatures (-180 ˚C) raises T_{db} further, however it is still lower

than T_d. The bias-fields applied to the 950 nm ceramic are not strong enough to shift the depoling temperature to higher temperature (Fig.5.49 (a)), in this case $T_{db} = T_s = T_{do} < T_d$.

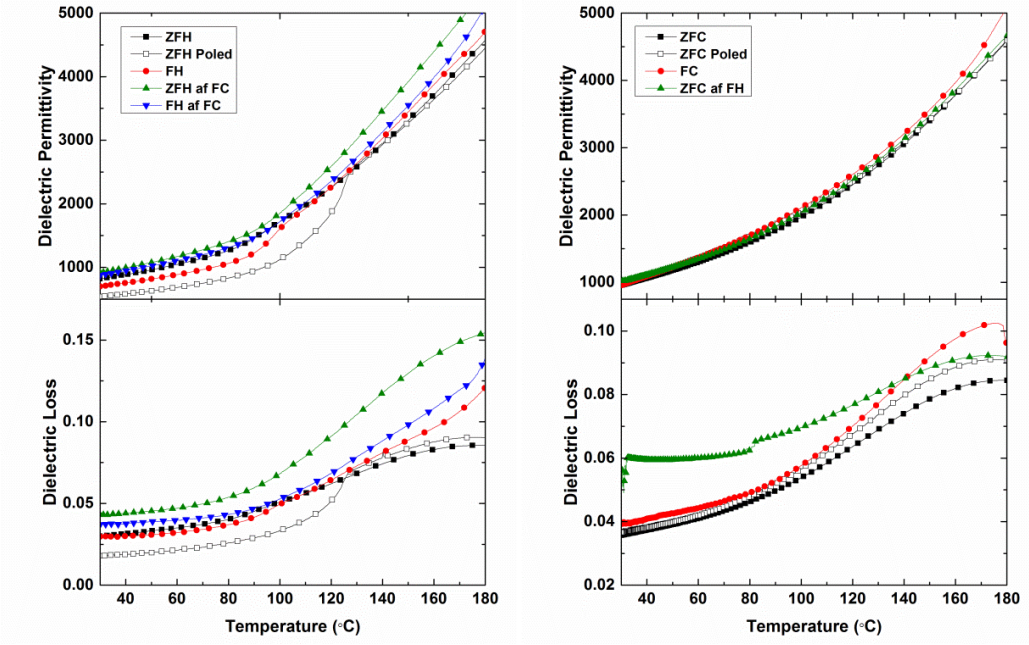

(a) (b)

Fig.5.49: Dielectric response of the 100 kHz data collected from the 950 nm ceramic during (a) heating and (b) cooling.

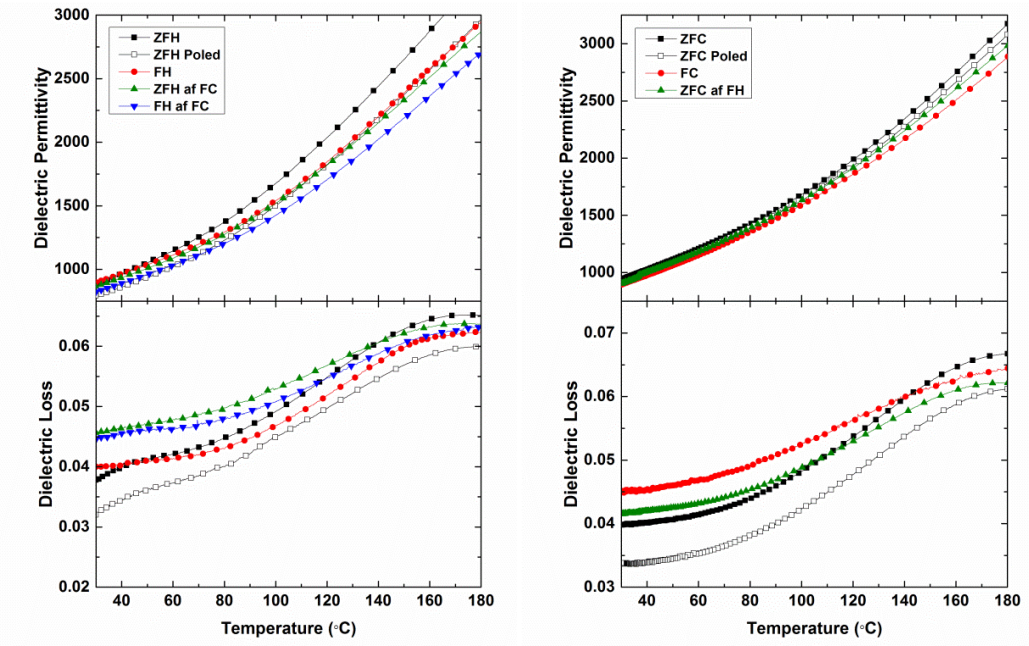

(a) (b)

Fig.5.50: Dielectric response of the 100 kHz data collected from the 350 nm ceramic during (a) heating and (b) cooling.

Table 5.10: The thermal depolarisation temperatures determined from the peak in the dielectric loss of the largest grain size BNBT-6 ceramics measured at 100 kHz. T_d: depoling after high field poling at room temperature, T_{do}: depoling after cooling in a bias-field, T_{db}: depoling in a bias-field.

Grain Size (nm)	**T_S (˚C)**	**T_d (˚C)**	**T_{do} (˚C)**	**T_{db} (˚C)** *FH af. FC*	**T_{db} (˚C)** *FH*	**T_{db} (˚C)** *FC*
6000	90	117	95 (3 kV/cm) 90 *	105	99 * 113 **	47
3500	86	117	98	105	-	40
950	88	127	-	95	102	

* 5 kV/cm

** 5 kV/cm applied at low temperature (-180 ˚C)

At temperatures below T_d, the dielectric permittivity of the different grain size BNBT-6 ceramics is lowest when they are poled in a high electric field. The polar state induced by mechanical stress and weak-bias fields does not lower the permittivity to the same values as that of the fully poled state. Above the depoling temperature, the permittivity increases for all of the dielectric runs, however only FH in a 5 kV/cm bias-field at -180 ˚C, shown in Fig.5.45(d) appears to influence the permittivity value above T_{bd}.

The dielectric response of ZFC and ZFC af. FH in either a 3 kV/cm or a 5 kV/cm bias field are identical (Fig.5.45, 5.47, 5.49). Neither of these measurements show any feature associated with depoling. A shoulder however reappears in the curve of both the dielectric permittivity and loss near room temperature when the 3.5 µm and 6 µm ceramics are cooled in a bias field (FC). A long-range ordered polar state is re-induced into the system at $T_{db\text{-}FC}$ and appears to be independent of the bias field strength. No such feature is observed for the 950 nm ceramic.

The effect of a bias-field on the dielectric properties of 350 nm ceramics was also measured (Fig.5.50). However, the bias-field appears to be too weak to induce a clear change in response at the depoling temperature.

5.2.6 Polarisation and Current vs. Electric Field

Fig.5.51 shows the temperature dependence of the P-I-E loops for each ceramic. The temperatures were selected with reference to the dielectric response of the ceramics. The temperature dependence of the remnant polarisation (P_r), saturation polarisation (P_{sa}) and coercive field (E_c) values, collected from the hysteresis loop measured at 10Hz, are summarised in Fig.5.52.

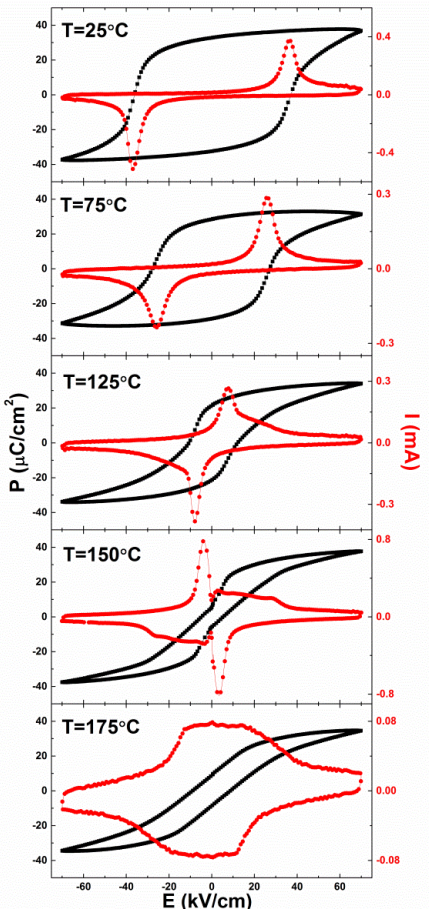
T=25°C
T=75°C
T=125°C
T=150°C
T=175°C
P (μC/cm²)
I (mA)
E (kV/cm)

(a)

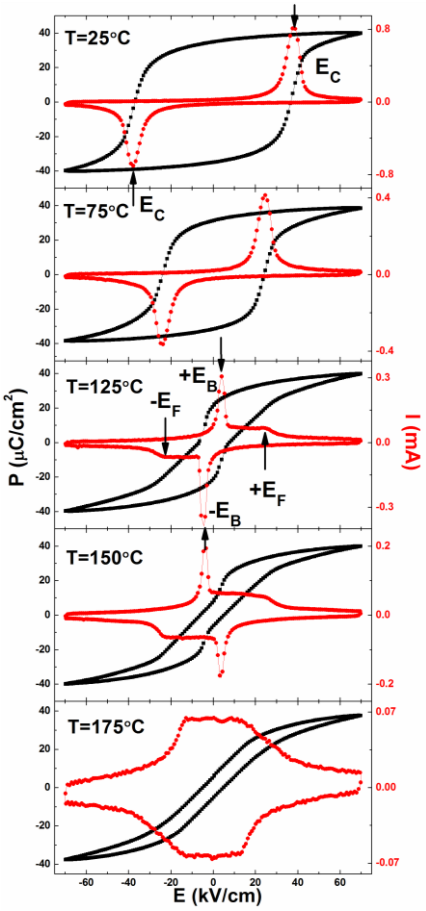
T=25°C
T=75°C
T=125°C
T=150°C
T=175°C
E_C
+E_B
-E_F
+E_F
-E_B
P (μC/cm²)
I (mA)
E (kV/cm)

(b)

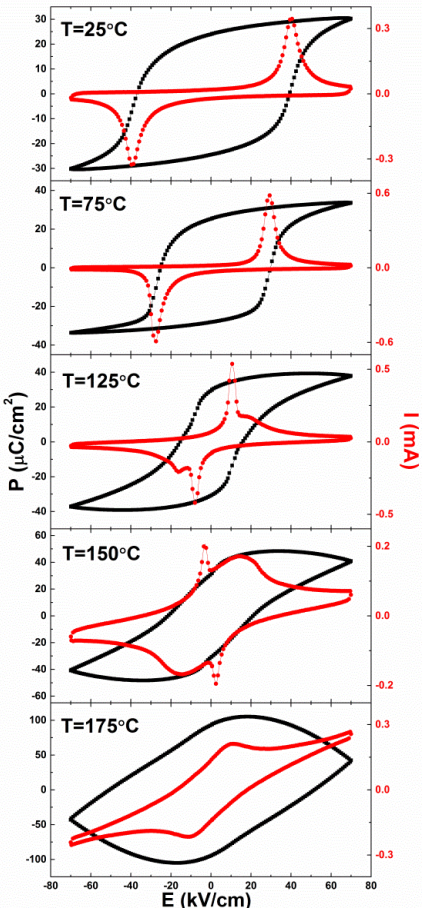
T=25°C
T=75°C
T=125°C
T=150°C
T=175°C
P (μC/cm²)
I (mA)
E (kV/cm)

(c)

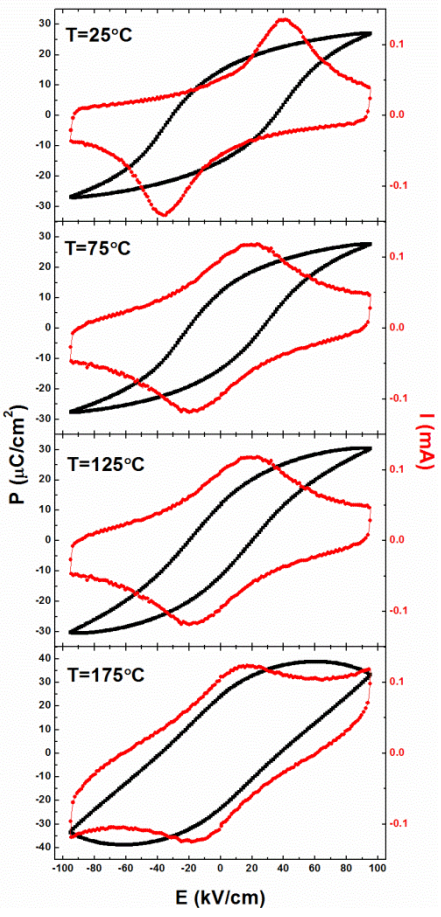
T=25°C
T=75°C
T=125°C
T=175°C
P (μC/cm²)
I (mA)
E (kV/cm)

(d)

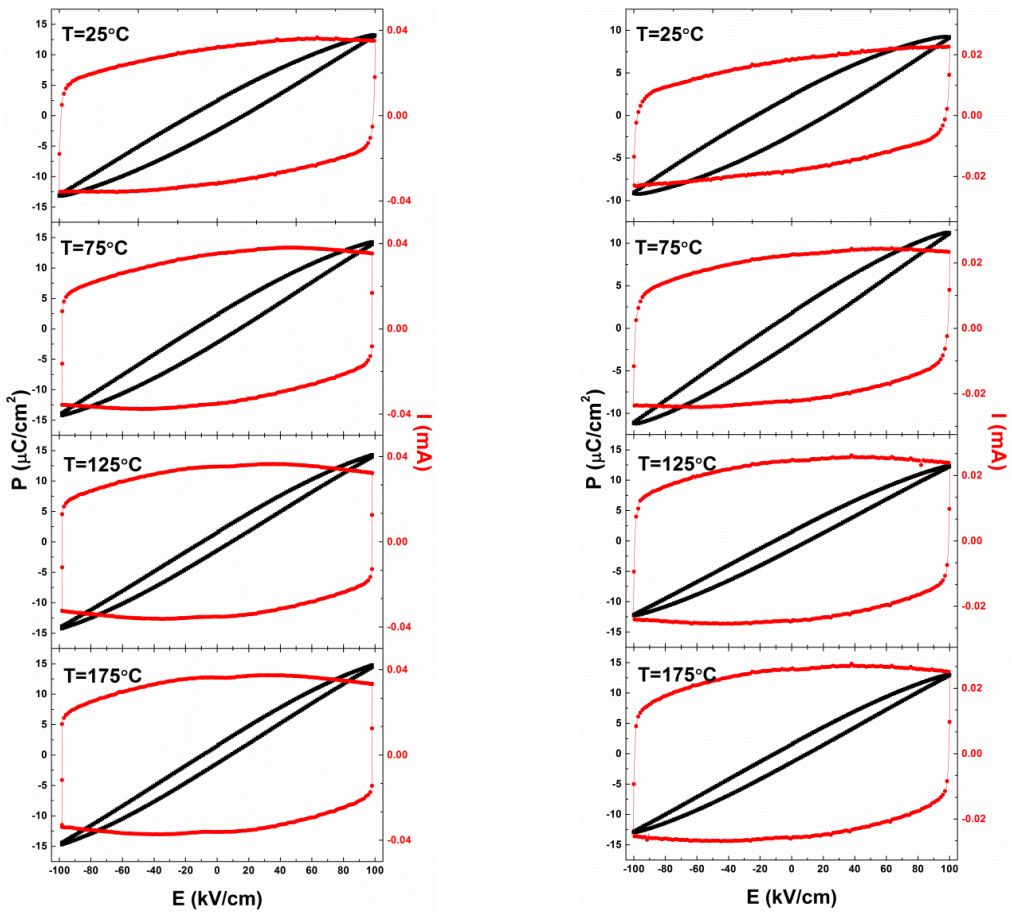

(e) (f)

Fig.5.51: Temperature dependence of the P-I-E loops of measured at 10 Hz for each BNBT-6 ceramics with grain size (a) 6 μm, (b) 3.5 μm, (c) 950 nm, (d) 350 nm, (e) 200 nm and (f) 100 nm.

The ferroelectric nature of the BNBT-6 ceramics was confirmed by the domain switching current peaks which were observed over the temperature range 25-175 ˚C for all of the ceramics, expect those with the smallest grain size ≤ 200 nm.

Fully saturated P-E loops could not be obtained for any of the ceramics over the measured temperature range. The low breakdown field typically associated with BNT-based materials is increased for ceramics with smaller grain size. However, the E_c value is also increased preventing accurate E_c and P_{sa} values being obtained for these ceramics. At high temperatures, effects from conductivity distort the P-E loops, increasing the value of P_r. This effect is clearly demonstrated in the 950 nm ceramic. The I-E loops also become slanted at these high temperatures. The inability to fully saturate the polarisation, particularly for the smaller grain size ceramics, can distort the true grain size effect in these materials.

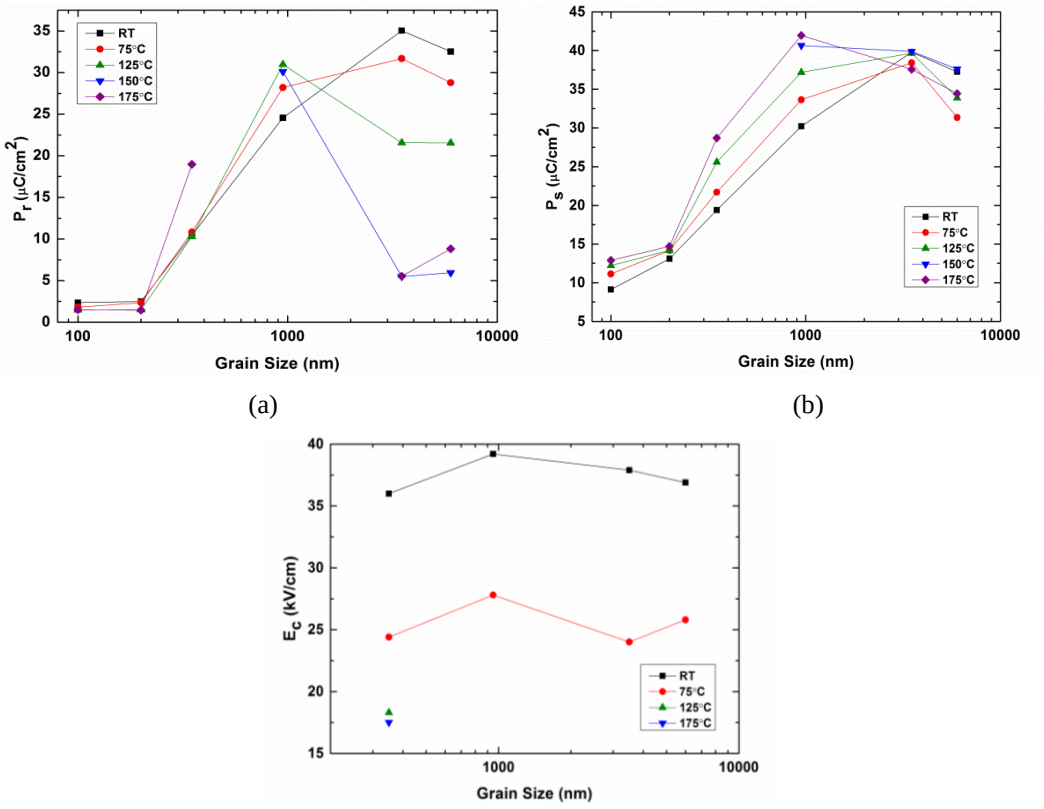

Fig.5.52: Grain size dependence of the (a) remnant polarisation (P_r), (b) saturation polarisation (P_s) and (c) coercive field (E_c) values, collected from the P-I-E loops measured at 10 Hz. The P_r value for the 950 nm grain size ceramic at 175 ˚C has been omitted as it is severely distorted by high conductivity.

At room temperature, both P_{sa} and P_r initially increase in value as the grain size is reduced from 6 μm to 3.5 μm before decreasing with further reduction in grain size. Back fields exerted by the high density of grain boundaries in the fine grain ceramics are thought to suppress domain reversal reducing P_{sa}, as well as favouring domain switch-back during electric field unloading decreasing P_r. As a result of the increased internal stresses created at the grain boundaries during poling, E_c typically increases with decreasing grain size.

Before saturation has occurred, the current peak in the I-E loop typically increases in value and shifts to higher electric field values as the strength of the applied is increased. When the polarisation is saturated, the position of the current peak will remain at E_c and the current value will continue to increase with increasing applied field. A different type of behaviour is observed in the micrometre grain size ceramics. As the applied field is increased from 90 kV/cm to 95 kV/cm and from 85 kV/cm to 90 kV/cm for the 3.5 μm and 6 μm ceramics, respectively, the current value of the peak begins to decrease (Fig.5.53).

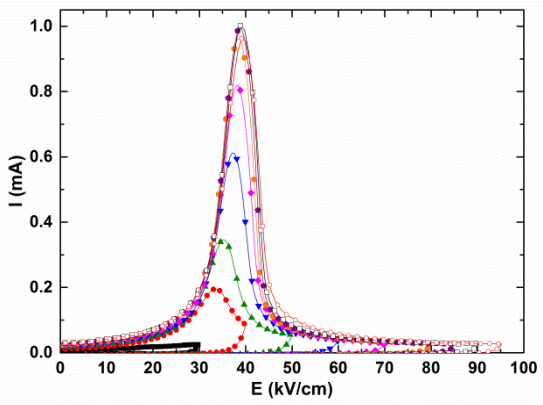

(a1)

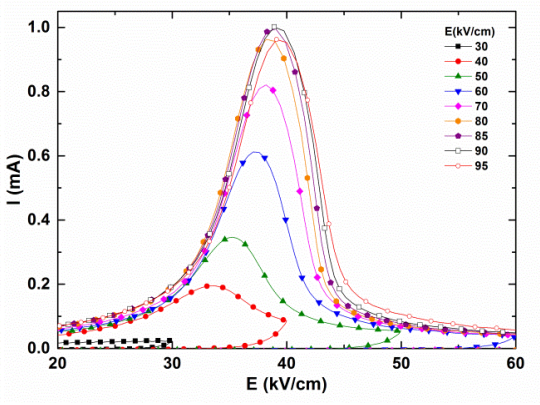

(a2)

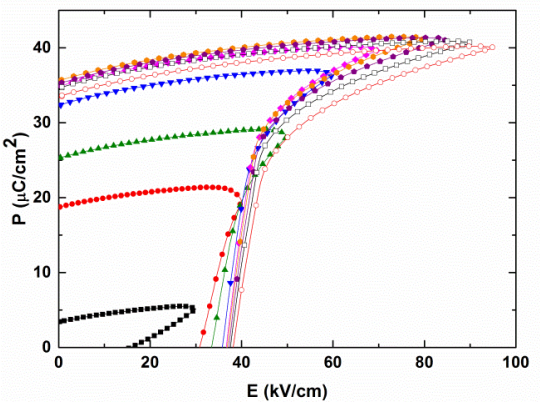

(a3)

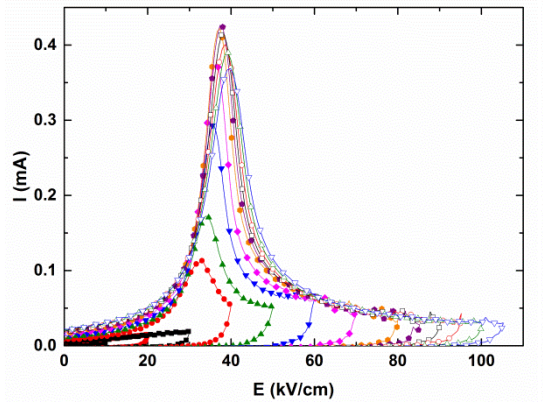

(b1)

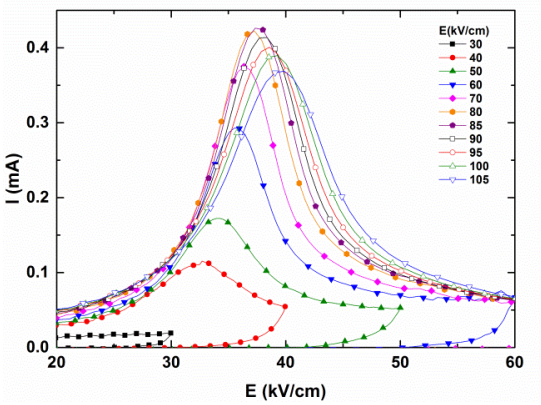

(b2)

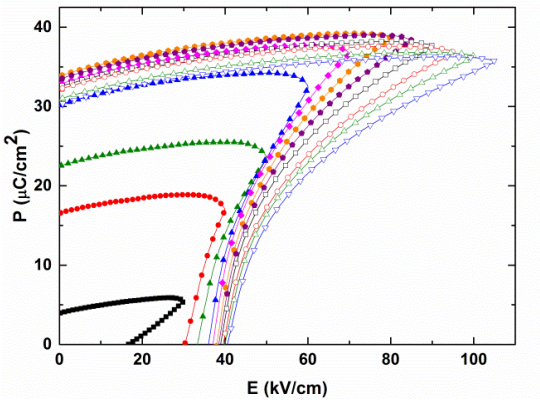

(b3)

Fig.5.53: Room temperature (a1)-(a2),(b1)-(b2) I-E and (a3), (b3) P-E loops for (a1)-(a3) 3.5 μm and (b1)-(b3) 6 μm grain size BNBT-6 ceramics, measured at 10 Hz.

Greater domain reversal is expected to occur as the domain walls become more active with increasing temperature. Any long-range FE order induced by the applied electric field will be easily broken by these active domain walls as the field is removed. As expected, the P-E loops of the largest grain size ceramics become slimmer with increasing temperature reducing P_r, however P_{sa} initially decreases at 75 ˚C before increasing with rising temperature. Meanwhile, the P_{sa} values recorded for the BNBT-6 ceramics with a grain size of 950 nm and smaller, increase continuously with increasing temperature. Conductivity clearly distorts the P_r values of the 950 nm and 350 nm ceramics, however not at temperatures of 125 ˚C and below, which show a general increase in P_r with increasing temperature. For each grain size, E_c clearly shift to lower fields with increasing temperature as a result of the increased thermal motion of the atoms in the lattice which lowers the energy barrier for polarisation reversal and domain wall reorientation.

At 125 ˚C, four current peaks appear in the I-E loops of the 950 nm, 3.5 µm and 6 µm BNBT-6 ceramics at $\pm E_F$ and $\pm E_B$. The peak at $\pm E_F$ broadens as the applied field is increased as shown in Fig.5.54. The multiple current peaks can be interpreted as follows: during cycling regime conditions the polarisation effects corresponding with $+E_F$ and $-E_F$ are recovered during electric field reversal at $-E_B$ and $+E_B$, respectively. At 125 ˚C, $\pm E_F$ and $\pm E_B$ both appear during electrical loading. As the temperature is increased, the threshold field $-E_B$ ($+E_B$) moves away from $+E_F$ ($-E_F$). At 150 ˚C, $\pm E_B$ appears as the electric field is removed indicating that the polarisation effects produced by $\pm E_F$ can be recovered during unloading. The corresponding P-E loops appear pinched between $+E_F$ and $-E_F$. At 175 ˚C, the P-E loop is similar to that expected for a relaxor ferroelectric. The $\pm E_F$ and $\pm E_B$ current peaks can no longer be identified at this temperature and are replaced by a broad peak spanning the loading and unloading sides of the hysteresis loop.

Although, no distinct domain switching peaks are observed in the I-E loops of the ceramics with grain size ≤200 nm, small current bumps, highlighted in Fig.5.51 (e), do appear in the loops at high temperatures. Conductivity is not thought to influence the shape of these loops, which show an increase in P_r value with increasing temperature (Fig.5.52 (b)). Domain switching is therefore still expected to occur at this small grain size.

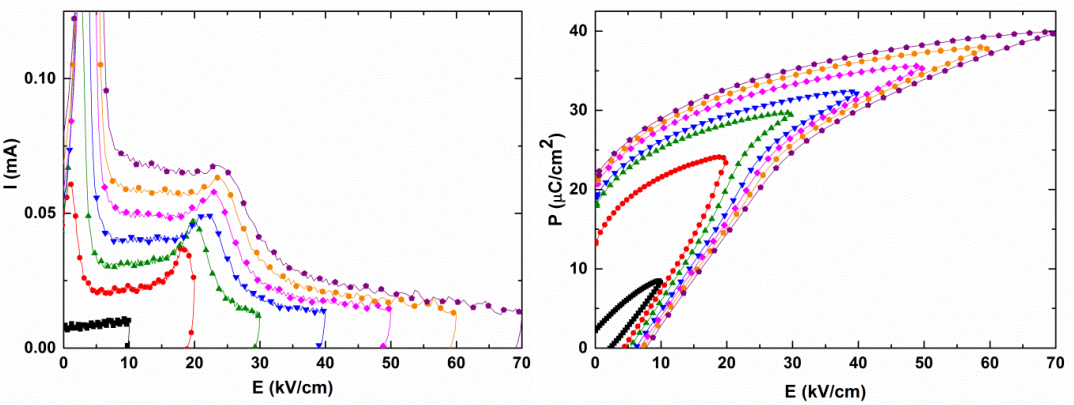

(a) (b)

Fig.5.54: (a) I-E and (b) P-E loops measured at 125 ˚C for the 3.5 μm BNBT-6 ceramic. (Frequncy: 10 Hz) Demonstrating the change in shape of the $+E_F$ peak with increasing applied field.

(i) Frequency Dependence

For each grain size, E_c shifts to higher electric fields with increasing frequency, as demonstrated in Fig.5.55 (a). Over the whole temperature range 25-175 ˚C, P_{sa} and P_r were found to decrease with increasing frequency for all of the ceramics, demonstrated in Fig.5.55 (a). This frequency dependence can be related to the relaxation time of the domain walls. At high frequencies, fewer domain walls can follow the applied electric field hindering the growth in size and number of domains parallel to the applied field. A higher strength field is required to force more of the domain walls that can still follow the field to switch the polarisation.

At temperatures above 75 ˚C, $\pm E_F$ and $\pm E_B$ also shift to higher electric fields with increasing frequency as demonstrated in Fig.5.55(b). Although, P_r continues to decrease with increasing frequency at this temperature, the frequency distribution is substantially smaller, as shown in Fig.5.55 (b).

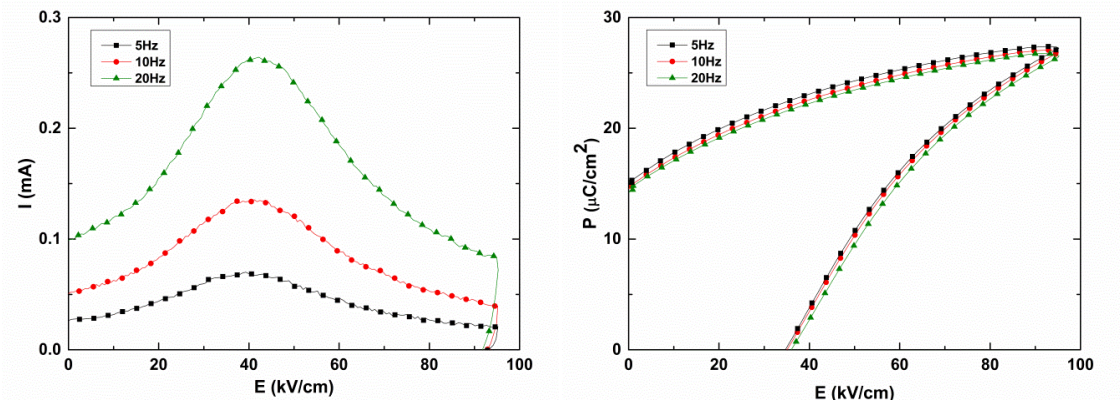

(a1) (a2)

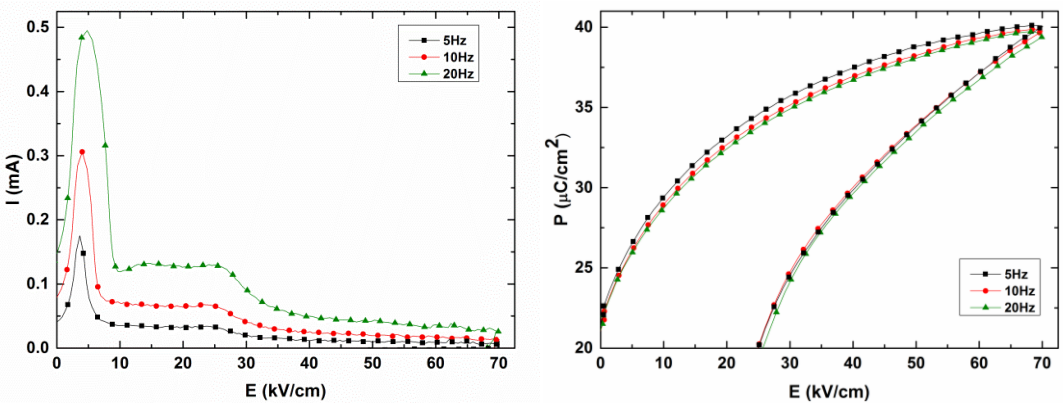

(b1) (b2)

Fig.5.55: (a1),(b1) I-E and (a2), (b2) P-E loops showing the frequency dependence of (a1)-(a2) 350 nm ceramic at room temperature and (b1)-(b2) 3.5 μm ceramic at 125 ˚C.

5.2.7 Piezoelectric Response (d_{33}) vs. Temperature

Fig.5.56 shows the grain size dependence of the piezoelectric constant d_{33} on depoling. As the grain size is reduced, the d_{33} decreases. Re-orientation of the spontaneous strain during electrical poling increases the internal stress at the grain boundaries of the BNBT-6 ceramics. Domain reversal will be suppressed in the finer grains by the large back fields exerted by the high density of grain boundaries, decreasing the in d_{33}.

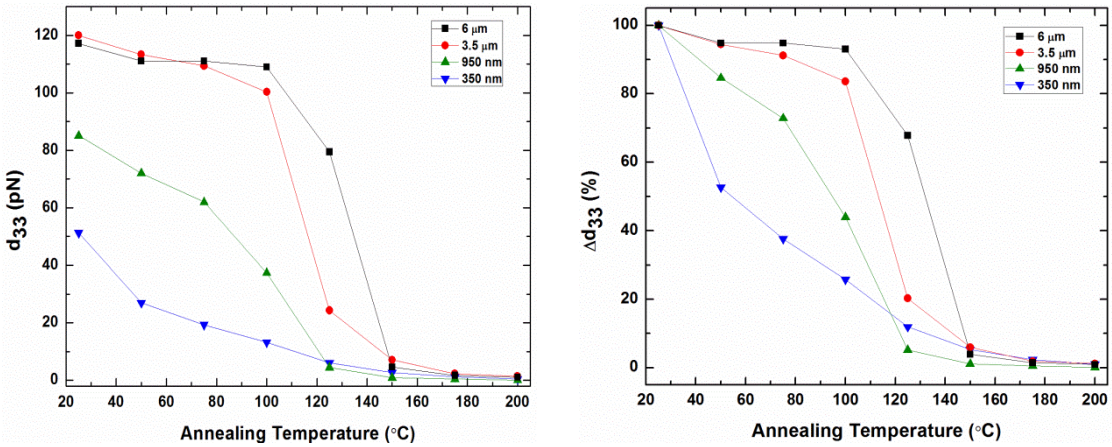

(a) (b)

Fig.5.56: (a) d_{33} and (b) Δd_{33} measured for each BNBT-6 grain size during depoling, after heating in silicon oil for 5 minutes at each temperature.

Below 100 ˚C, the d_{33} decreases only slightly on heating for the largest grain size ceramics. The d_{33} value then decreases sharply above this temperature until 150 ˚C, reducing in value from 109 to 5 pN and from 100 to 7 pN for the 6 μm and 3.5 μm ceramics, respectively. A similar trend is observed for the 950 nm ceramic, however the relatively high d_{33} value in this case is only maintained until 75 ˚C, where it then

decreases more rapidly with increasing temperature. The sharpest decrease in d_{33} value occurs between 25 and 50 ˚C for the 350 nm ceramic. None of the ceramics are fully depoled at 200 ˚C.

Room temperature d_{33} values of 1.9 pN and 3.3 pN were recorded for the 100 nm and 200 nm grain size BNBT-6 ceramics, respectively, after poling in a 60 kV/cm electric field for 10 minutes.

5.3 Discussion

5.3.1 Room Temperature

According to the literature, the structure of BNBT-6 in the unpoled state appears as a mixed *R3c*/*P4bm* phase when analysed using TEM.[162] Only a pseudo-cubic distortion is detected by XRD for this composition because of the short coherence length of the *R3c* and *P4bm* symmetries.[11] The rhombohedral and tetragonal distortions that form the room temperature structure only become visible to XRD with the application of an electric field. The small difference in free energy between the *R3c* and *P4bm* polar nanoregions (PNRs) at room temperature enable the easy interconversion of the two symmetries.[11] The crystal structure of the poled state of BNBT-6 is dependent on the strength of the poling field. For example, the *P4bm* phase in BNBT-6, detected by TEM, irreversibly transforms to *P4mm* symmetry at 32 kV/cm before undergoing a *P4mm*-to-*R3c* phase transition with increasing field strength. The original *R3c* phase was noted not to experience any phase transition on electrical poling.[198] A mixed *R3c*/*P4mm* phase was detected by XRD after poling in an electric field of 40-50 kV/cm. Mechanical stresses induced in the system by grinding and crushing have a similar effect on the structure of BNBT-6 as electrical poling. However, mechanical impact only partially changes the structure while poling changes it to its possible limit.[12]

A pseudo-cubic distortion was similarly observed in the room temperature XRD data collected from the crushed BNBT-6 ceramics (Fig.5.24). Using Rietveld refinement, a mixed phase of *R3c* and *P4bm* symmetries was found to provide the best quality of fit for the largest grain size ceramics. Although the mixed phase structure was not fitted to the 350 nm and 950 nm ceramic XRD data the degree of rhombohedral distortion is expected to decrease with decreasing grain size. The $Pm\bar{3}m$/*P4bm* mixed phase was found to best describe the room temperature structure of the crushed nanograin ceramic. The structure is dominated by the near cubic distortion while the *P4bm* symmetry appears only as a minor phase. A number of different phase combinations were refined for the XRD data, including *R3c*/*P4mm*, $Pm\bar{3}m$/*R3c*, *Cc*/*P4bm*, *Cc*/*R3c* as well as single phases. While the $Pm\bar{3}m$(*R3c*)/*P4bm* structure provided the best fit, the XRD data is not wholly satisfied by this refinement, particularly the *P4bm* symmetry. A more complex structure is expected to occur in this system. The powdered ceramics submitted for XRD were not annealed after crushing. The stresses induced in the system by the

mechanical impact are thought to have increased the distortion of the rhombohedral phase making it visible to XRD.

Backscattered SEM images of the ion-beam polished surface reveal a complex microstructure (Fig.5.25-5.30). The BNBT-6 ceramics do not show the cross-hatched domain structure associated with the *Cc*/*R3c* symmetry observed in unpoled BNT; rather the grains are dominated with striped domains seen in BNT after poling. However, the domain morphology is not as simple as in BNT, instead of filling the whole grain, the striped domains, which tend to be much finer, are often broken up and occasionally form a herringbone-type structure (Fig.5.27). This herringbone structure is not dissimilar to the lamellar domain pattern associated with *P4mm* symmetry observed in BNBT-11.[162] Without electron diffraction patterns, it is not possible to clearly distinguish between the *R3c* and *P4mm* symmetries in this material. The TEM images reported in the literature for BNBT-6 show very similar lamellar domain patterns for these two structures.[198] Areas of an individual grain, which otherwise show a clear domain structure, have been imaged without any domain pattern (Fig.5.27 and 5.28). Nanodomains consistent with *P4bm* symmetry[162] are thought to occupy this volume of the grain. The structure of the BNT-based materials are highly sensitive to mechanical impart.[12] Although the ceramics were thermally annealed prior to ion-beam polishing, mechanical stresses induced in the system by the polishing may still alter the domain structure of the fully annealed, unpoled state. The pseudo-cubic structure refined by XRD for the annealed ceramics is expected to result from distortions associated with *R3c* and *P4bm*. As well as increasing the rhombohedral distortion, the mechanical impact is also expected promote the *P4bm*-to-*P4mm* phase transition which may explain the complex microstructure observed in these ceramics. Electrical poling does not appear to dramatically alter the domain structure of these ceramics.

No domain pattern could be clearly seen in the smaller micro-grain BNBT-6 ceramics using back-scattered SEM (Fig.5.31). Either a fine striped structure occurs in these ceramics and because of the low resolution of the SEM detector at high magnification it remains hidden or the grains are dominated by PNRs.

As the grain size is reduced the dielectric permittivity decreases (Fig.5.38). Either fewer domain walls occur in the smaller grains or their movement is restricted. Electrical poling becomes difficult as the grain size is decreased. The increased density of grain

boundaries is expected to restrict the movement of the domain walls. A higher electric field E_c is therefore required to switch the polarisation in theses smaller grains (Fig.5.52). Opposition to domain switching from back fields exerted by the grain boundaries is also observed in the dielectric and piezoelectric response. The high density of grain boundaries in the smaller grain size ceramics hinders domain alignment limiting the decrease in dielectric permittivity (Fig.5.38) induced by electrical poling as well as the electromechanical d_{33}value (Fig.5.56).

The mechanical stress induced by crushing has a similar effect as a weak poling field on the crystal structure of BNBT-6, however it is unable to significantly reduce the multi-domain structure in ceramics with nanometre grain size.

Evidence of a room temperature mixed phase that includes a polar nanodomain structure is provided by the P-I-E loops measured for the 3.5 µm and 6 µm grain size BNBT-6 ceramics as shown in Fig.5.53. As the field strength is increased, a larger number of domains align with the applied field. This generally occurs in FEs by domain wall motion, by the growth of existing domains parallel to the applied field and by the nucleation and growth of new parallel domains. Nanodomains are known to act as nucleation sites for domain alignment. The reduction in current of the domain switching peak at high electric fields indicates that the density of available nucleation sites has decreased. The *P4bm* PNRs are thought to act as nucleation sites in BNBT-6 which undergone an irreversible electric-field induced *P4bm*-to-*R3c* structural transition. The reduction in conductivity at high electric fields further supports this observation.

5.3.2 Elevated Temperatures ≤ T_d

Rietveld refinement of the high temperature XRD data collected from the large micro-grain size ceramics shows the *R3c*/*P4bm* structure to transforms to a *Pm*$\bar{3}$*m*/*P4bm* mixed phase at 100 ˚C (Fig.5.24). Any long-range FE order induced by the mechanical impact it expected to disappear above this temperature. This is consistent with the feature T_s observed in the temperature dependent dielectric response for the unpoled ceramics (Fig.5.41). The frequency distribution also increases at this temperature.

Normal FE behaviour is observed in the P-E and I-E loops of all of the BNBT-6 ceramics at 75 ˚C, except for the ceramics with grain size ≤200 nm which do not show any distinct current peaks associated with domain switching (Fig.5.51). Ferroelectricity

is still expected to occur within these nanograin ceramics. Typical of many FEs, the coercive field E_c decreases with increasing temperature as polarisation reversal becomes easier at these elevated temperatures (Fig.5.52). At 125 ˚C, however, four current peaks $\pm E_F$ and $\pm E_B$ appear in the I-E loops of the 950 nm, 3.5 µm and 6 µm ceramics. In an applied field of 20 kV/cm, all four peaks can be clearly defined (Fig.5.54). As the applied field is increased, $\pm E_F$ broadens to such an extent that it can no longer be described as a single peak. The current of $\pm E_B$ also increases disproportionally relative to $\pm E_F$ with increasing field strength. These peaks are thought to be related to the increasing stability of the weakly polar *P4bm* phase with increasing temperature. The *P4bm* phase is expected to reversibly transform to *P4mm* then to *R3c* symmetries with increasing field strength. At low applied fields, the pre-existing *R3c* phase is expected to align with the applied field generating the peak at $\pm E_F$; the *P4bm* PNRs will also contribute to this peak by forming a long range order. As the field is increased, a range of phase transitions from *P4bm*-to-*P4mm*-to-*R3c* are thought to occur, broadening the peak at $\pm E_F$. The back-switching peak at $\pm E_B$ is very sharp as all of the pre-existing *P4bm* PNRs reform at this field strength. As the temperature is increased to 150 ˚C, $\pm E_B$ appear during electric field unloading for all three ceramics.

At 150 ˚C, the crystal structure of the BNBT-6 ceramics no longer appears as a mixed phase, instead the best fit was provided by the single $Pm\bar{3}m$ symmetry. A mixed phase is still expected to occur in BNBT-6 at this temperature, the short coherence length of the *R3c* and *P4bm* PNRs are not detected by XRD and instead appear cubic. The relaxor behaviour associated with these PNRs may account for the significant frequency dispersion in the dielectric response at temperatures above T_d. In a typical relaxor, the PNRs grow with decreasing temperature. A dynamic slowing of their fluctuations occurs below T_m and the system enters an isotropic relaxor state where the polar domains are randomly oriented. The detection of the tetragonal phase below T_d may result from a dipolar glass state[12] where the *P4bm* nanodomains form a short range order on cooling.

A long-range FE order is less likely to be retained at these elevated temperatures when the grain size is reduced. During heating the d_{33} of the small grain ceramics begins to decrease at lower temperatures than the larger micro-grain size ceramic (Fig.5.56). Back fields exerted by the high density of grain boundaries in the smaller grain size ceramics aid the switch back of the domains after poling reducing the d_{33}.

The influence of a DC bias-field on the depolarisation temperature of the BNBT-6 ceramics is not the same as in a classical relaxor. For example, in PMN the depoling temperature of the polar state induced by either poling the ceramic at room temperature T_d or during cooling T_{do} is independent of the initial poling field strength. When a weak bias field is applied during heating T_{db}, the polar state is retained at higher temperatures such that $T_{db}>T_d= T_{do.}$ For the largest micro-grain size BNBT-6 ceramics, the polar state induced by poling at room temperature in a 60 kV/cm electric field is more stable than that created by cooling the material in a weak bias-field of 5 kV/cm (ZFH af FC) (Fig.5.45). In this case, the polar order is clearly dependent on the strength of the poling field. Poling while cooling appears to induce the same state as mechanical stress caused by crushing. A bias field of 3 kV/cm applied during heating (FH af ZFC), does not appear to be strong enough to induce a polar order different to the annealed state. The depoling temperature however is raised when the bias field strength applied during heating is increased to 5 kV/cm. The depoling temperature approaches that of the fully poled state when the 5 kV/cm field is applied at temperatures below -180 ˚C. Unlike PMN, the depoling temperatures follow the trend $T_d> T_{db}>T_{do}$ for BNBT-6. In PMN, the induced phase transition is directly related to the dynamics of the micropolar regions, which form a long-range FE order on poling. Although BNBT-6 exhibits relaxor type behaviour, different phase transitions are expected to occur depending on the applied field strength. While high field poling transforms the *P4bm* PNRs to a *R3c* long-range FE order, the weak fields are thought to promote the *P4bm*-to-*P4mm* phase transition resulting in a mixed *P4bm*/*P4mm*/*R3c* polar state. The *P4mm* phase is expected to be less stable than the *R3c* polar order, reducing the depoling temperature of the system. Cooling in a bias-field re-introduces the polar order to the system which is normally lost after annealing. A similar explanation can be applied to the 950nm ceramics, however in this case the bias-field is not strong enough to induce the polar state during cooling.

5.3.4 High Temperatures ≥ T_d

The $Pm\bar{3}m$ symmetry refined for this system at 150 ˚C continues to fit the XRD data for all of the BNBT-6 ceramics up to 700 ˚C. According to TEM studies reported in the literature, BNBT-6 is not expected to enter a purely cubic phase until ~500 ˚C[171]. A subtle change in cubic unit cell volume is observed at this temperature for the larger grain size ceramics (Fig.5.23). The short coherence length of the *P4bm* PNRs is

believed to be responsible for the cubic structure refined for this system at lower temperatures. Further support for the *P4bm* structure is provided by the P-I-E loop data collected from the ceramics at 175 ˚C which show typical relaxor type behaviour (Fig.5.51). Small current bumps were also observed in the I-E loop of the 200 nm grain size ceramic at this temperature. The PNRs are expected to align with the applied field however they may not undergo an electric-field induced phase transition at this temperature as no features associated with $\pm E_F$ and $\pm E_B$ could be defined. Increased conductivity in the 950 nm ceramic distorts the hysteresis loops at this high temperature.

The frequency dispersion observed in the dielectric response of the BNBT-6 ceramics above T_d remains until T_m where it almost vanishes with increasing temperature (Fig.5.40). Poling is thought to influence the size of the *P4bm* nanodomains as the frequency distribution above T_m is further reduced in this state (Fig.5.42). Oxygen vacancies remaining in the smaller grain ceramics from SPS processing distort this trend, particularly for the low frequency data which do not converge at T_m but continue to increase with increasing temperature. The position of T_m only shows a slight shift towards higher temperature with decreasing grain size. The increased width of the peak may distort this result. The position of T_m is thought to be independent of grain size, particularly the range investigated in this study. The PNRs forming the domain structure of the MPB composition may be too small for their dynamics to be significantly affected by grain size. The increased stress exerted at the grain boundaries of the smaller grains, however is thought to hinder the domain wall motion suppressing the permittivity value at T_m.

5.3.4 Cooling

The influence of electrical and mechanical stresses on the structural transitions can be clearly seen when comparing the heating and cooling runs of the XRD results (Fig.5.24). A $Pm\bar{3}m$/*P4bm* structure was refined for the micro-grained ceramics at room temperature on cooling. Below T_{RE}/T_m, the frequency distribution in the dielectric permittivity decreases smoothly with decreasing temperature. The absence of T_s from the cooling run of all of the ceramics further supports this structure (Fig.5.41). A $Pm\bar{3}m$/*P4bm* structure is expected to occur for all of the ceramics at room temperature after annealing.

The depoling temperature measured during cooling T_{db} shifts towards room temperature when a bias field is applied to the annealed large micro-grain ceramics during cooling (Fig.5.45 and 5.47). This feature, not observed in BNT, becomes more distinct when the field is increased from 3 kV/cm to 5 kV/cm. The bias-field is unable to stabilise the long-range FE order until lower temperatures due to the thermal fluctuations of the nanodomains.

5.4 Summary

The effect of grain size on the structure and FE properties of ceramic BNBT-6 within the grain size range 100nm to 6μm was investigated. High density ceramics were successfully prepared from nanometre and micrometre grain size powders using SPS and conventional sintering techniques.

Room temperature crystal structure analysis reveal a pseudo-cubic distortion of *R3c* and *P4bm* symmetries in ceramic BNBT-6 which transform to a $Pm\bar{3}m$/*P4bm* mixed phase with decreasing grain size. While the $Pm\bar{3}m$(*R3c*)/*P4bm* structure provided the best fit, the XRD data is not wholly satisfied by this refinement. Mechanical impact has a similar effect as a weak poling field on the structure of the MPB composition and may account for the uncertainty surrounding the unpoled structure. Domain structures consistent with *R3c* and *P4mm* symmetries were observed in the micrograin ceramics. As the grain size is reduced the dielectric permittivity decreases. Either fewer domain walls occur in the smaller grains or their movement is restricted. Electrical poling in strong electric fields promotes the *R3c* symmetry in the micrograin ceramic while the increased density of grain boundaries in the smaller grain ceramics opposes domain reversal limiting the decrease in dielectric permittivity induced by poling. The field-strength dependence of T_d is consistent with the field-induced phase separation reported in the literature. Further evidence of a field induced *P4bm*-to-*P4mm*-to-*R3c* multiphase transition is provided by P-I-E loop tests.

The position of the high temperature permittivity peak T_m is independent of grain size, particularly the range investigated in this study. The PNRs forming the domain structure of the MPB composition are thought to be too small for their dynamics to be significantly affected by grain size. The increased stress exerted at the grain boundaries

of the smaller grains, however is believed to hinder the domain wall motion suppressing the permittivity value at T_m. This result is consistent with the grain size effect observed in other MPB compositions, including $Na_{0.5}K_{0.5}NbO_3$.

Grain size, in particular grain boundary density, clearly influences the FE properties of BNBT-6, retarding domain wall motion and long-range FE order thereby dramatically reducing the property enhancement associated with an MPB. However, it remains unclear what effect grain size has on the position of the MPB when considering structure. The structure remains cubiclike as the grain size is reduced, but rather than transforming to an irreversible long-range *R3c* FE order in high applied fields the smaller grain size ceramics are thought to remain cubiclike. The MPB structure reported in the literature for BNBT-7 is a cubiclike/tetragonal *P4mm* mixed phase in the equilibrium (or annealed) state. A characteristic of this MPB structure is that it maintains the cubiclike character after high field electrical poling. This structure also occurs in BNBT-6 after poling in a weak applied field, before fully transforming to the *R3c* structure in high fields. Back field exerted by the high density of grain boundaries are expected to suppress the poling effect of a high electric field in the small grain ceramics only allowing them to adopt the MPB structure. In this case, a reduction in grain size is similar to shifting the MPB to lower $BaTiO_3$ concentrations.

Chapter 6 Conclusions and Future Work

6.1 Powder Preparation and Ceramic Processing

To maintain the stoichiometry of the $Bi_{0.5}Na_{0.5}TiO_3$ (BNT) and $94\%Bi_{0.5}Na_{0.5}TiO_3$-$6\%BaTiO_3$ (BNBT-6) powders after solid state reaction only Na_2CO_3 that had been dried for 24 h at 200 ˚C and weighted while hot was used as a raw material. This precaution avoided oxygen vacancies being introduced into the system by the hydrophilic Na_2CO_3 powder. Different calcination conditions were required to prepare single phase powders of each composition. Powder mixtures of BNT were calcinated at 800 ˚C for 4h, whereas BNT and $BaTiO_3$ were found to form separately before combining to form BNBT-6, so to reduce the risk of non-stoichiometry from the loss of bismuth a two-step calcination method was applied. In this case, the BNBT-6 powder mixture was held at 800 ˚C for 4 h before increasing the temperature to 1000 ˚C for a further 4 h before cooling.

Following calcination, the powders were ball-milled to break down any agglomerates formed during calcination and to reduce the overall grain size of the powders. A typical milling period of 4 h at 350 rpm was used for BNT. Further optimisation of this powder processing step was required for BNBT-6. In this instance, a longer period of 8 h was necessary to homogenise the powder. To exclude the effect of ZrO_2 contamination from the grain size analysis, only nanograin powder prepared by sol-gel synthesis was used for ceramic processing, rather than powder prepared by high-speed ball-milling.

Conventional pressureless sintering was used to prepare large micrometer grain ceramics while spark plasma sintering (SPS) was used to process ceramics with grain sizes below 1 μm. The high pressures applied during SPS enabled low temperature sintering which limited grain growth allowing the nano- and micro-structure of the powders to be retained. Grain growth by SPS is limited as melting and a loss vacuum were observed during sintering at high temperature (> 1000 ˚C) for both materials. Evidence consistent with A-site vacancies, introduced into the composition following the volatilisation of the Bi and Na ions, were observed in the electrical properties of these ceramics.

The annealing treatment in air used to remove oxygen vacancies created in the reducing environment during SPS is dependent on the sintering temperature. To limit further grain growth, each ceramic was annealed 100 ˚C below the sintering temperature for 24h. Evidence of oxygen vacancies however were still observed in the electrical properties of the SPS ceramics, particular the ceramics sintered at high temperature. The annealing process is clearly restricted by the condition used to preserve the grain size. When there is no restriction on grain size, annealing is typically carried out 100-200 ˚C above the sintering temperature for a much shorter time (~ 1h). To reduce this effect an annealing temperature closer to the sintering temperature was used for the larger grain ceramics. Annealing time was also found to be important when annealing at low temperatures.

6.2 Grain Size Effect in $Bi_{0.5}Na_{0.5}TiO_3$

X-ray diffraction (XRD) structural analysis reveal the average room temperature structure of the crushed BNT ceramic to transform from rhombohedral *R3c* to monoclinic *Cc* with decreasing grain size. Nanotwins (NTs) which form the monoclinic defect structure have been imaged in the micro-grain size ceramics by transmission electron microscopy (TEM). A cross-hatched domain pattern, imaged by back-scattered scanning electron microscopy (SEM), occurs in grains with a *Cc* crystal structure. The high domain wall density associated with this structure results in an increase in dielectric permittivity with decreasing grain size. This cross-hatched pattern was found to transform on electrical poling to a striped domain structure. Electrical poling is expected to reduce the number of domain walls and therefore NTs by increasing the size of the domains aligned with the applied field transforming the crystal structure to rhombohedral. This observation is consistent with the dielectric permittivity measured for the micro-grain size ceramics which decreases after poling. As the grain size is decreased electrical poling becomes difficult as the increased density of grain boundaries restricts the movement of the domain walls increasing the electric field E_c required for polarisation reversal. The change in dielectric permittivity induced by poling also decreased in the smaller grain size ceramics. Back-field exerted by the grain boundaries aid the switch back of the domains when the field is removed. Fewer grains are able to expel the defect structure and so retain the *Cc* symmetry. This is supported by XRD, which shows the crystal structure of the 150 nm grain size ceramic to remain monoclinic after poling. The depolarisation temperature T_d could not be identified from

the dielectric loss of the poled ceramics with grain size ≤ 500 nm. No evidence of domain reversal was observed in the current-electric field (I-E) loops of the nano-grain ceramics, however a small d_{33} was measured for these ceramics. The defect structure responsible for the *Cc* symmetry is no longer expected to form within these grains due to the loss of domain walls. Instead a single grain-single domain type structure is thought to occur. Alternatively, the C_c defect structure may still occur and instead the reduction in dielectric permittivity results from a dilution effect caused by the high density of grain boundaries. Electrical poling preserves the long-range FE order associated with the defect-free structure in the large micro-grain ceramics, shifting the depoling temperature T_d to higher temperatures. The domain wall density increases at T_d reforming the monoclinic defect structure. Above this temperature, the dielectric permittivity increases with increasing grain size due to the high density of domain walls now present in the larger grains.

Evidence of a structural transition to the *P4bm* phase was found in the XRD patterns collected from the largest micro-grain size ceramic. A sharp increase in permittivity at T_{RE} is observed for the micro-grain ceramics with average grain size ≥ 1.5 μm in both the unpoled and poled states. Larger *P4bm* domains are thought to percolate the grains at this temperature causing the frequency dispersion to vanish between T_{RE} and T_m. Poling is thought to influence the size of the *P4bm* nanodomains, which remain detectable up to 550 ˚C. Whereas in the unpoled state, the *P4bm* phase transforms to the cubic $Pm\bar{3}m$ structure at 350 ˚C. The frequency distribution in the dielectric permittivity at temperatures above T_m is also greatly reduced after room temperature poling. The absence of the *P4bm* symmetry in smaller grain ceramics is thought to result from the short coherence length of the in-phase tilts which remain hidden to XRD. Instead a *Cc*-to- $Pm\bar{3}m$ structural transition is detected in these ceramics below T_m.

As the average grain size of the BNT ceramic is reduced the peak in the permittivity T_m broadens and shifts to higher temperatures. Although no static structural transition takes place at T_m, a gradual change in structure is expected to occur as the *P4bm* phase increases at the expense of the *R3c*/*Cc* structure. The phase below T_m may be more stress accommodating than the phase above T_m. The increased stress exerted at the grain boundaries of the smaller grains hinders the domain wall motion suppressing the permittivity value at temperatures above T_d.

6.3 Grain Size Effect in MPB composition 94%$Bi_{0.5}Na_{0.5}TiO_3$ -6%$BaTiO_3$

A pseudo cubic distortion was refined for the room temperature structure of the crushed BNBT-6 ceramics which transforms from a mixed phase of *R3c*/*P4bm* to *Pm*$\bar{3}$*m*/*P4bm* with decreasing grain size. Mechanical stress induced in the system by crushing has a similar effect on the crystal structure of BNBT-6 as electrical poling. Rietveld refinement of the XRD data collected from the poled 6μm ceramics shows the structure to fit well with the *R3c* symmetry. Electrical poling becomes difficult as the grain size is decreased. The increased density of grain boundaries is expected to restrict the movement of the domain walls. A higher electric field E_c is therefore required to switch the polarisation in theses smaller grains. Opposition to domain switching from back fields exerted by the grain boundaries is also observed in the dielectric and piezoelectric response. The high density of grain boundaries in the smaller grain size ceramics hinders domain alignment limiting the decrease in dielectric permittivity induced by electrical poling as well as the electromechanical d_{33}value.

Back-scattered SEM images reveal a complex lamellar domain structure in the large micro-grain ceramics. A herringbone domain structure consistent with a *P4mm* structure was imaged in a small number of the BNBT-6 grains. As well as increasing the rhombohedral distortion, mechanical impact is also expected promote the *P4bm*-to-*P4mm* phase transition which may explain the complex microstructure observed in these ceramics. No discernible change in domain morphology was observed in the BNBT-6 ceramics after poling. The grains in the ceramics with average grain size ≤ 350 nm are thought to be dominated by a nanodomain structure.

As the temperature is increased, XRD shows the *R3c*/*P4bm* structure refined for the large micro-grain ceramics transforms to a *Pm*$\bar{3}$*m*/*P4bm* mixed phase at 100 ˚C. Any long-range FE order induced by the mechanical impact it expected to disappear above this temperature. Dielectric measurements recorded in a weak DC bias-field demonstrate the field strength dependence of the polar order and depoling temperature. Poling while cooling appears to induce the same state as mechanical stress caused by crushing. Although BNBT-6 exhibits relaxor type behaviour, different phase transitions are expected to occur depending on the applied field strength. While high field poling transforms the *P4bm* polar nanoregions (PNRs) to a *R3c* long-range FE order, the weak fields are thought to promote the *P4bm*-to-*P4mm* phase transition resulting in a mixed

P4bm/*P4mm* /*R3c* polar state. The *P4mm* phase is expected to be less stable than the *R3c* polar order, reducing the depoling temperature of the system.

A long-range FE order is less likely to be retained at these elevated temperatures when the grain size is reduced. Back fields exerted by the high density of grain boundaries in the smaller grain size ceramics aid the switch back of the domains after poling reducing the d_{33} at lower temperatures.

Multiple current peaks appear in the I-E loops of the large micro-grain ceramics at 125 ˚C. These peaks are thought to be related to the increasing stability of the weakly polar *P4bm* phase with increasing temperature. As the field is increased, a range of reversible phase transitions from *P4bm*-to-*P4mm*-to-*R3c* are thought to occur. The crystal structure of the BNBT-6 ceramics no longer appears as a mixed phase at temperatures above T_d, instead the best fit was provided by the single $Pm\bar{3}m$ symmetry for all ceramics. A mixed phase is still expected to occur in BNBT-6 at this temperature, the structure only appears cubic due to the short coherence length of the *R3c* and *P4bm* nanodomains. The relaxor behaviour associated with these PNRs account for the significant frequency dispersion in the dielectric response at temperatures above T_d.

The frequency dispersion observed in the dielectric response of the BNBT-6 ceramics above T_d remains until T_m where it almost vanishes with increasing temperature. No significant change in temperature of T_m is observed between the different grain size ceramics. At high temperature, the PNRs forming the domain structure of the MPB composition are thought to be too small for their dynamics to be significantly affected by grain size.

6.4 Comparing the Grain Size Models

Ceramic grain size clearly influences the ferroelectric (FE) properties of both BNT and BNBT-6. As is also the case for other lead-free FEs, a high density of grain boundaries restricts domain wall motion and long-range FE order.

The grain size effect in BNT at temperature below T_d however is different from the MPB composition because of the C_c defect structure and the effect of the NTs on the FE domain structure and associated properties. At high temperatures, the permittivity peak

T_m is independent of grain size for BNBT-6 but shifts to higher temperatures as the grain size is reduced in BNT. A larger number of domain states are thought to be offered by the phase below T_m in BNT making it more stress accommodating whereas, the PNRs forming the domain structure in BNBT-6 are thought to be too small for their dynamics to be significantly affected by grain size. A critical grain size for the formation of a single grain-single domain structure is only expected to occur in BNBT-6 when the grain size approaches that of the nanodomains. This is consistent with the grain size effect observed in the MPB compositions $Na_{0.5}K_{0.5}NbO_3$.

Although a reduction in ceramic grain size dramatically reduces the property enhancement associated with an MPB, it remains unclear what effect grain size has on the position of the MPB when considering structure. Back field exerted by the high density of grain boundaries in BNBT-6 are thought to suppress the poling effect of a high electric field in the small grain ceramics only allowing them to adopt an MPB structure of cubiclike and tetragonal *P4mm* symmetries. If this is true, a reduction in grain size is similar to shifting the MPB to lower $BaTiO_3$ concentrations. A different model may well apply to other BNBT MPB compositions closer to the $BaTiO_3$ rich side of the boundary.

6.5 Future Work

6.5.1 Optimising the Processing Conditions

X-ray photoelectron spectroscopy should be used to check the stoichiometry of the different ceramics, chiefly the Bi:Na ratio. The grain size of the ceramic was altered by changing the sintering temperature. This is likely to have some influence on the final composition due to relatively low volatilisation temperature of the Bi and Na ions compared to the high sintering temperatures require for large grain growth. In addition to grain size, non-stoichiometry is expected to have some influence on the structure and properties of the system.

For a more comprehensive grain size study, a wider range and larger number of ceramic grain sizes should be investigated. For example, ceramics with average grain size ranging from 53 μm[84] down to 5 nm[226] have been investigated for $BaTiO_3$. Investigation into the grain size effect in $BaTiO_3$ started in 1976[84] and is still ongoing,

it is therefore reasonable to expect interesting features to have been missed in this research due to the small sample size tested.

Further optimisation of the annealing conditions would help to remove the oxygen vacancies in the low temperature SPS ceramics which distort the dielectric loss data. These multiple loss peaks may hide a weak T_d peak induced by poling in small grain size ceramics.

6.5.2 Improving the Quality of Crystal Structure Analysis

Distortion from the basic perovskite structure is very small in BNT and BNBT-6. Structural refinement of these materials is therefore difficult as the lattice parameters are numerically very close to cubic. The XRD analysis technique used in this research can only give limited detail on the structure of these materials. This is most noticeable at temperatures where the *P4bm* nanodomains form a significant fraction of the structure, because of their short coherence length the structure appears cubic at temperature far below the $Pm\bar{3}m$ structural transition. The structure of the small crystallites in the nanograin ceramics is also thought to be distorted in this way. Greater detail of the grain size effect on the structure of these materials could be gained from neutron diffraction and high resolution synchrotron XRD techniques.

6.5.3 Greater Correlation between Crystal and Domain Structures

The techniques used to visualise the FE domain structure revealed clear differences between BNT and BNBT-6 and between ceramics of different grain size. However, it was not possible to quantitatively distinguish between the *R3c*, C_c, *P4bm*, *P4mm* structures using these techniques. Electron backscatter diffraction (EBSD) analysis was employed to help identify the structure and orientation of the domains imaged by back-scattered SEM, however the crystallographic mapping proved inconsistent (data not given). It may not be possible to distinguish between the BNT and BNBT-6 crystal structures using this modelling technique. A defect structure was imaged in ceramic BNT using TEM, however, no domain pattern was observed in this sample. This may be related to the sample thickness as domain walls are noted by Thomas et al.[157] to be expelled from very thin samples. Following optimisation of lamella thickness, electron diffraction could be performed *in situ* with bright-field TEM to determine the domain structure, as demonstrated in [162]. Ideally, this technique should be performed on both BNT and BNBT-6 ceramics for a range of grain sizes. Hot-stage TEM would also be

useful to map the change in domain structure near T_d. While T_d is associated with a *R3c*-to-C_c transition in BNT, no monoclinic phase is detected in BNBT-6, instead a *R3c*-to-*P4bm* transition is thought to occur at this temperature. To explore this difference particular attention should be paid to the temperature evolution of the defect structure in BNT to see how the domain structure differs from BNBT-6 above room temperature.

6.5.4 Maintaining Continuity between Structure and Property Analysis

To ensure greater distinction between unstressed (mechanically and electrically) and electrical poled states, the crushed ceramics prepared for structural analysis should be fully annealed after crushing (excluding poled samples). Instead the structural data collected for this research is of a mechanical stressed 'semi-poled' state, whereas, electrical property measurements are of either annealed or poled states. Ideally, structural analysis should be carried out on bulk samples rather than powder as this is more representative of the ceramic, however effects from preferred orientation make refinement of this tricky system even more difficult.

For greater comparison with the electrical property results, a shorter temperature interval should be used to collect the structural data, with more focused data collection near temperatures T_d, T_{RE} and T_m. The 50 ˚C temperature interval used in this study missed narrow (< 25 ˚C) shifts in the temperature of these features with changing grain size.

A critical grain size for ferroelectricity was not detected for either BNT or BNBT-6 since a room temperature d_{33} was measured for both ceramics down to 80 nm and 100nm, respectively. To investigate the stability of the polar phase with increasing temperature, thermal depoling experiments should be performed on the nanograin BNT and BNBT-6 ceramics.

6.5.5 Separating Grain Size and Field-Strength Effects

To help separate the effect of grain size and relative field-strength on ceramic BNBT-6 the effect of electrical poling on the structure of ceramic BNBT-6 across the full grain size range (100 nm to 6 μm) and different poling field strengths should be investigated. To further test how grain size influences the position of the MPB other compositions with different concentration of $BaTiO_3$ ($0.05 \leq x \leq 0.10$) should be research, specifically BNBT-7 which has a MPB structure of cubiclike/tetragonal *P4mm* phases in the

equilibrium state and lies in close proximity with the boundary between cubiclike and MPB structures.

Chapter 7 Appendix

7.1 Grain Size Effect in $Bi_{0.5}Na_{0.5}TiO_3$: Crystal Structure

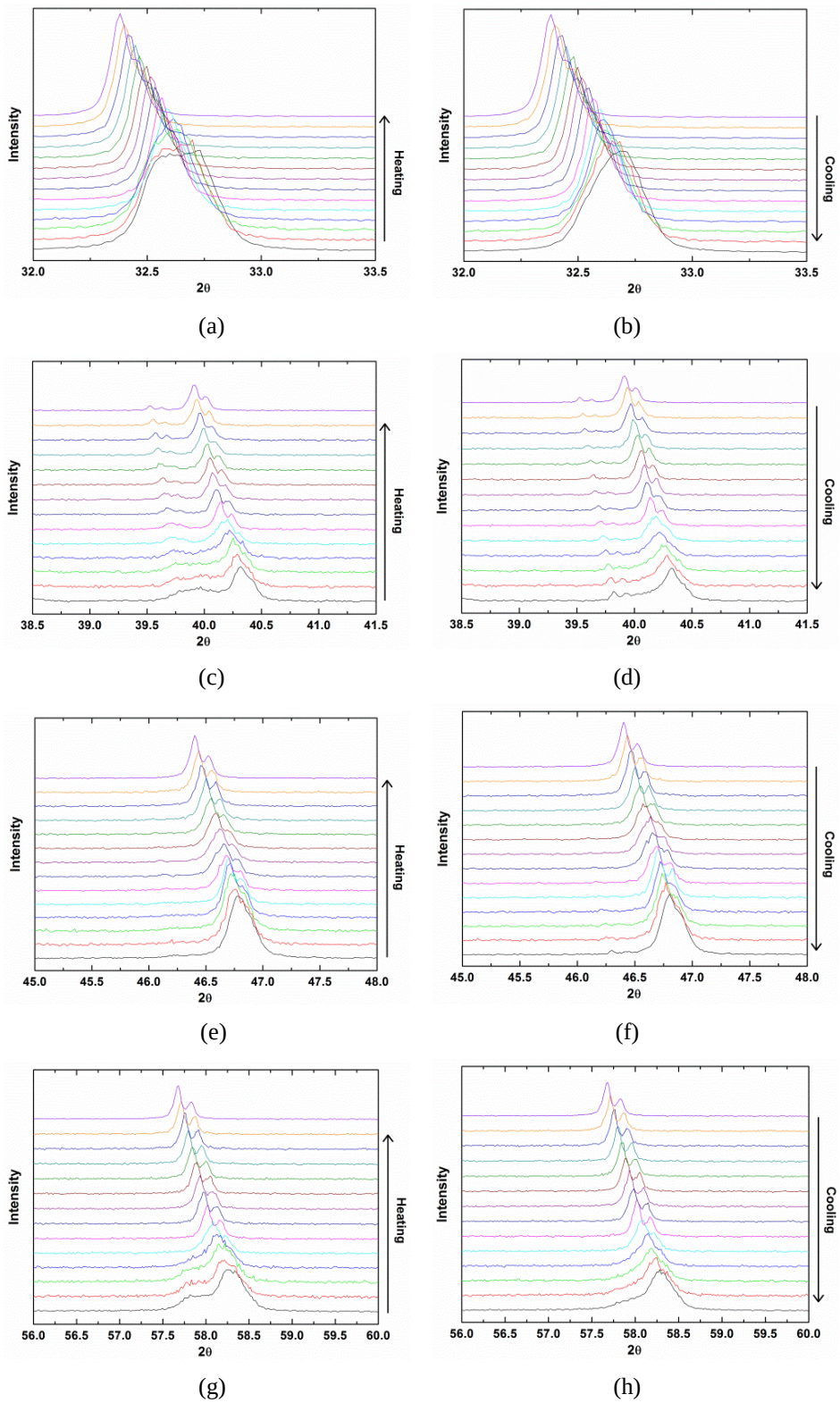

Fig.7.1.1: Powder XRD profiles of the crushed 1.5 µm grain size BNT ceramic showing the temperature evolution during heating and cooling of the Bragg reflections: (a)-(b) $(110)_{pc}$, (c)-(d) $(111)_{pc}$, (e)-(f) $(200)_{pc}$ and (g)-(h) $(211)_{pc}$.

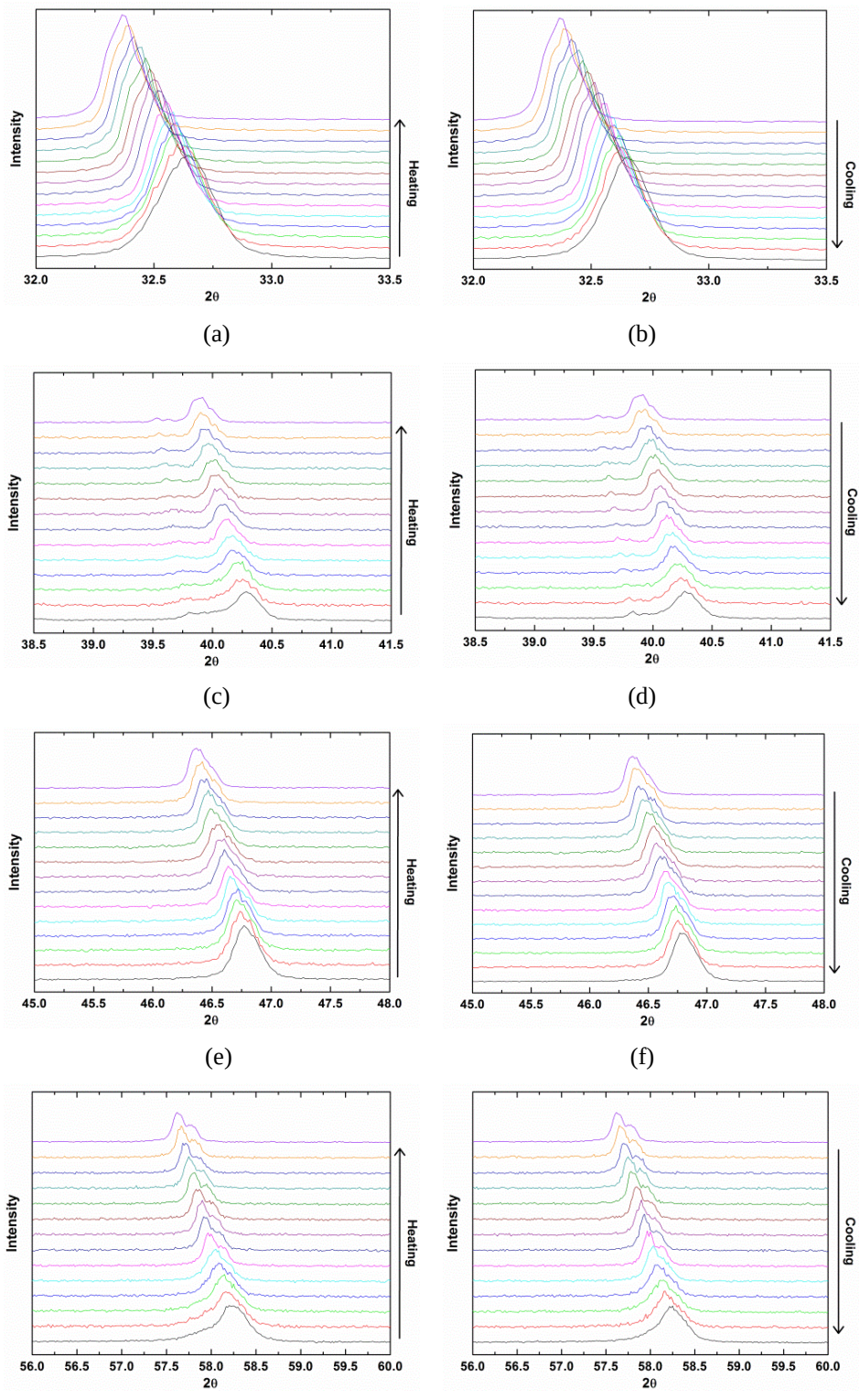

Fig.7.1.2: Powder XRD profiles of the crushed 500 nm grain size BNT ceramic showing the temperature evolution during heating and cooling of the Bragg reflections: (a)-(b) $(110)_{pc}$, (c)-(d) $(111)_{pc}$, (e)-(f) $(200)_{pc}$ and (g)-(h) $(211)_{pc}$.

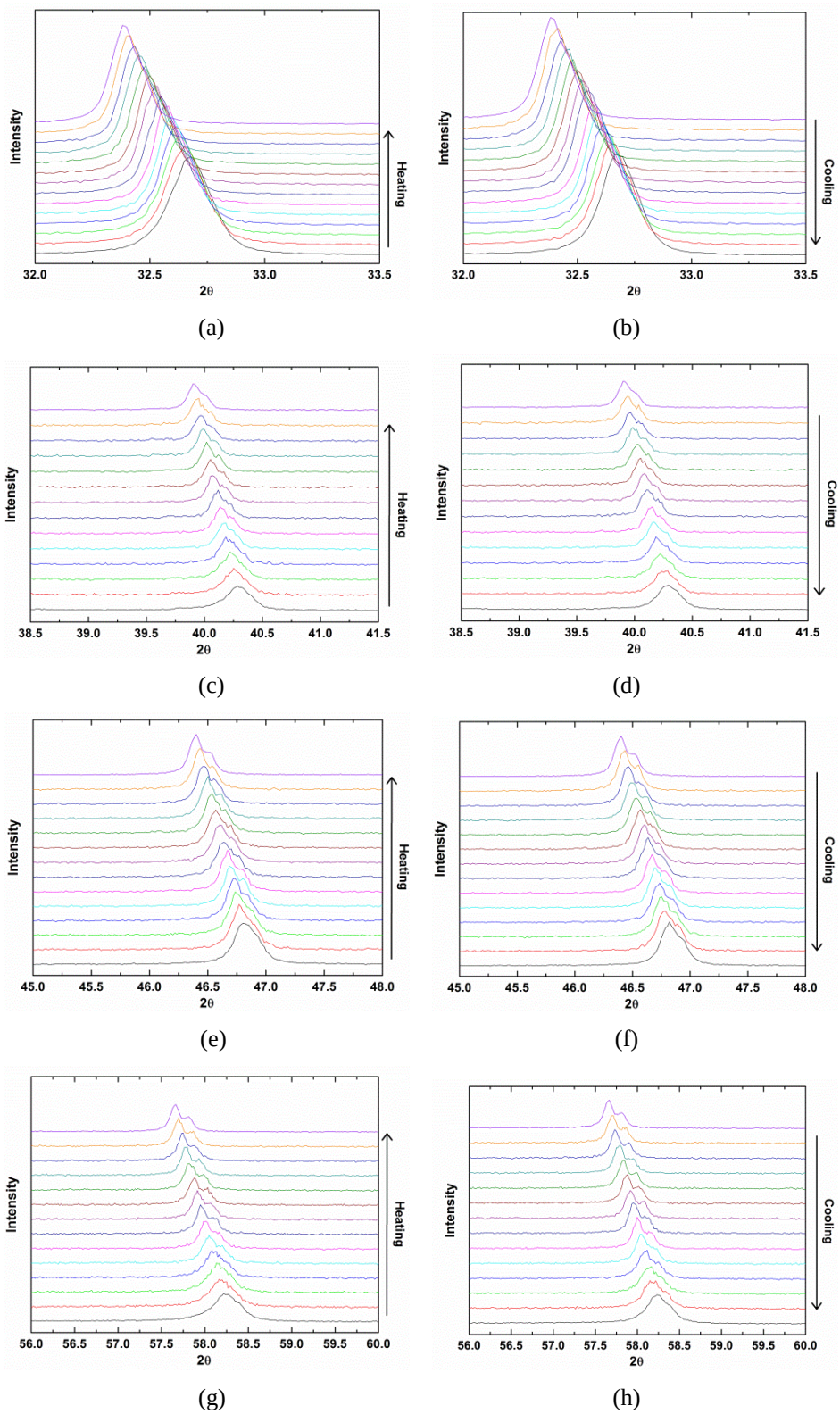

Fig.7.1.3: Powder XRD profiles of the crushed 150 nm grain size BNT ceramic showing the temperature evolution during heating and cooling of the Bragg reflections: (a)-(b) $(110)_{pc}$, (c)-(d) $(111)_{pc}$, (e)-(f) $(200)_{pc}$ and (g)-(h) $(211)_{pc}$.

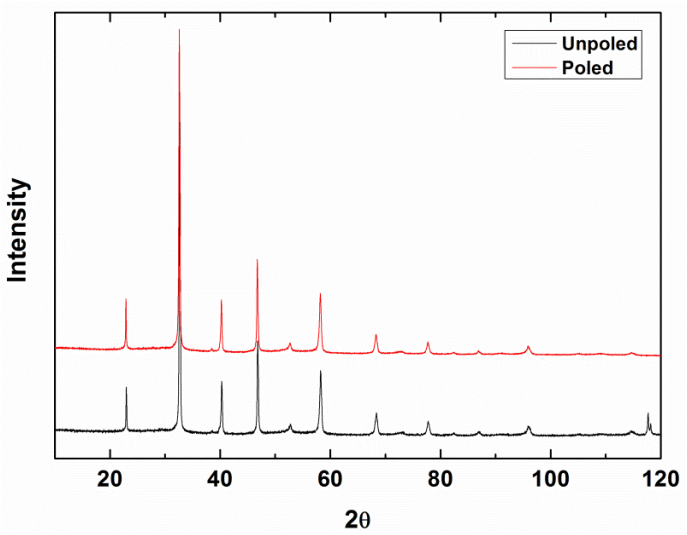

(a)

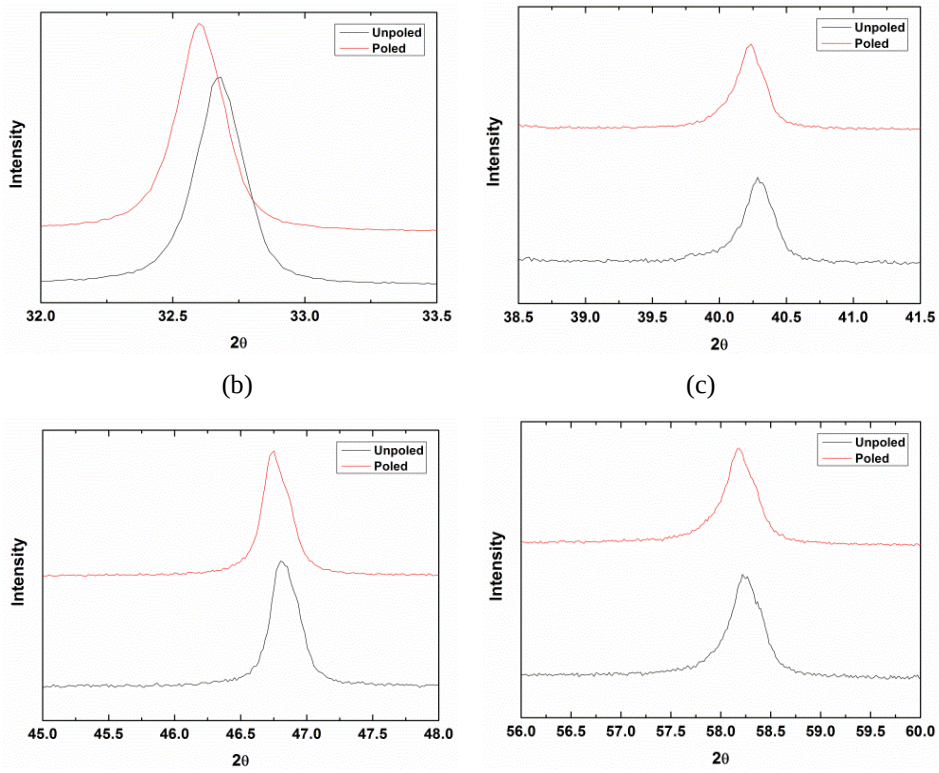

(b) (c)

(d) (e)

Fig.7.1.4: Room temperature powder XRD profiles of the crushed 150 nm grain size BNT ceramic in the unpoled and poled states, showing (a) the measured 2θ range (10-120 ˚) and the individual Bragg reflections: (b) $(110)_{pc}$, (c) $(111)_{pc}$, (d) $(200)_{pc}$ and (e) $(211)_{pc}$.

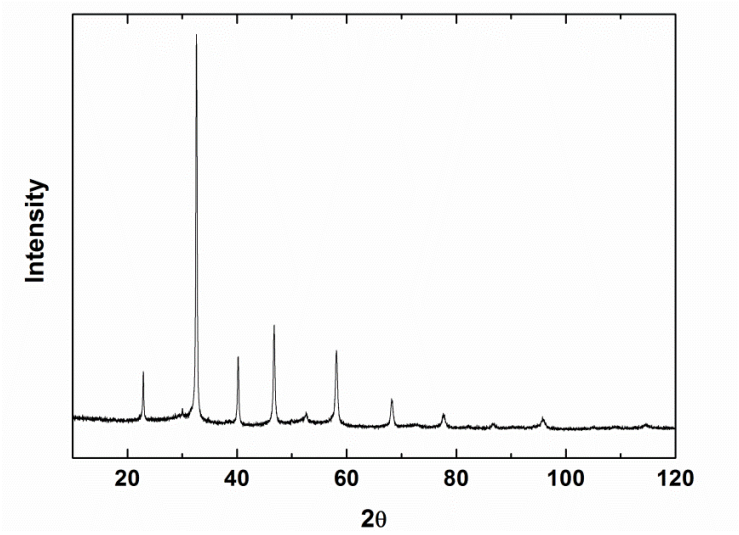

Fig.7.1.5: Powder XRD data collected from the crushed 80nm grain size BNT ceramic at room temperature.

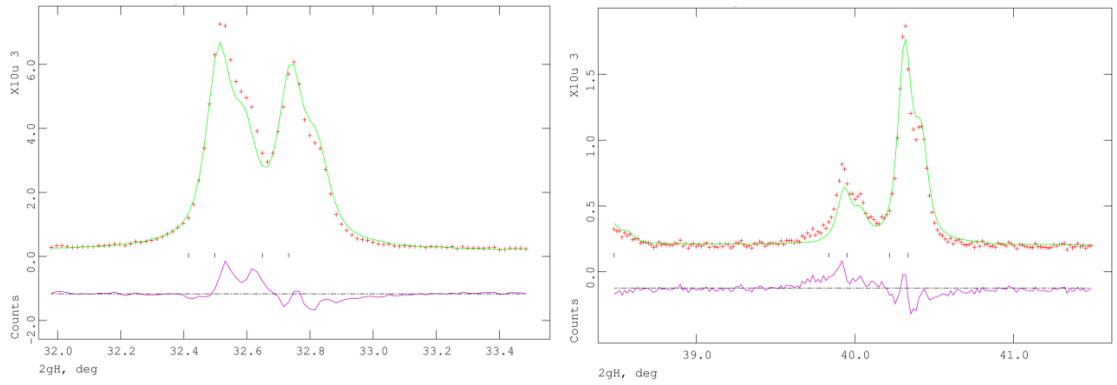

(a) (b)

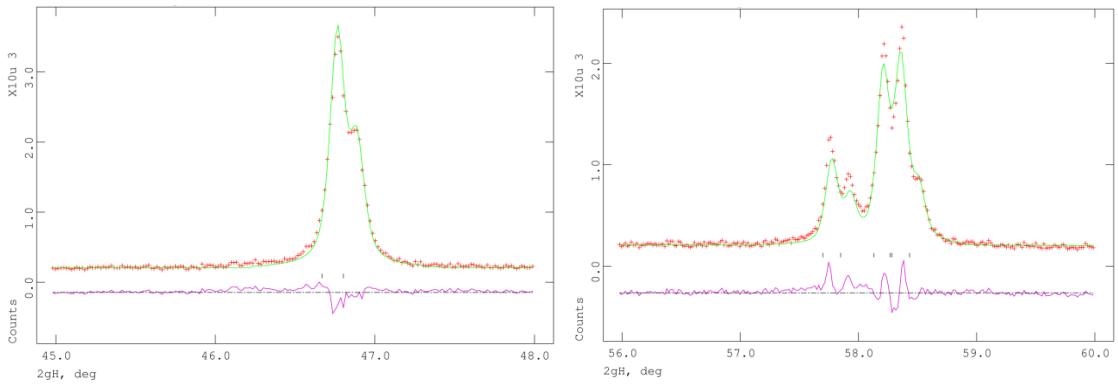

(c) (d)

Fig.7.1.6: Rietveld refinement of the room temperature XRD profile of the poled-crushed 10μm grain size BNT ceramic with a *R3c* structure model, showing the observed (red circles), calculated (continuous green line) and difference plot (continuous pink line at bottom) for (a) $(110)_{pc}$, (b) $(111)_{pc}$, (c) $(200)_{pc}$ and (d) $(211)_{pc}$. Fitting: wRp $_{R3c}$ = 9.69. (The quality of fit for tested *Cc* structural model, wRp_{Cc} = 10.41.)

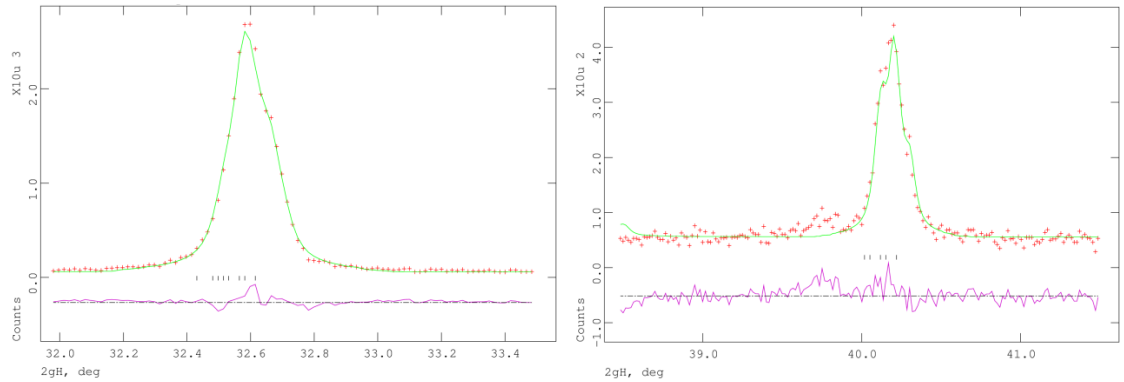

(a) (b)

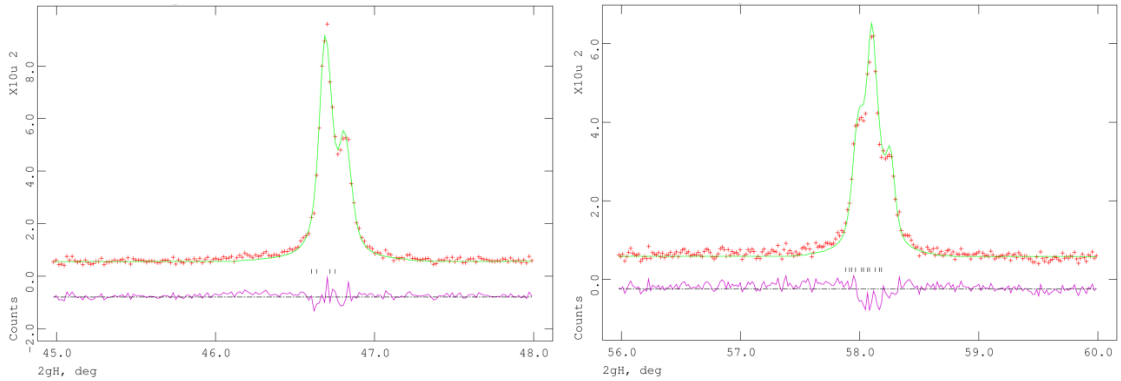

(c) (d)

Fig.7.1.7: Rietveld refinement of the XRD profile of the poled-crushed 10µm grain size BNT ceramic with a *Cc* structure model at 250˚C, showing the observed (red circles), calculated (continuous green line) and difference plot (continuous pink line at bottom) for (a) $(110)_{pc}$, (b) $(111)_{pc}$, (c) $(200)_{pc}$ and (d) $(211)_{pc}$. Fitting: wRp_{Cc} = 15.02. (The quality of fit for other tested structural models R3c: wRp_{R3c} = 15.22, *P4bm*: wRp_{P4bm} = 15.37 and $Pm\bar{3}m$: wRp_{Pm3m} = 15.10.)

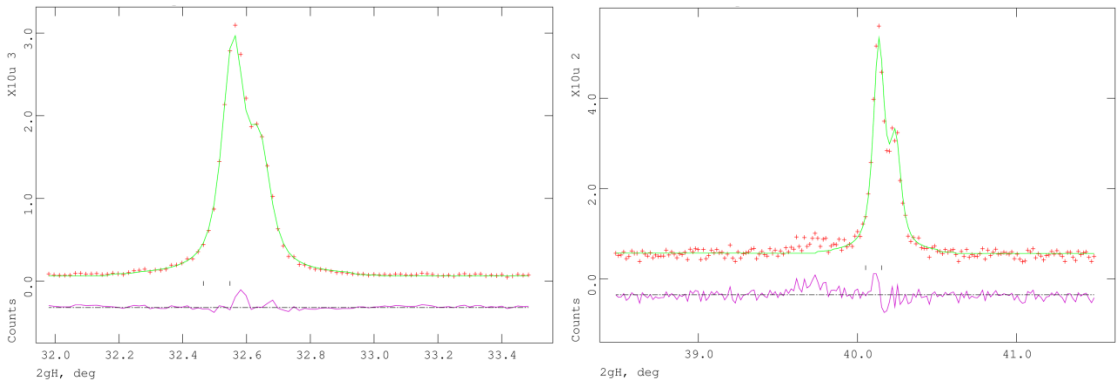

(a) (b)

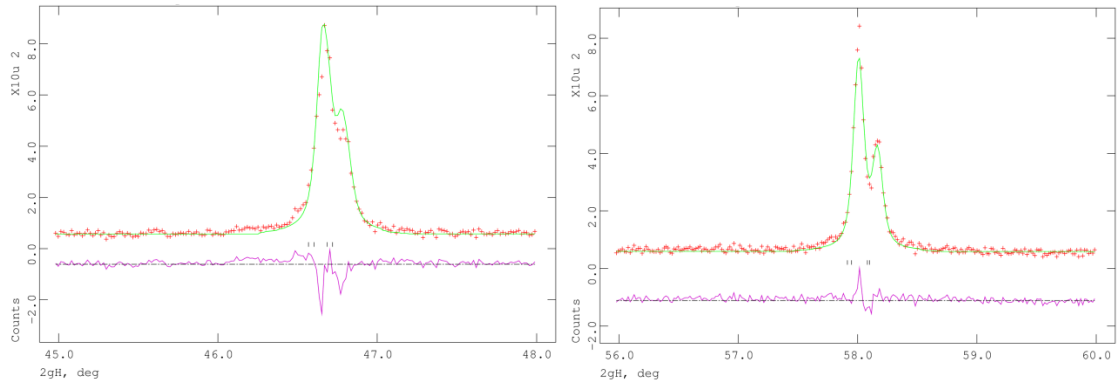

(c) (d)

Fig.7.1.8: Rietveld refinement of the XRD profile of the poled-crushed 10µm grain size BNT ceramic with a *P4bm* structure model, at 300˚C, showing the observed (red circles), calculated (continuous green line) and difference plot (continuous pink line at bottom) for (a) $(110)_{pc}$, (b) $(111)_{pc}$, (c) $(200)_{pc}$ and (d) $(211)_{pc}$.. Fitting: wRp_{P4bm} = 14.90. (The quality of fit for other tested structural models R3c: wRp_{R3c} = 15.75, *Cc*: wRp_{Cc} = 17.14 and $Pm\bar{3}m$: wRp_{Pm3m} = 14.83.)

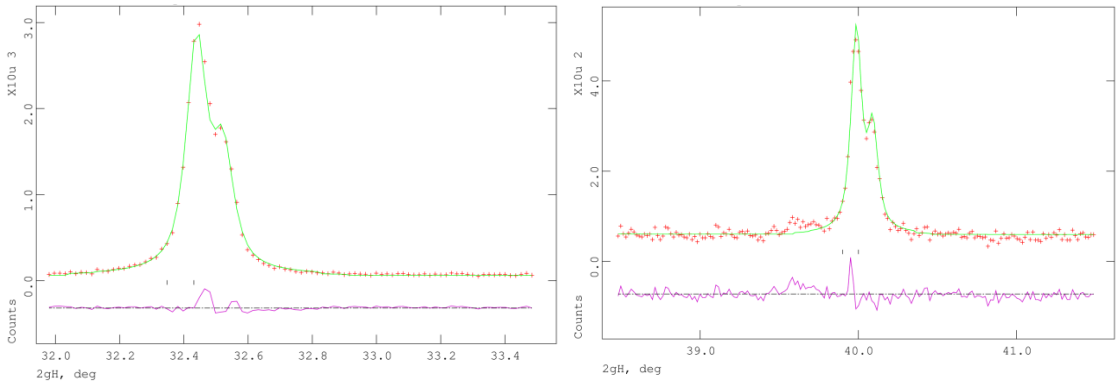

(a) (b)

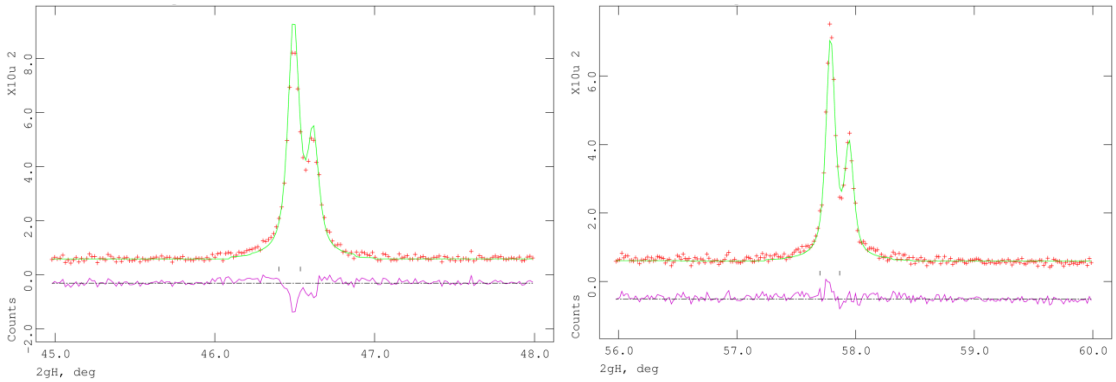

(c) (d)

Fig.7.1.9: Rietveld refinement of the XRD profile of the poled-crushed 10µm grain size BNT ceramic at 550˚C with a $Pm\bar{3}m$ structure model, showing the observed (red circles), calculated (continuous green line) and difference plot (continuous pink line at bottom) for (a) $(110)_{pc}$, (b) $(111)_{pc}$, (c) $(200)_{pc}$ and (d) $(211)_{pc}$. A small shoulder in the plot at 2θ=39.8˚, not fitted by the cubic model, is from the Pt holder. Fitting: wRp_{Pm3m} = 14.18. (The quality of fit for other tested structural models R3c: wRp_{R3c} = 14.69 and *P4bm*: wRp_{P4bm}= 14.35.)

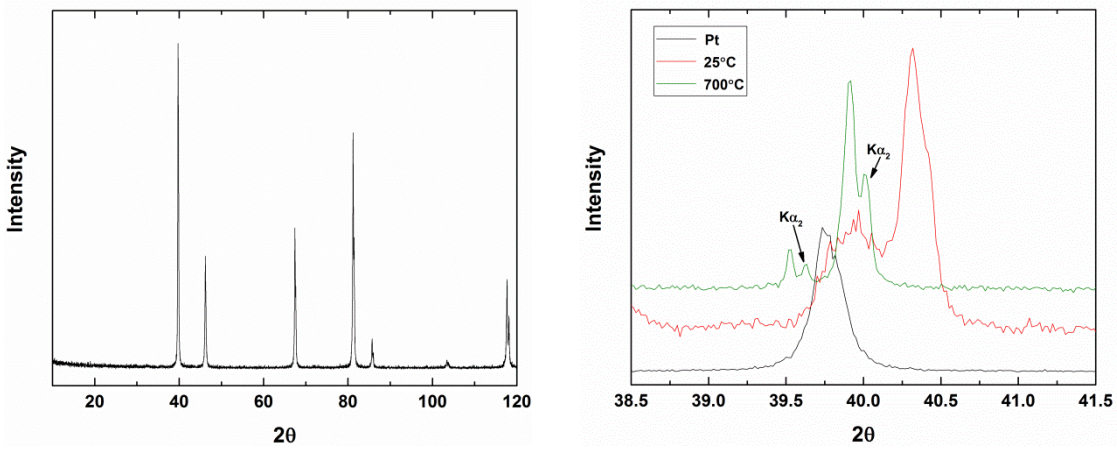

(a) (b)

Fig.7.1.10: (a) Room temperature XRD profile of the Pt holder and (b) showing the overlap of the Pt peak with the $(111)_{pc}$ Bragg peak of the crushed 1.5µm grain size BNT ceramic at 25˚C and 700˚C. The split peak at ~39.5˚ is from the Pt and is not related to the crystal structure of the ceramic.

7.2 Grain Size Effect in 94%$Bi_{0.5}Na_{0.5}TiO_3$-6%$BaTiO_3$: Crystal Structure

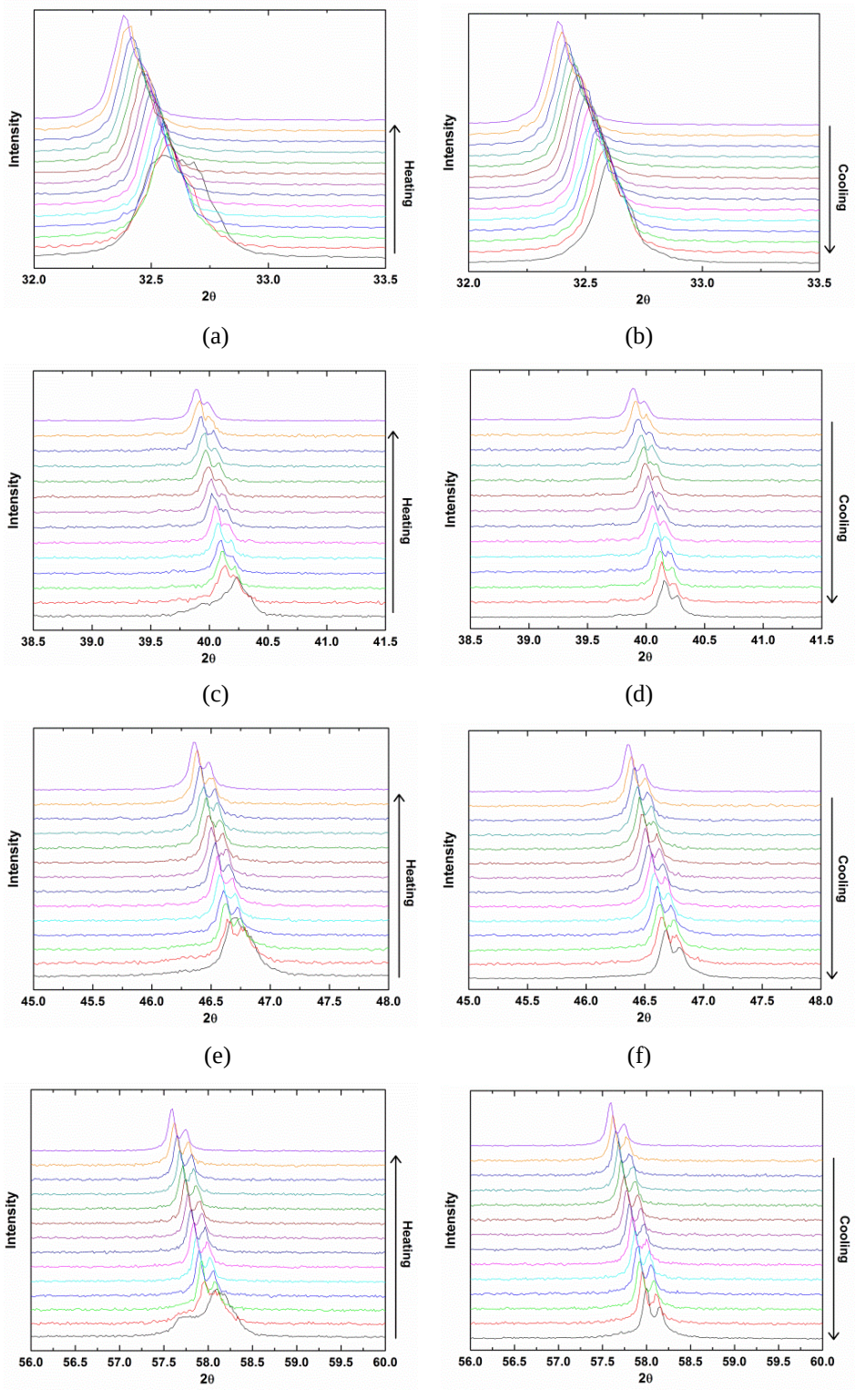

Fig.7.2.1: Powder XRD profiles of the crushed 3.5μm grain size BNBT-6 ceramic showing the temperature evolution during heating and cooling of the Bragg reflections: (a)-(b) $(110)_{pc}$, (c)-(d) $(111)_{pc}$, (e)-(f) $(200)_{pc}$ and (g)-(h) $(211)_{pc}$.

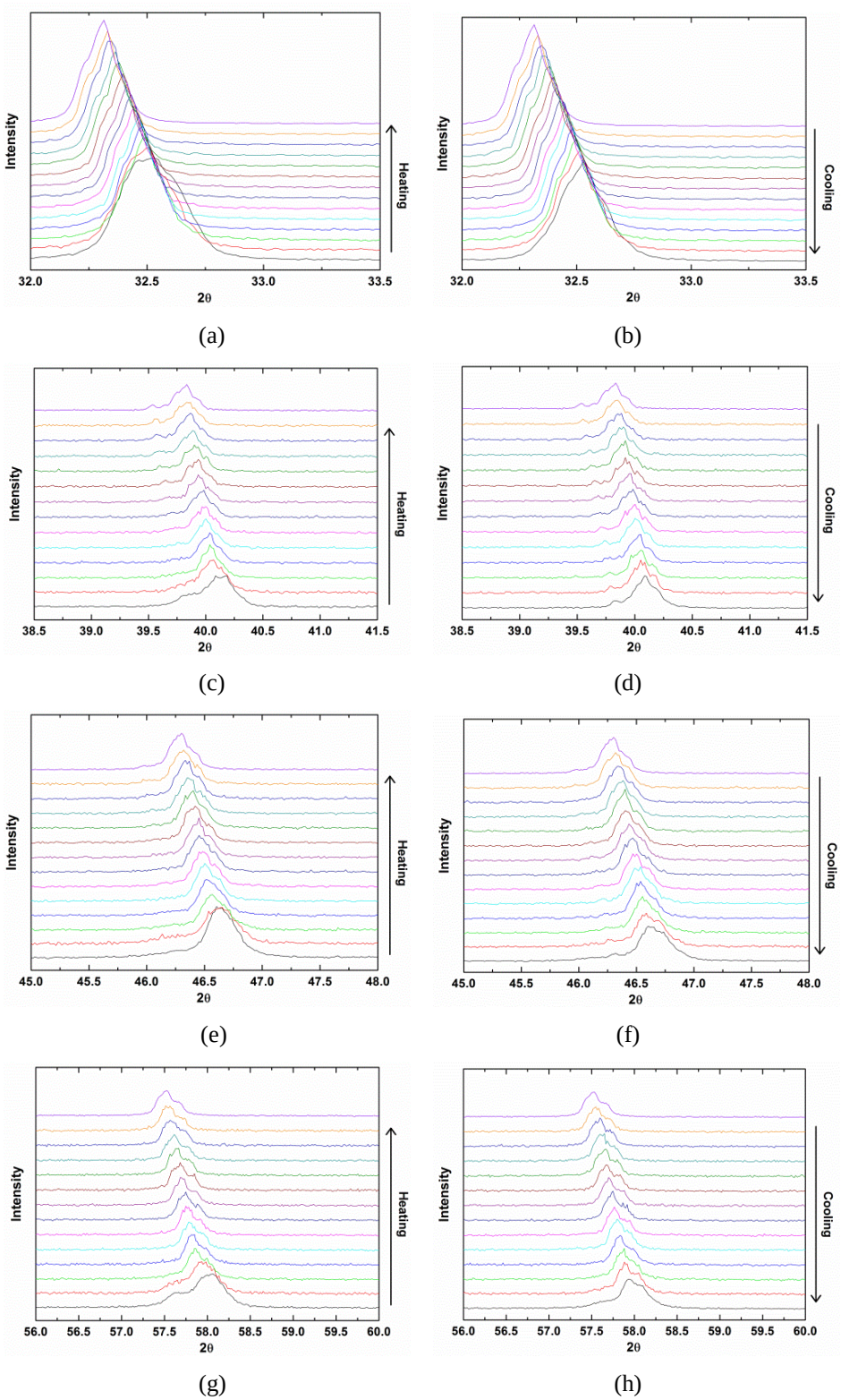

Fig.7.2.2: Powder XRD profiles of the crushed 950 nm grain size BNBT-6 ceramic showing the temperature evolution during heating and cooling of the Bragg reflections: (a)-(b) $(110)_{pc}$, (c)-(d) $(111)_{pc}$, (e)-(f) $(200)_{pc}$ and (g)-(h) $(211)_{pc}$.

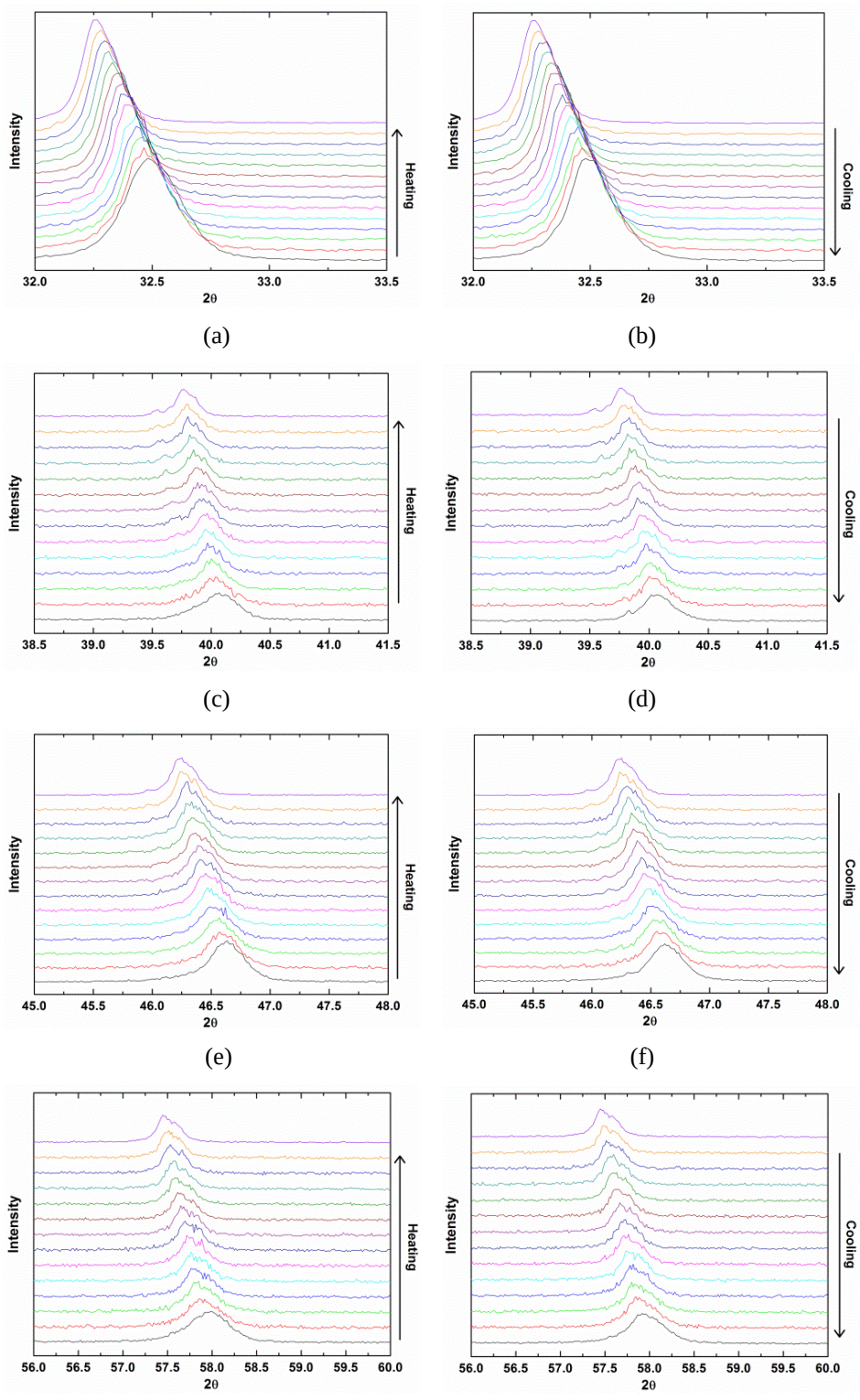

Fig.7.2.3: Powder XRD profiles of the crushed 350 nm grain size BNBT-6 ceramic showing the temperature evolution during heating and cooling of the Bragg reflections: (a)-(b) $(110)_{pc}$, (c)-(d) $(111)_{pc}$, (e)-(f) $(200)_{pc}$ and (g)-(h) $(211)_{pc}$.

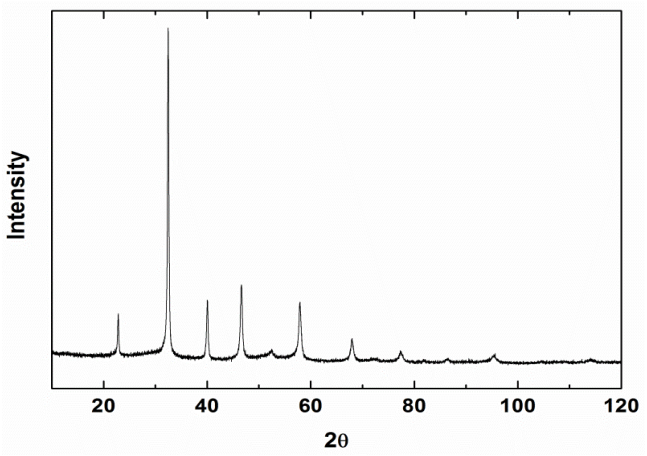

Fig.7.2.4: Powder XRD data collected from the crushed 100 nm grain size BNBT-6 ceramic at room temperature.

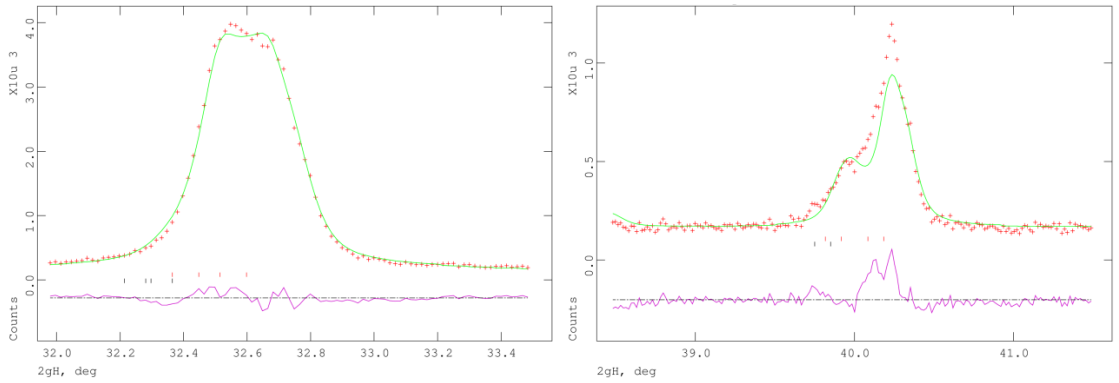

(a) (b)

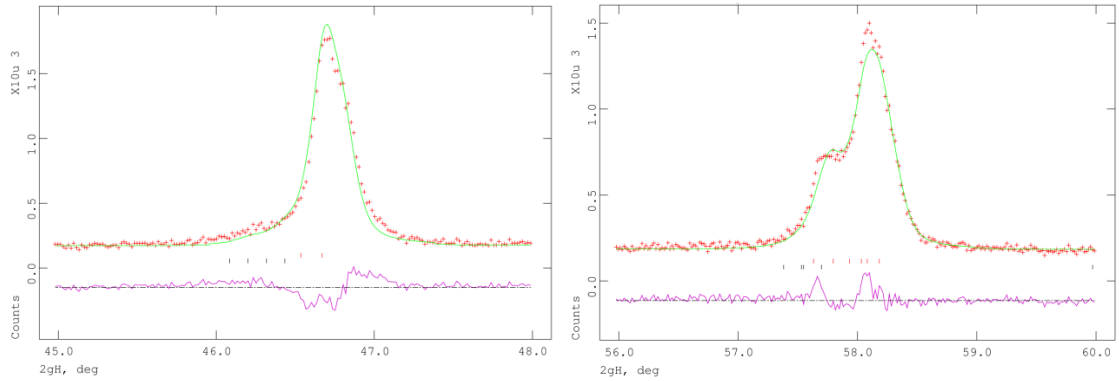

(c) (d)

Fig.7.2.5: Rietveld refinement of the room temperature XRD profile of the crushed 3.5µm grain size BNBT-6 ceramic with a *R3c+P4bm* structure model, showing the observed (red circles), calculated (continuous green line) and difference plot (continuous pink line at bottom) for (a) $(110)_{pc}$, (b) $(111)_{pc}$, (c) $(200)_{pc}$ and (d) $(211)_{pc}$. Fitting: $wRp_{R3c+P4bm}$ = 9.06. (The quality of fit for other tested structural

models *Pm$\bar{3}$m+P4bm*: $wRp_{Pm3m+P4bm}$ = 10.55, *R3c*: wRp_{R3c} = 10.68, *Cc*: wRp_{Cc} =9.46, *P4bm*: wRp_{P4bm}= 11.46 and *Pm$\bar{3}$m*: wRp_{Pm3m} = 11.30.) (a) $(110)_{pc}$, (b) $(111)_{pc}$, (c) $(200)_{pc}$ and (d) $(211)_{pc}$.

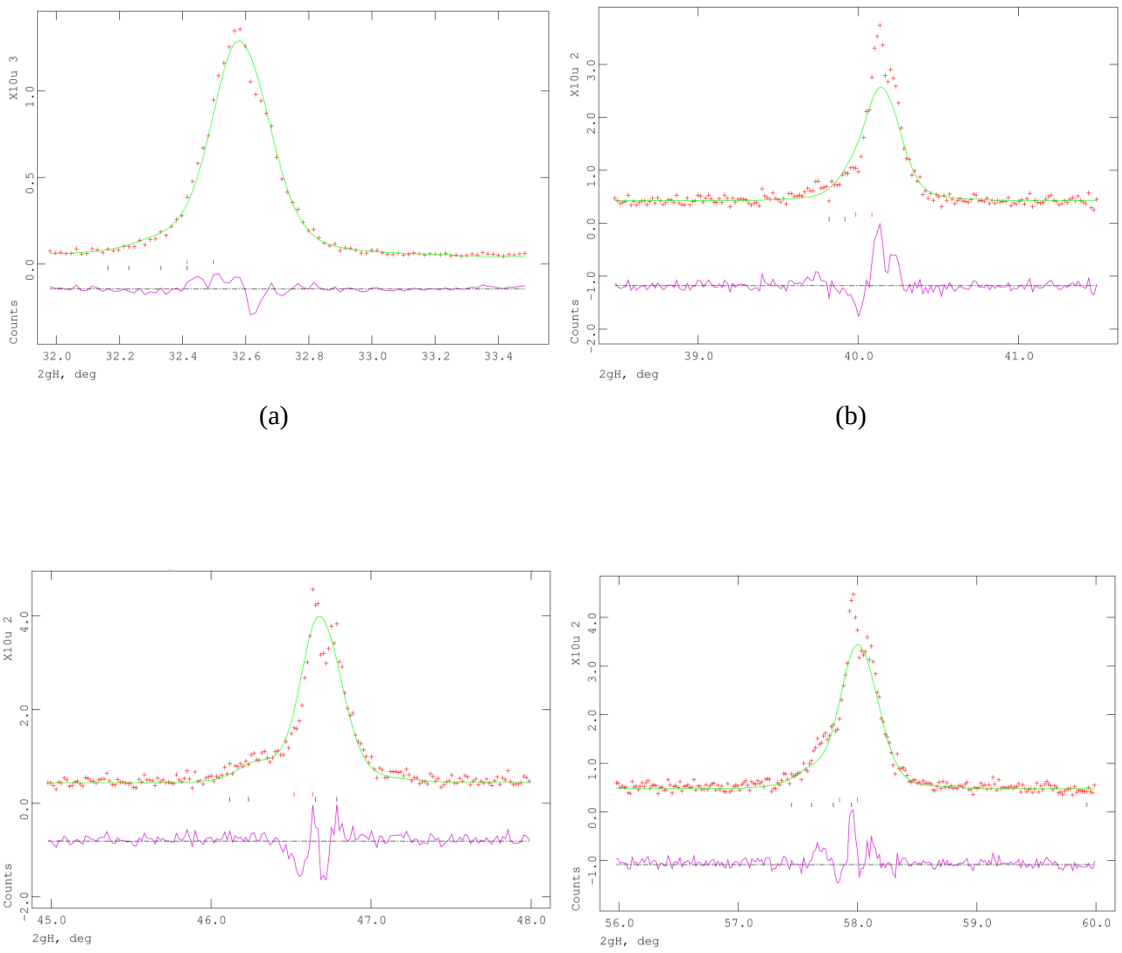

(a) (b)

(c) (d)

Fig.7.2.6: Rietveld refinement of the XRD profile of the crushed 3.5µm grain size BNBT-6 ceramic with a *Pm$\bar{3}$m+P4bm* structure model, at 100˚C, showing the observed (red circles), calculated (continuous green line) and difference plot (continuous pink line at bottom) for (a) $(110)_{pc}$, (b) $(111)_{pc}$, (c) $(200)_{pc}$ and (d) $(211)_{pc}$. Fitting: $wRp_{Pm3m+P4bm}$ = 15.89. (The quality of fit for other tested structural models *R3c+P4bm*: $wRp_{R3c+P4bm}$ = 16.22 and *R3c*: wRp_{R3c} = 16.37.) (a) $(110)_{pc}$, (b) $(111)_{pc}$, (c) $(200)_{pc}$ and (d) $(211)_{pc}$.

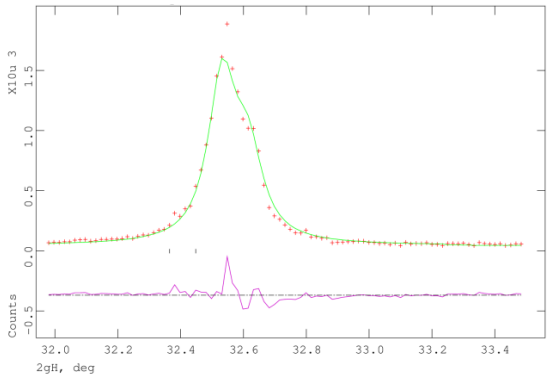
X10u 3
Counts
2gH, deg

(a)

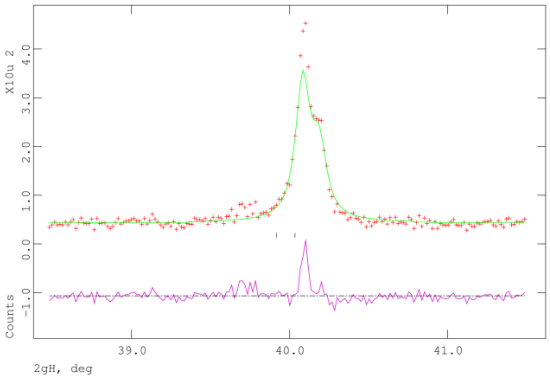
X10u 2
Counts
2gH, deg

(b)

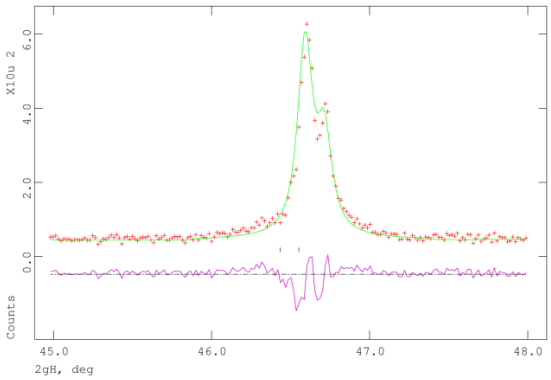
X10u 2
Counts
2gH, deg

(c)

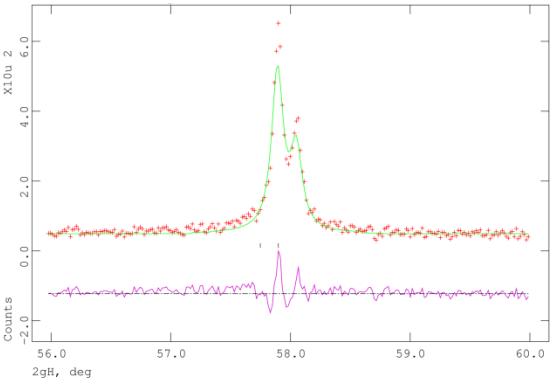
X10u 2
Counts
2gH, deg

(d)

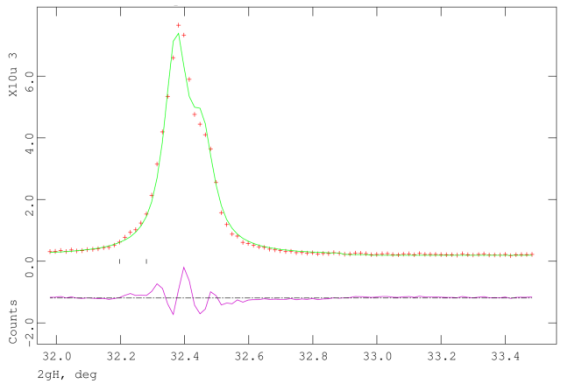
X10u 3
Counts
2gH, deg

(e)

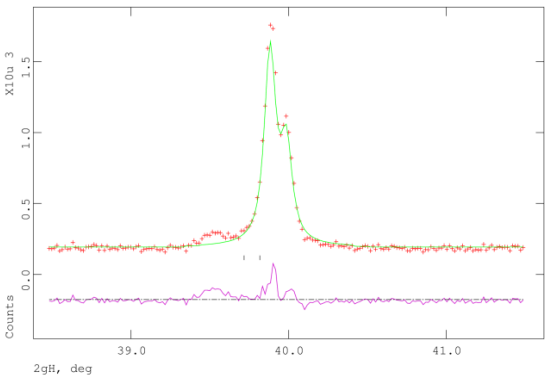
X10u 3
Counts
2gH, deg

(f)

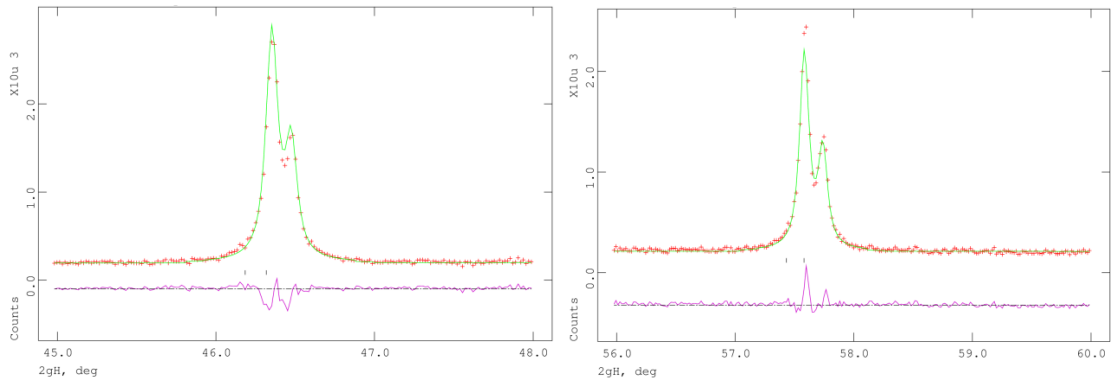

(g) (h)

Fig.7.2.7: Rietveld refinement of the XRD profile of the crushed 3.5µm grain size BNBT-6 ceramic with a $Pm\bar{3}m$ structure model, at (a)-(d) 200˚C (Fitting: wRp_{Pm3m} = 15.98) and (e)-(h) 700˚C (Fitting: wRp_{Pm3m} = 8.74), showing the observed (red circles), calculated (continuous green line) and difference plot (continuous pink line at bottom) for (a), (e) $(110)_{pc}$, (b), (f) $(111)_{pc}$, (c), (g) $(200)_{pc}$ and (d), (h) $(211)_{pc}$. A small shoulder in (b) at 2θ=39.5˚, not fitted by the cubic model, is from the Pt holder.

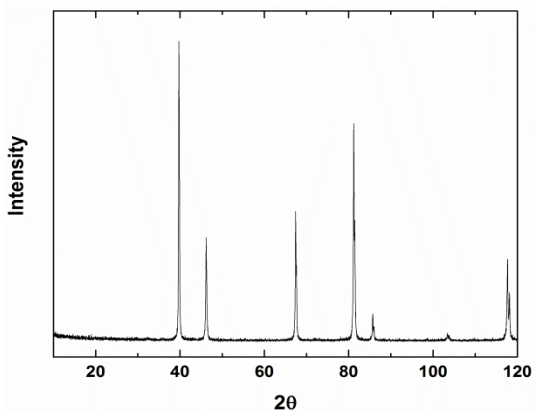

(a)

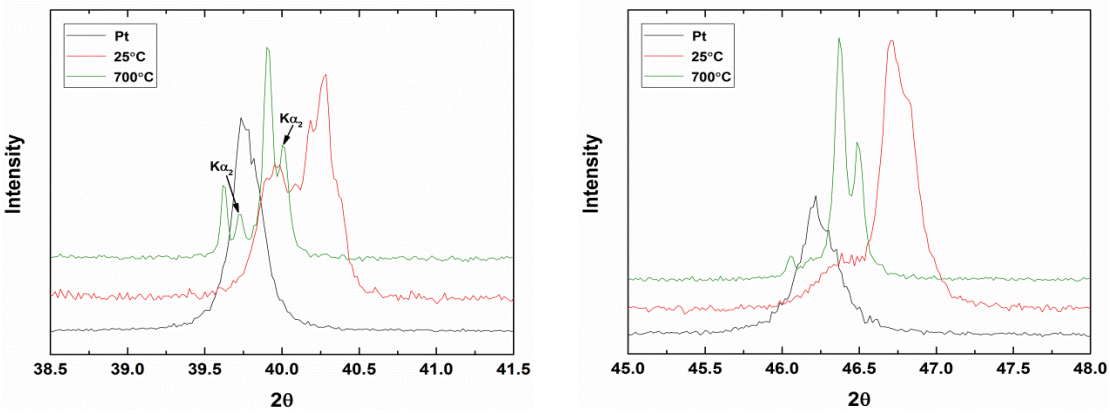

(b) (c)

Fig.7.2.8: (a) Room temperature XRD profile of the Pt holder and showing the overlap of the Pt peak with the (b) $(111)_{pc}$ and (c) $(200)_{pc}$ Bragg peaks of the crushed 6µm grain size BNBT-6 ceramic at 25˚C and 700˚C. The split peak in the 700˚C data at ~39.6˚ is from the Pt and is not related to the crystal structure of the ceramic.

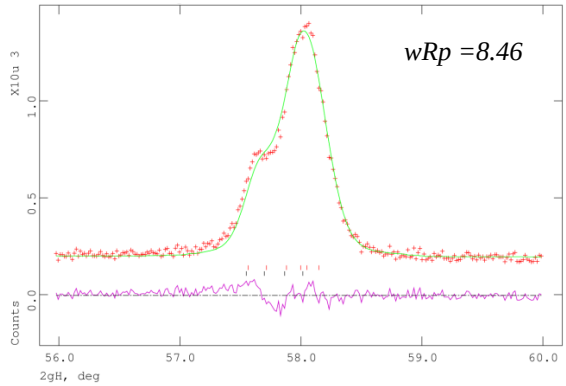

(a1)

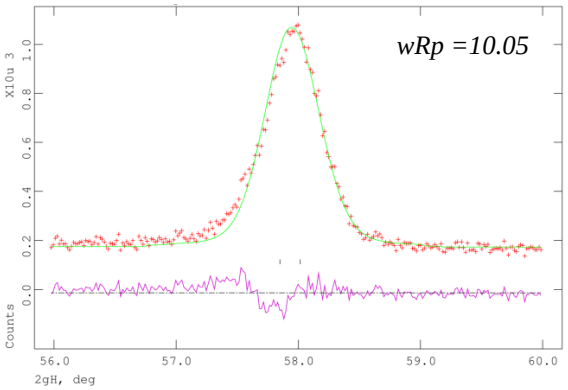

(a2)

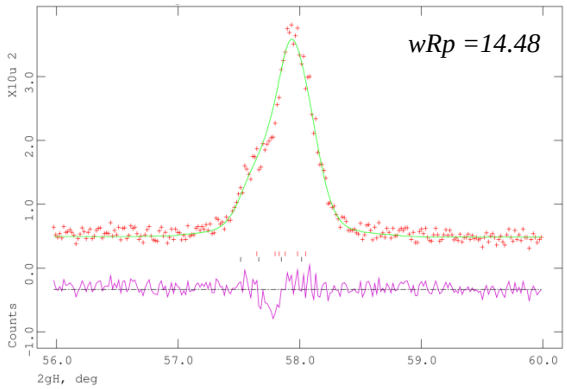

(b1)

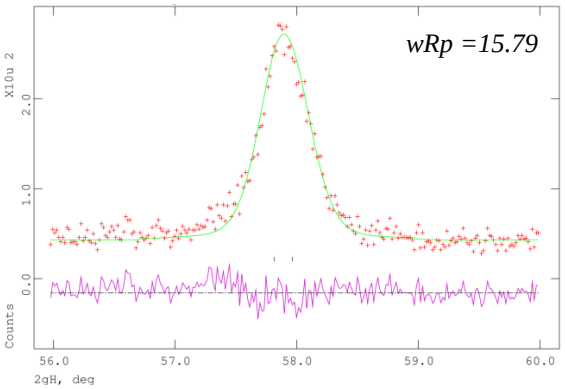

(b2)

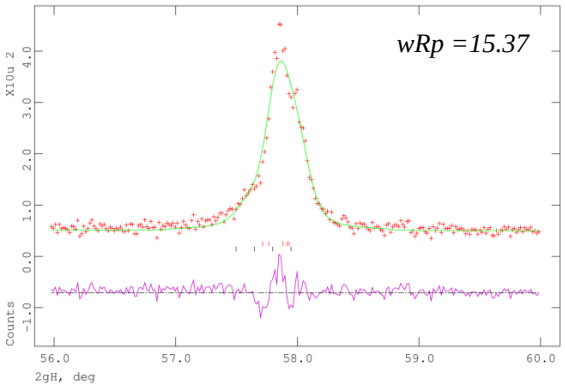

(c1)

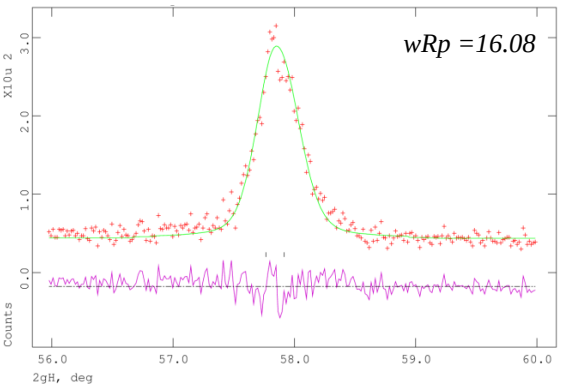

(c2)

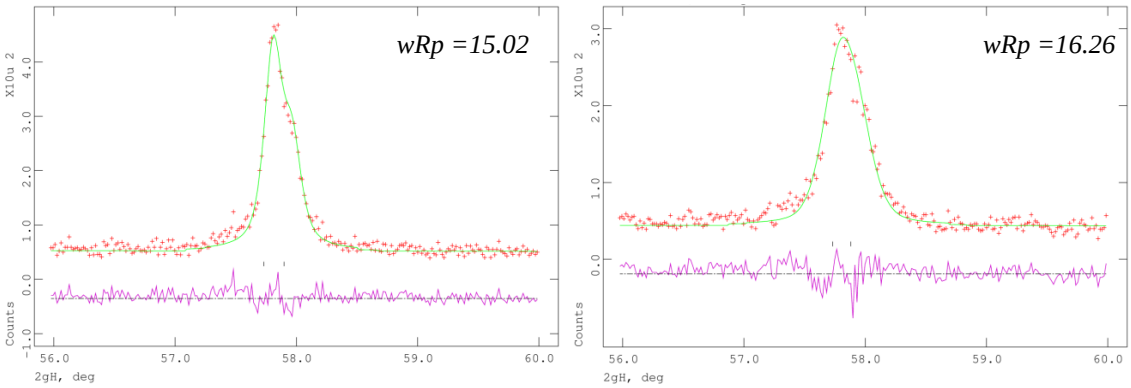

(d1) (d2)

Fig.7.2.9: Rietveld refinement of the XRD profile of the crushed (a1)-(d1) 950nm and (a2)-(d2) 350nm grain size BNBT-6 ceramics with *R3c+P4bm* and $Pm\bar{3}m$ structure models, respectively. Observed (red circles), calculated (continuous green line) and difference plot (continuous pink line at bottom) at (a1)-(a2) 25˚C, (b1)-(b2) 100˚C, (c1)-(c2) 150˚C and (d1)-(d2) 200˚C. Only the $(211)_{pc}$ Bragg peak is shown as it is not effected by any peaks from the Pt holder.

List of Publications

1. Viola, G., **McKinnon, R.**, Koval, V., Adomkevicius, A., Dunn, S., and Yan, H., *Journal of Physical Chemistry*, 2014, **118**, 16, 8564-8570

2. Viola, G., Tan, Y., **McKinnon, R.**, Wei, X., Yan, H., and Reece, M. J., *Applied Physics Letters*, 2014, **105**, 102906

3. Tan, Y., Zhang, J., Wu, Y., Wang, C., Koval, V., Shi, B., Ye, H., **McKinnon, R.**, Viola, G., and Yan, H., *Sci. Rep.*, 2015, **5**, 9953

References

[1] Hao, X., *Journal of Advanced Dielectrics*, 2013, **3**, 1330001

[2] Sawaguchi, E., Maniwa, H., and Hoshino, S., *Physical Review B*, 1951, **83**, 1078

[3] Shirane, G., Sawaguchi, E., and Takagi, Y., *Physical Review B*, 1951, **84**, 476-81

[4] Campbell, C. K., van Wyk, J. D., and Chen, R., *IEEE Transactions of Components and Packaging Technologies*, 2002, **25**, 211-216

[5] Chauhan, A., Patel, S., Vaish, R., and Bowen, C. R., *Materials*, 2015, **8**, 8009-8031

[6] Schönau, K. A., Schmitt, L. A., Knapp, M., Fuess, H., Eichel, R.-A., Kungl, H., and Hoffmann, M. J., *Physical Review B*, 2007, **75**, 184117

[7] Jaffe, B., Roth, R. S., and Marzullo, S., *Journal of Applied Physics*, 1954, **25**, 809-810

[8] Koichiro, S. and Masuda, Y., *Ferroelectrics*, 1974, **7**, 347-349

[9] Zvirgzds, J. A., Kapostinš, P. P., Zvirgzds, J. V., and Kruzina, T. V., *Ferroelectrics*, 1982, **40**, 75-77

[10] Vakhrushev, S. B., Isupov, V. A., Kvyatkovsky, B. E., Okuneva, N. M., Pronin, I. P., Smolenskey, G. A., and Syrnikov, P. P., *Ferroelectrics*, 1985, **63**, 153-160

[11] Jo, W., Schaab, S., Sapper, E., Schmitt, L. A., Kleebe, H.-J., Bell, A. J., and Rödel, J., *Journal of Applied Physics*, 2011, **110**, 074106

[12] Garg, R., Rao, B. N., Senyshyn, A., Krishna, P. S. R., and Ranjan, R., *Physical Review B*, 2013, **88**, 014103

[13] Takenaka, T., Maruyama, K., and Sakata, K., *Japanese Journal of Applied Physics*, 1991, **30**, 9B, 2236-2239

[14] Smolenskii, G. A., Isupov, V. A., Agranovskaya, A. I., Popov, S. N., *Sov. Phys. Solid State*, 1961, **2**, 2584-2594

[15] Kounga, A. B., Zhang S. T., Jo, W., Granzow, T., and Rödel, *J., Appl. Phys. Lett.*, 2008, **92**, 222902

[16] Zhang S. T., Kounga, A. B., Aulbach, E., Ehrenberg, H., and Rödel, *J., Appl. Phys. Lett.*, 2007, **91**, 112906

[17] Nagata, H., Yoshida, M., Makiuki, Y., and Takenaka, T., *Jpn. J. Appl. Phys.*, 2003, **42**, 7401-7403

[18] Viola, G., McKinnon, R., Koval, V., Adomkevicius, A., Dunn, S., and Yan, H., *Journal of Physical Chemistry*, 2014, **118**, 16, 8564-8570

[19] Isupov, V. A., *Ferroelectrics*, 2005, **315**, 123-147

[20] Gorfman, S., and Thomas, P. A., *J. Appl. Cryst.*, 2010, **43**, 1409-1414

[21] Love, G. R., *J. Am. Ceram. Soc.*, 1990, **73**, 323-328

[22] Fletcher, N. H., Hilton, A. D., and Ricketts, B. W., *J. Phys. D: Appl. Phys.*, 1996, **29**, 253-258

[23] Private Communication with Syfer Technology Ltd.

[24] Burn, I., and Smyth, D. M., *Journal of Materials Science*, 1972, **7**, 339-343

[25] Jaffe, B., *Proceedings of the IRE*, 1961, 1264-1267

[26] Hao, X., Zhai, J., Kong, L. B., and Xu, Z., *Progress in Materials Science*, 2014, **63**, 1-57

[27] Shirane, G., Sawaguchi, E., and Takagi, Y., *Phys. Rev.*, 1951, **84**, 476

[28] Shirane, G., *Phys. Rev.*, 1952, **86**, 219

[29] Cross, L. E., *J. Phys. Soc. Jpn.*, 1967, **23**, 77-82

[30] Tan, X., Ma, C., Frederick, J., Beckman, S., and Webber, K. G., *J. Am. Ceram. Soc.*, 2011, **94**, 4091-4107

[31] Shvartsman, V. V., and Lupascu, D. C., *J. Am. Ceram. Soc.*, 2012, **95**, 1-26

[32] Smolenskii, G. A., Isupov, V. A., Agranovskaya, A. I., Popov, S. N., *Sov. Phys. Solid State*, 1961, **2**, 2584-2594

[33] Bokov, A. A., and Ye, Z.-G., *Journal of Materials Science*, 2006, **41**, 31-52

[34] Cross, L. E., *Ferroelectrics*, 1987, **76**, 241-267

[35] Burns, G., and Dacol, F. H., *Solid State Communications*, 1983, **48**, 853-856

[36] Davies, P. K., and Akbas, M. A., *J. Phys. Chem. Solids*, 2000, **61**, 159

[37] Kleemann, W., *Journal of Materials Science*, 2006, **41**, 129-136

[38] Westphal, V., Kleemann, W., and Glinchuk, M., *Phys. Rev. Lett.*, 1992, **68**, 847-850

[39] Kleemann, W., *Int. J. Mod. Phys. B*, 1993, **7**, 2469-2507

[40] Simon, A., Ravez, J., and Maglione, M., *J. Phys.: Condens. Matter*, 2004, **16**, 963-970

[41] Laulhé, C., Hippert, F., Kreisel, J., Maglione, M., Simon, A., Hazemann, J. L., and Nassif, V., *Phys. Rev. B*, 2006, **74**, 014106

[42] Farhi, R., El Marssi, M., Simon, A., and Ravez, J., *Eur. Phys. J. B*, 1999, **9**, 599-604

[43] Imry, I., and Ma, S. K., *Phys. Rev. Lett.*, 1975, **35**, 1399-1401

[44] Viehland, D., Jang, S. J., and Cross, L. E., *J. Appl. Phys.*, 1990, **68**, 2916-2921

[45] Glazounov, A. E., and Tagantsev, A. K., *Appl. Phys. Lett.*, 1998, **73**, 856-858

[46] Levstik, A., Kutnjak, Z., Filipic, C., and Pirc, R., *Phys. Rev. B*, 1998, **57**, 11204-11211

[47] Ye, Z. -G., and Schmid, H., *Ferroelectrics*, 1993, **145**, 83–108

[48] Kim, T., Hanson, J. N., Gruverman, A., Kingon, A. I., and Streiffer, S. K., *Appl. Phys. Lett.*, 2006, **88**, 262907

[49] Noblanc, O., Gaucher, P., and Calvarin, G., *J. Appl. Phys.*, 1996, **79**, 4291–4297

[50] Jiang, F. M., and Kojima, S., *Phys. Rev. B*, 2000, **62**, 8572–8575

[51] Shvartsman, V. V., and Kholkin, A. L., *Phys. Rev. B*, 2004, **69**, 014102
136

[52] Samara, G. A., *J. Phys.: Condens. Matter*, 2003, **15**, R367-R411

[53] Ye, Z.-G., and Schmid, H., *Ferroelectrics*, 1993, **145**, 83-108

[54] Aksel, E., and Jones, J. L., *J. Am. Ceram. Soc.*, 2010, **23**, 10, 3012-3016

[55] Davis, M., *J. Electroceram*, 2007, **19**, 23-45

[56] Jaffe, B., Cook, W. R., Jaffe, H., *Piezoelectric Ceramics* (Academic, 1971)

[57] Noheda, B., *Current Opinion in Solid State Materials Science*, 2002, **6**, 27-34

[58] Haun, M. J., Furman, E., Jang, S. J., and Cross, L. E., *Ferroelectrics*, 1989, **99**, 63

[59] Du, X., Zheng, J., Belegundu, U., and Uchino, K., *Applied Physics Letters*, 1998, **72**, 2421

[60] Noheda, B., Cox, D. E., Shirane, G., Gonzalo, J. A., Cross, L. E., and Park, S.-E., *Applied Physics Letters*, 1999, **74**, 2059

[61] Noheda, B., Gonzalo, J. A., Cross, L. E., Guo, R., Park, S.-E., Cox, D. E., and Shirane, G., *Physical Review B*, 2000, **61**, 8687-8695

[62] Rödel, J., Jo, W., Seifert, K. T. P., Anton, E.-M., and Granzow, T., *J. Am. Ceram. Soc.*, 2009, **92**, 6, 1153-1177

[63] Guo, R., Cross, L. E., Park, S.-E., Noheda, B., Cox, D. E., and Shirane, G., *Physical Review Letters*, 2000, **84**, 5423-5426

[64] Cox, D. E., Noheda, B., Shirane, G., Uesu, Y., Fujishiro, K., and Yamada, Y., *Applied Physics Letters*, 2001, **79**, 400-402

[65] Kisi, E. H., Piltz, R. O., Forrester, J. S., and Howard, C. J., *J. Phys.: Condens. Matter*, 2003, **15**, 3631-3640

[66] Glazer, A. M., Thomas, P. A., Baba-Kishi, K. Z., Pang, G. K. H., and Tai, C. W., *Physical Review B*, 2004, **70**, 184123

[67] Noheda, B., and Cox, D. E., *Phase Transitions*, 2006, **79**, 5-20

[68] Bell, A. J., *Journal of Materials Science*, 2006, **41**, 13-25

[69] Yan, H., Inam, F., Viola, G., Ning, H., Zhang, H., Jiang, Q., Zeng, T., Gao, Z., and Reece, M. J., *Journal of Advanced Dielectrics*, 2011, **1**, 107-118

[70] Jin, Y. M., Wang, Y. U., Khachaturyan, A. G., Li, J. F., and Viehland D., *Journal of Applied Physics*, 2003, **94**, 3629-3640

[71] Wang, Y. U., *Physical Review B*, 2007, **76**, 024108

[72] Viehland, D., *Journal of Applied Physics*, 2000, **88**, 4794-4806

[73] Damjanovic, D., *IEEE Transactions of Ultrasonics, Ferroelectrics, and Frequency Control*, 2009, **56**, 8, 1574-1585

[74] Ahart, M., Somayazulu, M., Cohen, R. E., Ganesh, P., Dera, P., Mao, H., Hemley, R. J., Ren, Y., Liermann, P., and Wu, Z., *Nature*, 2008, **451**, 545-549

[75] Ganesh, P., and Cohen, R. E., *J. Phys.: Condens. Matter*, 2009, **21**, 064225

[76] Wu, Z., and Cohen, R. E., *Physical Review Letters*, 2005, **95**, 037601

[77] Singh, A. K., Mishra, S. K., Ragini, Pandey, D., Yoon, S., Baik, S., and Shin, N., *Applied Physics Letters*, 2008, **92**, 022910

[78] Damjanovic, D., *J. Am. Ceram. Soc.*, 2005, **88**, 2663-2676

[79] Fu, H., and Cohen, R. E., *Nature*, 2000, **403**, 281-283

[80] Cohen, R. E., *Nature*, 2006, **441**, 941-942

[81] Damjanovic, D., *Applied Physics Letters*, 2010, **97**, 062906

[82] Budimir, M., Damjanovic, D., and Setter, N., *Phys. Rev. B*, 2006, **73**, 174106

[83] Heitmann, A. A., and Rossetti, Jr, G. A., *J. Am. Ceram. Soc.*, 2014, **97**, 6, 1661-1685

[84] Kinoshita, K., and Yamaji, A., *Journal of Applied Physics*, 1976, **47**, 371-373

[85] von Arx, A., and Bantle, W., *Helv. Phys. Acta.*, 1944, **17**, 298-318

[86] Smolensky, G. A., Isupov, V. A., Agranovskaya, A. I., and Krainik, N. N., *Soviet Phyics-Solid State*, 1961, **2**, 2651

[87] Buhrer, C. F., *The Journal of Chemical Physics*, 1962, **36**, 798-803

[88] Ivanova, V. V., Kapyshev, A. G., Venevtsev, Yu. N. and Zhdanov, G. S., *Izv. AN SSSR, Ser. fiz.*, 1962, **26**, 354

[89] Hagiyev, M. S., Ismailzade, I. H., and Abiyev, A. K., *Ferroelectrics*, 1984. **56**, 215-217

[90] Gorfman, S., and Thomas, P. A., *J. Appl. Cryst.*, 2010, **43**, 1409-1414

[91] Isupov, V. A., *Ferroelectrics*, 2005, **315**, 123-147

[92] Pronin, I. P., Syrnikov, P. P., Isupov, V. A., Egorov, V. M., Zaitseva, N. V., and Ioffe, A. F. *Ferroelectrics*, 1980, **25**, 395-397

[93] Isupov, V. A., Pronin, I. P., and Kruzina, T. V., *Ferroelectrics Letters*, 1984, **2**, 205-208

[94] Vakhrushev, S. B., Kvyatkovskii, B. E., Malysheva, R. S., Okuneva, N. M., Plachenova, E. L., Syrnikov, P. P., *Kristallografiya*, 1989, 34, 1, 154-158

[95] Suchanicz, J., Roleder, K., Kania, A., and Hańderek, J., *Ferroelectrics*, 1988, **77**, 107-110

[96] Suchanicz, J., and Ptak, W. S., *Ferroelectrics Letters*, 1990, **12**, 71-78

[97] Roleder, K., Suchanicz, J., and Kania, A., *Ferroelectrics*, 1989, **89**, 1-5

[98] Tu. C.-S., Siny, I. G., and Schmidt, V. G., *Physical Review B*, 1994, **49,** 17, 550-559

[99] Siny, I. G., Smirnova, T. A., and Kruzina, T. V., *Ferroelectrics*, 1991, **124**, 207-212

[100] Siny, I. G., Husson, E., Beny, J. M., Lushnikov, S. G., Rogacheva, E. A., and Syrnikov, P. P., *Ferroelectrics*, 2000, **248**, 57-78

[101] Park, S.-E., Chung, S.-J., Kim, I.-T., and Hong, K. S., *J. Am. Ceram. Soc.*, 1994, **77**, 10, 2641-2647

[102] Park, S.-E., and Chung, S.-J., *J. Am. Ceram. Soc.*, 1996, **79**, 5, 1290-1296

[103] East, J., and Sinclair, D. C., *Journal of Materials Science Letters*, 1997, **46**, 422-425

[104] Ge, W., Devreugd, C. P., Phelan, D., Zhang, Q., Ahart, M., Li, J., Luo, H., Boatner, L. A., Viehland, D., and Gehring, P. M., *Physical Review B*, 2013, **88**, 174115

[105] Suchanicz, J., *Materials Science and Engineering*, 1998, **B55**, 114-118

[106] Suchanicz, J., and Kwapuliński, J., *Ferroelectrics*, 1995, **165**, 249-253

[107] Suchanicz, J., Roleder, K., Kwapuliński, J., and Jankowska-Sumara, I., *Phase Transitions*, 1996, **57**, 173-182

[108] Suchanicz, J., *Ferroelectrics*, 1998, **209**, 561-568

[109] Suchanicz, J., *Ferroelectrics*, 1997, **200**, 319-325

[110] Jones, G. O., and Thomas, P. A., *Acta Cryst.*, 2000, **B56**, 426-430

[111] Jones, G. O., and Thomas, P. A., *Acta Cryst.*, 2002, **B58**, 168-178

[112] Geday, M., Kreisel, J., Glazer, A. M., and Roleder, K., *J. Appl. Cryst.*, 2000, **33**, 909-914

[113] Roleder, K., Franke, I., Glazer, A. M., Thomas, P. A., Miga, S., and Suchanicz, J., *J. Phys.: Condens. Matter*, 2002, **14**, 5399-5406

[114] Kreisel, J., Glazer, A. M., Jones, G., Thomas, P. A., Abello, L., and Lucazeua,

G., *J. Phys.: Condens. Matter*, 2000, **12**, 3267-3280

[115] Kreisel, J., Bouvier, P., Dkhil, B., Thomas, P. A., Glazer, A. M., Welberry, T. R., Chaabane, B., and Mezouar, M., *Physical Review B*, 2003, **68**, 014113

[116] Dorcet, V., and Trolliard, G., *Acta Materialia*, 2008, **56**, 1753-1761

[117] Yao, J., Ge, W., Yang, Y., Luo, L., Li, J., Viehland, D., Bhattacharyya, S., Zhang, Q., and Luo, H., *Journal of Applied Physics*, 2010, **108**, 064114

[118] Yao, J., Ge, W., Luo, L., Li, J., Viehland, D., and Luo, H., *Applied Physics Letters*, 2010, **96**, 222905

[119] Jones, G. O., Kreisel, J., Jennings, V., Geday, M. A., Thomas, P. A., and Glazer, A. M., *Ferroelectrics*, 2002, **270**, 191-196

[120] Kreisel, J., Glazer, A. M., Bouvier, P., and Lucazeua, G., *Physical Review B*, 2001, **63**, 174106

[121] Petzelt, J., Kamba, S., Fábry, J., Noujni, D., Porokhonskyy, V., Pashkin, A., Franke, I., Roleder, K., Suchanicz, J., Klein, R., and Kugel, G. E., *J. Phys.: Condens. Matter*, 2004, **16**, 2719-2731

[122] Shuvaeva, V. A., Zekria, D., Glazer, A. M., Jiang, Q., Weber, S. M., Bhattacharya, P., and Thomas, P. A., *Physical Review B*, 2005, **71**, 174114

[123] Prasad, K., Kumari, K., Chandra, K. P., Yadav, K. L., and Sen, S., *Advances in Applied Ceramics*, 2007, **106**, 5, 241

[124] Ge, W., Luo, C., Devreugd, C. P., Zhang, Q., Ren, Y., Li, J., Luo, H., and Viehland, D., *Applied Physics Letters*, 2013, **103**, 241941

[125] Aleksandrova, I. P., Sukhovskiĭ, A. A., Ivanov, Yu. N., Yablonskaya, Yu. E., and Yakhrushev, S. B., *Physics of the Solid State*, 2008, **50**, 3, 496-501

[126] Balagurov, A. M., Koroleva, E. Yu., Naberezhnov, A. A., Sakhnenko, V. P., Savenko, B. N., Ter-Oganessian, N. V., and Vakhrushev S. B., *Phase Transitions*, 2006, **79**, 163-173

[127] Dorcet, V., and Trolliard, G., *Acta Materialia*, 2008, **56**, 1753-1761

[128] Burton, B. P., and Cockayne, E., *Ferroelectrics*, 2002, **270**, 173 Daniels, J. E., Jo, W., Rödel, J., Honkimäki, V., and Jones, J. L., *Acta Materialia*, 2010, **58**, 2103-2111

[129] Gröting, M., and Albe, K., *Physical Review B*, 2014, **89**, 054105

[130] Burton, B. P., and Cockayne, E., *Fundamental Physics of Ferroelectrics*, 2001, **582**, 82-

[131] Gröting, M., Kornev, I., Dkhil, B., and Albe, K., *Physical Review B*, 2012, **86**, 134118

[132] Gröting, M., Hayn, S., and Albe, K., *Journal of Solid State Chemistry*, 2011, **184**, 2041-2046

[133] Levin, I., and Reaney, I. M., *Adv. Funct. Mater.*, 2012, **22**, 3445-3452

[134] Soukhojak, A. N., Wang, H., Farrey, G. W., and Chiang, Y.-M., *Journal of Physics and Chemistry of Solids*, 2000, **61**, 301-304

[135] Yao, J., Ge, W., Luo, L., Li, J., Viehland, D., and Luo, H., *Applied Physics Letters*, 2010, **96**, 222905

[136] Dvořák, V., *Ferroelectrics*, 1974, **7**, 1-9

[137] Yao, J., Yan, L., Ge, W., Luo, L., Li, J., and Viehland, D., *Physical Review B*, 2011, **83**, 054107

[138] Kusz, J., Suchanicz, J., Böhm, H., and Warczewski, J., *Phase Transitions*, 1999, **70**, 223-229

[139] Dorcet, V., Trolliard, G., and Boullay, P., *Chem. Mater.*, 2008, **20**, 5061-5073

[140] Trolliard, G., and Dorcet, V., *Chem. Mater.*, 2008, **20**, 5074-5082

[141] Dorcet, V., Trolliard, G., and Boullay, P., *Journal of Magnetism and Magnetic Materials*, 2009, **321**, 1758-1761

[142] Chou, C.-S., Yang, R.-Y., Chen, J.-H., and Chou, S.-W., *Powder Technology*, 2010, **199**, 264-271

[143] Thomas, P. A., Trujillo, S., Boudard, M., Gorfman, S., and Kreisel, J., *Solid State Sciences*, 2010, **12**, 311-317

[144] Beanland, R., and Thomas, P. A., *Scripta Materialia*, 2011, **65**, 440-443

[145] Gorfman, S., Glazer, A. M., Noguchi, Y., Miyayama, M., Luo, H., and Thomas, P. A., *J. Appl. Cryst.*, 2012, **45**, 444-452

[146] Hao, X., Zhai, J., Kong, L. B., and Xu, Z., *Progress in Materials Science*, 2014, **63**, 1-57

[147] Aksel, E., Forrester, J. S., Kowalski, B., Jones, J. L., Thomas, P. A., Page, K., Suchomel, M. R., *Applied Physics Letters*, 2011, **98**, 152901

[148] Aksel, E., Forrester, J. S., Kowalski, B., Jones, J. L., and Thomas, P. A., *Applied Physics Letters*, 2011, **99**, 222901

[149] Rao, B. N., and Ranjan, R., *Physical Review B*, 2012, **86**, 134103

[150] Rao, B. N., Fitch, A. N., and Ranjan, R., *Physical Review B*, 2013, **87**, 060102

[151] Rao, B. N., Datta, R., Chandrashekaran, S. S., Mishra, D. K., Sathe, V., Senyshyn, A., and Ranjan, R., *Physical Review B*, 2013, **88**, 224103

[152] Jeong, I., Park, C. Y., Kim, D. J., Kim, S., Moon, B. K., Kim, I. W., and Ahn, C. W., *Z. Kristallogr.*, 2011, **226**, 150-154

[153] Keeble, D. S., Barney, E. R., Keen, D. A., Tucker, M. G., Kreisel, J., and Thomas, P. A., *Adv. Funct. Mater.*, 2013, **23** 185-190

[154] Aksel, E., Forrester, J. S., Nino, J. C., Page, K., Shoemaker, D. P., and Jones, J. L., *Physical Review B*, 2013, **87**, 104113

[155] Davis, M., Budimir, M., Damjanovic, D., and Setter, N., *Journal of Applied Physics*, 2007, **101**, 054112

[156] Ma, C., Guo, H., Tan, X., *Adv. Funct. Mater.*, 2013, **23**, 5261-5266

[157] Beanland, R., and Thomas, P. A., *Physical Review B*, 2014, **89**, 174102

[158] Chu, B.-J., Chen, D.-R., Li, G.-R., and Yin, Q.-R., *Journal of the European Ceramic Society*, 2002, **22**, 2115-2121

[159] Zhang, S.-T., Kounga, A. B., Aulbach, E., and Deng, Y., *J. Am. Ceram. Soc.*, 2008, **91**, 3950-3954

[160] Zhang, S.-T., Kounga, A. B., Aulbach, E., Ehrenberg, H., and Rödel, J., *Applied Physics Letters*, 2007, **91**, 112906

[161] Xu, C., Lin, D., and Kwok, K. W., *Solid State Sciences*, 2008, **10**, 934-940

[162] Ma, C., Tan, X., Dul'kin, E., and Roth, M., *Journal of Applied Physics*, 2010, **108**, 104105

[163] Ma, C., and Tan, X., *Solid State Communications*, 2010, **105**, 1497-1500

[164] Craciun, F., Galassi, C., and Birjega, R., *Journal of Applied Physics*, 2012, **112**, 124106

[165] Chen, C.-S., Chen, P.-Y., and Tu, C.-S., *Journal of Applied Physics*, 2014, **115**, 014105

[166] Ranjan, R., and Dviwedi, A., *Solid State Communications*, 2005, **135**, 394-399

[167] Chen, M., Xu, Q., Kim, B. H., Ahn, B. K., Ko, J. H., Kang, W. J., and Nam, O. J., *Journal of the European Ceramic Society*, 2008, **28**, 843-849

[168] Rout, D., Moon, K.-S., Rao, V. S., and Kang, S.-J. L., *Journal of the Ceramic Society of Japan*, 2009, **117**, 797-800

[169] Eerd, B. W., Damjanovic, D., Klein, N., Setter, N., and Trodahl, J., *Physical Review B*, 2010, **82**, 104112

[170] Luo, L., Ge, W., Li, J., Viehland, D., Farley, C., Bodnar, R., Zhang, Q., and Luo H., *Journal of Applied Physics*, 2011, **109**, 113507

[171] Ma, C., and Tan, X., *J. Am. Ceram. Soc.*, 2011, **94**, 4040-4044

[172] Datta, K., Richer, A., Göbbels, M., Neder, R. B., and Mihailova, B., *Physical Review B*, 2014, **90**, 064112

[173] Ge, W., Cao, H., DeVreugd, C., Li, J., and Viehland, D., *J. Am. Ceram. Soc.*, 2011, **94**, 3084-3087

[174] Yao, Y., Yang, Y., Ren, S., Zhou, C., Li, L., and Ren, X., *EPL*, 2012, **100**, 17004

[175] Cordero, F., Craciun, F., Trequattrini, F., Mercadelli, E., and Galassi, C., *Physical Review B*, 2010, **81**, 144124

[176] Yao, Y., Sun, Z., Ji, Y., Yang, Y., Tan, X., and Ren, X., *Sci. Technol. Adv. Mater.*, 2013, **14**, 035008

[177] Yao, J., Monsegue, N., Murayama, M., Leng, W., Reynolds, W. T., Zhang, Q., Luo, H., Li, J., Ge, W., and Viehland, D., *Applied Physics Letters*, 2012, **100**, 012901

[178] Zhang, H., Deng, G., Studer, A. J., Li, X., Zhao, X., and Luo, H., *Scripta Materialia*, 2014, **86**, 5-8

[179] Foronda, H., Deluca, M., Aksel, E., Forrester, J. S., and Jones, J. L., *Materials Letters*, 2014, **115**, 132-135

[180] Schutz, D., Deluca, M., Krauss, W., Feteira, A., Jackson, T., and Reichmann, K., *Adv. Funct. Mater.*, 2012, **22**, 2285-2294

[181] Maurya, D., Murayama, M., Pramanick, A., Reynolds, W. T., An, K., and Priya, S., *Journal of Applied Physics*, 2013, **113**, 114101

[182] Jo, W., and Rödel, J., *Applied Physics Letters*, 2011, **99**, 042901

[183] Simons, H., Daniels, J., Jo, W., Dittmer, R., Studer, A., Avdeev, M., Rödel, J., and Hoffman, M., *Applied Physics Letters*, 2011, **98**, 082901

[184] Daniels, J., Jo, W., Rödel, J., Rytz, D., and Donner, W., *Applied Physics Letters*, 2011, **98**, 252904

[185] Picht, G., Töpfer, J., and Hennig, E., *Journal of the European Ceramic Society*, 2010, **30**, 3445-3453

[186] Daniels, J. E., Jo, W., Rödel, J., and Jones, L. J., *Applied Physics Letters*, 2009, **95**, 032904

[187] Jo, W., Daniels, J. E., Jones, J. L., Tan, X., Thomas, P. A., Damjanovic, D., and Rödel, J., *Journal of Applied Physics*, 2011, **109**, 014110

[188] Daniels, J. E., Jo, W., Rödel, J., Honkimäki, V., and Jones, J. L., *Acta Materialia*, 2010, **58**, 2103-2111

[189] Simons, H., Daniels, J. E., Glaum, J., Studer, A.J., Jones, J. L., and Hoffman, M., Applied Physics Letters (2013) **102**, 062902

[190] Jo, W., Daniels, J., Damjanovic, D., Kleemann, W., and Rödel, J., *Applied Physics Letters*, 2013, **102**, 192903

[191] Shi, J., Fan, H., Liu, X., and Li, Q., *Phys. Status Solidi A*, 2014, 1-6

[192] Maurya, D., Pramanick, A., Feygenson, M., Neuefeind, J. C., Bodnar, R. J., and Priya, S., *J Mater. Chem. C.*, 2014, **2**, 8423

[193] Zeng, W., Zhou, X., Chen, J., Liao, J., Zhou, C., Cen, Z., Yang, T., Yang, H., Zhou, Q., Chen, G., and Yuan C., *Applied Physics Letters*, 2014, **104**, 242910

[194] Schneider, D., Jo, W., Rödel, J., Rytz, D., and Granzow, T., *Journal of Applied Physics*, 2014, **116**, 044111

[195] Ge, W., Yao, J., DeVreugd, C., Li, J., Viehland, D., Zhang, Q., and Luo, H., *Solid State Communications*, 2011, **151**, 71-74

[196] Luo, C., Ge, W., Zhang, Q., Li, J., Luo, H., and Viehland, D., *Applied Physics Letters*, 2012, **101**, 141912

[197] Ge, W., Luo, C., Zhang, Q., Devreugd, C. P., Ren, Y., Li, J., Luo, H., and Viehland, D., *Journal of Applied Physics*, 2012, **111**, 093508

[198] Ma, C., Guo, H., Beckman, S. P., and Tan, X., *Physics Review Letters*, 2012, **109**, 107602

[199] Kitanaka, Y., Ogino, M., Hirano, K., Noguchi, Y., Miyayama, M., Kagawa, Y., Moriyoshi, C., Kuroiwa, Y., Torii, S., and Kamiyama, T., *Japanese Journal of Applied Physics*, 2013, **52**, 09KD01

[200] Ma, C., Guo, H., and Tan, X., *Adv. Funct. Mater.*, 2013, **23**, 5261-5266

[201] Zheng, M., Hou, Y., Zhu, M., Zhang, M., and Yan H., *Journal of the European Ceramic Society*, 2014, **34**, 2275-2283

[202] Carreaud, J., Gemeiner, P., Kiat, J. M., Dkhil, B., Bogicevic, C., Rojac, T., and Malic, B., *Physical Review B*, 2005, **72**, 174115

[203] Algueró, M., Ricote, J., Jiménez, R., Ramos, P., Carreaud, J., Dkhil, B., Kiat, J. M., Holc, J., and Kosec, M., *Applied Physics Letters*, 2007, **91**, 112905

[204] Spaldin, N. A., *Science*, 2004, **304**, 1606-1607

[205] Kniepkamp, H. and Heywang, W., *Z. Angew. Phys.*, 1954, **6**, 385

[206] Ghosh, D., Sakata, A., Carter, J., Thomas, P. A., Han, H., Nino, J. C., and Jones, J. L., *Adv. Funct. Mater.*, 2014, **24**, 885-896

[207] Buessem, W. R., Cross, L. E., Goswami, A. K., *J. Am. Ceram. Soc.*, 1966, **49**, 33

[208] Tan, Y., Zhang, J., Wu, Y., Wang, C., Koval, V., Shi, B., Ye, H., McKinnon, R., Viola, G., and Yan, H., *Sci. Rep.*, 2015, **5**, 9953

[209] Martirena, H. T., and Burfoot, J. C., *J. Phys. C: Solid State Phys.*, 1974, **7**, 3182-3192

[210] Buessem, W. R., Cross, L. E., Goswami, A. K., *J. Am. Ceram. Soc.*, 1966, **49**, 36

[211] Yoon, S., Dornseiffer, J., Xiong, Y., Grüner, D., Shen Z., Iwaya, S., Pithan, C., Waser, R., *J. Eur. Ceram. Soc.* 2011, **31**, 1723

[212] Uchino, K., Sadanaga, E., and Hirose, T., *J. Am. Ceram. Soc.*, 1989, **72**, 1555-1558

[213] Arlt, G., Hennings, D., and de With, G., *Journal of Applied Physics*, 1985, **58**, 1619-1625

[214] Känzig, W., *Phys. Rev.*, 1955, **98**, 549-550

[215] Arlt, G., *Ferroelectrics*, 1987, **76**, 451

[216] Arlt, G., and Pertsev, N. A., *Journal of Applied Physics*, 1991, **70**, 2283-2289

[217] Pertsev, N. A., and Arlt, G., *Journal of Applied Physics*, 1993, **74**, 4105-4112

[218] Frey, M. H., and Payne, D. A., *Physical Review B*, 1996, **54**, 3158-316

[219] Shih, W. Y., Shih, W.-H., and Aksay, I. A., *Physical Review B*, 1994, **50**, 15576-15585

[220] Frey, M. H., Xu, Z., Han, P., and Payne, D. A., *Ferroelectrics*, 1998, **206-207**, 337-353

[221] Zhao, Z., Buscaglia, V., Viviani, M., Buscaglia, M. T., Mitoseriu, L., Testino, A., Nygren, M., Johnsson, M., and Nanni, P., *Physical Review B*, 2004, **70**, 024107

[222] Buscaglia, M. T., Viviani, M., Buscaglia, V., Mitoseriu, L., Testino, A., Nanni, P., Zhao, Z., Nygren, M., Harnagea, C., Piazzi, D., and Galassi, C., *Physical Review B*, 2006, **73**, 064114

[223] Xiao, C. J., Jin, C. Q., and Wang, X. H., *Materials Chemistry and Physics*, 2008, **111**, 209-212

[224] Deng, X., Wang, X., Wen, H., Chen, L., Chen, L., and Li, L., *Applied Physics Letters*, 2006, **88**, 252905

[225] Wang, X., Deng, X., Wen, H., and Li, L., *Applied Physics Letters*, 2006, **89**, 162902

[226] Petkov, V., Buscaglia, V., Buscaglia, M. T., Zhao, Z., and Ren, Y., *Physical Review B*, 2008, **78**, 054107

[227] Fang, C., Zhou, D., and Gong, S., *Physica B*, 2011, **406**, 1317-1322

[228] Zhao, M.-L., Wang, C.-L., Zhong, W.-L., Wang, J.-F., and Li, Z.-F., *Chin.*

Phys. Lett., 2003, **20**, 290-292

[229] Zhang, H., Yan, H., Ning, H., Reece, M. J., Eriksson, M., Shen, Z., Kan, Y., and Wang, P., *Nanotechnology*, 2009, **20**, 385708

[230] Viola, G., Chong, K. B., Eriksson, M., Shen, Z., Zeng, J., Yin, Q., Kan, Y., Wang, P., Ning, H., Zhang, H., Fitzpatrick, M. E., Reece, M. J., and Yan, H., *Applied Physics Letters*, 2013, **103**, 182903

[231] Buessem, W. R., Cross, L. E., and Goswami, A. K., *J. Am. Ceram. Soc.*, 1966, **49**, 33-36

[232] Jiang, Q., Ning, H., Zhang, Q., Cain, M., Reece, M. J., and Yan, H., *J. Mater. Chem. C*, 2013, **1**, 5628-5631

[233] Jiang, Q. H., Liu, F. T., Nan, C.-W., Lin, Y.-H., Reece, M. J., Yan, H. X., Ning, H. P., and Shen, Z. J., *Applied Physics Letters*, 2009, **95**, 012909

[234] Eriksson, M., Yan, H., Viola, G., Ning, H., Gruner, D., Nygren, M., Reece, M. J., and Shen, Z., *J. Am. Ceram. Soc.*, 2011, **94**, 3391-3396

[235] Arlt, G., *Ferroelectrics*, 1990, **104**, 217-227

[236] Jublot, M., and Texier, M., *Micron*, 2014, **56**, 63-67

[237] Booker, G. R., Shaw, A. M. B, Whelan, M. J., and Hirsch, P. B., *Philos. Mag.*, 1967, **16**, 1185-91

[238] Kamaladasa, R. J., and Picard, Y. N., *Microscopy: Science, Technology, Applications and Education*, 2010, 1583-1590

[239] Grüner, D., and Shen, Z., *J. Am. Ceram. Soc.*, 2010, **93**, 48-50

[240] Potnis, P. R., Tsou, N.-T., and Huber, J. E., *Materials*, 2011, **4**, 417-447

[241] Kalinin, S. V., and Bonnell, D. A., *Physical Review B*, 2002, **65**, 125408